

**Dolomitization in the Uteland Butte Member of the Eocene Green River Formation,  
Uinta Basin, Utah**

by

Federico Rueda Chaparro

A thesis submitted in partial fulfillment of the requirements for the degree of

Master of Science

Department of Earth and Atmospheric Sciences  
University of Alberta

© Federico Rueda Chaparro, 2018

## ABSTRACT

The lacustrine Green River Formation (GRF) is an important oil-producing formation in the Uinta Basin, Utah (USA). In recent years, the unconventional carbonate reservoirs in the Uteland Butte member (UBM), base of the GRF, have been targeted because their estimated oil and gas resources. The stratigraphic interval of interest is limited by the D and C Shales, in which there are three dolomite layers named PZ2, PZ1', and PZ1 that vary from 1.5 to 8 feet in thickness and have up to 30% porosity but only a maximum of 0.1 mD permeability.

The objectives for this study are to characterize the depositional facies types and determine how they are related to dolomitization, to elucidate the dolomitization and how porosity and permeability are related this process, and to delineate the regional geometry of the dolomite layers. This study employed several methods: outcrop and core descriptions; petrographic analysis (transmitted light, cathodoluminescence, and scanning electron microscopy); mineralogical identification and ordering of dolomites (XRD); elemental composition of dolomite crystals (EDS and EMPA); major and trace element analysis (ICP-MS); and conventional and clumped oxygen and carbon stable isotope.

Deposition of the Uteland Butte member took place during transgressive-regressive cycles that were driven by climate variations. The PZ layers were deposited in a shallow littoral environment as intraclastic, grainstones, and ooid ostracod grainstone-packstone, and in the sublittoral environments as mudstone, peloidal bioturbated mudstones, and ostracod wackestones. The carbonate facies are dolomitized to variable degrees and are characterized by (i) selective dolomitization of matrix, peloids, ooids, and intraclast, and (ii) variable preservation



of the precursor textures. However, bioclasts are not dolomitized. The dolomitization process crosscut all facies boundaries from the distal sublittoral setting toward the littoral near-shore area. There is no discernible relationship between dolomitization and facies.

Dolomites are characterized by %Ca that ranges from 49% to 59% with a strong mode in 52 to 55%, and low cation ordering that range from 0.2 to 0.5.  $\delta^{13}\text{C}$  for dolomite range from 6‰ to -5.4‰ (VPDB) suggesting a high organic activity and/or organic matter decay, coupled with organic matter oxidation by sulfate reducing bacteria. The  $\delta^{18}\text{O}$  for dolomite range from 0.9 to -7.3‰ (VPDB) and it is interpreted as gradual increase in lake water temperature. The calculated dolomitizing fluid temperature is between 14 to 36 °C. Dolomitization was driven by climate changes. During the warmer climate periods, evaporation and reduced river inflow increased salinity sufficiently to create density-driven reflux of lake water in the subaqueous parts of the lake area, which promoted dolomitization. At the same time, the landward parts of the lake fell dry to form a playa, where dolomite formed from evaporating groundwater by evaporative pumping. This process overprinted the areas previously dolomitized by reflux. Dolomitization in the Uteland Butte member is thus interpreted as the result of two different and superimposed processes: density-driven reflux and evaporative pumping.

Increased fresh water input during more humid climate periods stopped dolomitization and promoted deposition of lime mud.  $\delta^{13}\text{C}$  for calcite range from 1‰ to -1‰ (VPDB), and the  $\delta^{18}\text{O}$  range from -5.8 to -10.1‰ (VPDB), with a calculated temperature for calcite precipitation of around 3 and 12 °C.

The dolomite crystal sizes range from 0.25 to 6  $\mu\text{m}$  and porosity is mainly intercrystal. Dolomite layers PZ1, PZ1', and PZ2 display four dolomite textures: planar e, planar s, nonplanar-a, and planar-c. Dolomitization contributed to the lithification of the lime mud sediments preserving the primary porosity inherited from the parental lime mud

sediments/limestone. Moreover, the mole-per-mole dolomite-calcite replacement likely enhanced the porosity of the PZ layers. Dolomite crystals planar-e, planar-s and nonplanar-a textures are correlated with porosity and permeability. Planar textures (planar-e and planar-s) are associated with the highest values of porosity and permeability. However, dolomite textures, crystal size, and shapes are highly variable throughout the PZ layers. In general, the variations in porosity and permeability within each PZ layer and across the entire study area are too small to influence exploration or development strategies. The best areas for exploration and development are the ones that are most highly overpressured, generally toward the basin center.

## ACKNOWLEDGMENTS

I would like to express my most sincere gratefulness to the Utah Geological Survey for providing the funding and the information for this research, and especially to Michael D Vanden Berg who envisaged this project.

Also, I would like to express my deep gratitude to Dr. Hans G. Machel for having opened the door and let me to start my most significant project, for his recurrent and enriching discussions, for his patience, and for his useful criticism to my work. I learnt too much from Dr. Machel not only in the scientific but also in the personal field.

I would also like to thank Dr. David L. Bish, Dr. Stephen E. Kaczmarek, and Dr. Stefano Bernasconi for their invaluable help, discussions, and constructive recommendations.

I must say thank you to my wife Maria Mercedes Molina Rojas for having accepted my offer to come to Canada and leave almost everything that matters to her. I know she has been doing a big sacrifice but I am also sure that we will be picking the harvest sooner than later...“¡Gracias amor!” My children Esteban, Santiago, and Sara were also one of the most important reasons that let me think on continue with my graduate studies. All my efforts, projects, and goals are because of you; my loved children. Finally, I am so grateful to my parents Nhora and Serafin, to my brothers and sister Gustavo, Laura, Nicolas, Andres and Cristian who always have encouraged me to pursue my goals.

## TABLE OF CONTENTS

	Page
<b>CHAPTER 1 INTRODUCTION.....</b>	<b>1</b>
1.1 Research objectives.....	4
1.2 Previous work .....	4
1.3 Study area and stratigraphic interval of interest .....	7
1.4 Dolomite theoretical framework .....	8
 <b>CHAPTER 2 GEOLOGICAL FRAMEWORK.....</b>	 <b>12</b>
2.1 Basin and lake evolution.....	12
2.2 Paleohydrology .....	14
2.3 Sedimentology .....	16
2.4 Stratigraphy.....	17
2.5 Facies and Depositional Environments.....	18
 <b>CHAPTER 3 METHODOLOGY .....</b>	 <b>20</b>
3.1 Field work: Outcrops .....	20
3.2 Core description and sampling.....	21
3.3 Petrography .....	23
3.3.1 Transmitted light microscopy .....	23
3.3.2 Cathodoluminescence microscopy.....	24
3.3.3 Scanning electron microscopy (SEM) .....	24
3.4 X-Ray diffractometry.....	25
3.5 Major and Trace Elements Analysis .....	26

3.5.1	Electron microprobe analysis (EMPA) .....	26
3.5.2	Inductively coupled plasma mass spectrometry (ICP-MS) analysis .....	26
3.6	Stable Isotope Analysis .....	27
3.6.1	Conventional carbon and oxygen stable isotope analysis .....	27
3.6.2	Clumped isotopes .....	29
<b>CHAPTER 4</b>	<b>FACIES .....</b>	<b>30</b>
4.1	Lithofacies .....	33
4.1.1	Silty mudstone - F1 .....	33
4.1.2	Lime mudstone – F2 .....	35
4.1.3	Ostracod wackestone – F3 .....	37
4.1.4	Peloid wackestone – packstone – F4 .....	39
4.1.5	Mollusc wackestone – floatstone – F5 .....	41
4.1.6	Intraclast packstone- grainstone – F6 .....	44
4.1.7	Ooid grainstone – packstone – F7 .....	46
4.1.8	Ostracod grainstone – packstone – F8 .....	48
4.1.9	Brown claystone – F9 .....	50
4.1.10	Coal - F10 .....	52
4.2	Facies associations .....	53
4.2.1	Marginal swamp (A) .....	55
4.2.2	Marginal carbonates (B) .....	55
4.2.3	Massive carbonates (C) .....	56
4.2.4	Laminated oil rich mudstones (D) .....	56
4.3	Facies successions and cyclicity .....	58
4.4	Facies and dolomitization .....	61

<b>CHAPTER 5</b>	<b>DIAGENESIS</b>	<b>63</b>
5.1	Diagenetic history from core and thin section petrography	63
5.1.1	Petrographic observations	63
5.1.1.1	Cracks - Phase 1a	65
5.1.1.2	Meniscus cement - Phase 1b	66
5.1.1.3	Molds I- Phase 2a	66
5.1.1.4	Blocky calcite cement - Phase 2b	66
5.1.1.5	Variably lithified sediment – Phase 2c	68
5.1.1.6	Replacive dolomite - Phase 3a	68
5.1.1.7	Dolomite cement - Phase 3b	68
5.1.1.8	Molds II – Phase 4	70
5.1.1.9	Isopachous quartz cement rims – Phase 5a	70
5.1.1.10	Chert nodules – Phase 5b	70
5.1.1.11	Euhedral quartz – Phase 5c	72
5.1.1.12	Pyrite – Phase 6	72
5.1.1.13	Mechanical compaction features – Phase 7	75
5.1.1.14	Equant calcite – Phase 8	75
5.1.1.15	Molds and vugs – Phase 9	75
5.1.1.16	Blocky ferroan calcite cement– Phase 10	77
5.1.1.17	Subhorizontal stylolites and sutured seams– Phase 11	77
5.1.1.18	Oil impregnation– Phase 12	77
5.1.1.19	Subvertical stylolites and solution seams– Phase 13	79
5.1.1.20	Vertical fractures– Phase 14	79
5.1.1.21	Drusy calcite cement– Phase 15	79
5.1.2	Interpretation	81

5.1.2.1	Phase 1a – 1b .....	83
5.1.2.2	Phase 2a – 2b – 2c .....	83
5.1.2.3	Phase 3a – 3b .....	84
5.1.2.4	Phase 4.....	85
5.1.2.5	Phase 5a – 5b – 5c .....	85
5.1.2.6	Phase 6.....	86
5.1.2.7	Phase 7.....	86
5.1.2.8	Phase 8.....	87
5.1.2.9	Phase 9.....	87
5.1.2.10	Phase 10.....	87
5.1.2.11	Phase 11 .....	88
5.1.2.12	Phase 12.....	88
5.1.2.13	Phase 13.....	88
5.1.2.14	Phase 14.....	89
5.1.2.15	Phase 15.....	89
5.1.3	Burial history.....	89
5.2	Dolomite .....	91
5.2.1	Observations.....	91
5.2.1.1	Crystal shapes.....	91
5.2.1.2	Crystal sizes.....	95
5.2.1.3	Cathodoluminescence.....	98
5.2.1.4	Stoichiometry .....	99
5.2.1.5	Ordering.....	109
5.2.1.6	Conventional carbon and oxygen isotope data.....	112
5.2.1.7	Clumped-isotopes thermometry .....	114

5.2.1.8	Elemental compositions.....	114
5.2.2	Interpretations .....	119
5.2.2.1	Crystal shapes.....	119
5.2.2.2	Crystal size .....	120
5.2.2.3	Cathodoluminescence.....	120
5.2.2.4	Stoichiometry .....	121
5.2.2.5	Ordering.....	122
5.2.2.6	Conventional carbon and oxygen isotope data.....	123
5.2.2.7	Clumped-isotopes thermometry .....	131
5.2.2.8	Elemental compositions.....	132
5.3	Porosity .....	137
5.4	Permeability .....	146
<b>CHAPTER 6</b>	<b>DISCUSSION .....</b>	<b>149</b>
6.1	Individual dolomite layers .....	149
6.1.1	Dolomite: Replacement.....	149
6.1.2	Mg <sup>2+</sup> source .....	150
6.1.3	Interpretation and model of dolomitization.....	153
6.1.4	Calcite – Dolomite – Chert: Chemical Lake water evolution .....	160
6.2	Stratigraphic interval D and C Shales .....	162
6.3	Regional paleogeography.....	163
6.4	Dolomitization and reservoir properties .....	165
6.4.1	Geometry of the dolomite PZ layers .....	165
6.4.2	Porosity and permeability .....	170



<b>CHAPTER 7</b>	<b>CONCLUSIONS AND FUTURE WORK .....</b>	<b>178</b>
7.1	Conclusions.....	178
7.2	Future work.....	181
<b>REFERENCES</b> .....		<b>183</b>
<b>APPENDIX 1</b> .....		<b>201</b>
<b>APPENDIX 2</b> .....		<b>204</b>
<b>APPENDIX 3</b> .....		<b>211</b>
<b>APPENDIX 4</b> .....		<b>214</b>
<b>APPENDIX 5</b> .....		<b>217</b>
<b>APPENDIX 6</b> .....		<b>220</b>
<b>APPENDIX 7</b> .....		<b>226</b>
<b>APPENDIX 8</b> .....		<b>228</b>

## LIST OF FIGURES

Page

- Figure 1.1:** Eocene intermountain lake basins and associated uplifts. Modified from Dickinson et al (1988). Study area highlighted by red rectangle. DCU: Douglas Creek Uplift, RSU: Rock Springs Uplift, STB: Sevier Thrust Belt, UiU: Uinta Uplift, UnU: Uncompahgre Uplift. ....2
- Figure 1.2:** Location of study area (red outline), wells and outcrops. Modified from Vanden Berg et al. (2014).....9
- Figure 1.3:** (A) Stratigraphic chart of the GRF modified from Logan et al. (2016). (B) Gamma ray and porosity logs of the entire UBm highlighting the interval of interest, which is located at central section of the UBm (well: UT 15-30). (C) Composite of gamma ray, porosity, permeability, and lithology logs of the interval of interest. ....10
- Figure 2.1:** Paleogeographic evolution of North America during the Laramide Orogeny (A) and (B). (A) Late Cretaceous. (B) Early Paleocene. Both images retrieved from Ron Blakey website at [http://deeptimemaps.com/wp-content/uploads/2016/05/NAM\\_key-75Ma\\_LateK.png](http://deeptimemaps.com/wp-content/uploads/2016/05/NAM_key-75Ma_LateK.png). (C) and (D) Early Eocene: Intermountain and coexisting lacustrine basins. (D) enlargement of (C) showing Lake Gosiute (G), Uinta (U), Piceance (P), and Flagstaff (F), and Claron basins. The boundary between Uinta and Flagstaff basins is outlined in red, image retrieved from Ron Blakey website at [http://deeptimemaps.com/wpcontent/uploads/2016/05/NAM\\_key50Ma\\_Eocene.png](http://deeptimemaps.com/wpcontent/uploads/2016/05/NAM_key50Ma_Eocene.png). .13
- Figure 2.2:** Paleogeographic location of the Uinta Basin and surrounding uplifts. Arrows represent potential paleocurrents that likely fed Lake Uinta. UB - Uinta Basin (Foreman et al., 2012; Vanden Berg et al., 2014), UP - Uinta Uplift (Baars and Stevenson, 1981; Foreman et al., 2012), UU–SL - Uncompahgre Uplift (Sweet and Soreghan, 2012) – San Luis Mountains (Kluth, 1986), MU - Monument Upwarp (Hintze et al., 2000), SRS - San Rafael Swell (Doelling, 2002), SeOB - Sevier Orogenic Belt (Hintze et al., 2000).....15
- Figure 2.3:** Schematic representation of lake types according to sediment and water supply (controlled by climate) versus accommodation rate (controlled by tectonism) (Carroll and Bohacs, 1999). Image from Carroll and Bohacs (1999). ....16
- Figure 4.1:** Facies F1 - Silty mudstone. (A) Transmitted light photomicrograph (TLP) of an organic poor bed with ostracod shell fragments (white arrows); aligned parallel to stratification (horizontal axis), silt material is mainly quartz (yellow arrow); well: BBC 14-1, sample 24, 6672.8 ft., plane polarized light (PPL). (B) TLP of densely packed shell fragments (light yellow band) interbedded with organic-rich mudstone (dark areas); well: BBC 14-1, sample 7, 6705.3 ft., PPL. (C) Core photograph of silty mudstone facies interbedded with organic-rich laminae (white arrow), densely packed shell laminae (yellow arrow), and organic-poor silt laminae (light gray), and dewatering structures (red arrow); well: BBC 14-1, 6705'4" to 6705'11". ....34
- Figure 4.2:** Facies F2 - Lime mudstone. (A) TLP of lime mudstone with scarce and well preserved disarticulated ostracods shells (arrows); well: BBC 14-1, sample 17, 6692.6 ft, PPL. (B) TLP of interbedded lenses (yellow dashed lines) of dolomitized peloids (Pel)

- embedded in microsparitic calcite cement (stained pink); bitumen (?) between peloids (dark areas); well: N -628, sample 3, 8205.6 ft., PPL. (C) Core photograph of lime mudstone facies characterized by massive and planar stratification; well: BBC 14-1, 6702'8" to 6703'4". .....36
- Figure 4.3:** Facies 3 - Ostracod wackestone-packstone. (A) TLP of ostracod wackestone with disarticulated ostracods shells (arrows) aligned to bedding; well UT 15-13, sample 12, 7016.4 ft.; PPL. (B) TLP of gyrogonite (white arrows) associated with ostracod shell fragments (yellow arrows); well: 14-3, sample 27, 7373.65 ft.; PPL. (C) Core photograph of ostracod wackestone facies characterized by massive stratification and elongated chert nodules/bed (yellow dashed outline); well: BBC 14-1, 6685'4" to 6686' .....38
- Figure 4.4:** Facies F4 - Peloidal wackestone-packstone. (A) TLP of peloidal (white arrows) wackestone with scarce and disarticulated ostracods shells (yellow arrows); stratification disrupted by biological activity (blue arrow); well: N 6-28, sample 9, 8542.5 ft.; PPL. (B) TLP of peloids (arrows) within a microcrystalline dolomite matrix and clay material; well: UT 15-13, sample 13, 7017.4 ft.; PPL. (C) Core photograph of peloidal wackestone - packstone facies showing bioturbation structures (arrows) and chert nodule (yellow dashed outline); well: UT 15-13, 7017'1" to 7017'8". .....40
- Figure 4.5:** Facies F5 - Molluscan bearing wackestone-floatstone. (A) TLP of molluscan bearing floatstone with centimetre-size shells of pelecypods (white arrow), gastropods (yellow arrows), and disarticulated ostracods shells (blue arrows); well: PW 13-06, sample 5, 5537.3 ft.; PPL. B) TLP of organic rich wackestone with pelecypods (white arrow), gastropods (green arrow); and ostracods (red arrows); black colour in matrix due to high organic matter content; well: N 6-28, sample 8, 8234.6 ft.; PPL. (C) Core photograph of interbedding coquina layer (at the top) with molluscan floatstone (at the base); well: BBC 14-1, 6696'1" to 6697'1". .....42
- Figure 4.6:** Core photograph of molluscan limestone facies (F5) with partial silicification of gastropods (red arrows) and pelecypods (yellow arrows); well UT 11-20, depth: (A) 4974.2 to 4974.7 ft, (B) 4975 to 4975.3 ft. ....43
- Figure 4.7:** Facies F6 - Intraclast peloid packstone-grainstone. (A) TLP of centimetre-size dolomitized intraclasts (white arrow), peloids (Pel), and blocky calcite cement (yellow arrow); well: 14-1, sample 12, 6683.95 ft.; PPL. (B) TLP of well-rounded intraclasts (white arrows), ostracods shell fragments (yellow arrow) within a dolomitized matrix; well: BBC 14-1, sample 13, 6684.90 ft.; PPL. (C) Core photograph of intraclastic peloidal facies. Rip-up intraclast particles (white arrows) within a dolomitized micrite (?) matrix; well: BBC 14-1, 6684'11" to 6685'5". .....45
- Figure 4.8:** Facies F7 - Ooid grainstone - packstone. (A) TLP of ooid grainstone with ooids partially dissolved and scarce articulated ostracods shells (yellow arrows); well: PW 13-06, sample 6, 5539.5 ft.; PPL. (B) Detail of microphotograph (A) that shows micritization of ooids (yellow arrow). Note ooids are completely dolomitized; PPL. (C) Core photograph of ooid grainstone facies with massive stratification; well: PW 13-06, 5539'3" to 5539'11". .....47
- Figure 4.9:** Facies F8 - Ostracod grainstone - packstone. (A) TLP of ostracod grainstone. The internal voids of ostracods are partially filled with dolomitized pellets (?) and micrite (white arrows); the resting voids were filled with blocky ferroan calcite cement (pale

- purple areas); well: DS 11-20, sample 11, 4998.5 ft.; PPL. (B) TLP of ostracod grainstone facies. Microcrystalline dolomite partially fills the internal cavity of articulated ostracods shells (white arrows); well: DS 11-20, sample 11, 4998.5 ft.; PPL. (C) Core photograph of ostracod grainstone facies with chert nodules (white arrows); well: BBC 14-1, 6680'0" to 6680'8". .....49
- Figure 4.10:** Facies F9 - Brown arenaceous claystone. (A) TLP of brown mudstone with disarticulated ostracod shell fragments aligned subparallel to bedding, with subangular to rounded and very fine sand quartz grains (white arrows); well: UI 16, sample 16, 4713.2 ft.; PPL. (B) TLP of interbedded laminae of coquinas (pale pink-red) and arenaceous claystone (light brown area), and fish bones (arrows); well: UI 16, sample 16, 4713.2 ft.; PPL. (C) Core photograph of brown and fissile claystone; well: UI 16, 4712'11" to 4712'6". .....51
- Figure 4.11:** Facies F11 - Coal. Thin coal seam in Willow Creek Canyon outcrop. Seam coals are vertically associated with claystone (F9) (base) and dolowackestone (F3) (top). .....52
- Figure 4.12:** Vertical association of facies from silty mudstone (F1) at the base, mollusc wackestone – floatstone (F5), and lime mudstone (F2) coarsening upward to peloid wackestone – packstone (F4) at the top. Idealized stratigraphic cycle: At the base is the oil rich mudstone facies (F1); followed by mollusc wackestone – floatstone facies (F5); and dolopackstone facies at the top (F6) Photograph of well: BBC 14-1, 6702' to 6706'1". .....54
- Figure 4.13:** Schematic representation of the lateral facies distribution in the Uinta Basin profile. Time of deposition of the molluscan wackestone – floatstone facies (F5) is different from the time of deposition of the other carbonate facies (F2, F3, F4, F6, F7, and F8). F5 was deposited in a fresh water setting during the initial stage of regression, whereas the facies F2, F3, F4, F6, F7, and F8 were deposited during the maximum regression (see Chapter 4, Sections 4.3 and 4.4 for further discussion). .....57
- Figure 4.14:** Correlation of stratigraphic cycles C1 to C5 (right column) within D and C shales. ....59
- Figure 4.15:** Mineralogical composition for carbonate facies. Volume percentage (vertical axis) estimated from thin sections using semi-quantitative charts (Baccelle and Bosellini, 1965). .....61
- Figure 4.16:** Schematic representation of facies distribution and dolomitization. F5 was not dolomitized. ....62
- Figure 5.1:** Dolomite textural classification proposed by Gregg and Sibley (1984), Sibley and Gregg (1987) and modified by Wright. Image modified from Machel (2004). ....64
- Figure 5.2:** Carbonate grain size and mineral crystal size classification; Folk, 1962. ....65
- Figure 5.3:** (A) TLP of intraclast (green dash outline) with cracks that surrounded peloids (arrow) and crosscut dolomitized matrix; well: N 6-28, sample: 5, 8223.2 ft.; plane polarized light (PPL). (B) Detail of photomicrograph (A). Polygonal micro-cracks (arrows) crosscutting microcrystalline dolomitized matrix (brown area), cracks are completely filled with blocky calcite cement; PPL. (C) Crossed-polarized photomicrograph (XPL) (B), blocky calcite cement fills cracks (arrow). (D) Cracks

present in the nearshore area are filled with blocky calcite cement (arrows); Nine Mile outcrop, pen for scale. (E) TLP of ooid dolograstone with microcrystalline meniscus cement at grains contacts (arrows); well: PW 13-06, sample 6, 5539.5 ft.; PPL. (F) TLP of molds of bioclasts filled with blocky calcite cement (arrow); well: UT 15-13, sample 5, 6982.2 ft.; PPL .....67

**Figure 5.4:** (A) TLP of very fine dolomite in matrix; pyrite and hydrocarbon droplets (black spots); well: BBC 14-1, sample: 17, 6692.6 ft.; PPL. (B) TLP of very fine dolomite in matrix (light brown area) and dolomitized intraclasts (yellow dashed outlines), bioclasts (arrows) not dolomitized; well: BBC 14-1, sample: 13, 6684.9 ft.; PPL. (C) TLP of matrix-selective dolomitization (dark brown area), shell fragments (white arrows) and gyrogonite bioclast (green arrow) not dolomitized; well: BBC 14-3, sample: 27, 7373.6 ft.; PPL. (D) TLP of planar-c dolomite cement (arrows) partially fills intraparticle pore; well: IU 16, sample: 14, 4729.9 ft.; PPL. (E) TLP of rims of planar-c dolomite cement (arrows) grow around dolomitized peloids and ooids (yellow dashed outlines); well: DS 11-20, sample 12, 4999.35 ft.; PPL. (F) TLP of planar-c dolomite cement (arrows) around dolomitized peloids (?) within ostracod shells; well: PW 13-06, sample: 6, 5539.5 ft.; PPL.....69

**Figure 5.5:** (A) TLP of ostracod mold (black arrow) filled with dolomite (yellow arrow) and chalcedony (Ch); well: PW 13-06, sample: 8, 5543.5 ft.; PPL. (B) Crossed-polarized light image of (A). Feathered texture of the chalcedony that fills internal ostracod (?) pore; XPL. (C) Partial (yellow dashed line) and complete dissolution (arrow) of ostracod shells; steinkerns (Ste) within an aphanocrystalline dolomitized matrix; well BBC 14-1, sample: 9, 6680.1 ft.; PPL. (D) TLP of rims of very fine crystalline quartz as cement (arrows) around dolomitized peloids (Pel); well: BBC 14-1, sample: 12, 6683.95 ft.; PPL. (E) Crossed-polarized light image of (D). Quartz cement (arrows), and calcite cement (yellow, green, and blue area); XPL. (F) TLP of rims of equant quartz cement (arrow) in intraparticle pore. Dark brown and black spots are hydrocarbons; well: N 6-28, sample: 7, 8230.2 ft.; PPL. ....71

**Figure 5.6:** (A) TLP of a chert nodule. Ostracod shells (arrow) mimetically replaced by microcrystalline quartz. Intraparticle pore filled by chalcedony (light brown area); well: BBC 14-3, sample: 28, 7374 ft.; PPL. (B) Crossed-polarized light image of (A), quartzine (arrow) nucleated at the walls of the ostracod shells. Granular microcrystalline quartz (GM) precipitated around bioclasts; XPL. (C) Same image (A) and (B); XPL + gypsum plate. (D) TLP of a chert nodule with an articulated ostracod (arrow) partially replaced by quartz and dolomite, internal void filled with chalcedony; well: BBC 14-3, sample: 29, 7375 ft.; PPL. (E) Crossed-polarized light image of (D), several chalcedony nucleated along the internal walls of the ostracod shell (green arrows); some chalcedony have radial fibrous to feathered habit (red arrow); XPL. (F) TLP of megaquartz crystals (red arrow) fill a void post-dating chalcedony cement (feathered crystals); well: BBC 14-3, sample: 29, 7375 ft.; XPL.....73

**Figure 5.7:** (A) TLP of euhedral quartz (arrows) within an aphanocrystalline dolomite matrix (dark brown area). Quartz crystals with dolomite inclusions; well: UT 15-13, sample: 11, 7009.9 ft.; PPL. (B) and (C) TLP of euhedral quartz within aphanocrystalline dolomite matrix (light brown area). Some quartz (green arrows) crystallized along shells (red arrow); (B) Well: UT 15-13, sample: 11, 7009.9 ft.; PPL. (C) Well: BBC 14-3, sample: 28, 7374.05 ft.; PPL. (D) TLP of fine crystalline pyrite with cubic and octahedral shape

(arrows) associated with calcite (red areas) within a chert nodule (Ch); well: PW 13-06, sample: 11, 5552.3 ft. (E) Reflected light photomicrograph of medium to coarse pyrite with octahedral shapes (bright area) that encloses aphanocrystalline dolomite (arrow) within a chert nodule (Ch); well: N 6-28, sample: 6, 8223.7 ft. (F) Reflected light photomicrograph of very fine crystalline and framboidal pyrite (bright area) within dolomitized matrix; well: PW 13-06, sample: 10, 5545.3 ft. ....74

**Figure 5.8:** (A) TLP of densely packed ostracod (black arrows) and gastropod shell (yellow arrow); well: DS 11-20, sample 14, 5017 ft.; PPL. (B) TLP of elongated and dolomitized peloids (steinkerns?) (white arrows), and flattened ostracod shells (yellow arrow) aligned parallel to bedding; well: UT 15-13, sample: 7, 6989 ft.; PPL. (C) TLP of equant calcite (EC) in interparticle pores. Crystal size ranges from 10 to 20  $\mu\text{m}$ ; well: IU 16, sample: 14, 4729.9 ft.; PPL. (D) TLP of equant calcite cement (EC) and ferroan calcite cement (FC) in contact along a possible dissolution front (yellow dashed line); well: DS 11-20, sample: 13, 5000.3 ft.; PPL. (E) Crossed-polarized image of (D). (F) TLP of partial dissolution of bioclast. Original metastable calcium carbonate of gastropod shell fragments (yellow arrows), which was partially dissolved and then filled by blocky ferroan calcite cement (white arrows); well: PW 13-06, sample: 14, 5565.9 ft. ....76

**Figure 5.9:** (A) TLP of blocky ferroan calcite cement (FC) in ostracod intraparticle pore (dark purple), encasing patches/clusters of microcrystalline dolomite (arrow); well: IU 16, sample: 14, 4729.9 ft.; PPL. (B) Crossed-polarized light image of (A). (C) TLP of blocky ferroan calcite cement (white arrow) in space developed by partial dissolution of shell fragment (yellow arrow); well: BBC 14-1, sample: 6, 6666.5 ft.; PPL. (D) TLP of irregular to hummocky subhorizontal stylolites forming an anastomosing set (arrow); well: IU 16, sample: 16, 4733.2 ft.; PPL. (E) TLP of swarms of microstylolites or sutured seams (arrows), subvertical fracture post-dates stylolites and is completely filled by blocky calcite cement; well: UT 15-13, sample: 6, 6983.9 ft.; PPL. (F) TLP of hydrocarbon within intercrystal pores of dolomitized matrix and moldic pores; well: N 6-28, sample: 7, 8230.2 ft.; PPL. ....78

**Figure 5.10:** (A) TLP of subvertical serrated stylolites (white arrow) with amplitude up to 2500  $\mu\text{m}$  associated to subvertical fractures (green arrow); well: N 6-28, sample: 1, 8199.3 ft.; PPL. (B) TLP of anastomosing sutured seam (arrow) that crosscuts stratification (horizontal axis); well: N 6-28, sample: 8, 8234.6 ft.; PPL. (C) TLP of subvertical fractures (arrows) that crosscut stratification (horizontal axis) and ostracod shells. Fractures filled by blocky calcite cement; well: BBC 14-1, sample: 20, 6701.4 ft.; PPL. (D) TLP of drusy calcite cement with crystal size increasing from medium crystalline (white arrow) at the stylolite wall toward a very coarse crystalline (blue arrow) in the center; well: N 6-28, sample: 12, 8267.4 ft.; PPL. (E) Crossed-polarized light image of (A). (F) TLP of hydrocarbon (arrows) as inclusions in calcite crystals (entire photomicrograph); well: N 6-28, sample: 12, 8267.4 ft. ....80

**Figure 5.11:** Burial curve of a synthetic well located within the study area (red star in the inset map) correlated with diagenetic environments as identified in this study (left column), modified from Schamel (2015); DS: Diagenetic settings based on Machel's (1999) diagenetic environments; Pal: Paleogene, N: Neogene, Q: Quaternary, LOW: Liquid oil window. ....90

- Figure 5.12:** Stratigraphic correlation of PZ layers with location (depth) of selected polished thin section for layers PZ1, PZ1', and PZ2. Numbers in the inset map stand for wells/outcrops as 1: BBC 14-1, 2: BBC 14-3, 3: N 6-28, 4: UT 15-13, 5: PW 13-06, 6: DS 11-20, 7: UI 16, 8: WCC, and 9: NMC.....92
- Figure 5.13:** (A) SEM image of planar-e dolomite texture. Note the straight dolomite faces and well defined rhombohedral habit (yellow dashed lines); well: N 6-28, sample: 7, 8230.2 ft. (B) SEM image of planar-s dolomite, some dolomite crystals have irregular faces (yellow dashed lines) and internal holes (white arrows); post-dolomitization authigenic quartz (Qz) encases some dolomite crystals; well: PW 13-06, sample: 12, 5557.4 ft. (C) SEM image of nonplanar-a dolomite, dolomite crystals have irregular and lobate crystal faces (yellow dashed outlines) and internal holes (white arrows); well: UT 15-13, sample: 11, 7009.9 ft. (D) SEM image of planar-c dolomite; interparticle pore (red dashed line) partially filled by dolomite cement (yellow dashed outlines) and authigenic quartz (Qz); well: N 6-28, sample: 9, 8242.5 ft.....93
- Figure 5.14:** Distribution of dolomite textures for each PZ layer. N: North, S: South. The cross section is shown in Figure 5.12.....94
- Figure 5.15:** Percentage distribution of dolomite crystal size populations. POP 1: 0.25  $\mu\text{m}$  to 1.5  $\mu\text{m}$ , POP 2: 1.5  $\mu\text{m}$  to 3.0, POP 3: 3.0  $\mu\text{m}$  to 6.0  $\mu\text{m}$ . ....96
- Figure 5.16:** Dolomite crystal size distribution for each PZ layer. All PZ layers present a right-skewed and left tail distribution. ....97
- Figure 5.17:** Validation of dolomite CSD: (A) Normal and (B) lognormal distributions. AD: Anderson-Darling value. ....98
- Figure 5.18:** (A) TLP of dolomudstone at the base of PZ1 with dolomite crystals in matrix (dark red area); well: PW 13-06, sample: 10, 5545.3 ft. (B) Cathodoluminescence photomicrograph of the same area in (A) with no visible luminescence contrast. ....99
- Figure 5.19:** High-resolution diffractogram of the  $d_{104}$  dolomite peak that displays three remarkable characteristics: (i)  $d_{104}$  peak ( $30.86^\circ 2\theta$  represented by vertical black line) shifted toward lower  $2\theta$  values (ideal dolomite  $d_{104}$  peak, red dashed line), in this particular sample =  $0.13^\circ 2\theta$  (left red arrow); (ii) split  $d_{104}$  peak (green arrows) and side humps (black arrow) that define an asymmetrical  $d_{104}$  reflection; and (iii) wide peak with a full width of half maximum intensity (FWHM) of  $0.31^\circ 2\theta$ , higher than the ideal dolomite [FWHM =  $0.155^\circ 2\theta$  for Eugui dolomite (Jones et al., 2001)]. Well PW 13-06, sample: 8, 5543.5 ft. XRD diffractogram from Indiana University (CuK $\alpha$  radiation). ....100
- Figure 5.20:** Graphic comparison between the %Ca<sub>Dol</sub> values calculated from (A) XRD data and (B) EMPA data. (A) All samples show a split  $d_{104}$  peak with one or several humps, each of them possibly represent a different %Ca<sub>Dol</sub> population with a unique  $d_{104}$  at different  $2\theta$  value. Each  $d_{104}$  “subpeak” is represented by a blue line. The calculated value of %Ca<sub>Dol</sub> for each inferred population is indicated at the right side of each  $d_{104}$  “subpeak”. (B) %Ca<sub>Dol</sub> frequency distribution for each sample measured by EMPA. The %Ca<sub>Dol</sub> arithmetic mean for each population is indicated at the top of each bin. ....104
- Figure 5.21:** Correlation between  $d_{104}$  (vertical axis) calculated from XRD data and %Ca<sub>Dol</sub> (horizontal axis) calculated from EMPA data. Red line: linear regression.....105

- Figure 5.22:** Frequency distribution of calcium mole percentage in dolomite crystals (%Ca<sub>Dol</sub>) for each PZ layer. %Ca<sub>Dol</sub> calculated by mean of the equation by Lumsden (1979). .... 106
- Figure 5.23:** %Ca<sub>Dol</sub> populations. POP1%Ca fluctuates between 49 to 56.5 %Ca and POP2%Ca fluctuates between 56.5 to 59 %Ca. POP1%Ca is the most abundant (92%). ..... 107
- Figure 5.24:** Dolomite stoichiometry variation in depth; horizontal axis: %Ca<sub>Dol</sub> (%), vertical axis: depth (ft). See map inset for well locations; numbers in the inset map stand for wells/outcrops as 1: BBC 14-1, 2: BBC 14-3, 3: N 6-28, 4: UT 15-13, 5: PW 13-06, 6: DS 11-20, 7: UI 16, 8: WCC, and 9: NMC. .... 108
- Figure 5.25:** %Ca<sub>Dol</sub> variation with depth. Data for PZ1 layer, well PW 13-06. Black horizontal lines: top and base of the PZ layer, red line: linear regression. .... 109
- Figure 5.26:** Correlation between cation ordering and %Ca<sub>Dol</sub> populations for all PZ layers combined. Baymag dolomite, synthetic dolomites (Kaczmarek and Sibley, 2011), and Eugui dolomite (www.ruff.info) values plotted as reference. .... 111
- Figure 5.27:** Ordering variation with depth. Data for PZ1 layer, well PW 13-06. Black horizontal lines: top and base of the PZ layer, red line: linear regression. .... 111
- Figure 5.28:**  $\delta^{13}\text{C}$  frequency distribution for dolomites (all PZ dolomite layers) and calcites (interbedded limestones). .... 113
- Figure 5.29:**  $\delta^{18}\text{O}$  frequency distribution of dolomite (all PZ dolomite layers) and calcite (interbedded limestone).  $\delta^{18}\text{O}_{\text{Dol}}$  increment from parental  $\delta^{18}\text{O}$  calcite from -5‰ and 1‰ (VPDB). .... 113
- Figure 5.30:** Elemental compositions of dolomites and calcites. .... 115
- Figure 5.31:** Na, Sr, Fe, and Mn concentration in dolomites and geographical distribution. Numbers in the horizontal axis stand for wells/outcrops as; 1: BBC 14-1, 2: BBC 14-3, 3: N 6-28; 4: UT 15-13; 5: PW 13-06; 6: DS 11-20; 7: I 16; 8: WCC; 9: NMC. .... 117
- Figure 5.32:** Al, Si, Zn, and Pb concentration in dolomites and geographical distribution. Numbers in the horizontal axis stand for wells/outcrops as; 1: BBC 14-1, 2: BBC 14-3, 3: N 6-28; 4: UT 15-13; 5: PW 13-06; 6: DS 11-20; 7: I 16; 8: WCC; 9: NMC. .... 118
- Figure 5.33:** Total organic carbon (TOC) and S2 logs of well N 6-28. Dolomite PZ layers are highlighted in blue. Logs courtesy of Michael Vanden Berg, 2015. .... 124
- Figure 5.34:** Idealized processes that may have created low  $\delta^{13}\text{C}$  values in dolomites: Oxidation of low  $\delta^{13}\text{C}$  organic matter [-25 to -30‰ PDB (e.g., Tucker and Wright, 1990; Machel 2001)] created  $^{13}\text{C}$ -depleted bicarbonate anions (red rectangle). Pyrite (blue rectangle) formed as by-product from the hydrogen sulfide and detrital iron ( $\text{Fe}^{2+}$  in lake water) reaction. Modified from Berner et al., 1985. .... 125
- Figure 5.35:** Calculated Sr/Ca and Na/Ca molar concentration of the ancient Uinta Lake (yellow line), the Great Salt Lake (green line), and fresh lakes waters (blue line). .... 134
- Figure 5.36:** Sr concentration variation of dolomite crystals with depth. PZ1 layer, well PW 13-06. Horizontal black lines: top and base of the PZ layer, red line: regression line. .... 135
- Figure 5.37:** Horizontal porosity variation for each PZ layer. Porosity values measured from core plug samples. Red dashed line represents porosity average correlation between wells.



- Numbers along the horizontal axes and in the inset map stand for wells/outcrops as follows: 1: BBC 14-1, 2: BBC 14-3, 3: N 6-28, 4: UT 15-13, 5: PW 13-06, 6: DS 11-20, 7: UI 16, 8: WCC, 9: NMC. .... 140
- Figure 5.38:** Porosity variation with depth. Porosity values measured from core plugs; horizontal axis: porosity (%), vertical axis: depth (ft). Number in the inset map 1: BBC 14-1, 2: BBC 14-3, 3: N 6-28, 4: UT 15-13, 5: UT: 13-06, 6: DS 11-20, 7: UI 16, 8: WCC, 9: NMC. .... 141
- Figure 5.39:** (A) SEM image of planar-e texture characterized by straight dolomite crystal faces; well: UT 15-13, sample: 13, 7017.4 ft, PZ1' layer. (B) SEM image of planar-s texture characterized by straight and irregular dolomite crystal faces; well: N 6-28, sample: 9, 8242.5 ft, PZ2 layer. (C) SEM image of nonplanar-a texture characterized by irregular dolomite crystal faces and more densely packed crystals; well: UT 15-13, sample: 11, 7009.9 ft, PZ1 layer. (D) Same image as (A) highlighting porosity area (white area), estimated porosity: 43.38%. (E) Same image as (B) highlighting porosity area, estimated porosity: 12.4%. (F) Same image as (C) highlighting porosity area, estimated porosity: 7.82%. .... 142
- Figure 5.40:** Frequency distribution of porosity calculated from density logs for PZ layers and interbedded limestones. .... 145
- Figure 5.41:** Geographical distribution of permeability for each PZ layer. Data from core plug samples. Red dashed line represents permeability average correlation between wells. Numbers in the horizontal axis and in the inset map stand for wells/outcrops as 1: BBC 14-1, 2: BBC 14-3, 3: N 6-28, 4: UT 15-13, 5: PW 13-06, 6: DS 11-20, 7: UI 16, 8: WCC, 9: NMC. .... 147
- Figure 5.42:** Pore throat shapes. (A) Sheet-like pore throat shape (yellow lines) between dolomite crystals in planar-e and planar-s textures; well: N 6-28, sample: 7, 8230.20 ft. (B) Irregular pore throat shape (yellow lines) between dolomite crystals in nonplanar-a texture; well UT 15-13, sample: 11, 7009.90 ft. .... 148
- Figure 6.1:** Location of metapyroxenite (blue star) and the Uinta basin (yellow area). Additional potential sources of  $Mg^{2+}$  were located toward south/southwest of the Uinta Basin (Chapter 2, Section 2.2). Red arrow represents the probable paleo-river drainage. Figure modified from Case (1991). .... 151
- Figure 6.2:** Interpretation of dolomitization of an individual PZ-layer in the UBm. See text for discussion. .... 158
- Figure 6.3:** Decrease of the  $\delta^{18}O$  values for the Claron Basin (blue area) of about 5‰ (A), Flagstaff Basin (green area) of about 7‰ (B), and Uinta basin (yellow area) of about 6‰ (C), probably caused by tectonism (Davis et al., 2009). (C) Tectonic uplifting took place after UBm deposition around 45 My. The  $\delta^{18}O$  values of the dolomites in the PZ layers is highlighted by the red oval in the lower right corner of (C). Vertical axis in the inserted  $\delta^{18}O$  plots is time (My.), figure modified from Davis et al. (2009). .... 164
- Figure 6.4:** Isopachous map for PZ1 layer. Thickness measured from logs (data courtesy of Michael D. Vanden Berg, 2015), cores, and outcrops. .... 167

<b>Figure 6.5:</b> Isopachous map for PZ1' layer. Thickness measured from logs (data courtesy of Michael D. Vanden Berg, 2015), cores, and outcrops. ....	168
<b>Figure 6.6:</b> Isopachous map for PZ2 layer. Thickness measured from logs (data courtesy of Michael D. Vanden Berg, 2015), cores, and outcrops. ....	169
<b>Figure 6.7:</b> Porosity ( $P_D$ ) calculated from density logs for PZ layers and interbedded limestones. Numbers in the inset map stand for wells/outcrops as 1: BBC 14-1, 2: BBC 14-3, 3: N 6-28, 4: UT 15-13, 5: PW 13-06, 6: DS 11-20, 7: UI 16, 8: WCC, 9: NMC. ....	171
<b>Figure 6.8:</b> Preservation of textures from the precursor limestone. (A) TLP of dolopackstone, matrix-selective dolomitization, in which bioclasts (gyronite: blue arrow, ostracods shells: white arrows) were not replaced, well: BBC 14-3, sample: 28, 7374.05 ft. (B) TLP of dolograinstone, mimetic dolomite replacement of ooids, well: PW 13-06, sample: 6, 5539.5 ft. (C) TLP of dolomudstone, aphanocrystalline dolomite matrix and microvugs filled with hydrocarbons (arrows), well: UT 15-13, sample: 5, 6682.2 ft. (D) TLP of intraclastic dolowackestone, matrix completely dolomitized; ostracod shell fragments (arrows) were not dolomitized; well: BBC 14-1, sample: 13, 6684.9 ft. ....	173
<b>Figure 6.9:</b> Dolomite texture versus porosity for each PZ layer. Dolomite texture determined from SEM images and porosity estimated by image analysis software (Chapter 5, Section 5.3.1). ....	174
<b>Figure 6.10:</b> Scheme representing the tortuosity factor ( $\tau$ ) as the ratio of the length of the fluid flow pathway ( $L_a$ ) to the length of the sample ( $L$ ). Image from Azar et al. (2008). ....	175
<b>Figure 6.11:</b> Porosity vs. permeability plot of the PZ layers. Data from core plugs (Tables 5.10 and 5.12), courtesy of Michael D. Vanden Berg. ....	176
<b>Figure 6.12:</b> Dolomite textures percentage for each PZ layer. PZ1 layer has the most abundant planar-e texture of all PZ layers. Data from SEM images petrography. ....	177

## LIST OF TABLES

	Page
<b>Table 3.1:</b> Detailed location, operator and core location of selected wells, and outcrops used in this research.....	22
<b>Table 4.1:</b> Summary of lithofacies identified between the D and C shales.....	31
<b>Table 4.2:</b> Lithofacies correlation between Logan et al. (2016) and this project. ....	32
<b>Table 4.3:</b> Facies associations regarding to genetic vertical and horizontal relation, sedimentary structures, and rock textures.....	53
<b>Table 4.4:</b> Thickness and calculated time of deposition for each idealized cycles identified within D and C shales. TAve: Thickness average of each cycle; thickness in ft.....	60
<b>Table 5.1:</b> Paragenetic sequence. Phases 1 (cracks and meniscus cement), 2 (molds and equant-blocky calcite cement), 3b (dolomite cement), and 8 (equant calcite cement) took place along the near shoreline area only. These diagenetic products are highlighted red.....	82
<b>Table 5.2:</b> Mean size and standard deviation (St.Dev) of dolomite crystals. ....	96
<b>Table 5.3:</b> Comparison of %Ca <sub>Dol</sub> values obtained from XRD (Indiana University) and EMPA. The difference of the %Ca between XRD and EMPA ( $\Delta$ ) was calculated taking as base of reference the values from EMPA data. EMPA-XRD arithmetic mean = 0.5. ....	103
<b>Table 5.4:</b> Cation ordering and %Ca <sub>Dol</sub> by well and PZ layer (n = 64). Data from XRD. ....	110
<b>Table 5.5:</b> Isotopic signatures for PZ layers and interbedded limestone layers. ....	112
<b>Table 5.6:</b> Calculated dolomitizing fluid temperature (T) for PZ layers in wells PW 13-06 and N 6-28. Litho: Lithology, L: Limestone, D: Dolostone, %Dol: Dolomite percentage in the carbonate fraction.....	114
<b>Table 5.7:</b> Calculated $\delta^{18}\text{O}$ of lake water ( $\delta^{18}\text{O}_w$ ) for calcite precipitation, assuming lake water temperatures between 3 °C and 12°C (MacGinitie, 1969).....	127
<b>Table 5.8:</b> Calculated temperatures (T °C) of dolomitizing fluids based on estimated lake water $\delta^{18}\text{O}$ composition varying from -10‰ to 0‰ SMOW and measured $\delta^{18}\text{O}_{\text{Dol}}$ values from conventional isotopes analysis. Temperatures values that deemed unreasonable for dolomitization are highlighted in red color; temperatures calculated using the dolomite-water system isotopic fractionation equation proposed by Sheppard and Schwarcz (1970). See text for discussion.....	130
<b>Table 5.9:</b> Sr and Na concentrations and ratios to Ca <sup>2+</sup> of calculated dolomitizing fluid compared to current fresh water from lakes in the region and saline water form Great Salt Lake.....	133
<b>Table 5.10:</b> Porosity values from plugs. Data furnished by Core Lab and courtesy of Michael D. Vanden Berg.....	138
<b>Table 5.11:</b> Porosity estimated from SEM images. ....	143

<b>Table 5.12:</b> Permeability values from plugs. Data furnished by Core Lab and courtesy of Michael D. Vanden Berg.....	146
---	-----

## **CHAPTER ONE**

### **INTRODUCTION**

Lacustrine basins around the world are host of significant accumulations of hydrocarbons. For example, the fluvial-lacustrine Bohay Bay Basin in China is responsible for about one third of the country's total petroleum production (Hao et al., 2009). In Brazil, roughly 85% of oil produced from continental margin fields is sourced from lacustrine rocks (Mello and Maxwell 1990). In the United States, the lacustrine Green River Formation (GRF) in the Uinta Basin, Utah, hosts a very large accumulation of conventional oil and gas, as well as one of the largest immature oil shale resources, with an estimated 1.32 trillion barrels of initial oil in place (Johnson et al. 2010). While most drilling efforts in the Uinta Basin target more conventional sandstone reservoirs, the thin carbonates in the informal named Uteland Butte member (UBm) at the base of the GRF has gained interest in recent years as an unconventional reservoir targeted with horizontal drilling. Recently, Johnson et al. (2015) estimated a mean undiscovered resource of 177 million barrels of oil and 218 billion cubic feet of gas for the unconventional reservoirs in the UBm.

The Uinta Basin is part of a cluster of lake basins that is located near the junction of Utah, Wyoming, and Colorado (Figure 1.1). The geological evolution of these lake basins started with the Sevier orogeny during Jurassic through early Cenozoic times (Johnson, 1985) that defined the western margin by uplifting of the Sevier Thrust Belt. Once the Sevier orogeny stopped, the Laramide Orogeny deformed the ancient foreland basin into smaller sedimentary basins during mid Cretaceous to early Paleogene, thus creating the lacustrine basins (Johnson,

1985) at the central area of the ancient Rocky Mountains foreland basin. The Laramide orogeny created the physiographic boundaries of the lake basins as we know them today, including those of the Uinta Basin. The east-west trend Uinta Uplift likely rose prior to the end of the Cretaceous (Hansen, 1965) and was a source of sediments for Paleocene formations (Johnson, 1985). The NW-SE trend Uncompahgre uplift and the NE-SW San Rafael Swell uplifting started in the Maastrichtian (Johnson, 1985; Fouch, 1976). The north-south trend anticline Douglas Creek Arch likely started to rise at the end of Cretaceous (Tweto, 1975). The three lakes developed in the Laramide foreland basin and were filled with up to several thousand meters of deposits during early Tertiary times.

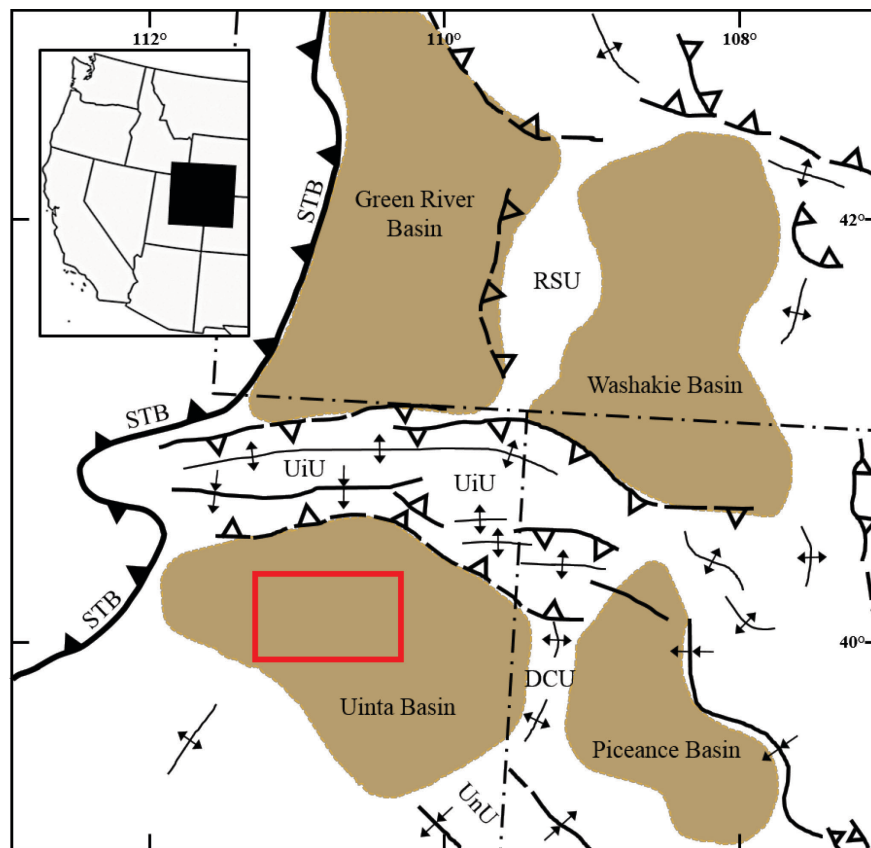


**Figure 1.1:** Eocene intermountain lake basins and associated uplifts. Modified from Dickinson et al (1988). Study area highlighted by red rectangle. DCU: Douglas Creek Uplift, RSU: Rock Springs Uplift, STB: Sevier Thrust Belt, UiU: Uinta Uplift, UnU: Uncompahgre Uplift.

The GRF was deposited in the Eocene epoch between 53 and 45 Ma (Smith, 2007; Smith et al. 2008). The basal parts of the GRF are thought to be deposited in fresh water environments, as evidenced by an abundance of fresh water molluscs (Johnson, 1985; Smith, 2007; Smith et al., 2008) and it is represented by the UBm (Johnson et al., 2010). The middle intervals of the GRF contain layers of ‘oil shale’ that were likely deposited in brackish lake water environment generated by regression of lake water (Johnson et al., 2010). The upper section of the GRF were deposited in much shallower water level and hypersaline environments, as evidenced by halite and sodium carbonate salt beds with thickness reaching up to 5.8 meters (Dyner et al., 1985; Johnson, 1985; Long, 2006; Smith et al., 2008; Johnson et al., 2010).

The UBm ranges in thickness from about 15 to 120 meters, being thickest near the depositional center of the Uinta Basin to the north and west (Vanden Berg et al., 2014; Johnson et al., 2016). This member represents the first ‘transgression’ of ancient Lake Uinta (Vanden Berg et al., 2013; Johnson et al., 2016) and is composed of a succession of interbedded limestones, dolostones, organic-rich calcareous mudstones, siltstones, and a few sandstones (Bereskin et al., 2004; Vanden Berg et al., 2014; Johnson et al., 2016).

Pusca (2003) defined the depositional environments for the UBm as shallow lake to playa environments for the carbonate rocks, and as distal lake for the shales. In the so far most comprehensive study on facies and depositional environments of the UBm, Logan (2015) identified depositional environments ranging from littoral, sublittoral, to profundal, based on outcrops and core well descriptions located at the eastern boundary of the Uinta Basin.

This study focuses on the distal Uteland Butte facies in the deeper portion of the basin mostly in Duchesne County (Utah), and of particular interest to understand the origin of thin dolomite beds (<0.5 to 2.5 m) that exhibit very high porosity, but low permeability, and act as

significant hydrocarbon reservoirs, which are targeted with horizontal drilling and hydraulic fracturing techniques.

## **1.1 Research objectives**

This project pursues solutions to several questions related to the dolomitization process(es) within the UBm and how this relates to petroleum production potential. The specific objectives of this study include:

- 1) Characterization and analysis of facies types for the Uteland Butte member as they relate to dolomitization;
- 2) Determination of the process(es) of dolomitization;
- 3) Investigation of how porosity and permeability are related to dolomitization;
- 4) Characterization of the geometry (lateral and vertical extent) of the dolomite layers in the study area;
- 5) Possible implications for petroleum reservoir development.

## **1.2 Previous work**

There is a substantial body of literature on the Uinta Basin and the GRF (e.g., Picard, 1955; Johnson, 1985; Remy, 1992; Smith, 2007; Johnson et al., 2016; Tänavsuu-Milkeviciene et al., 2017), which cover a large range of aspects that includes the tectonic evolution, sedimentology, paleoclimate, and several others. However, only a few studies have dealt with dolomitization.



The first notable attempt to explain dolomitization in the GRF was by Eugster and Surdam (1973), who invoked evaporation in playa flats as the chief cause and location of dolomitization. Implicit to their ‘playa model’ is that the lake margin was very shallow and even drying up during times of prolonged evaporation. In their own words (Eugster and Surdam 1973, Abstract): *“In these playa flats alkaline brines evolved through evaporation and precipitation of calcium carbonate and protodolomite in the capillary zone near the ground-water table. Dolomitic mudstones, marlstones, and calcareous and siliciclastic sandstones were the products of occasional floods on the playa.”*

Williamson and Picard (1974) identified dolomite as a replacement of the microcrystalline and fine-crystalline calcite matrix (micrite and sparite) of certain layers and concluded that dolomitization took place very early in the diagenetic history, prior to lithification. These authors did not identify any specific relationship between facies and dolomitization but nevertheless concluded that dolomitization was promoted by episodic evaporation coupled with high Mg/Ca ratios in the lake water. In addition, they argued that the  $\text{Mg}^{2+}$  necessary for dolomitization was likely flushed in by river drainage in the form of admixed clay minerals. However, they did not find a correlation between acid-insoluble residues and dolomite contents (Williamson and Picard, 1974).

Ryder et al. (1976) differentiated two genetic types of dolomite associated with depositional environments: (i) an open lacustrine (profundal) environment in which dolomite formed from  $\text{Mg}^{2+}$  that was released from interbedded algae-rich laminites; and (ii) near shore (littoral) environments where the fine-grained carbonate sediments were dolomitized as a result of pumping of brines enriched in  $\text{Mg}^{2+}$  by evaporation. The latter conforms to the “playa-lake” by Eugster and Surdam (1973).

Desborough (1978) proposed that dolomitization took place in organic-rich (oil shale to-be) layers when the lake was chemically stratified. While he worked mainly in the Parachute Creek Member of the GRF of the Piceance Basin (Figure 1.1), he also applied this ‘model’ to the Uinta Basin. Accordingly, blue-green algae concentrate  $Mg^{2+}$  in the chlorophyll molecules through photosynthesis, which was released during post-mortem decay near the water-sediment interface, thereby promoting dolomitization (Desborough, 1978).

Cole and Picard (1978), working in the Parachute Creek Member on the eastern side of the Uinta Basin and in the neighboring Piceance Basin, did more detailed mineralogical work than previous studies. They reported that dolomite is abundant throughout the Parachute Creek Member and most abundant in the oil shale lithofacies. In the Uinta Basin, the dominant carbonate minerals were found to be dolomite, ankerite, and calcite, and analcime, potassium feldspar, quartz, and albite were also found in the nearshore facies. Cole and Picard (1978) suggested that dolomite formed as result of biological and chemical conditions of the lake water.

Pitman (1996) was the first researcher to systematically apply stable isotope geochemistry to the dolomite problem in the GRF for both the Douglas Creek and Parachute Creek Members. Based on carbon isotope data, Pitman (1996) identified two types of dolomite: ‘primary’ and ‘diagenetic’. The primary dolomites have  $\delta^{13}C$  values ranging from about -2 to +2 ‰ PDB (Pee Dee Belemnite), whereas the diagenetic dolomites have  $\delta^{13}C$  values ranging from about +2 to +4 ‰ PDB. According to Pitman (1996), the primary dolomites were formed by gradual increases in the dissolved bicarbonate concentration when the lake evolved from hydrologically ‘open’ to hydrologically ‘closed’, catalyzed by increased photosynthetic activity. On the other hand, Pitman (1996) interpreted the origin of the diagenetic dolomite as mediated by bacterial sulfate reduction. Pitman (1996) did not differentiate between direct formation of dolomite from aqueous solution and replacement of carbonate mud.

Long (2006) investigated dolomitization in several intervals of the GRF and identified two different dolomite crystals based on their lithology occurrence. The first dolomites are related to the oil shale layers. Long (2006) interpreted these dolomites to have formed as a by-product of bacterial methanogenesis process that promoted dolomite precipitation. The second dolomites are related to micrite layers in the “Tgl member”, which correlates with UBm. Long (2006) interpreted these dolomites formed as replacement under evaporitic conditions.

Logan et al (2016) completed a comprehensive facies analysis of the UBm located on the eastern side of the Uinta Basin. The UBm in this area contains more proximal facies (e.g., grainstones, deltaic and mouth-bar sand units, etc.) and little dolomite, compared to the more distal UBm on the west side of the basin (the focus of this study), where the unit is a productive oil and gas reservoir.

In summary, previous studies agree on one point: the dolomite(s) in the GRF, and more specifically in the UBm, formed syndepositionally and/or very early diagenetically. However, these studies offered several possibilities for the source of  $Mg^{2+}$ , the driving mechanism for dolomitization (hydrologically and/or geochemically), with some disagreement as the dolomite(s) being primary or a replacement product of lime mud.

### **1.3 Study area and stratigraphic interval of interest**

The study area covers the central to southwestern parts of the Uinta Basin, mostly in Duchesne County (Figure 1.2). The stratigraphic interval of interest is within the middle portion of the UBm, defined at the bottom and top by the informally named D Shale and C Shale, respectively. Within this interval there are three prominent and regionally extensive dolomite

layers named PZ1, PZ1', and PZ2 (operator designations). These dolomite beds, as well as numerous other thin dolomite beds throughout the UBm, have significant reservoir potential due to their high porosity and lateral extent (Figure 1.3).

#### **1.4 Dolomite theoretical framework**

Dolomite,  $\text{CaMg}(\text{CO}_3)_2$ , is a rhombohedral carbonate mineral of Mg and Ca, commonly found in sedimentary rocks. When a rock consists of more than 90% dolomite, it is commonly referred to as dolostone, although many authors refer to such rocks also with the mineral name dolomite.

The origin of the mineral dolomite has been a focus of a large number of investigations for more than 200 years. Dolomites are important for several reasons including: (1) dolomite is a common carbonate mineral in ancient carbonate successions yet rare in recent carbonate sediments; (2) dolomite has not been synthesized in laboratories at low-diagenetic temperatures (less than about 30°C) inorganically or organically; and (3) most natural dolomites formed via replacement of pre-existing limestones, and many dolomitized carbonates form prolific reservoir rocks for hydrocarbons (Tucker and Wright, 1990; McKenzie, 1991; Purser et al., 1994; Warren, 2000; Machel 2004; Gregg et al. 2015; Kaczmarek et al 2017).

In natural diagenetic environments, dolomite most commonly forms via dolomitization, which is the replacement of calcite by dolomite, or subordinately via direct precipitation from aqueous solution in the form of cements (e.g., Machel, 2004). In addition, dolomite can also form at the sediment-water interface as mud. The latter type is also known as 'penecontemporaneous' dolomite (Budd, 1997).

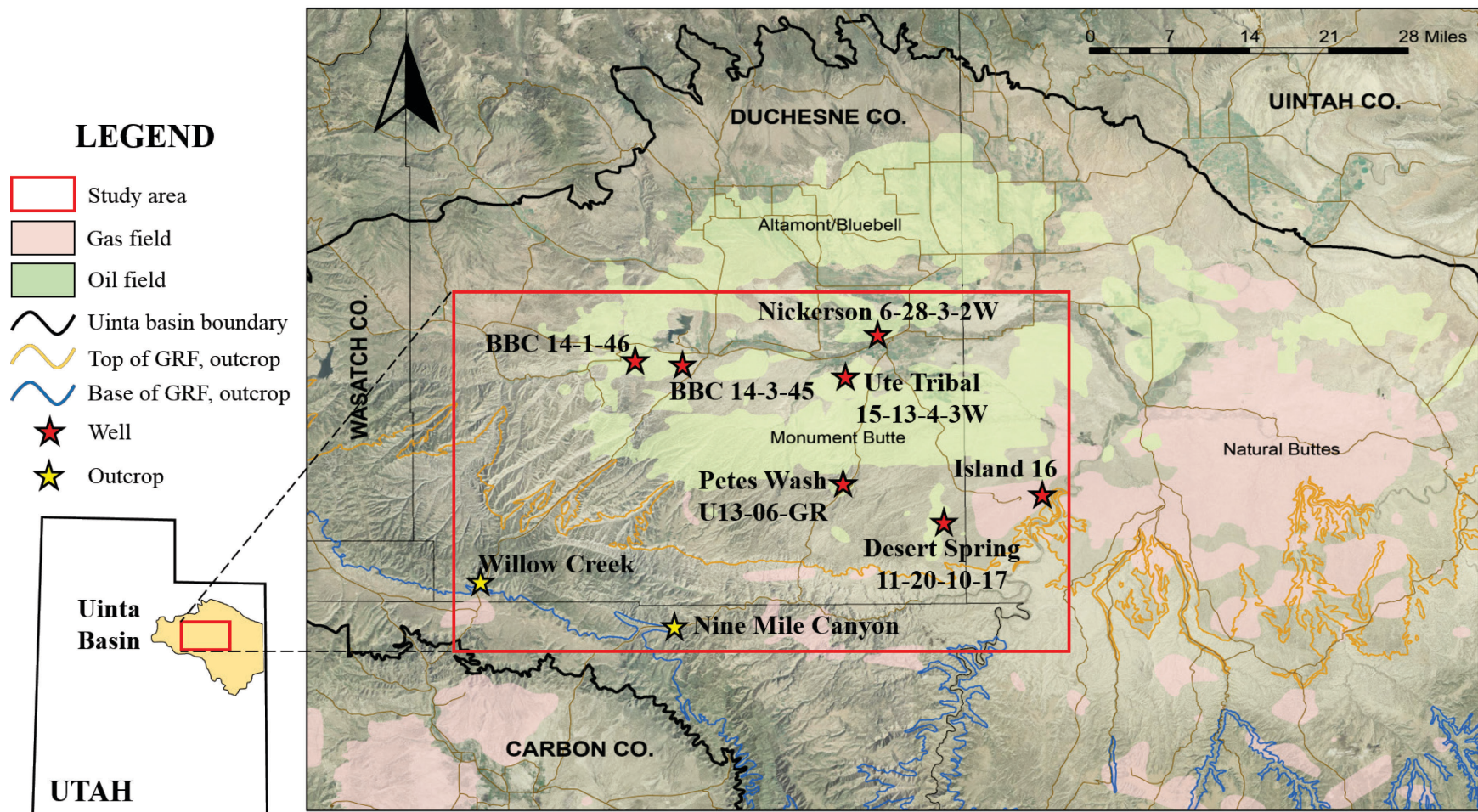


**Figure 1.2:** Location of study area (red outline), wells and outcrops. Modified from Vanden Berg et al. (2014).

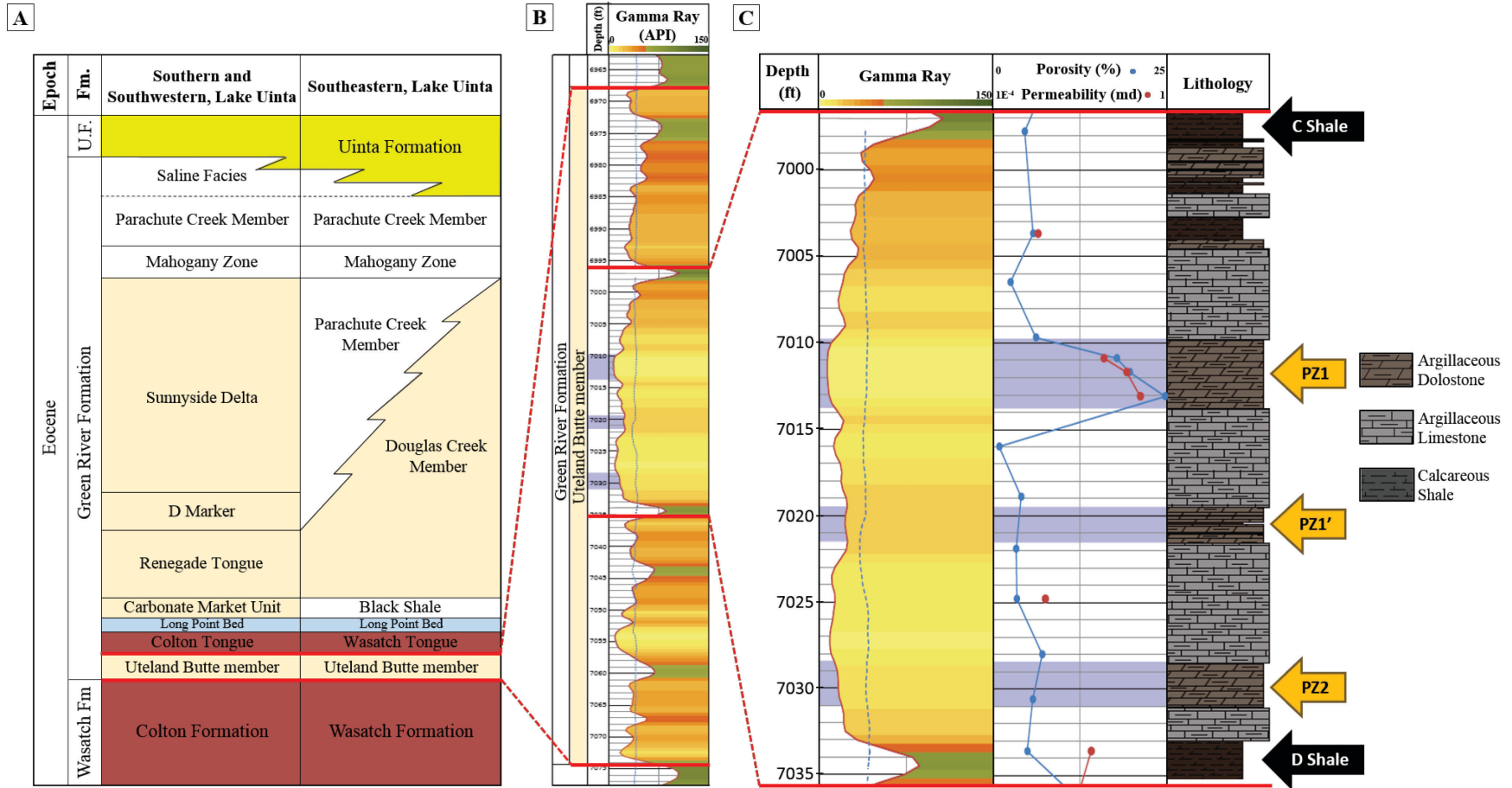


**Figure 1.3:** (A) Stratigraphic chart of the GRF modified from Logan et al. (2016). (B) Gamma ray and porosity logs of the entire UBm highlighting the interval of interest, which is located at central section of the UBm (well: UT 15-30). (C) Composite of gamma ray, porosity, permeability, and lithology logs of the interval of interest.

Over the years many models of dolomitization have been proposed, most of them with the aim to explain the genesis of reservoir-sized geobodies of dolostones, among them the microbial model, the mixing zone model, the related reflux and sabkha models, several seawater models, the compaction model, two thermal convection models, a topography driven model, a tectonic model, and the hydrothermal model (Machel, 2004). In addition, there are viable models for dolomitization that do not form reservoir-sized dolomite/dolostone geobodies, such as the Coorong and playa models (Eugster and Surdam, 1974; Warren, 2000). This study attempts to explain dolomitization of the GRF UBm within the framework of these models.

## **CHAPTER TWO**

### **GEOLOGICAL FRAMEWORK**

#### **2.1 Basin and lake evolution**

The formation of the Uinta Basin began in the Jurassic up to the early Cenozoic by the development of the Sevier Orogenic belt that resulted from the collision of the Farallon and the North American plate. (Johnson, 1985). The uplifted Sevier Orogenic belt became the west boundary of the Lake Uinta.

Later, during late Cretaceous to early Paleocene, the Laramide Orogeny caused retreat of the Rocky Mountains foreland basin and formed a series of regional uplifts (Johnson, 1985; Johnson et al., 2016) that transformed the epicontinental foreland basin into several smaller basins that filled with lakes in the early Eocene (Dickinson et al., 1988) (Figure 2.1A and B).

In the early Eocene, tectonic and climatic conditions allowed the development of four lacustrine basins: the Uinta Basin that occupied the area between Sevier and Laramide structures; the Gosiute Basin to the north in what is now southwest Wyoming; the Piceance Basin to the east in what is now Colorado; and the Claron Basin to the south (Figure 2.1 C, D).

The Uinta Basin is a structural, asymmetric basin located in the northeastern part of Utah, bounded in the north by the Uinta Mountains, in the east by the Douglas Creek Arch, in the south by the San Rafael Swell and the Uncompahgre Uplift, and in the west by the Wasatch Mountains.



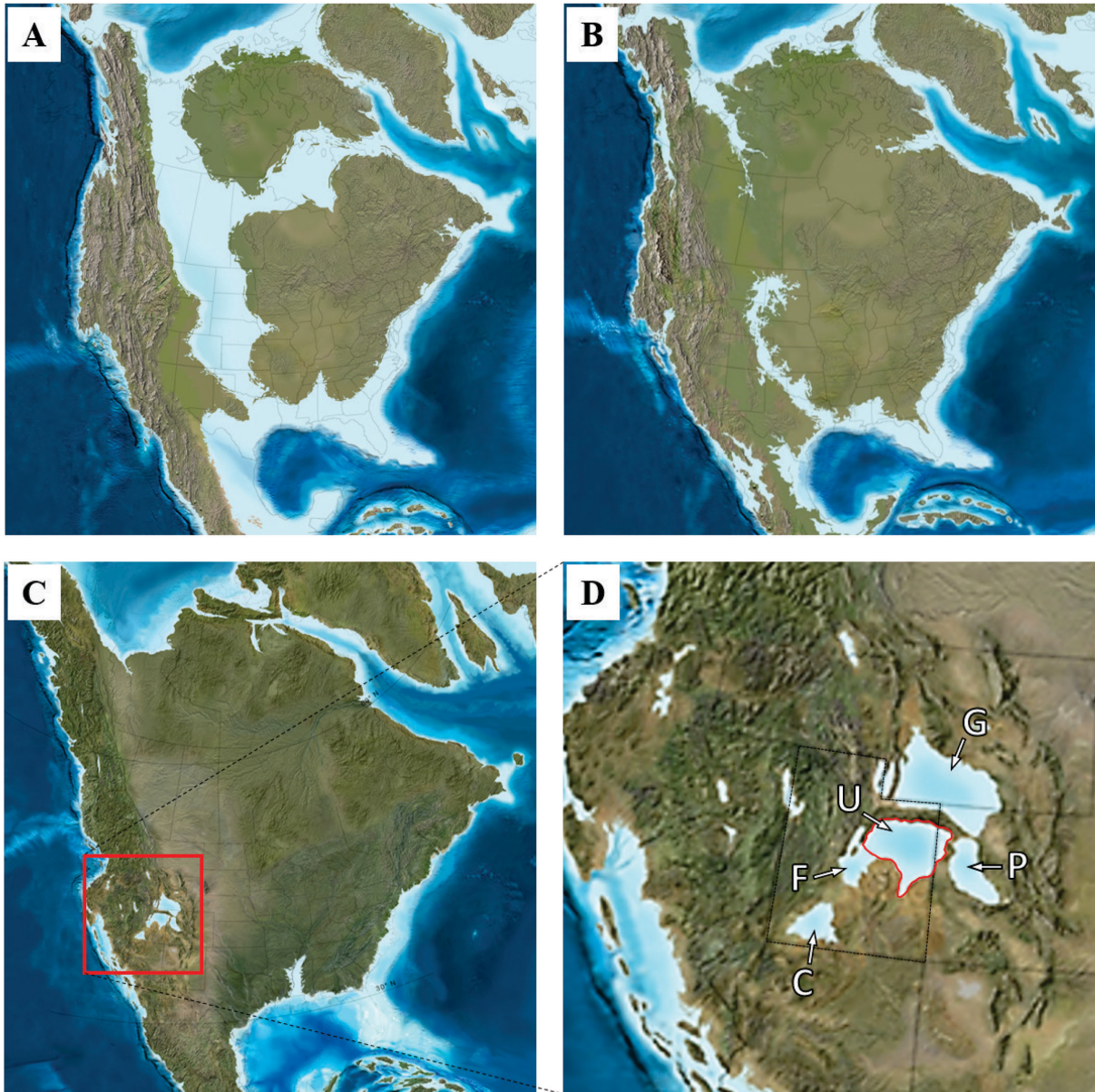


**Figure 2.1:** Paleogeographic evolution of North America during the Laramide Orogeny (A) and (B). (A) Late Cretaceous. (B) Early Paleocene. Both images retrieved from Ron Blakey website at [http://deeptimemaps.com/wp-content/uploads/2016/05/NAM\\_key-75Ma\\_LateK.png](http://deeptimemaps.com/wp-content/uploads/2016/05/NAM_key-75Ma_LateK.png). (C) and (D) Early Eocene: Intermountain and coexisting lacustrine basins. (D) enlargement of (C) showing Lake Gosiute (G), Uinta (U), Piceance (P), and Flagstaff (F), and Claron basins. The boundary between Uinta and Flagstaff basins is outlined in red, image retrieved from Ron Blakey website at [http://deeptimemaps.com/wpcontent/uploads/2016/05/NAM\\_key50Ma\\_Eocene.png](http://deeptimemaps.com/wpcontent/uploads/2016/05/NAM_key50Ma_Eocene.png).

## **2.2 Paleohydrology**

The tectonic events of the late Paleocene to early Eocene controlled the extent of drainage within the catchment area, and thereby sizes and connections of the Uinta and Gosiute lakes therein.

Ancient Lake Uinta was fed by streams from the surrounding paleo-highs. The basin received water from the Uinta Mountains to the north, and thereby sediments from the erosion of Precambrian to Cretaceous bedrock, including large deposits of Paleozoic carbonates (Hansen, 1965; Pusca, 2003; Smith et al., 2008).

From the west, sediment was supplied by the Wasatch Mountains (Sevier Thrust Belt), from erosion of Paleozoic and Mesozoic carbonates (Davis, 2008; Gierlowski-Kordesch et al., 2008).

The drainage from the south came from the San Rafael Swell, eroding mostly Paleozoic sedimentary rocks that ranged from marine shales of the Mancos Shale Formation to alluvial plains and fluvial clastics of the Morrison Formation (Doelling, 2002), and from the Mojave region transported by the California paleoriver (Dickinson et al., 2012). Drainage and sediments were also derived from the Uncompahgre Uplift in the southeast (Cashion, 1967; Dickinson et al., 1988; Davis et al. 2009; Johnson et al. 2010; Smith et al. 2008), mostly composed of Proterozoic metamorphic rocks (Case, 1991) (Figure 2.2).



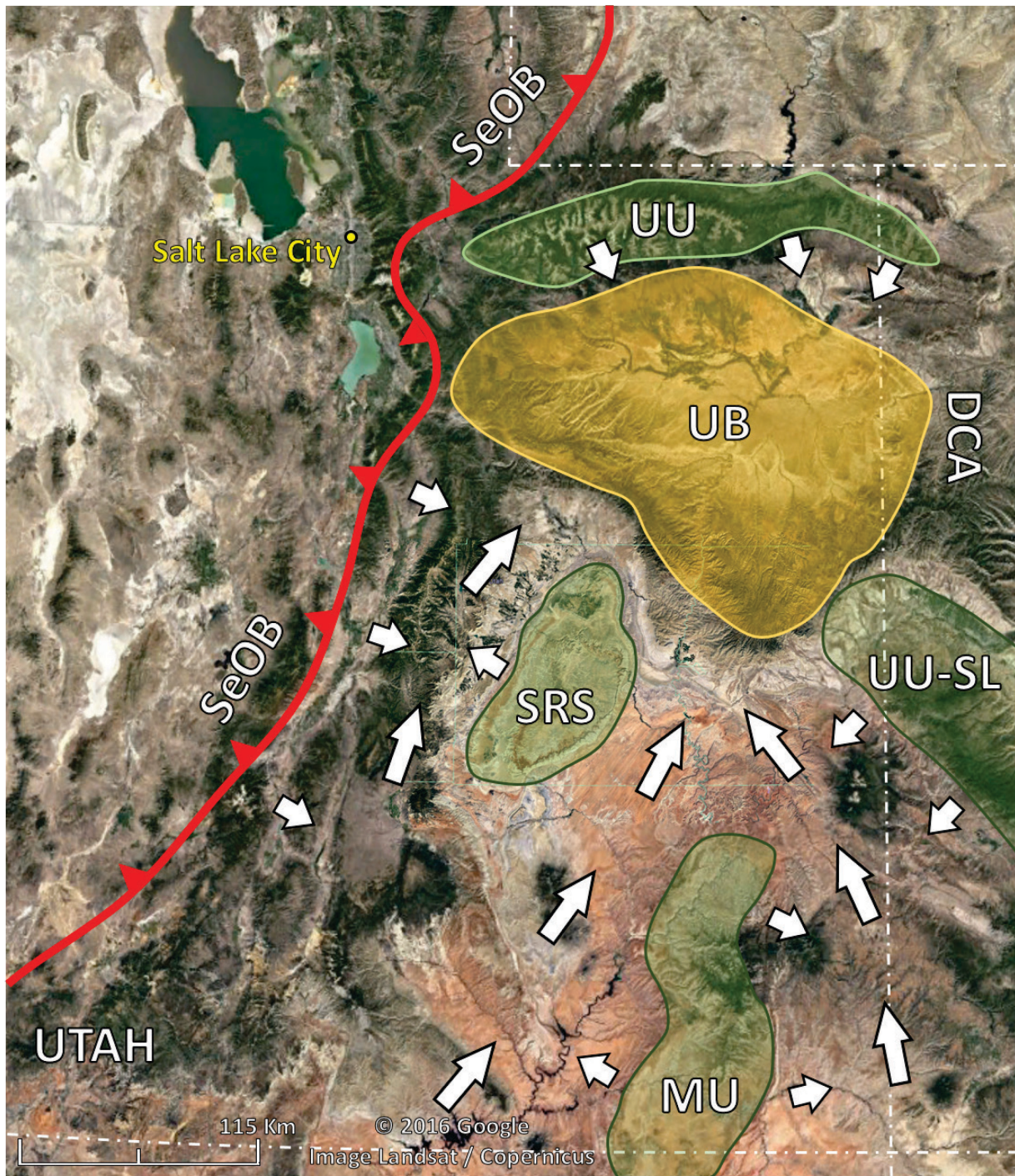


**Figure 2.2:** Paleogeographic location of the Uinta Basin and surrounding uplifts. Arrows represent potential paleocurrents that likely fed Lake Uinta. UB - Uinta Basin (Foreman et al., 2012; Vanden Berg et al., 2014), UP - Uinta Uplift (Baars and Stevenson, 1981; Foreman et al., 2012), UU-SL - Uncompahgre Uplift (Sweet and Soreghan, 2012) – San Luis Mountains (Kluth, 1986), MU - Monument Upwarp (Hintze et al., 2000), SRS - San Rafael Swell (Doelling, 2002), SeOB - Sevier Orogenic Belt (Hintze et al., 2000).

## 2.3 Sedimentology

The sedimentological evolution of these lakes was governed by climatic and tectonic factors that defined depositional settings and facies associations. Carroll and Bohacs (1999) established a lake classification based on facies associations: overfilled, balanced, and underfilled lake (Figure 2.3). According to Carroll and Bohacs (1999), the most common associations are fluvial-lacustrine, fluctuating profundal, and evaporite facies, which are the result of climate (sediment supply) and tectonism (accommodation rate) fluctuations.

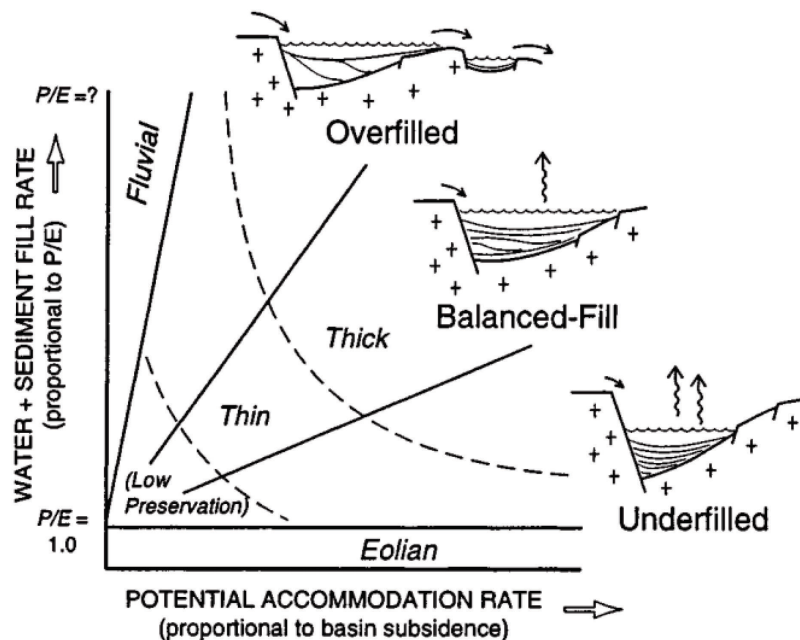


**Figure 2.3:** Schematic representation of lake types according to sediment and water supply (controlled by climate) versus accommodation rate (controlled by tectonism) (Carroll and Bohacs, 1999). Image from Carroll and Bohacs (1999).

The overfilled lakes are characterized by marlstone and fresh water coquinas interbedded with thin coal seams. Balanced-fill lakes record the flooding and desiccation phases by organic rich calcareous mudstone and dolomitic grainstone with evidences of subaerial

exposure. The underfilled lake types display a wide variety of facies association from alluvial-fan, laminated oil shales, and evaporite minerals such as trona and halite (Carroll and Bohacs, 1999).

Based on the lithologic characteristics and facies associations, sedimentation in Lake Uinta during deposition of the UBm was controlled mainly by periodic fluctuations of the lake water level and a balance between accommodation space and sediment infill. The UBm is characterized by shallowing upward sequences defined by organic rich shales, molluscan limestones and coquina, and dolomudstone to ooidal dolograins, which likely represent deposition in high-frequency flooding and dry cycles. Therefore, as defined by Carroll and Bohacs' (1999) lakes classification, deposition of the UBm most likely took place in the underfilled or balanced-fill lake types.

## **2.4 Stratigraphy**

The Green River Formation is conformably bounded at the base by the late Paleocene to early Eocene Wasatch Formation (Roehler, 1991) in the east and the Colton Formation in the west. The overlying Uinta Formation represents the fluvial sediments that eventually filled Lake Uinta. The age of deposition is between ca. 54 and 45 million years (Smith, 2007) corresponding to the early and middle Eocene epoch (Eugster et al., 1973; Ryder et al., 1976; Johnson, 1985). The GRF varies in thickness from about 2200 m in the center to northwestern area of the basin to about 600 m in the southeastern area (Schamel, 2015).

The Uteland Butte is the basal member of the GRF in the Uinta Basin (Cashion, 1964; Davis et al., 2009; Johnson et al., 2016). Its thickness also varies according to its location within

the Uinta Basin, with about 120 m being thickest in the north close to the Uinta Uplift, and thinning to about 15 m in the southeastern portion (Johnson et al., 2016). The age of deposition for the UBm is estimated as ca. 54 to 52 m.y. based on paleontological evidence (Remy, 1992). Moreover, using  $^{40}\text{Ar}/^{39}\text{Ar}$  radiometric dating of sanidine and biotite crystals deposited within the Leavitt Creek and Tabernacle Butte tuffs (Parachute Member), Smith (2007) arrived at 53 to 52 m.y. for the UBm, GRF in the Uinta Basin.

The GRF was first divided into four members (from top to base) by Bradley (1931) as follows: (1) Douglas Creek, (2) Garden Gulch, (3) Parachute Creek, and (4) Evacuation Creek. Since then, several other authors have provided different and in parts overlapping subdivisions for the GRF. Morgan and Bereskin (2003) were the first to identify and define the UBm at the base of the GRF. Logan et al. (2016) summarized the stratigraphic nomenclature of the GRF based on previous studies. In this project, the stratigraphic nomenclature of Logan et al. (2016) will be used, as shown in Figure 1.3.

## **2.5 Facies and Depositional Environments**

The lithofacies of the UBm generally consists of interbedded limestones, dolostones, calcareous mudstones, siltstones, and a few sandstones. The main allochem particles in the limestones are ostracods, ooids, fresh water molluscs (disarticulated pelecypods or tubiform gastropods), algae, fish fragments, peloids, and intraclasts (Morgan et al., 2003; Bereskin et al., 2004). Bereskin et al. (2004) interpreted the GRF as deposits from two main environments: (1) marginal lacustrine carbonates flats, deltaic, and inter-deltaic environments; and (2) open, deeper lacustrine facies. Similarly, Ryder et al. (1976) identified three main environments: (1)

open lacustrine; (2) marginal lacustrine deltaic and inter-deltaic mudflats and paludal; and (3) alluvial deltaic plain, high mud flat, and alluvial fan, based on outcrop observations and well logs from the lower section of the GRF. In outcrops located in the southern margin of the Uinta Basin, Long (2006) identified cyclic intercalations of massive biomicrites with ostracods, gastropods, bivalves, and charophytes at the base, dark organic rich micrites with nodules in the middle, then grading into shales toward the top. Most recently, and based on outcrops and cores located on the east boundary of the basin, Logan et al. (2016) described the UBm as intercalations of grey to green siltstones, dolomudstone to dolograinsstone with abundant peloids, ostracods, and rock fragments, molluscan lime wackestone to mudstone, sandstones, coal seams, and oil shale. Logan et al. (2016) interpreted the depositional environments of the UBm as a fresh water ramp margin with minor influence of fluvial systems, based on the absence of stromatolites, lack of evaporite minerals, and abundance of bivalves, gastropods, and ostracods with in the limestone beds.



## **CHAPTER THREE**

### **METHODOLOGY**

This study investigates the depositional, diagenetic, and geochemical characteristics of the dolomites PZ layers of the UBm as a means to better understand the dolomitization processes. This study employed a wide variety of investigative methods including: 1) outcrop and core descriptions; 2) petrographic analysis by means of transmitted light and cathodoluminescence microscopy; 3) scanning electron microscopy (SEM); 4) mineralogical identification via semi-quantitative major element analysis and ordering of dolomites through X-ray diffractometry (XRD); 5) elemental composition by X-ray spectrometry (EDS coupled with SEM); 6) electron microprobe analysis (EPMA); 7) trace element analysis using inductively coupled plasma mass spectrometry (ICP-MS), and 8) conventional and clumped oxygen and carbon stable isotope analysis. In addition, a few extant data (such as ROCK-EVAL and porosity/permeability core plug data) were incorporated in the discussion and interpretation. The methodology of acquisition and reliability of this data is not further discussed here but can be found in the respective sources (to be cited later).

#### **3.1 Field work: Outcrops**

Two Ute land Butte outcrops were studied in the spring of 2015, located in the southwestern portion of the Uinta Basin: Nine Mile Canyon and Willow Creek Canyon (Figure



1.2). A stratigraphic column was created for each outcrop area based on centimetre-scale descriptions of lithology, fossils, sedimentary structures, and contact types. The Willow Creek Canyon section covers a thickness of 175.7 ft (53.5 m) and contains the entire UBm. The Nine Mile Canyon section covers a thickness of 34.6 ft (10.5 m) and includes only the upper portion of the UBm (Appendix 1). Table 3.1 contains detailed location information for each outcrop section.

### **3.2 Core description and sampling**

Core selection was based on three main features: well location, recovery of the UBm, and core accessibility. Cores that cover the interval of interest (excluding the BBC 14-3-45 well that only captured the PZ1 dolomite layer) and are located in the west-central area of the Uinta Basin were selected. These cores vary from shallow (south) to deep (north) depositional environments, and incorporate geologic characteristics of the basin center not exposed at outcrop. Table 3.1 contains detailed location information for the cores included in this study.

Once the wells were chosen, the cores that are housed at the Utah Geological Survey (UGS) in Salt Lake City (UT) were first logged at centimetre-scale and sampled from November 11<sup>th</sup> to November 14<sup>th</sup>, 2014. The remainder of the chosen cores were located in a private storage facility in Denver, CO, and were logged there from February 15<sup>th</sup> to February 20<sup>th</sup>, 2015.

The fundamental criteria for sampling was the ability to cover the entirety of dolomite layers PZ1, PZ1' and PZ2 from base to top. In addition, interbedded layers of limestone and dolostones below, between, and above the three layers of interest were also sampled, but with less coverage. A total of 167 samples were taken from the cores for further analysis.

Stratigraphic columns were built for each described core (Appendix 2) in base of previous core descriptions (Vanden Berg, personal communication, 2015) complemented with own core descriptions and information obtained from thin section petrography.

<b>Code</b>	<b>Operator at time of drilling (current operator)</b>	<b>Well/Outcrop name</b>	<b>Well/Outcrop location</b>	<b>Current location of core</b>
BBC 14-1	Bill Barrett Corp. (Rig II)	14-1-46	N 40° 9' 26.5" W 110° 30' 48.1"	Utah Core Research Center, Salt Lake City
BBC 14-3	Bill Barrett Corp. (Rig II)	14-3-45	N 40° 9' 23.7" W 110° 26' 17.4"	Utah Core Research Center, Salt Lake City
N 6-28	Newfield	Nickerson 6-28-3- 2W	N 40° 11' 40.8" W 110° 7' 1.6"	Newfield facility in Houston
UT 15-13	Newfield	Ute Tribal 15-13-4- 3W	N 40° 7' 45.5" W 110° 10' 7.9"	Newfield facility in Houston
PW 13-06	EOG Resources (QEP Energy)	Petes Wash 13-06 GR	N 39° 58' 44.1" W 110° 10' 7.2"	Utah Core Research Center, Salt Lake City
DS 11-20	Chandler (QEP Energy)	West Desert Spring 11-20-10-17	N 39° 55' 39.0" W 110° 1' 54.2"	Utah Core Research Center, Salt Lake City
IU 16	Wexpro (QEP Energy)	Island Unit 16	N 39° 57' 24.2" W 109° 51' 49.8"	Utah Core Research Center, Salt Lake City
WCC		Willow Creek Canyon	N 39° 50' 17.2" W 110° 47' 3.3"	
NMC		Nine Mile Canyon	N 39° 46' 35.5" W 110° 28' 58.5"	

**Table 3.1:** Detailed location, operator and core location of selected wells, and outcrops used in this research.

In addition to the outcrops and core information, extant data were used in this research, such as porosity and permeability values measured from core plugs by Core Laboratories Company (USA). This information was provided by Michael Vanden Berg. The data is described in Chapter 5, Sections 5.3 and 5.4.

### **3.3 Petrography**

#### **3.3.1 Transmitted light microscopy**

A total of 140 polished thin sections were investigated using a Zeiss Jenapol Polarizing Microscope under 3.2X, 10X, and 20X magnifications. All thin sections were partially stained, for easier determination of calcite versus dolomite mineralogy, by dipping them halfway into a solution of 1.5% HCl acid + 0.2 grams (g) of Alizarin red solution + 2.0 g of Potassium ferricyanide, following a procedure proposed by Dickson (1965). Detailed descriptions were generated for each thin section using rock classifications of Dunham (1962), with modifications by Embry and Klovan (1971), and focused on mineralogical composition as well as identification of bioclasts, coated grains, sedimentary structures, and bioturbation (Appendix 3). In addition, the carbonate grains were classified according to Flügel (2010) and semi-quantitative estimates of matrix, carbonate grains, and siliciclastic material were made using charts by Baccelle and Bosellini (1965).

### **3.3.2 Cathodoluminescence microscopy**

Cathodoluminescence microscopy was performed using an Olympus BH-2 microscope coupled with a cold cathode Premier American Technologies Luminoscope Model ELM-3R. Each thin section was placed in the vacuum chamber with the pressure reduced to about 0.07 Torr, then irradiated by an electron beam with a voltage of 10-15 kV and a current of about 0.5 mA. Luminescent images were recorded using a digital camera Pentax K-5.

Twenty-one thin sections from the PZ1, PZ1', PZ2 dolomite layers were selected from four wells: Nickerson 6-28-3-2W, Ute Tribal 15-13-4-3W, Petes Wash 13-06 GR, and Island Unit 16, which are located along a traverse that stretches from distal (north) to proximal (south) parts of the ancient lake (Figure 1.2).

### **3.3.3 Scanning electron microscopy (SEM)**

A total of ten polished thin sections were selected for SEM petrography and energy dispersive X ray spectroscopy (EDS) analysis (Appendix 4). All samples were coated with a carbon film to improve conductivity and thus image resolution. The equipment used was a Zeiss EVO LS15 EP using an electron beam with an accelerating voltage of 25.0 kV, located in the SEM laboratory at the Department of Earth and Atmospheric Sciences (EAS Department), University of Alberta.

### 3.4 X-Ray diffractometry

A total of 76 powder samples were analyzed in the X-ray diffractometry laboratory, EAS Department, University of Alberta. Approximately 1 g of each sample was mixed with an internal quartz standard, then mounted on a zero-background plate. Samples were powdered using a low speed micro-drill with tungsten carbide and diamond bits. The equipment used was an Ultima IV Rigaku X-ray Diffractometer, which uses a cobalt tube with a radiation wavelength ( $\lambda$ ) value of 1.78899 Å, run at 40 kV and 35 mA. All scans were run from 2° to 100° 2 $\theta$ , using a 0.02° 2 $\theta$  step size with a scan speed of 2° 2 $\theta$  per minute. The resulting peaks were then corrected with the quartz internal standard *d*101 peak (31.035° 2 $\theta$ ). Identification of minerals was done by Jade 9 software. The results are tabulated in Appendix 5.

As part of collaborative work, a total of 21 powdered samples were analyzed at the X-Ray diffractometry laboratory in the EAS Department at Indiana University Bloomington (USA), and a total of 47 powdered samples were analyzed at the X-Ray diffractometry laboratory in the Department of Geosciences at Western Michigan University (USA). All powders were acquired using a low speed micro-drill with tungsten carbide and diamond bits. The equipment used at the Indiana University laboratory was a Bruker D8 X-ray Diffractometer, which uses a copper tube with a radiation wavelength ( $\lambda$ ) value of 1.540562 Å, run at 45 kV and 35 mA. All scans were run from 2° to 70° 2 $\theta$ , using a 0.02° 2 $\theta$  step size with a step time of 0.6° 2 $\theta$  per minute. The equipment used at the Western Michigan University laboratory was a Second Generation Bruker D2 Phaser X-ray Diffractometer, which uses a copper tube with a radiation wavelength ( $\lambda$ ) value of 1.54 Å. All scans were run from 20° to 60° 2 $\theta$ , using a 0.008° 2 $\theta$  step size with a step time of 0.48° 2 $\theta$  per minute. Results are presented in Appendix 5.

### **3.5 Major and Trace Elements Analysis**

#### **3.5.1 Electron microprobe analysis (EMPA)**

Given the aphanocrystalline size of dolomite crystals identified with SEM (see detailed explanation in chapter 5, section 5.2.1.1), electron microprobe analysis was selected to obtain quantitative dolomite chemical values.

A total of four highly polished thin sections of PZ1, PZ1', and PZ2 were analysed using the Electron Micro Probe Cameca SX100 equipped with five wavelength dispersive spectrometer (WDS) of the Electron Microprobe Laboratory, EAS Department, University of Alberta. Operating conditions were: 40° takeoff angle; beam energy of 15 keV; 20 nA beam current; and 3 µm beam diameter. Prior to analysis, each thin section was coated with carbon film to enhance conductivity over the polished thin section surface. For data corrections, a series of standard measurements (dolomite, siderite, strontianite, and K-253 NIST RM glass) were conducted before the analysis. The results are summarized in Appendix 6.

#### **3.5.2 Inductively coupled plasma mass spectrometry (ICP-MS) analysis**

A total of 50 samples from the PZ1, PZ1', and PZ2 dolostones and interbedded limestones were analyzed for major and trace element concentrations in the Canadian Centre for Isotopic Microanalysis laboratory at the University of Alberta. The measurements were carried out using a Perkin-Elmer Elan 6000 Inductively Coupled Plasma – Mass Spectrometer (ICP-MS) with a cross-flow nebulizer, a 40 MHz RF-generator, with a working power between 600 and 1600 W.

Powdered samples of 200 mg were digested overnight in 10 ml of nitric acid 8N. After digestion, solid and liquid phases were separated by centrifuge. Concentrations were determined for 10 elements: Mg, Ca, Al, Si, Fe, Mn, Na, Zn, Sr, and Pb. The results are presented in Appendix 7.

### **3.6 Stable Isotope Analysis**

#### **3.6.1 Conventional carbon and oxygen stable isotope analysis**

A total of 74 samples were selected for conventional carbon and oxygen stable isotope analysis, including 18 samples from PZ1, 9 from PZ1', and 12 from PZ2. The rest of the samples are from interbedded layers of limestone and dolostones below, between, and above the three layers of interest. All samples were analyzed in the Isotope Science Laboratory at the University of Calgary. Calcite and dolomite were analyzed by a continuous flow isotope ratio mass spectrometry (CF-IRMS) using a Thermo Finnigan GasBench coupled to a DeltaV<sup>Plus</sup>. The powders were taken using a low speed micro-drill with tungsten carbide and diamond bits. A powdered sample of approximately 300 µg was then weighted into a vial and approximately 200 µl of anhydrous phosphoric acid was added for digestion at 25°C for a specific time. The evolved CO<sub>2</sub> was then sampled automatically by the Gas Bench and introduced into the DeltaV<sup>Plus</sup> stable isotope ratio mass spectrometer for analysis of  $\delta^{13}\text{C}$  and  $\delta^{18}\text{O}$  ratios (Applied Geochemistry Group, 2014).

Since previous XRD analyses revealed that many samples contain variable mixtures of calcite and dolomite (with generally very minor contributions of quartz and silicates), the

bimineralic carbonate samples were subjected to a selective chemical separation as follows: first, an aliquot of CO<sub>2</sub> was sampled at variable times of about 2-8 hours and deemed to represent calcite only; a second aliquot of CO<sub>2</sub> was retrieved after about 72 hours, at which time all carbonates had been digested, and deemed to represent dolomite. Unexpectedly, and unfortunately, it turned out that the first aliquot also contains some CO<sub>2</sub> from dolomite (further discussed below). Internal lab reference materials were run at the beginning and the end of each set of samples (nine samples per set) and were used to normalize the data and to correct any equipment deviation. All results are reported in the permil notation (‰) relative to the international VPDB scale for  $\delta^{13}\text{C}$  and  $\delta^{18}\text{O}$  (Applied Geochemistry Group, 2014).

While it is common practice in stable isotope research to separate calcite and dolomite through differential phosphoric acid digestion, commonly 1 to 2 hours for calcite and >8 to 12 hours for dolomite (Degens and Epstein, 1964; Al-Aasm et al., 1990; Ray and Ramesh, 1998; Walters et al., 1972; McCrea, 1950; Swart et al., 1991), these acid digestion times could not be used in our work due to the automated system in operation at the University of Calgary. As a consequence, the maximum acid digestion time (hours) was exceeded, which resulted in variable amount of dolomite dissolved along with the calcite (to produce the first aliquot of CO<sub>2</sub>, as described previously). Therefore, many isotopic values from bimineralic carbonate samples, and initially deemed to be valid for calcite, are not trustworthy.

The problem was identified by comparing the calcite/dolomite ratios determined by XRD with the calcite/dolomite ratios determined by the amounts of CO<sub>2</sub> of the first and second aliquots. Once this problem was identified many of the samples previously deemed to represent calcite were excluded from the data analysis and/or flagged as calcite-dolomite mixtures. The only values deemed to reliably represent calcite are those that fulfill the following requirements: (1) monomineralic calcite samples (100% calcite), and (2) samples with calcite/dolomite ratios



less than 5% (maximum error allowed) based on XRD data. Moreover, samples with >5% dolomite also contain minor amount of quartz, illite, albite, and/or muscovite. Therefore, dolomite contamination is considered negligible. The results are presented in Appendix 8.

### **3.6.2 Clumped isotopes**

The clumped isotope technique was applied to a small subset of samples because it allows for estimation of the temperature of carbonate mineral formation regardless of fluid chemical composition. (Ghosh et al., 2006; Eiler, 2007). The relation between  $^{13}\text{C}$  and  $^{18}\text{O}$  of dolomite crystals is totally independent of the isotopic composition from dolomite precursor fluid (Millán et al., 2016; Ghosh et al., 2006).

A total of 26 samples from the PZ1, PZ1', and PZ2 dolostones, as well as the interbedded limestones (splits of the powdered samples previously drilled for XRD and conventional isotope analysis), were selected to be run on a collaborative basis at the Department of Earth Sciences at Swiss Federal Institute of Technology (Switzerland). The analytical procedure is described in Millán et al. (2016). At the time of this writing, only a small subset of these 26 samples had been run with an insufficient number of duplicate and re-runs. Hence, the data presented in this research have to be considered preliminary and not sufficiently verified.

## **CHAPTER FOUR**

### **FACIES**

The facies deposited in lake basins are controlled by a number of independent and partially interdependent external factors such as: drainage area, type of surrounding rock outcrop, topography, tectonism, and climate, as well as internal agents, such as oxygen availability, nutrients, water chemistry, etc. (Gierlowski-Kordesch, 2010; Barron, 1990). In some cases, even small changes in these factors can impact depositional environments creating disproportionate variations in lateral and vertical facies architecture. Conversely, changes in facies allow, within limits, conclusions about the aforementioned internal and external agents.

Facies types were identified and characterized using outcrop, core, and thin section descriptions from the stratigraphic interval between the D and C shales, located in the middle section of the UBm at the base of the GRF. These facies types were created based on detailed and systematic descriptions of: (1) depositional rock textures: rock type, grain size, sorting, and packing; (2) bioclasts; (3) other carbonate grains: coated grains, peloids, and intraclasts; (4) sedimentary structures: stratification, bedding, laminations, and bioturbation; and (5) siliciclastic material. The facies were numbered from 1 to 10 in the order of overall shallowing depositional environments (Table 4.1).

	FACIES NAME	LITHOLOGY	BIOCLASTS	OTHER CARBONATE GRAINS	SEDIMENTARY STRUCTURES	CLASTIC MATERIAL	ENVIRONMENT
1	Silty mudstone	Silty mudstone	Ostracod shell fragments	-	Planar parallel, wavy discontinuous	Clay	Distal sublittoral to profundal
2	Lime mudstone	Dolomudstone	Scarce ostracod shell fragments	Scarce peloids	Structureless	Coarse silt subangular quartz grains and clay	Distal littoral - sublittoral carbonate mud flats
3	Ostracod wackestone	Dolowackestone	Ostracod shells, scarce fish bones and charophytes	Peloids	Massive, plane parallel	Scarce silt quartz grains	Littoral
4	Peloid wackestone-packstone	Silty dolowackestone - dolopackstone	Scarce ostracods and fish bones	Peloids	Wavy discontinuous, plane parallel	Coarse silt subangular quartz grains and clay	Littoral
5	Mollusc mudstone-wackestone-floatstone	Wackestone - floatstone	Pelecypods, gastropods, and ostracods	-	Massive	Scarce silt quartz grains	Littoral - Sublittoral
6	Intraclast grainstone-packstone	Dolograinstone - dolopackstone	Scarce ostracod shell fragments	Intraclasts	Structureless	-	Littoral shoreline
7	Ooid grainstone-packstone	Dolograinstone - dolopackstone	Ostracods and rare charophytes	Ooids, scarce peloids, oncoids and intraclasts	Massive, cross lamination	-	Littoral Shoreline
8	Ostracod grainstone-packstone	Dolograinstone - dolopackstone	Ostracods	Scarce ooids and peloids	Structureless, wavy discontinuous	Coarse silt to fine sand, subangular quartz grains	Littoral near shore and shoreline
9	Brown claystone	Arenaceous claystone	Scarce ostracod shell fragments and fish bones	-	Plane parallel	Coarse silt rounded quartz grains	Distal littoral
10	Coal	Coal	Plant fragments	-	-	-	Supralittoral swamps

**Table 4.1:** Summary of lithofacies identified between the D and C shales.

In the most detailed work on depositional facies in the entire section of the UBm, Logan et al. (2016) defined a total of 18 lithofacies types, which are based on outcrops near the eastern margin of the Uinta Basin complemented by the core from central Uintah County (central-east side of basin). Table 4.2 provides a correlation of facies types from Logan et al. (2016) with those established in this study. Several facies types defined by Logan et al. (2016) are not found in the central-west part of the basin because the east part of the basin contains more proximal facies, and also the stratigraphic interval of interest is just a section of the entire UBm.

<b>This research</b>		<b>Logan (2015)</b>	
	<b>Facies Name</b>		<b>Facies Name</b>
<b>1</b>	Silty oil shale	18	Laminated silt-rich oil shale
<b>2</b>	Lime mudstone	17	Argillaceous mudstone
<b>3</b>	Ostracod wackestone	3	Ostracod Lime Wackestone/ Mudstone
<b>4</b>	Peloidal wackestone - packstone	5	Oolitic Lime Mudstone/ Wackestone
<b>5</b>	Molluscan mudstone - wackestone - floatstone	4	Molluscan Lime Mudstone/ Wackestone
		11	Bioclastic Floatstone to Rudstone
<b>6</b>	Intraclast grainstone - packstone	6	Intraclastic-ostracod Lime Packstone/ Grainstone
<b>7</b>	Ooid grainstone - packstone	9	Oolitic packstone/ grainstone
<b>8</b>	Ostracod grainstone - packstone	7	Ostracod Packstone/ Grainstone
<b>9</b>	Brown claystone	W	Green, Brown & Maroon
<b>10</b>	Coal	15	Coal
-	-	1	Grey/ Green
-	-	2	Calcareous to Dolomitic Mudstone
-	-	8	Oncolite-ostracod grainstone
-	-	10	Pisolite packstone/ grainstone
-	-	12	Ostracod Sandstone
-	-	13	Structureless Sandstone
-	-	14	Cross-Stratified Sandstone
-	-	16	Illitic Oil Shale

**Table 4.2:** Lithofacies correlation between Logan et al. (2016) and this project.

## **4.1 Lithofacies**

This section provides descriptions and images of the most distinctive facies types encountered in the study area. Furthermore, this section offers an interpretation of the depositional environments based on described features. Diagenetic features are mostly excluded and were not considered in the interpretations of the depositional environments, unless these features appear to be integral parts of the depositional setting. For example, pyrite that formed syndepositionally that indicates an anoxic depositional setting, or syndepositional length-slow chalcedony that suggests an evaporitic depositional setting. Dolomitization is also excluded.

### **4.1.1 Silty mudstone - F1**

The silty mudstone lithofacies (F1) is a finely laminated, black to dark gray, organic-rich silty mudstone with up to 10% quartz grains, which range from coarse to fine silt size and are subangular, poorly sorted, and erratically distributed (Figure 4.1). Bioclasts are mostly thin, disarticulated ostracod shell fragments, many with preserved fish-hook shape terminations (Scholle and Ulmer-Scholle, 2003), 0.3 to 0.5 mm in length, aligned parallel to stratification. These shells form densely packed coquinas with thicknesses of 0.5 to 1 mm (Figure 4.1B). These layers are interbedded with lean, organic-poor clay layers and laminae that appear light gray in hand specimens. Scarce dewatering structures truncate some laminations (Figure 4.1C).

*Depositional environment.* Clay sized material was deposited in a low-energy setting below fair-weather wave base, probably in a distal sublittoral to profundal environment, allowing for accumulation of sediment from suspension. Preservation of organic matter (black area in thin section, Figure 4.1B) and the absence of bioturbation suggest an anoxic depositional

environment likely developed by thermal and/or chemical lake water stratification (Collinson, 1979; Bohrer and Schultze, 2008; Tucker and Wright, 2009; Long, 2006), whereby deposition of the organic-rich layers took place below the chemocline. On the other hand, the lean clay laminae likely represent periods of low organic matter production and/or vertical fluctuations of the chemocline paired with increased fresh water inflow via river(s).

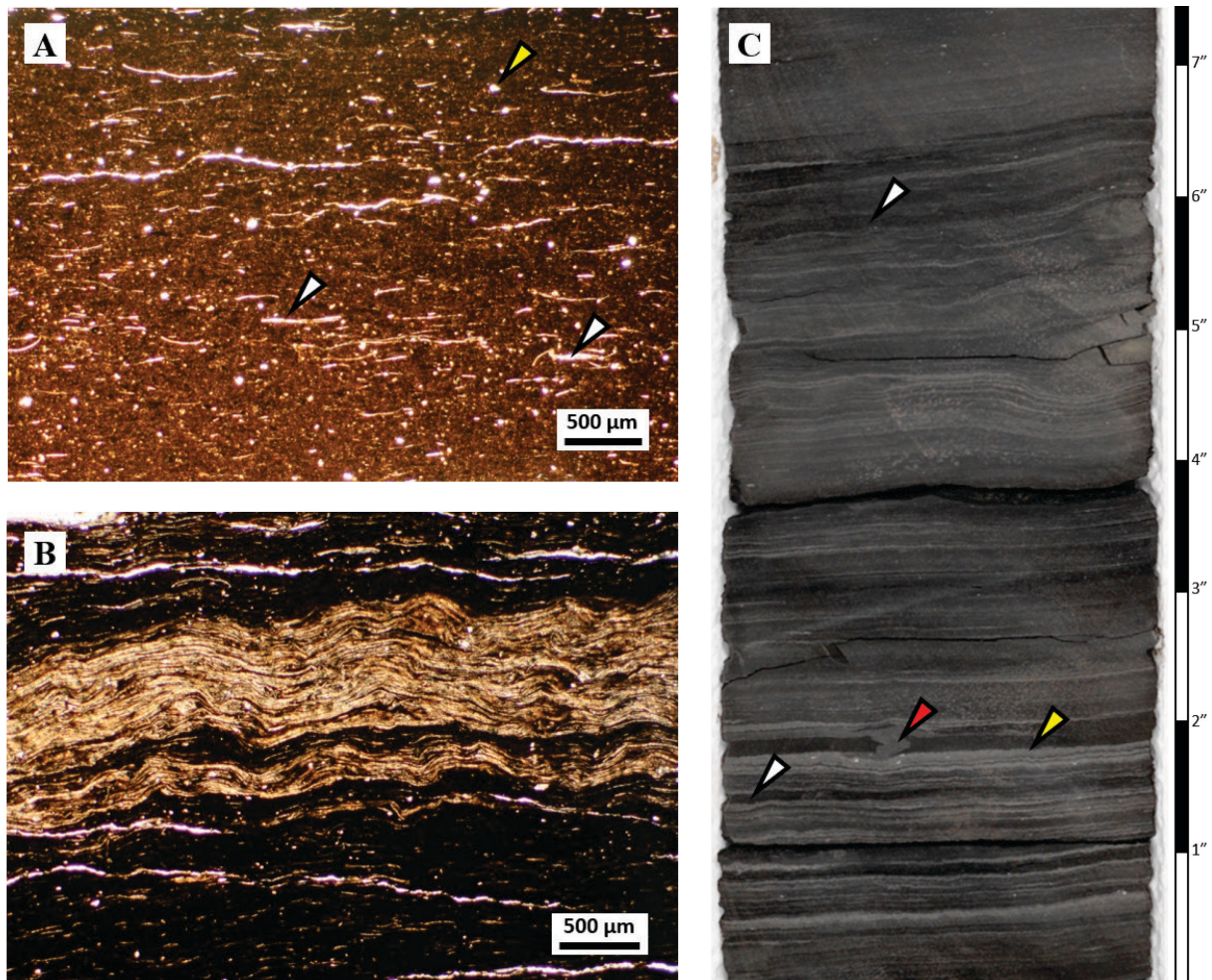


**Figure 4.1:** Facies F1 - Silty mudstone. (A) Transmitted light photomicrograph (TLP) of an organic poor bed with ostracod shell fragments (white arrows); aligned parallel to stratification (horizontal axis), silt material is mainly quartz (yellow arrow); well: BBC 14-1, sample 24, 6672.8 ft., plane polarized light (PPL). (B) TLP of densely packed shell fragments (light yellow band) interbedded with organic-rich mudstone (dark areas); well: BBC 14-1, sample 7, 6705.3 ft., PPL. (C) Core photograph of silty mudstone facies interbedded with organic-rich laminae (white arrow), densely packed shell laminae (yellow arrow), and organic-poor silt laminae (light gray), and dewatering structures (red arrow); well: BBC 14-1, 6705'4" to 6705'11".



#### 4.1.2 Lime mudstone – F2

The lime mudstone lithofacies (F2) is light brown, commonly homogeneous, microcrystalline lime mudstone (completely dolomitized with the exception of bioclasts), bioclasts (ostracod shell), with about 3% clay minerals, and rounded, poorly sorted grains of quartz ranging from fine to medium silt (Figure 4.2). Accessory minerals are microcrystalline pyrite (less than 3%), occasional authigenic, euhedral, prismatic, and microcrystalline quartz (less than 1%), and quartzine (length-slow chalcedony) crystals filling intraparticle pores. Bioclast content is low, generally less than 3%, and is mainly composed of articulated or fragmented ostracod shells ranging in size from 0.05 to 0.2 mm (Figure 4.2A). This facies shows massive to planar parallel stratification and rare bioturbation structures are present in core. This facies is occasionally interbedded with thin laminae consisting of irregular or lenticular carbonate grains such as peloids (likely steinkerns) and scarce ooids transported from different environments (likely from nearshore areas), forming small lenses of peloidal grainstones (Figure 4.2B).

*Depositional environment.* The microcrystalline matrix that makes up most of this facies type probably crystallized directly from lake water as lime mud suggesting a low energy setting. Furthermore, excellent preservation of disarticulated and unbroken ostracod shells (Figure 4.2A) implies that these bioclasts were not transported, suggesting a low energy environment with quiet water below the fair-weather wave base. Moreover, the low content of clays ( $\leq 3\%$ ) suggests a depositional environment located relatively far away from the source of siliciclastic input (rivers) and/or represents times of significantly reduced input of rivers. Episodic storm events, evidenced by lime mud beds that interfinger with peloidal grainstone lenses (Figure 4.2B), disrupted the generally calm setting. The presence of quartzine likely

represents brief periods of subaerial exposure with evaporation (further discussed in Chapters 5 and 6).

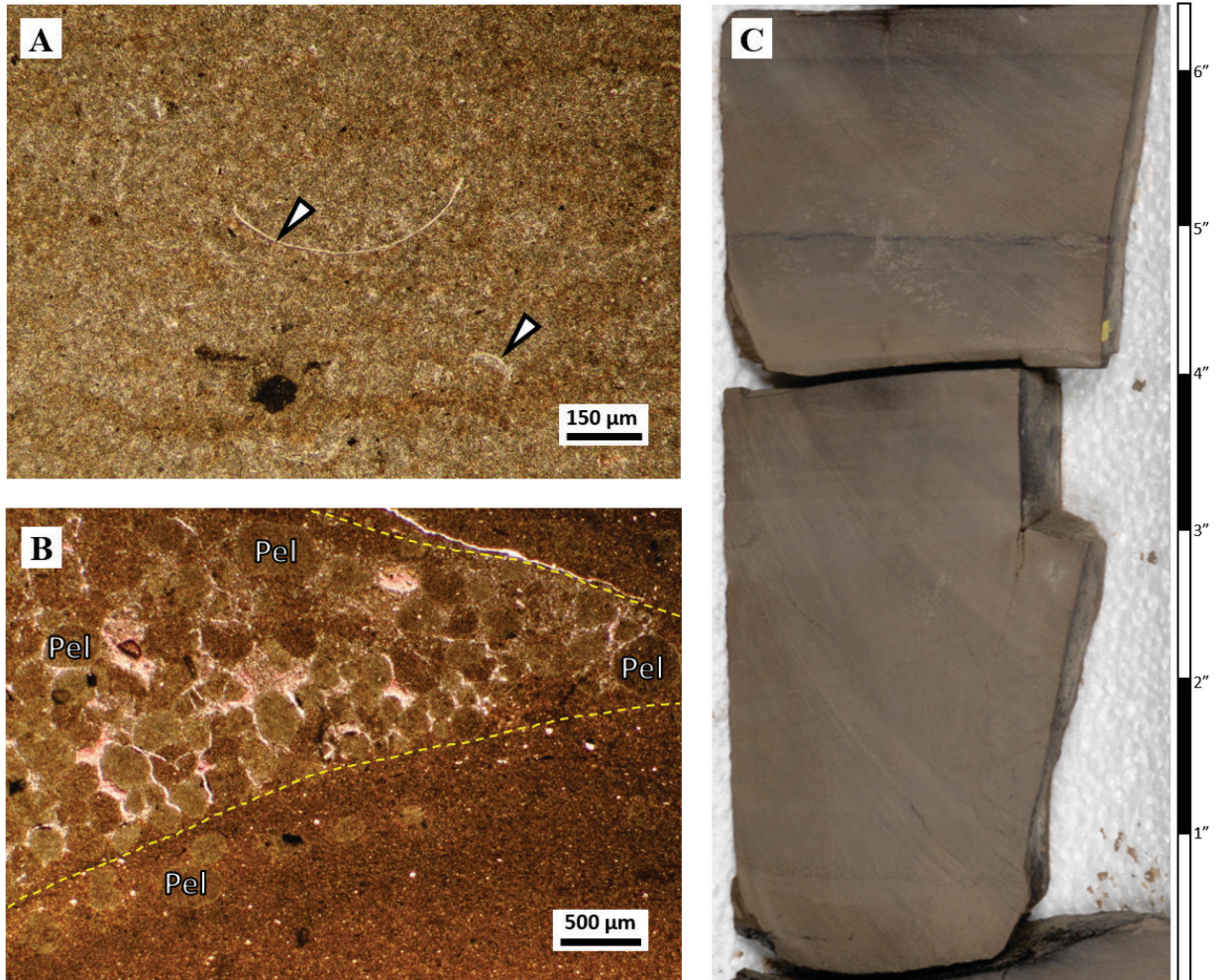


**Figure 4.2:** Facies F2 - Lime mudstone. (A) TLP of lime mudstone with scarce and well preserved disarticulated ostracods shells (arrows); well: BBC 14-1, sample 17, 6692.6 ft., PPL. (B) TLP of interbedded lenses (yellow dashed lines) of dolomitized peloids (Pel) embedded in microsparitic calcite cement (stained pink); bitumen (?) between peloids (dark areas); well: N - 628, sample 3, 8205.6 ft., PPL. (C) Core photograph of lime mudstone facies characterized by massive and planar stratification; well: BBC 14-1, 6702'8" to 6703'4".



### 4.1.3 Ostracod wackestone – F3

The ostracod wackestone lithofacies (F3) is brown, microcrystalline matrix with <10 vol-% of siliciclastic material. Fragmented ostracod shells are abundant (Figure 4.3A), fish bones and minor to rare elliptical gyronites [charophytes female reproduction organ (Flügel, 2010)] with size ranging from 0.02 to 0.05 mm (Figure 4.3B). Dolomitized peloids are also relatively common and range from 0.01 to 0.05 mm in size. Stratification is mostly planar or slightly wavy, whereas some layers are bioturbated. Accessory minerals are microcrystalline pyrite (less than 1 vol-%), and scarce quartz grains. This facies hosts conspicuous chert nodules with irregular shapes and sizes, commonly with cm-dimensions and elongated parallel to bedding (Figure 4.3C).

*Depositional environment.* The most important differences between facies F2 and F3 is the relative abundance of peloids and ostracods in facies F3, and the chert nodules that appear to be absent in facies F2. Again, the microcrystalline matrix that makes up most of this facies F3 probably crystallized directly from lake water as lime mud. The setting probably located in distal littoral below the fair-weather wave base. In-situ deposition of benthic ostracod (Figure 4.3A) indicates an oxygenated environment. Furthermore, gyrogonites (Figure 4.3B) also points to shallow water depths within a littoral setting (Håkanson and Jansson, 1983, Flügel, 2010), whereas the association of ostracods with charophytes (gyrogonites) suggests brackish lake water (Flügel, 2010). Chert nodules with quartzine suggests episodic evaporitic conditions (Folk and Pittman 1971, Pittman and Folk, 1971; Eugster and Hardie, 1978; Scholle and Ulmer-Scholle, 2003; Warren, 2006; Flügel, 2010). The chert nodules thus can be interpreted as an integral part of the depositional setting even though, in the strictest sense, they are a diagenetic feature (as the dolomite is that now makes up the matrix).

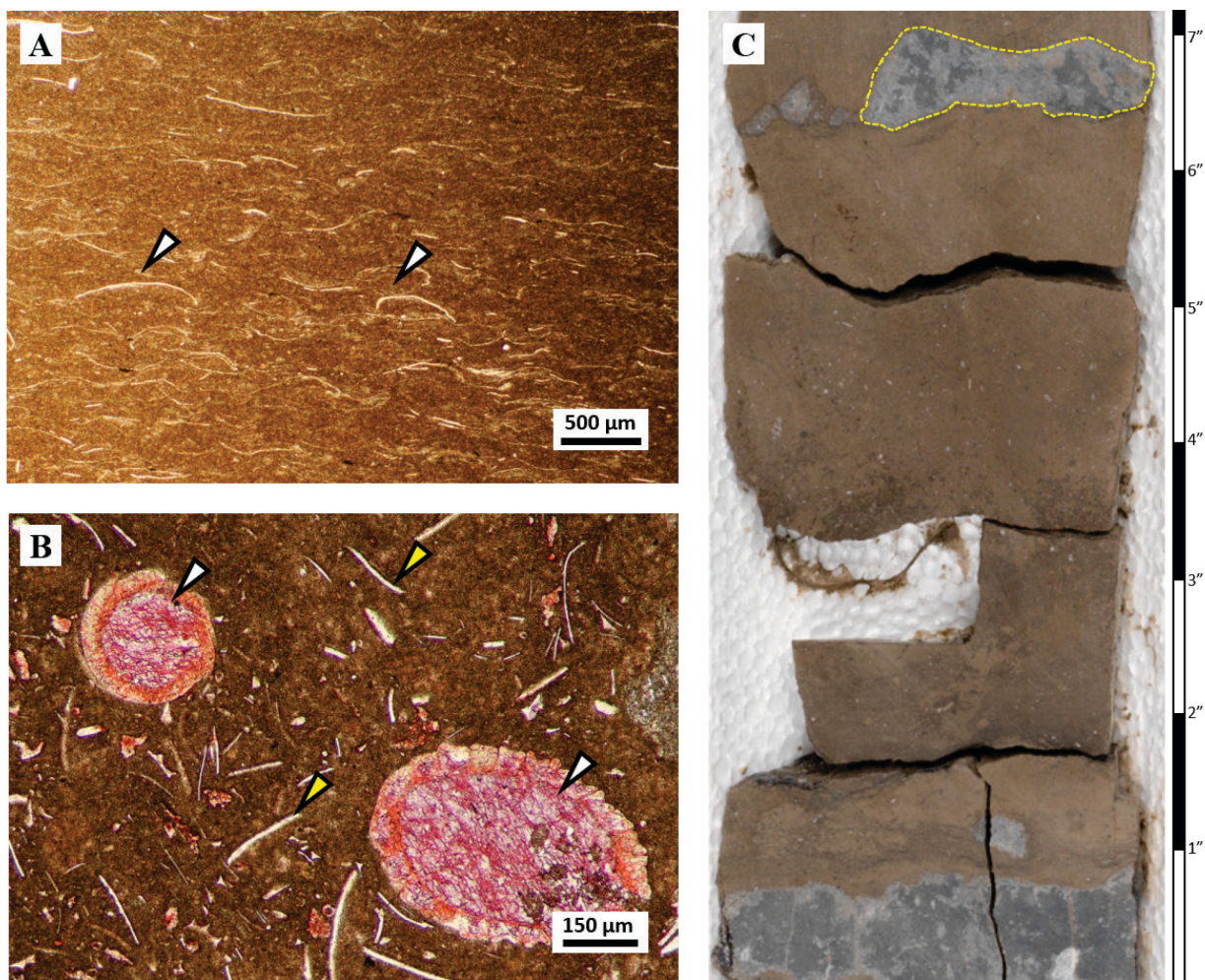


**Figure 4.3:** Facies 3 - Ostracod wackestone-packstone. (A) TLP of ostracod wackestone with disarticulated ostracods shells (arrows) aligned to bedding; well UT 15-13, sample 12, 7016.4 ft.; PPL. (B) TLP of gyrogonite (white arrows) associated with ostracod shell fragments (yellow arrows); well: 14-3, sample 27, 7373.65 ft.; PPL. (C) Core photograph of ostracod wackestone facies characterized by massive stratification and elongated chert nodules/bed (yellow dashed outline); well: BBC 14-1, 6685'4" to 6686'.

#### **4.1.4 Peloid wackestone – packstone – F4**

The peloid wackestone – packstone lithofacies (F4) is light brown, dolomitized matrix, wackestone – packstone with less than 5% of well sorted quartz grains. These particles are fine silt in size. The most abundant carbonate grains are peloids, which are light green to gray in color and elongated in shape, with grain size from 0.05 to 1 mm (Figure 4.4A and B). Bioclast are mostly disarticulated and fragmented ostracod shells and fish bones. Euhedral, prismatic, and microcrystalline authigenic quartz is present as accessory mineral. F4 hosts chert nodules with irregular shapes and sizes, commonly with cm-dimensions parallel to bedding. Pyrite is present as very fine and scattered crystals. Frequent bioturbation structures are present in this facies.

*Depositional environment.* The most important differences between facies F3 and F4 is the lack of gyronites and the relative abundance of peloids in facies F4 (Figures 4.4A and B). The occurrence of angular and dolomitized peloids suggest energy changes (such as storms) that were imported from different depositional settings within the lake. Bioturbation structures (Figure 4.4A) reflect oxygenated environments. Similar to F3, this facies presents scarce and scattered authigenic euhedral quartz suggesting evaporitic environments (Folk and Pittman, 1971; Folk and Siedlecka, 1974; Ulmer-Scholle et al., 1993; Flügel, 2010). Peloidal wackestone – packstone facies is associated with ostracod wackestone – packstone facies (F3), deposited in a depositional environment probably located in the littoral setting above the fair-weather wave base.



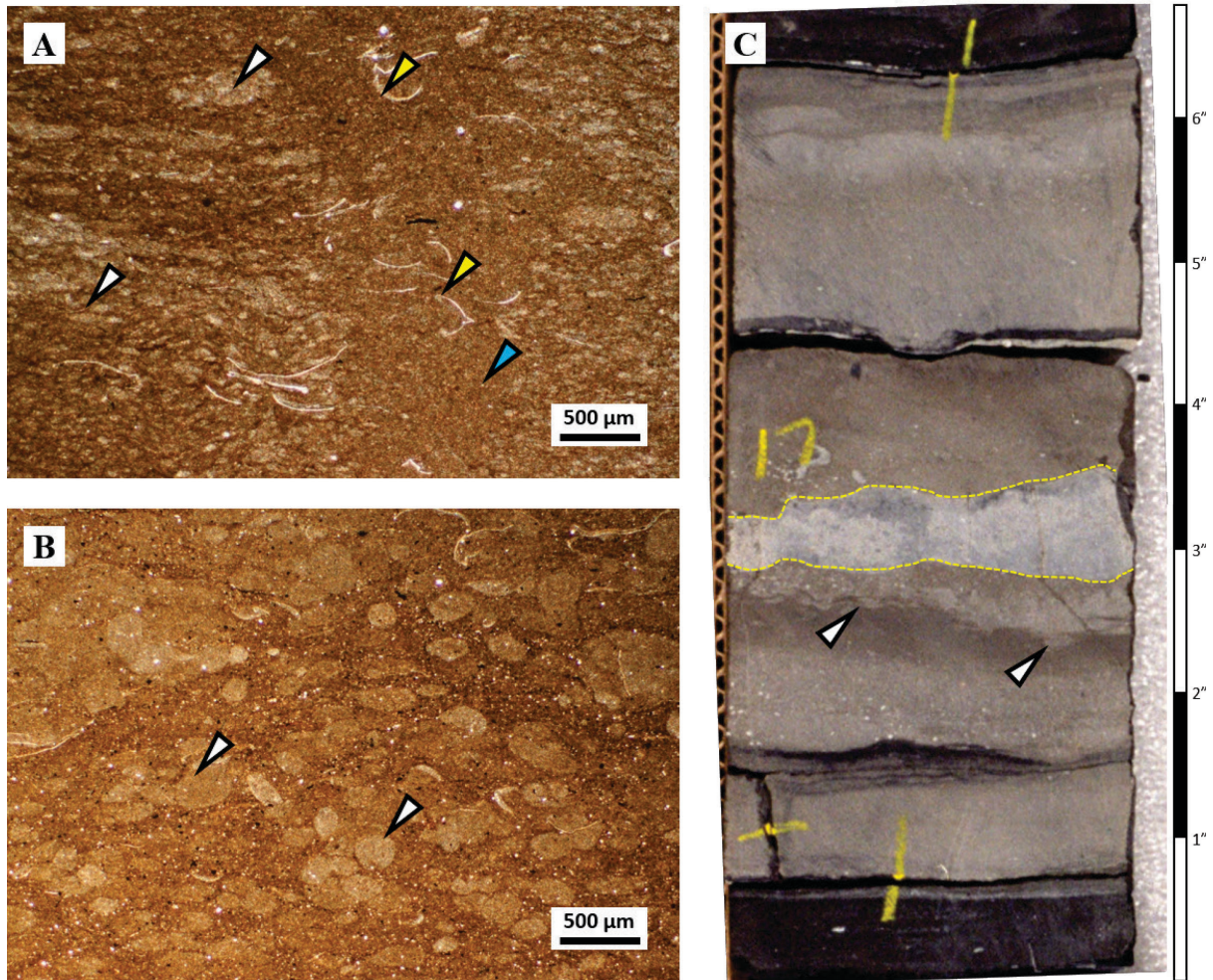


**Figure 4.4:** Facies F4 - Peloidal wackestone-packstone. (A) TLP of peloidal (white arrows) wackestone with scarce and disarticulated ostracods shells (yellow arrows); stratification disrupted by biological activity (blue arrow); well: N 6-28, sample 9, 8542.5 ft.; PPL. (B) TLP of peloids (arrows) within a microcrystalline dolomite matrix and clay material; well: UT 15-13, sample 13, 7017.4 ft.; PPL. (C) Core photograph of peloidal wackestone - packstone facies showing bioturbation structures (arrows) and chert nodule (yellow dashed outline); well: UT 15-13, 7017'1" to 7017'8".

#### 4.1.5 Mollusc wackestone – floatstone – F5

The mollusc wackestone - floatstone lithofacies (F5) is light to dark gray, wackestone to floatstone with micrite in matrix. Bioclasts are mainly elongated and tubiform gastropods, centimeter-size pelecypods, and ostracods shells usually broken and aligned sub-parallel to bedding. Gastropods are the most abundant fossil in this facies. Pelecypod shells range from 0.1 to 3 cm. Disarticulated and fragmented ostracods shells are smaller in comparison to molluscan bioclasts (Figure 4.5A and B). There are frequent thin coquinas layers displaying good preservation of shells (Figure 4.5C). Accessory minerals are microcrystalline pyrite and anhedral microcrystalline dolomite (less than 5%). Scarce quartz detritus particles (<3%) range from medium to very fine silt size and are poor to moderate sorted. Beds are typically structureless and usually have sharp non-erosive contacts at the top. Partial silicification of gastropods and pelecypods is present in this facies (Figure 4.6).

*Depositional environment.* F5 represents an environment variable in energy due to the variable particle size present in this facies that ranges from centimeter for some pelecypods and gastropods (Figure 4.5C) down to microns for the matrix (Figures 4.5A and B). Lacustrine pelecypods and gastropods are usually distributed in nearshore or flood plain settings (Cohen, 2003; Flügel, 2010) within a high energy setting. In contrast, microcrystalline calcite probably crystallized directly from lake water, which suggests a low energy setting. Furthermore, interbedding of molluscan wackestone and coquina layers (Figure 4.5C) points to a rapid water energy change. Molluscan wackestone – floatstone probably was deposited in the littoral environment with well oxygenated water, above the fair-weather wave base, close to the shoreline. Additionally, the *Australorbis* and *Physa* gastropods (LaRocque, 1956) indicates fresh water conditions (Picard, 1955; LaRocque, 1956; Williamson and Picard, 1974).



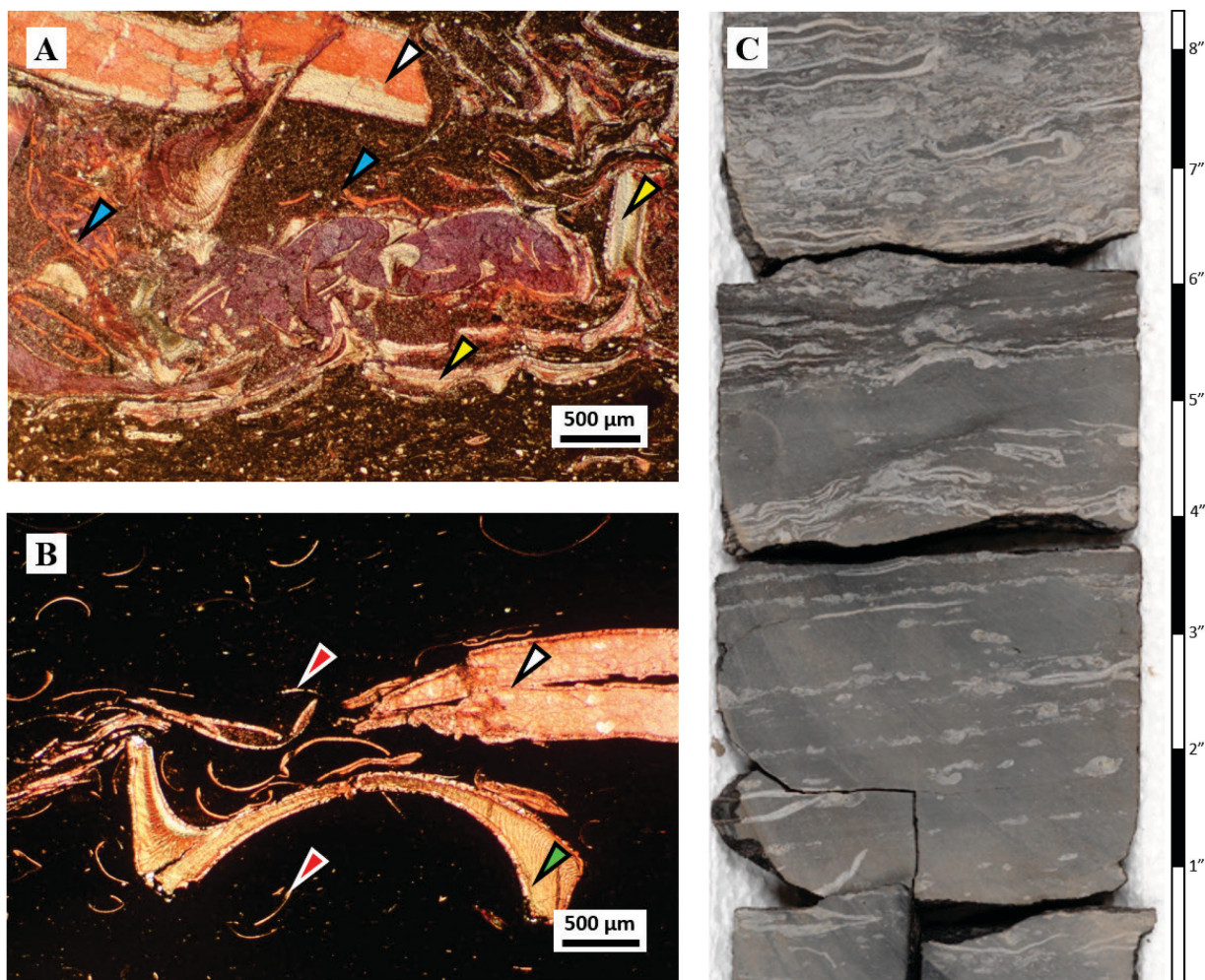


**Figure 4.5:** Facies F5 - Molluscan bearing wackestone-floatstone. (A) TLP of molluscan bearing floatstone with centimetre-size shells of pelecypods (white arrow), gastropods (yellow arrows), and disarticulated ostracods shells (blue arrows); well: PW 13-06, sample 5, 5537.3 ft.; PPL. (B) TLP of organic rich wackestone with pelecypods (white arrow), gastropods (green arrow); and ostracods (red arrows); black colour in matrix due to high organic matter content; well: N 6-28, sample 8, 8234.6 ft.; PPL. (C) Core photograph of interbedding coquina layer (at the top) with molluscan floatstone (at the base); well: BBC 14-1, 6696'1" to 6697'1".

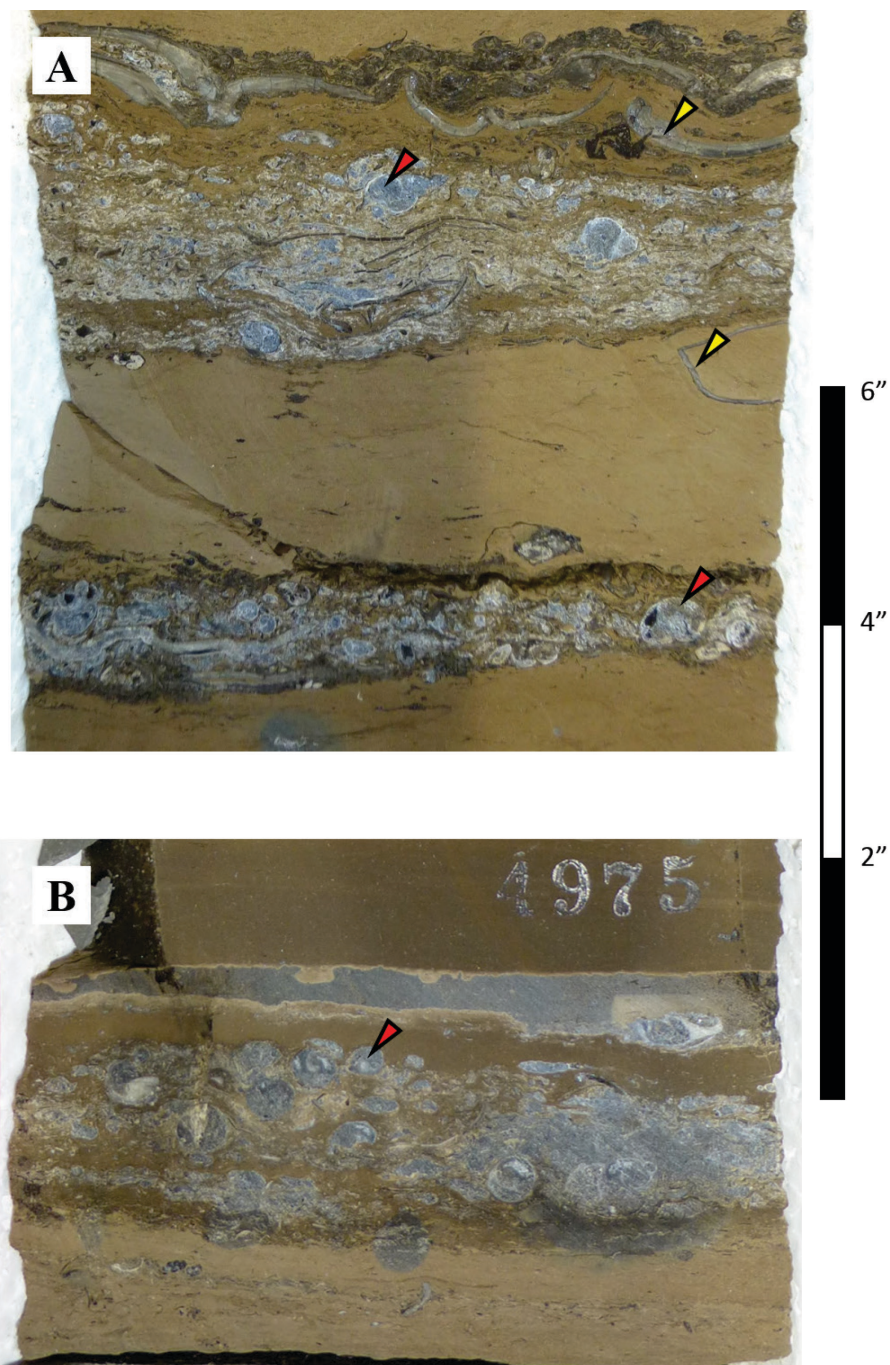


**Figure 4.6:** Core photograph of molluscan limestone facies (F5) with partial silicification of gastropods (red arrows) and pelecypods (yellow arrows); well UT 11-20, depth: (A) 4974.2 to 4974.7 ft, (B) 4975 to 4975.3 ft.

#### **4.1.6 Intraclast packstone- grainstone – F6**

The intraclast packstone – grainstone lithofacies (F6) is light brown, packstone to grainstone composed mainly by dolomitic intraclasts and peloids, and minor ooids. Bioclasts are mainly ostracods shells fragments erratically distributed (Figure 4.7A and B). Intraclasts are angular to well-rounded, poorly sorted, and particle size ranges from 0.2 mm to 10 mm. The intraclasts are composed by microcrystalline dolomite in matrix and shells (likely ostracods). Furthermore, intraclasts show circumgranular cracks around irregular to globular particles of microcrystalline dolomite. Cracks are filled with blocky calcite cement (Figure 4.7A). Peloids are composed exclusively by microcrystalline dolomite and display elongated shapes. Bioclasts are mainly disarticulated and fragmented ostracod shells (Figure 4.7B). Rare (1%) quartz particles with fine silt size.

*Depositional environment.* Rock texture and carbonate grains sizes (from 0.2 mm to 10 mm) are characteristics of a high energy environment. Intraclast particles have a different texture and color in comparison with the texture features of facies F6, which suggests deposition, dolomitization, and partial lithification took place in a different depositional area, likely in the littoral to supralittoral environment. Moreover, intraclasts show pedogenesis features such as circumgranular cracks (Figures 4.7A) that imply the intraclast were exposed to eogenetic process (Esteban and Klappa, 1983; Freytet and Verrecchia, 2002; Flügel, 2010). After exposure, the partially endured sediments were ripped out by storms. Part of this material was subjected to reworking by wave action which caused them to evolve into well rounded particles (Figure 4.7B). Finally, these particles were transported to the current environment of deposition. Lithofacies F6 was probably located in near shore areas affected by wave action.



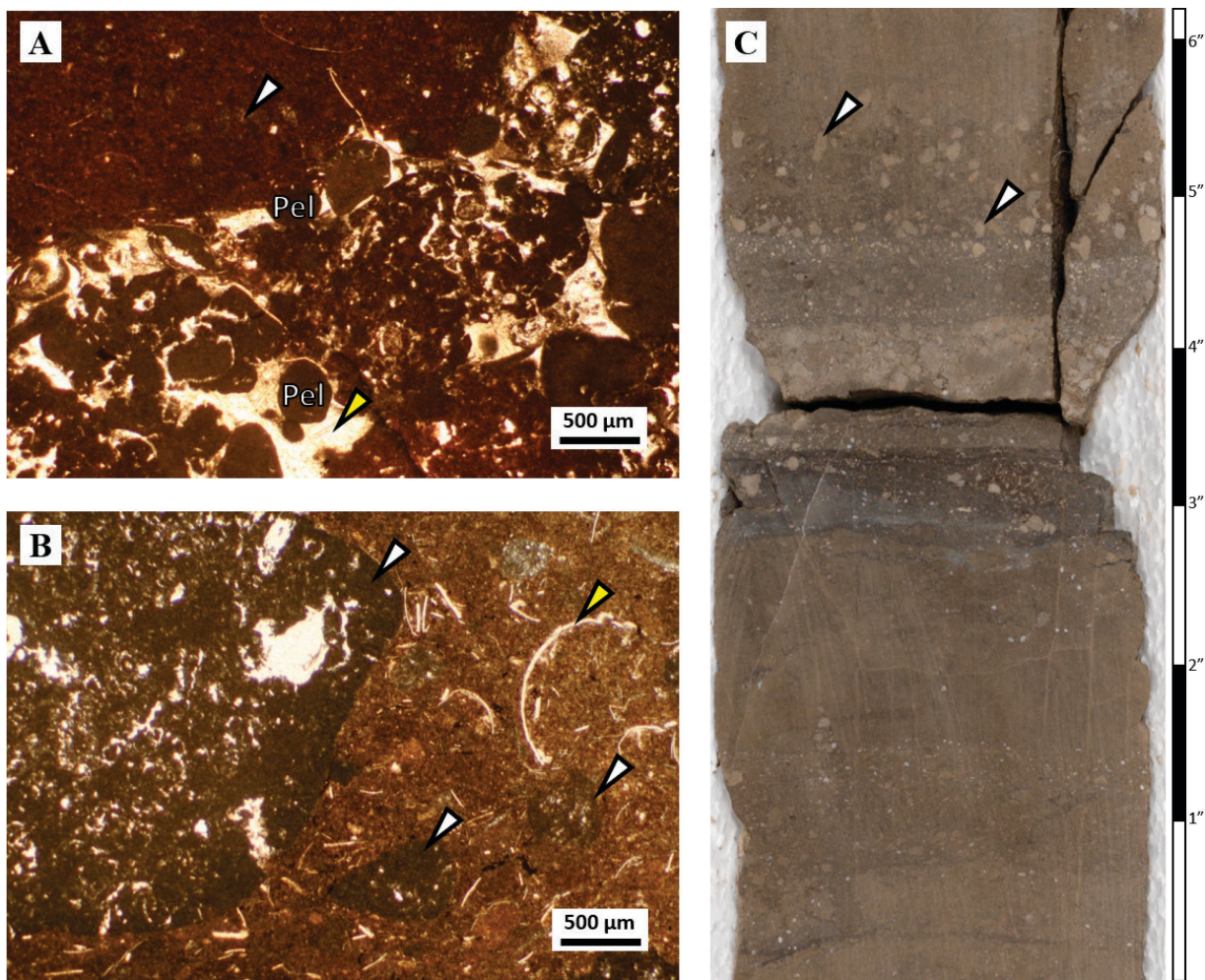


**Figure 4.7:** Facies F6 - Intraclast peloid packstone-grainstone. (A) TLP of centimetre-size dolomitized intraclasts (white arrow), peloids (Pel), and blocky calcite cement (yellow arrow); well: 14-1, sample 12, 6683.95 ft.; PPL. (B) TLP of well-rounded intraclasts (white arrows), ostracods shell fragments (yellow arrow) within a dolomitized matrix; well: BBC 14-1, sample 13, 6684.90 ft.; PPL. (C) Core photograph of intraclastic peloidal facies. Rip-up intraclast particles (white arrows) within a dolomitized micrite (?) matrix; well: BBC 14-1, 6684'11" to 6685'5".

#### **4.1.7 Ooid grainstone – packstone – F7**

The ooid grainstone – packstone lithofacies (F7) is dark brown, grainstone to packstone mainly composed by well-sorted and completely dolomitized ooids, peloids, and intraclasts, and rare (<2%) ostracods shells. Ooids show spherical to sub-spherical shapes with concentric layers of dolomitized micrite (Figure 4.8A). Some ooids present micritization (Figure 4.8B). The core of ooids is composed of bioclast (ostracod shell fragments), quartz particles, peloids, and intraclasts. Ooids size ranges from 0.2 to 1.5 mm. Accessory minerals are euhedral, microcrystalline, double-terminated, authigenic quartz and microcrystalline pyrite. F7 facies present massive stratification (Figure 4.8C).

*Depositional environment interpretation.* The concentric and well defined internal structure of the ooids (Figures 4.8A and B) and lack of detrital grains suggest that the ooid grainstone – packstone facies (F7) was deposited in a high energy environment close to the shore area, influenced by wave agitation with low input of siliciclastic material and above the fair-weather wave base. Micritization of ooids might indicates a high microbe activity environment in the photic zone. Additionally, authigenic, euhedral and double-terminated quartz precipitated within the interparticle open space indicate a probable saline environments (Flügel, 2010).



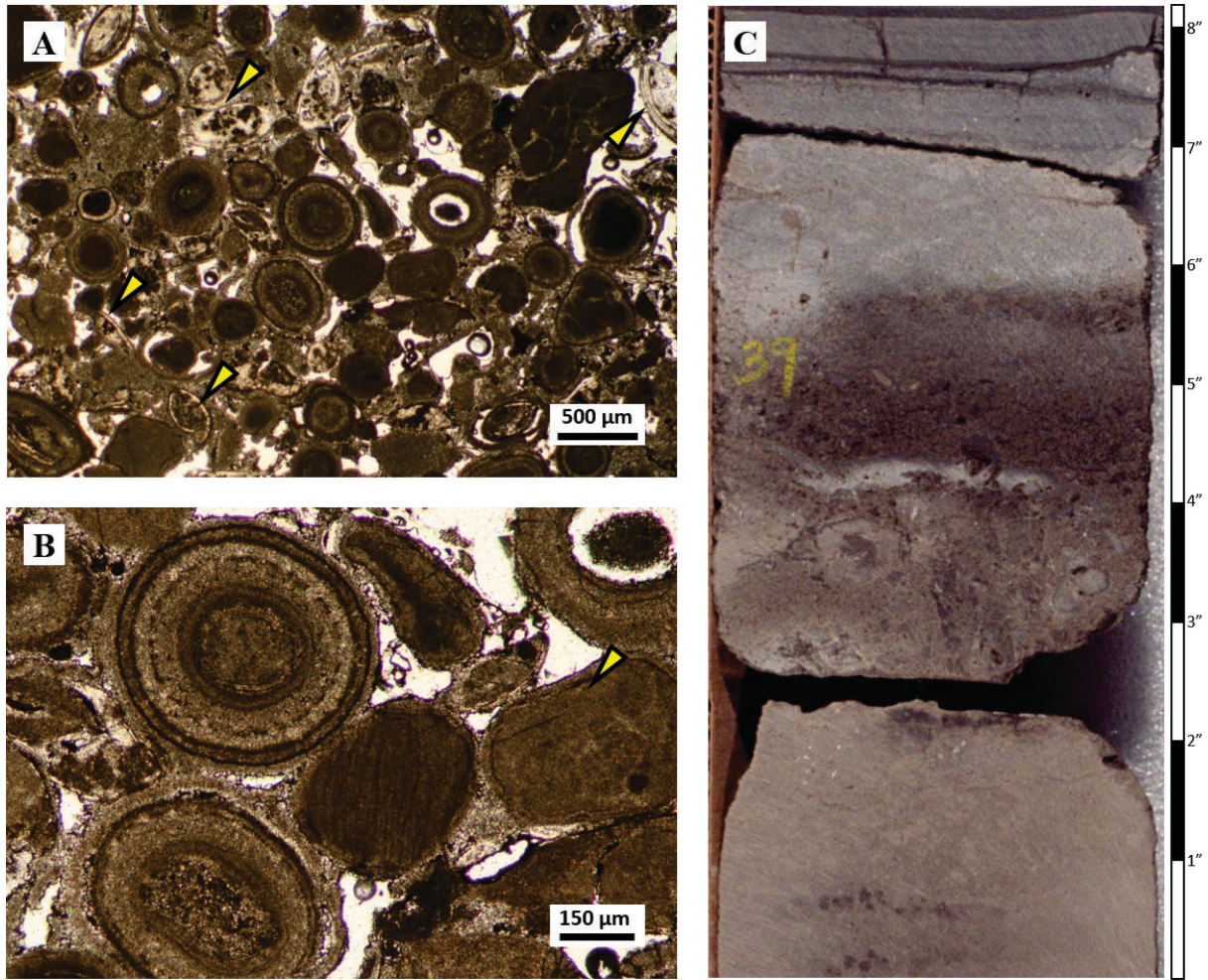


**Figure 4.8:** Facies F7 - Ooid grainstone - packstone. (A) TLP of ooid grainstone with ooids partially dissolved and scarce articulated ostracods shells (yellow arrows); well: PW 13-06, sample 6, 5539.5 ft.; PPL. (B) Detail of microphotograph (A) that shows micritization of ooids (yellow arrow). Note ooids are completely dolomitized; PPL. (C) Core photograph of ooid grainstone facies with massive stratification; well: PW 13-06, 5539'3" to 5539'11".

#### 4.1.8 Ostracod grainstone – packstone – F8

The ostracod grainstone – packstone lithofacies (F8) is light brown, ostracod bearing grainstone – packstone. Carbonate grains are mainly ostracod shells (40 – 50%) densely packed, articulated, and deformed shells; minor dolomicrite pellets, and scarce peloids. Moreover, internal cavity of ostracods is filled with dolomitized micrite and pellets (?) (Figure 4.9A). Some ostracods shells present constructive micritization. Siliciclastic material is scarce (<2%) and is mainly composed by medium silt to very fine subangular quartz. Microcrystalline pyrite is present as accessory mineral. Some layers host chert nodules, mainly composed by quartzine, with elongated shapes and variable sizes, commonly with cm-dimensions, parallel to bedding (Figure 4.9C). In core, F8 presents parallel and massive stratification.

*Depositional environment.* The depositional environment of ostracod grainstone - packstone lithofacies (F8) is interpreted as a shallow setting with moderate to high energy, probably located in mud flats within littoral environments. The abundance of ostracods was likely promoted by optimal lake water conditions that boosted ostracod reproduction rate. Additionally, shell constructive micritization was probably generated by algae (Flügel, 2010). In this case, this environment must be located in euphotic zone with high nutrient concentration (Scholle and Ulmer-Scholle, 2003; Flügel, 2010). Quartzine in chert nodules suggests evaporitic conditions (Folk and Pittman 1971, Pittman and Folk, 1971; Eugster and Hardie, 1978; Scholle and Ulmer-Scholle, 2003; Warren, 2006; Flügel, 2010).



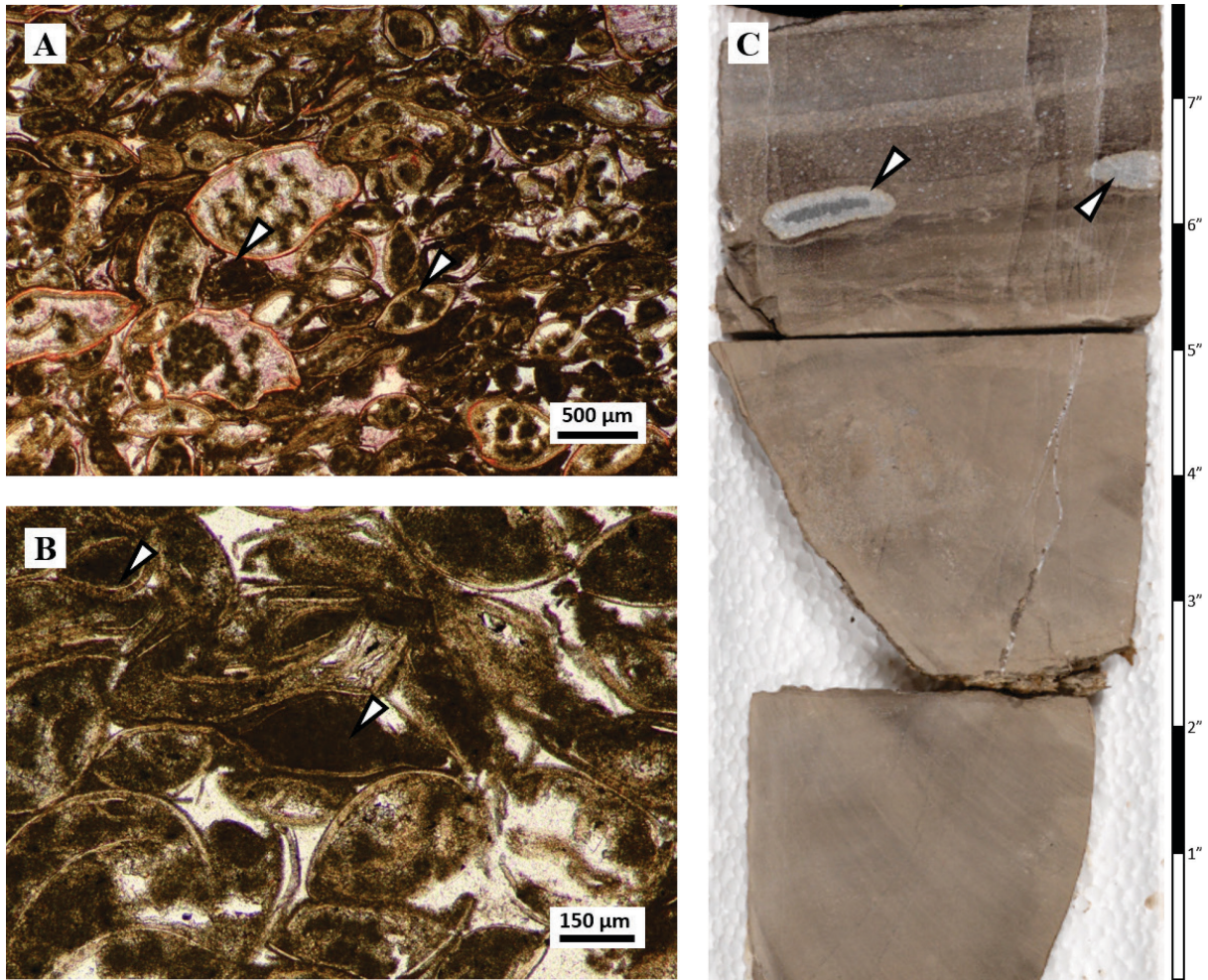


**Figure 4.9:** Facies F8 - Ostracod grainstone - packstone. (A) TLP of ostracod grainstone. The internal voids of ostracods are partially filled with dolomitized pellets (?) and micrite (white arrows); the resting voids were filled with blocky ferroan calcite cement (pale purple areas); well: DS 11-20, sample 11, 4998.5 ft.; PPL. (B) TLP of ostracod grainstone facies. Microcrystalline dolomite partially fills the internal cavity of articulated ostracods shells (white arrows); well: DS 11-20, sample 11, 4998.5 ft.; PPL. (C) Core photograph of ostracod grainstone facies with chert nodules (white arrows); well: BBC 14-1, 6680'0" to 6680'8".

#### **4.1.9 Brown claystone – F9**

The brown claystone facies (F9) is characterized by light brown to grey arenaceous claystone, in places fissile, with quartz grains up to 15 %. These particles are well sorted, subangular to rounded, with size that range from very fine to fine sand. Bioclasts are mainly thin and disarticulated fragments of shells (likely ostracod shells) and fish bones with particle sizes varying from 0.05 to 0.3 mm (Figure 4.10A). This facies is interbedded with laminae of ostracod coquinas (Figure 4.10B). F9 show plane parallel and wavy stratification; thicknesses vary from about 0.1 to 2.5 m. Scarce bioturbation is present in facies F9.

*Depositional environment.* Arenaceous claystone facies is vertically associated with thin coal seams and is present only at the landward area of the basin (Willow Creek outcrop). This association suggests a low energy environment close to the shoreline settings (Ryder et al., 1976) and close to the siliciclastic input areas (deltas). Interbedded claystone and coquina layers indicate episodic ostracod blooms. Bioturbation indicates an oxygenated environment.



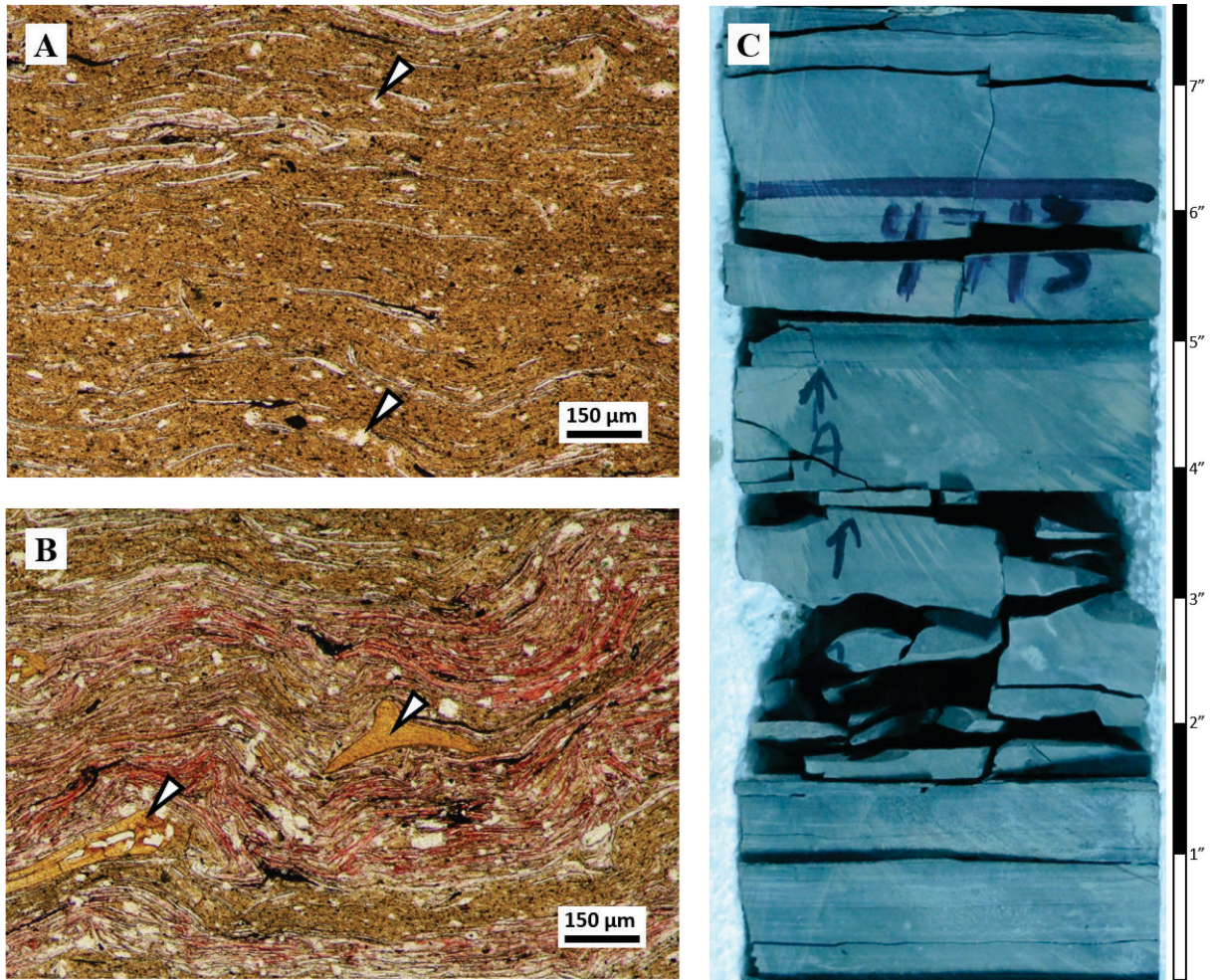


**Figure 4.10:** Facies F9 - Brown arenaceous claystone. (A) TLP of brown mudstone with disarticulated ostracod shell fragments aligned subparallel to bedding, with subangular to rounded and very fine sand quartz grains (white arrows); well: UI 16, sample 16, 4713.2 ft.; PPL. (B) TLP of interbedded laminae of coquinas (pale pink-red) and arenaceous claystone (light brown area), and fish bones (arrows); well: UI 16, sample 16, 4713.2 ft.; PPL. (C) Core photograph of brown and fissile claystone; well: UI 16, 4712'11" to 4712'6".

#### 4.1.10 Coal - F10

Coal facies (F10) is defined by dark brown to black coal seams with average bed thickness of 0.03 m (Figure 4.11). There is presence of some recognizable plant structures. Coal seams are associated vertically with brown arenaceous claystone facies (F9) and ostracod wackestone (F3). This facies is present only in Willow Creek outcrop.

*Depositional environment.* The coal seam facies represents a swamp environment close to the lacustrine basin (Uinta Basin). This setting is likely the in-land expression of cyclic rising of water table caused by transgression events (Reinson, 1992; Keighley et al., 2003).



**Figure 4.11:** Facies F11 - Coal. Thin coal seam in Willow Creek Canyon outcrop. Seam coals are vertically associated with claystone (F9) (base) and dolowackestone (F3) (top).



## 4.2 Facies associations

A typical vertical association of facies is shown core photograph Figure 4.12. Facies associations such as this allow for the recognition of lacustrine depositional environments on a larger scale depending on water agitation levels and relative water depth (Tānavsuu-Milkeviciene and Sarg, 2012). Grouping of facies into genetically related units is based on vertical and lateral association, rock textures, and sedimentary structures. The main depositional environments are defined by the lake water column: (1) supralittoral zone located above the lake water table and subjected to subaerial weathering and cyclic flooding, (2) littoral zone, which is highly influenced by wave activity and limited at the base by the fair-weather wave base (FWWB); (3) sublittoral zone, which is between the FWWB and the storm wave base (SWB); and (4) profundal zone that is below the SWB (Tānavsuu-Milkeviciene and Sarg, 2012) (Figure 4.13). The facies associations are therefore related to depositional environments as shown in Figure 4.13. The littoral and sublittoral zones are located within the photic zone. Facies associations are summarized in Table 4.3.

Facies associations			
Code	Name	Facies	Environment
A	Marginal swamps	F9, F2, F3, F10	Supralittoral
B	Marginal carbonates	F2, F6, F7, F8	Littoral to sublittoral
C	Massive carbonates	F2, F3, F4, F5	Littoral to sublittoral
D	Laminated mudstones	F1	Profundal

**Table 4.3:** Facies associations regarding to genetic vertical and horizontal relation, sedimentary structures, and rock textures.

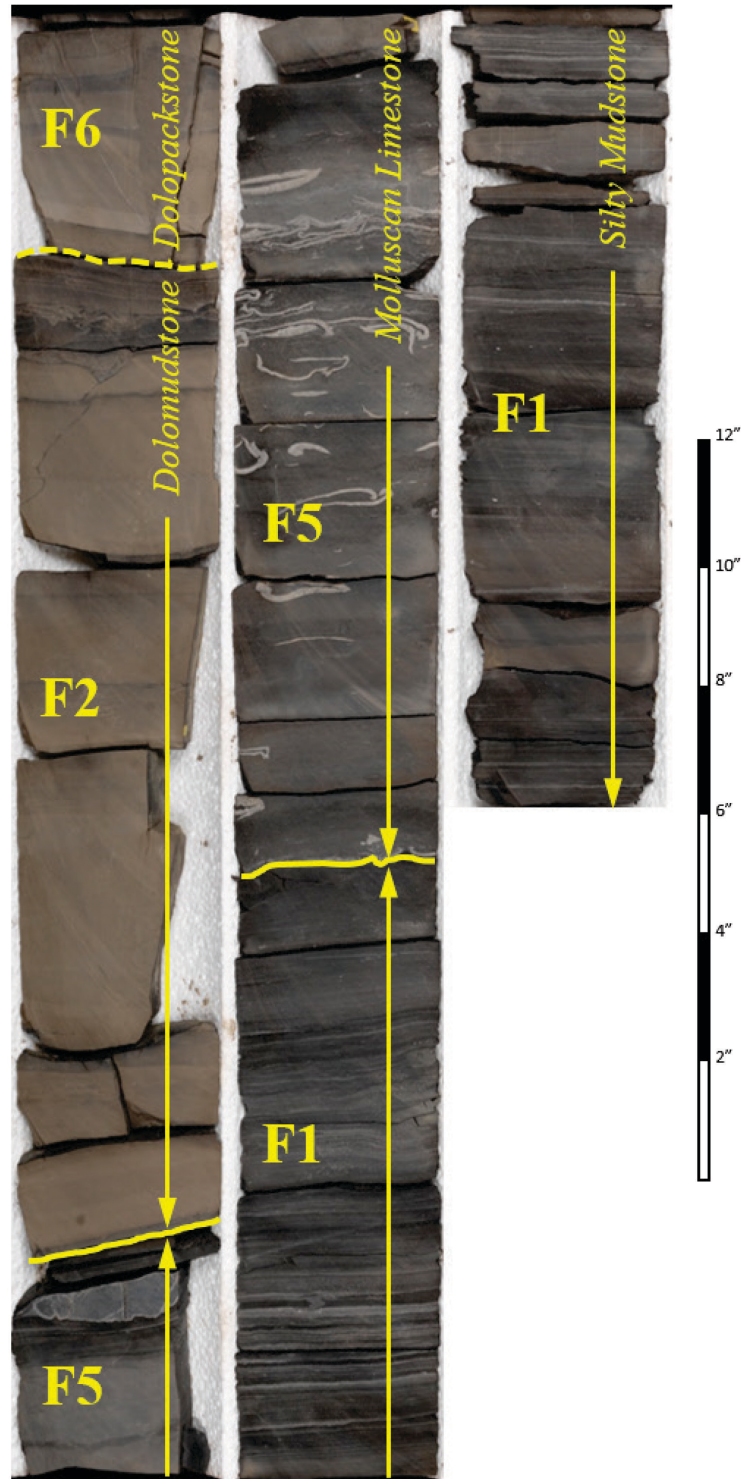


**Figure 4.12:** Vertical association of facies from silty mudstone (F1) at the base, mollusc wackestone – floatstone (F5), and lime mudstone (F2) coarsening upward to peloid wackestone – packstone (F4) at the top. Idealized stratigraphic cycle: At the base is the oil rich mudstone facies (F1); followed by mollusc wackestone – floatstone facies (F5); and dolopackstone facies at the top (F6) Photograph of well: BBC 14-1, 6702' to 6706'1".

#### **4.2.1 Marginal swamp (A)**

Marginal swamp environment is defined by a vertical association of brown claystone (F9), lime mudstone (F2), ostracod dolowackestone (F3), and coal (F10) facies. The paleogeographic location for this association could be placed out of the lake basin (landward), bordering the coastal line. Moreover, coal seams (F10) and lacustrine deposit (F2 and F3) associations were created likely by transgression events that created swamps at the initial stage and later on deposition of ostracod wackestone lacustrine facies in the supralittoral environment.

#### **4.2.2 Marginal carbonates (B)**

Marginal carbonates environments are defined by lateral association of ooid grainstone (F7), intraclast grainstone – packstone (F6) and ostracod grainstone – packstone (F8) facies, which indicate high energy environment influenced by wave action (Gierlowski-Kordesch, 2010). Eventually, part of this zone was subaerial exposed by regression of lake water table. The exposure areas were subjected to weathering and erosion that generated intraclastic carbonate grains. This facies association occurs at the top of dolomite layer PZ1 in well Petes Wash 13-06 GR (landward) as well as at the top of dolomite layer PZ1 in well 14-1-46 (basin ward), suggesting an isolated, extensive, and flat carbonate ramp with very low or no interaction with siliciclastic sediments, deposited in the littoral setting. Based on ooids and pisoids abundance, cycle thickness, and comparing with modern lacustrine stromatolites, Ryder et al. (1976) estimate the water depth for this environment ranging from 10 cm to 9 m.

#### **4.2.3 Massive carbonates (C)**

This facies association is composed by lime mudstone (F2), ostracod wackestone (F3), peloid wackestone – packstone (F4), and molluscan wackestone – floatstone (F5). The vertical association of facies F3 with F2 suggests that they were deposited in adjacent and probably overlapping depositional environments. Furthermore, similar sedimentary structures and the vertical association of facies F3 and F4 also suggests close depositional environments. This facies association is characterized by massive carbonates with a high matrix:grains ratio, fine size carbonate grains, and scarce to moderate ostracods shell fragments and fish bones. Grain size of carbonate grains and increment of matrix percentage suggest an environment of moderate to low energy between the fair weather wave base and the storm wave base. This environment was ideal for benthic organisms (ostracods mainly) that reworked sediments. The organic activity partially obliterated primary sedimentary structures. Furthermore, biological activity indicates an oxygenated setting. This environment was influenced by episodic storms that formed lenses of peloidal grainstone interfinger with lime mudstones (Figure 4.2B).

#### **4.2.4 Laminated oil rich mudstones (D)**

This facies association is characterized by laminated oil rich mudstones interbedded with laminae of lean silty mudstone and coquinas laminae. The high organic matter content values suggest an anoxic environment located below the SWB within the anoxic zone where lack of oxygen and light create adverse conditions for living organisms allowing preservation of organic matter. However, this setting changed periodically toward a more oxygenated depositing light gray, poor-organic mudstone likely promoted by water level fluctuations.

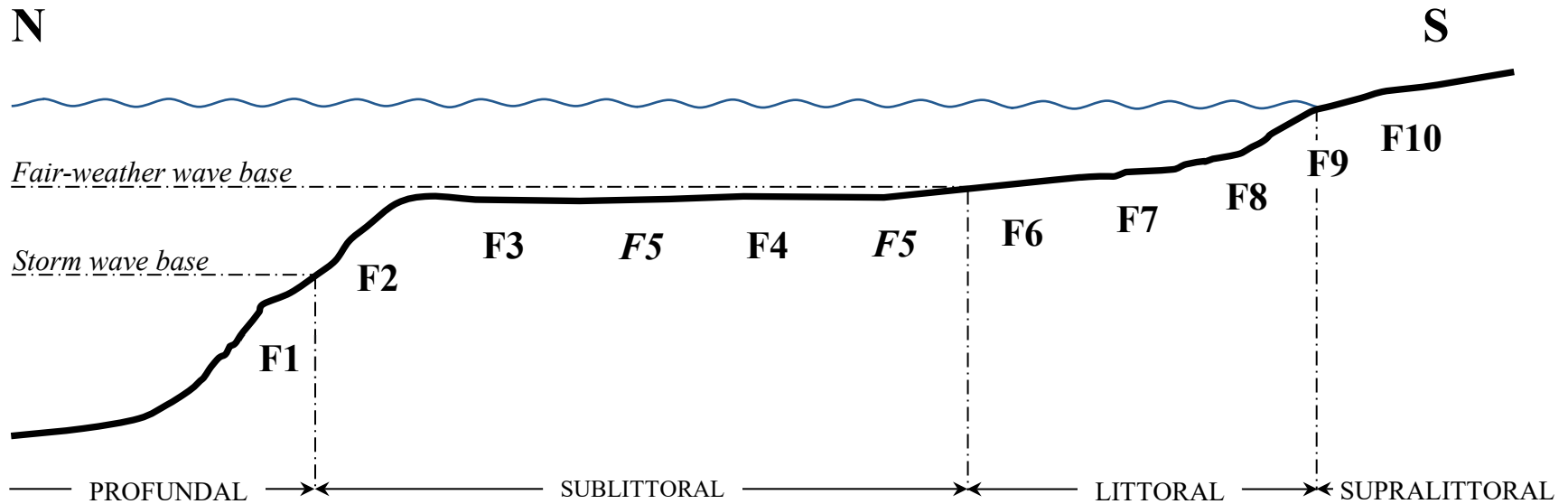


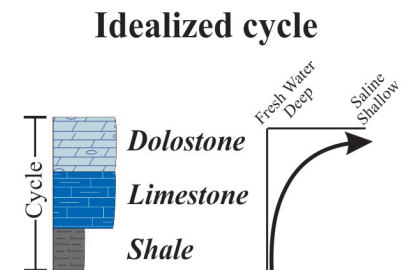
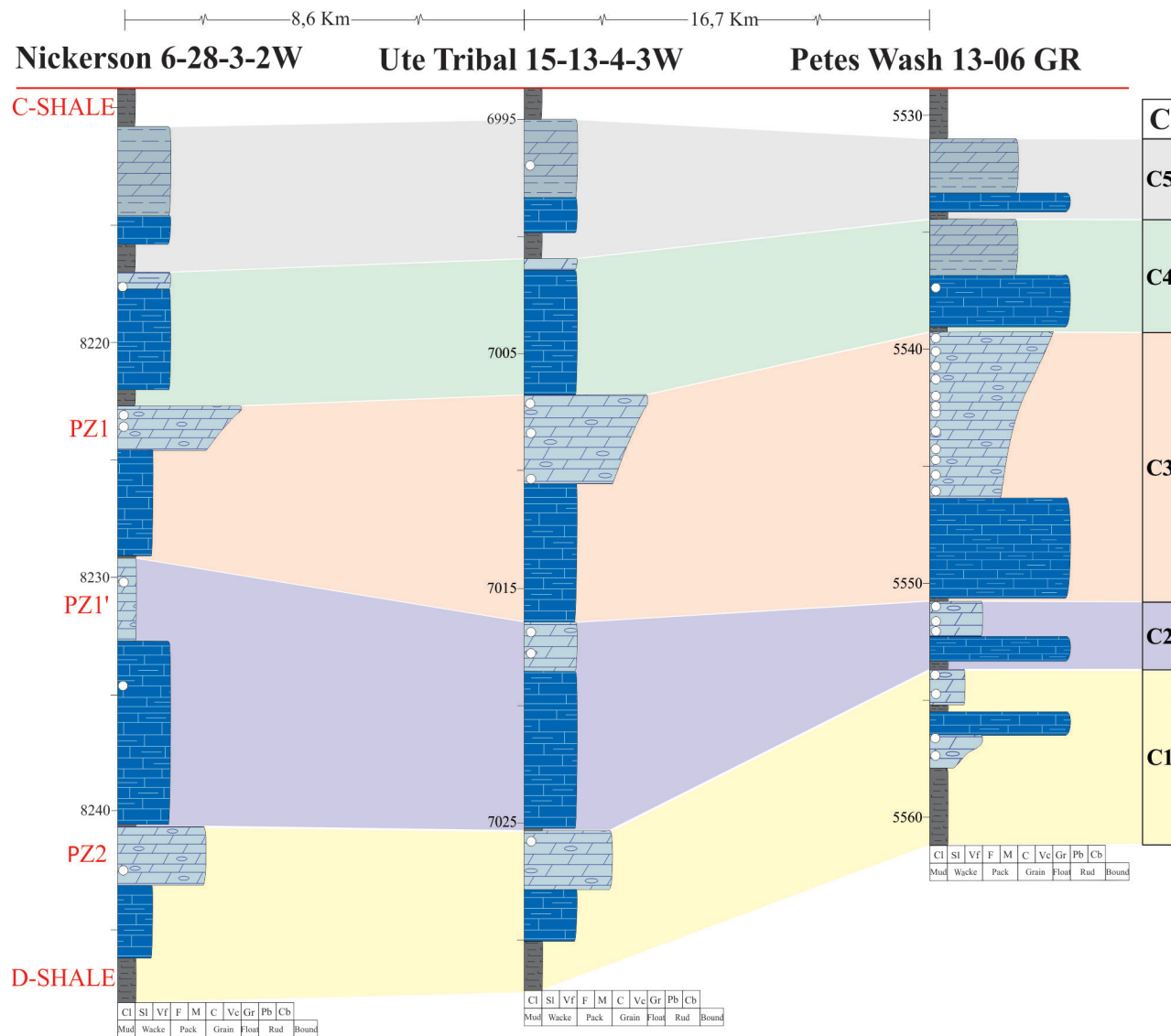
**Figure 4.13:** Schematic representation of the lateral facies distribution in the Uinta Basin profile. Time of deposition of the molluscan wackestone – floatstone facies (F5) is different from the time of deposition of the other carbonate facies (F2, F3, F4, F6, F7, and F8). F5 was deposited in a fresh water setting during the initial stage of regression, whereas the facies F2, F3, F4, F6, F7, and F8 were deposited during the maximum regression (see Chapter 4, Sections 4.3 and 4.4 for further discussion).

### 4.3 Facies successions and cyclicity

Individual facies are arranged vertically, defining repetitive cycles or successions that help to determine the Uinta Basin evolution throughout deposition of the interval of interest. Thickness of this interval ranges from 22.9 ft landward up to 39 ft basinward. Fluctuations in lake level was recorded by vertical variation of facies.

The cycle is defined at the base by oil rich mudstone, following at the middle of the cycle with a molluscan wackestone – floatstone layer, and top of each cycle with an intraclastic dolograinstone, ooid dolograinstone, or an ostracod dolograinstone – dolopackstone (Figure 4.12). This cycle is interpreted as result of a transgression-regression event, in which the oil rich mudstone (F1) is considered as the flooding surface and the intraclast grainstone – packstone facies (F6) is considered as the regressive surface. The cycle is repeated five times between D and C shales, showing local variations (Figure 4.14).

The silty mudstone is interpreted as result of a period of flooding promoted by either a water input rate higher than output rate (climate) or by a higher accommodation rate than sediment supply rate (tectonism) (Ryder et al., 1976; Carrolls and Bohacs, 1999). As result, deposition of silty mudstone facies moved landward (Ryder et al., 1976). At the same time, wackestone and floatstone facies moved landward as well. Due to the water table increment, the supralittoral zone might have inundated establishing supralittoral swamps, which favoured deposition of lenticular coal seams. After flooding, a gradual water table drop moving back the depositional environments basinward, partially exposing the already deposited grainstone – packstone layers to subaerial conditions. Pedogenesis features, such as circumgranular cracks (Figure 4.7A and B), were developed at the top of layer PZ1 in wells Petes Wash 13-06 GR and Nickerson 6-28-3-2W, which supports this interpretation.



### LEGEND

- Cherty Dolostone
- Argillaceous Dolostone
- Interb. Dolostone and Shale
- Dolomitic Limestone
- Argillaceous Limestone
- Interb. Limestone and Shale
- Calcareous Shale
- Sample

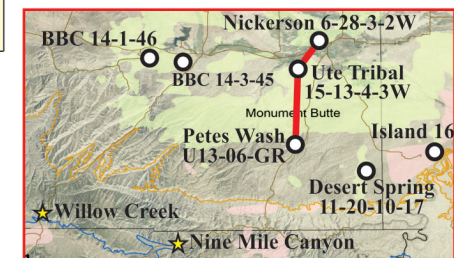


**Figure 4.14:** Correlation of stratigraphic cycles C1 to C5 (right column) within D and C shales.

This interpretation is consistent with the findings by Tānavsū-Milkeviciene et al. (2017) who defined three major depositional cycles for the entire section of the GRF. The section of interest here might be correlated with the first depositional cycle defined by Tānavsū-Milkeviciene et al. (2017), which was controlled by short climate variations. During high humidity episodes (high inflow), water lake level rose up pushing the marginal facies associations landward. In contrasts, dry episodes (low inflow) caused a lake water drop moving back the marginal facies basinward (Tānavsū-Milkeviciene et al., 2017).

The idealized depositional cycles represent a period of deposition of about 10 to 16 thousand of years (ky) (Table 4.4). This time interval was calculated based on average of the sediment accumulation rate defined by Smith et al. (2008) at the base of the GRF. Smith (2008) defined a deposition rate of about 150 mm/ky for the basin-margin areas (Indian Canyon outcrop, southwest of the study area close to the Nine Mile Canyon outcrop described in this project). The cyclicity was likely controlled by periodic climate variations with the same time interval (10 to 16 ky).

Cycle	Thickness of cycles								Time (ky)
	BBC 14-1	BBC 14-3	N 6-28	UT 15-13	PW 13-06	DS 11-20	IU 16	TAve	
C5	8.0	6.4	6.2	6.0	3.4	1.5	3.0	4.9	10.0
C4	3.9	5.8	5.7	5.8	4.8	7.3	8.0	5.9	12.0
C3	8.0	9.6	6.5	9.7	11.5	3.2	7.4	8.0	16.2
C2	8.8	8.0	11.4	9.1	2.9	3.6	4.9	6.8	14.1
C1	7.3	4.0	7.5	6.8	7.5	6.0	3.6	6.5	12.4

**Table 4.4:** Thickness and calculated time of deposition for each idealized cycle identified within D and C shales. TAve: Thickness average of each cycle; thickness in ft.



#### 4.4 Facies and dolomitization

Facies and dolomitization relationship show three main factors: (i) pervasive matrix dolomitization occurred in facies F2, F3, F4, F6, F7 and F8 (ii) the underlying and fresh water mollusc wackestone – floatstone facies (F5) was not dolomitized, and (iii) dolomitization took place at the top of each cycle (Figure 4.14).

All carbonate facies were dolomitized to variable degrees except for molluscan limestone facies (F5). The relative percentages of dolomite and calcite in each facies (Figure 4.15) suggest that dolomitization crosscut facies boundaries, having taken place from the sublittoral environment (lime mudstone facies – F2) to the littoral (near shore) environment (ooid grainstone facies – F8) (Figure 4.16). However, the fresh water molluscan wackestone - floatstone facies (F5) was not dolomitized (dolomite volume <10%).

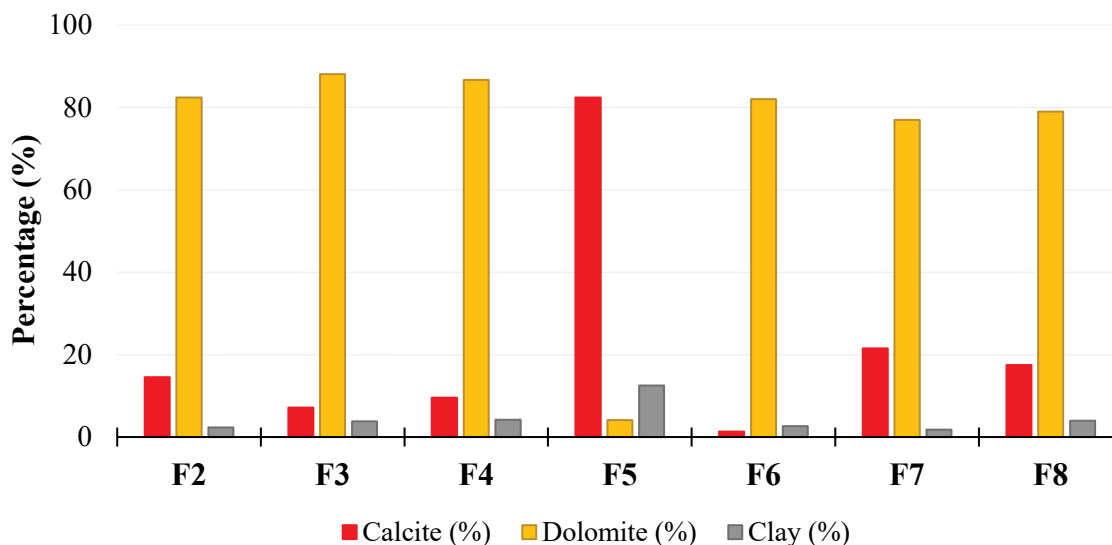


**Figure 4.15:** Mineralogical composition for carbonate facies. Volume percentage (vertical axis) estimated from thin sections using semi-quantitative charts (Baccelle and Bosellini, 1965).

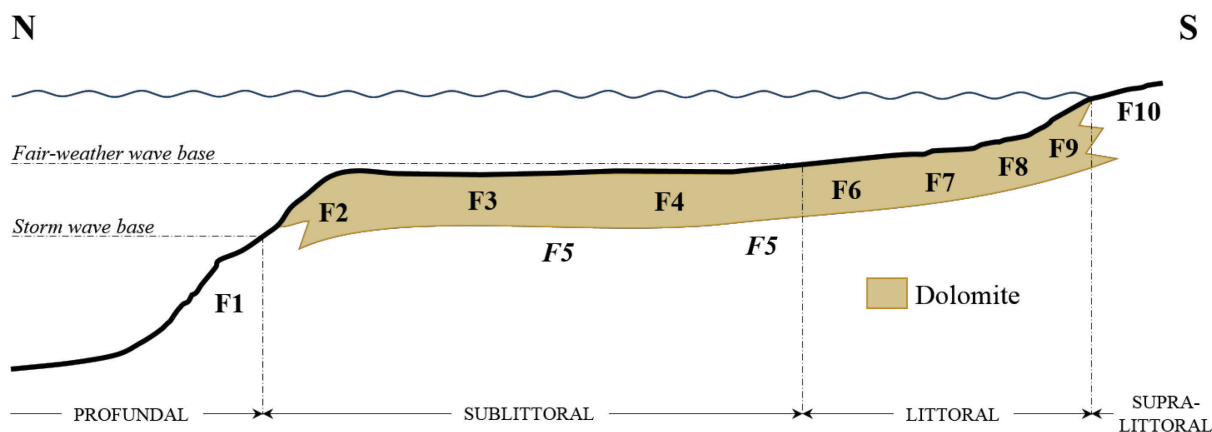


**Figure 4.16:** Schematic representation of facies distribution and dolomitization. F5 was not dolomitized.

The vertical variation of facies from F1 (base of the cycles) grading toward facies F5 (fresh water molluscan limestone), and the occurrence of the dolomitized facies F2, F3, F4, F6, F7, and F8 (top of the cycles), suggest that deposition was controlled by transgressive/regressive cycles. Thereby, facies F1 represents the maximum flooding event, turning the study area into a deeper depositional setting (profundal). After the transgression maximum, the lake water dropped and the depositional environment changed from a profundal to a sublittoral setting, allowing precipitation/deposition of micrite in a fresh water setting (as evidenced by the fossil associations). During this period of time, dolomitization of already deposited carbonate sediments (facies F5) was not possible because of a relatively low Mg/Ca ratio and low temperature of the lake water (fresh water setting). Near the maximum regression of the lake water the depositional environment had changed to an overall shallow littoral/sublittoral setting, in which the already deposited carbonate sediments were partially dolomitized. Dolomitization was likely driven by increased Mg/Ca ratio and temperature of the lake water (see Chapter 6 for further discussion).

## **CHAPTER FIVE**

### **DIAGENESIS**

The stratigraphic interval of study shows a composite of diagenetic events from near-surface to deep burial diagenetic settings. Special attention was paid to dolomitization, i.e., how this process is related to the petrophysical properties (porosity and permeability) of petroliferous dolomite layers PZ1, PZ1', and PZ2. Additional diagenetic processes such as mechanical compaction, cementation, dissolution, fracturing, and stylolitization are also considered because they also affected the reservoir properties.

Fifteen diagenetic events were identified based on thin section petrographic descriptions. The relative timing of the diagenetic features was interpreted based on textural relationships. However, the duration of some event remains uncertain because of diagenetic complexity. A summary of diagenetic events and their temporal relationship are given in the Table 5.1, a paragenetic sequence chart (Section 5.1.2).

#### **5.1 Diagenetic history from core and thin section petrography**

##### **5.1.1 Petrographic observations**

This section describes the characteristics of the diagenetic features according to their temporal occurrence from the earliest to the latest diagenetic products. Dolomite textural

description and classification were completed following Gregg and Sibley's (1984) and Sibley and Gregg's (1997) dolomite textural classification modified by Wright (2001) (Figure 5.1). Four types of dolomite textures were identified using thin section and scanning electron microscopy (SEM). These were classified as planar-e, planar-s, nonplanar-a, and cement categories. Detailed descriptions of texture and crystal size on the SEM scale are presented in Section 5.2.1.1 and 5.2.1.2.

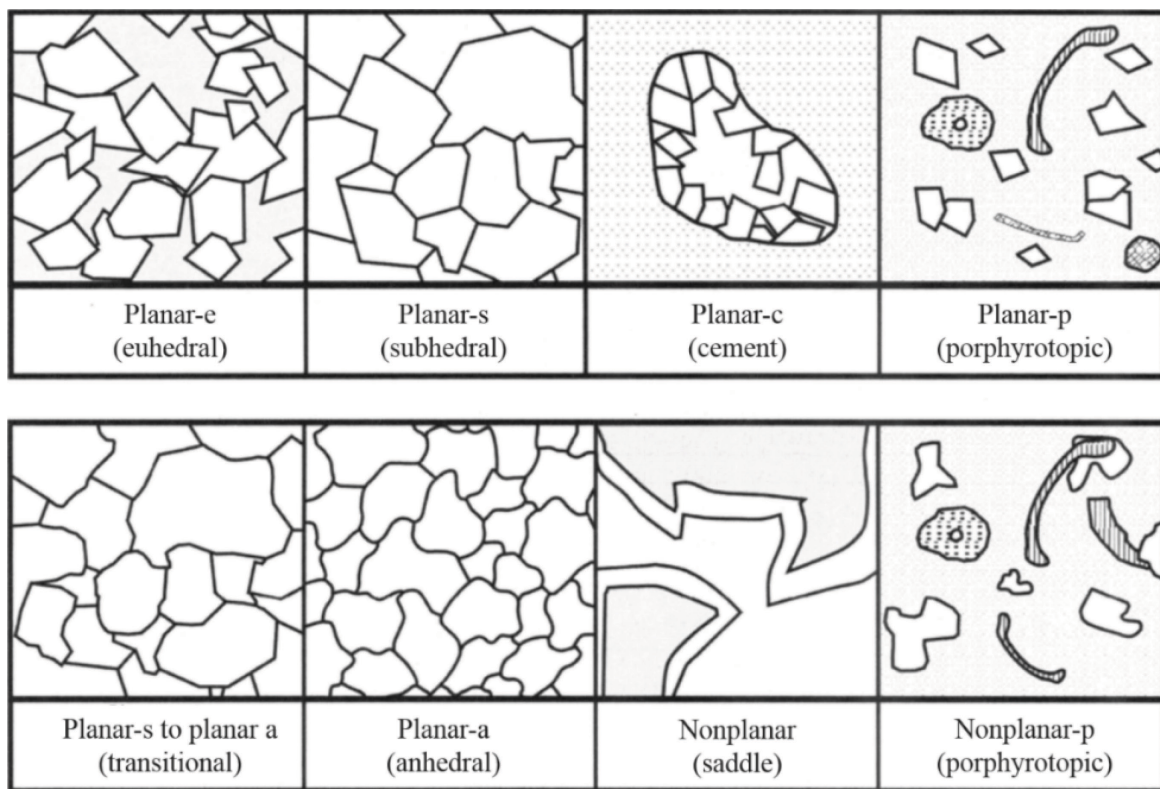


**Figure 5.1:** Dolomite textural classification proposed by Gregg and Sibley (1984), Sibley and Gregg (1987) and modified by Wright. Image modified from Machel (2004).

Additionally, mineral crystal size and carbonate grain size follow the classification proposed by Folk (1962) (Figure 5.2).

	Transported constituents	Authigenic constituents	
64 mm	Very coarse calcirudite	Extremely coarse crystalline	4 mm
16 mm	Coarse calcirudite		
4 mm	Medium calcirudite		
1 mm	Fine calcirudite	Very coarse crystalline	1 mm
0.5 mm	Coarse calcarenite	Coarsely crystalline	0.25 mm
0.25 mm	Medium calcarenite		
0.125 mm	Fine calcarenite	Medium crystalline	0.062 mm
0.062 mm	Very fine calcarenite		
0.031 mm	Coarse calcilutite	Finely crystalline	0.016 mm
0.016 mm	Medium calcilutite		
0.008 mm	Fine calcilutite	Very finely crystalline	0.004 mm
0.004 mm	Very fine calcilutite		
		Aphanocrystalline	

**Figure 5.2:** Carbonate grain size and mineral crystal size classification; Folk, 1962.

#### 5.1.1.1 Cracks - Phase 1a

Cracks are usually random with no preferential direction and are polygonal in shape. Cracks do not crosscut but rather preferentially skirt carbonate grains, becoming circumgranular cracks (Figure 5.3A). Sub-millimetre sized cracks are present in dolomitized micrite rock fragments (Figure 5.3A to C) and are filled with calcite cement (Figure 5.3C). These intraclasts are exclusively present at the top of layer PZ1 toward the basin center in wells BBC 14-1, BBC 14-3, and N 6-28. Larger and wider cracks are present exclusively in the Nine Mile outcrop in ostracod dolopackstone (Figure 5.3D) and show the same pattern as the smaller scale features.

#### **5.1.1.2 Meniscus cement - Phase 1b**

Meniscus cement precipitated at carbonate grain contacts (Figure 5.3E), partially filling interparticle pores. Meniscus cement shows a geographical variation in its relative abundance as follows: in nearshore areas, meniscus cement is preferentially developed within intraclastic grainstone, ooid grainstone, and ostracod grainstone facies (F6, F7, and F8), in which the meniscus cement is more abundant in well PW 13-06 at the top of layer PZ1. Basinward meniscus cement is not present. The original carbonate mineral that precipitated as meniscus cement was replaced by dolomite, which obliterated the original texture of meniscus cement.

#### **5.1.1.3 Molds I- Phase 2a**

Molds were created by dissolution of mainly mollusk shells (Figure 5.3F). Such molds are present only within dolomitized intraclasts (Facies F6) and are completely filled with calcite cement. These molds have preserved the original shapes without any evidence of mechanical deformation (Figure 5.3F).

#### **5.1.1.4 Blocky calcite cement - Phase 2b**

Blocky calcite crystal ranges from medium to coarse crystalline in size. This cement fills moldic porosity and cracks (Figure 5.3A to D) in intraclastic grainstone and ostracod grainstone facies (F6 and F8).



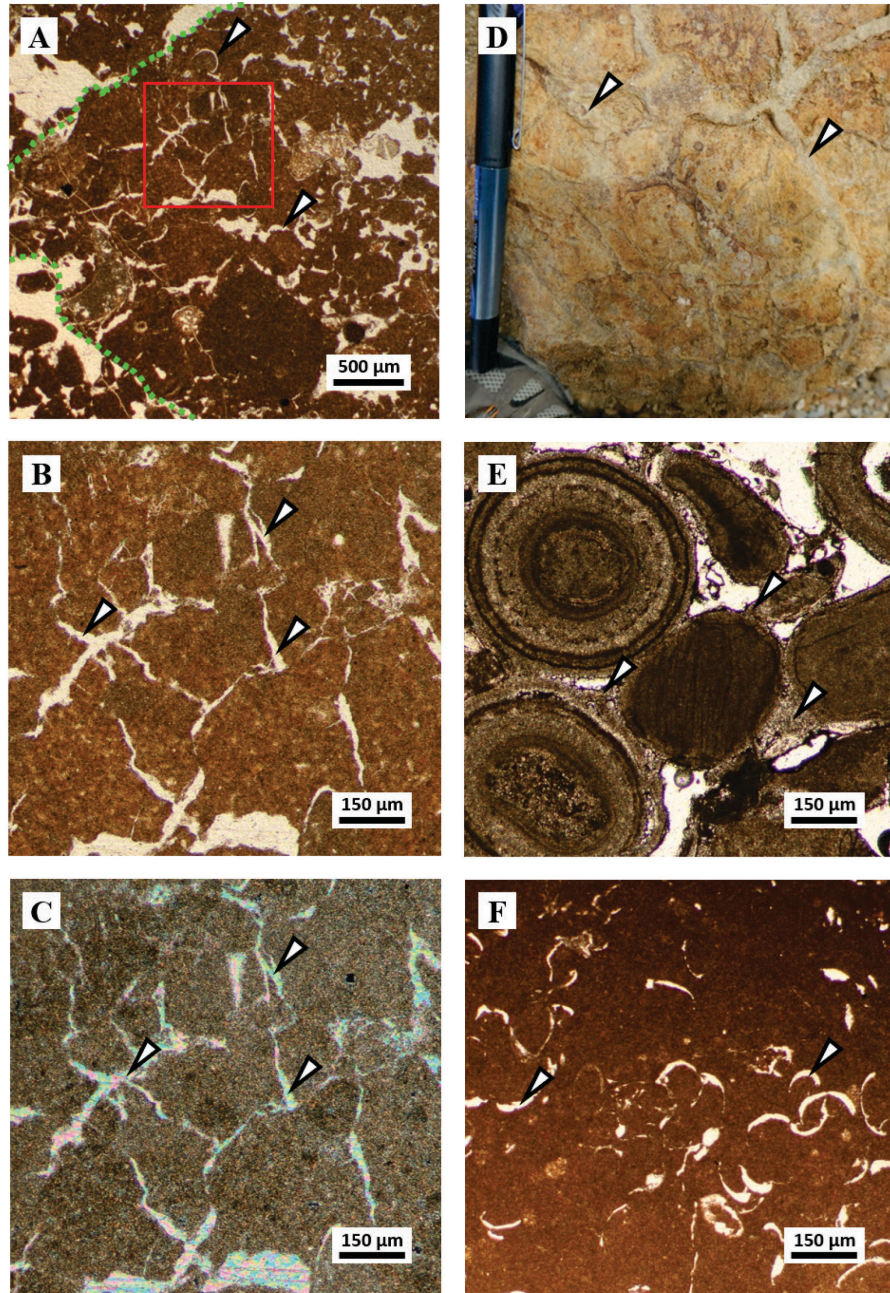


**Figure 5.3:** (A) TLP of intraclast (green dash outline) with cracks that surrounded peloids (arrow) and crosscut dolomitized matrix; well: N 6-28, sample: 5, 8223.2 ft.; plane polarized light (PPL). (B) Detail of photomicrograph (A). Polygonal micro-cracks (arrows) crosscutting microcrystalline dolomitized matrix (brown area), cracks are completely filled with blocky calcite cement; PPL. (C) Crossed-polarized photomicrograph (XPL) (B), blocky calcite cement fills cracks (arrow). (D) Cracks present in the nearshore area are filled with blocky calcite cement (arrows); Nine Mile outcrop, pen for scale. (E) TLP of ooid dolograins with microcrystalline meniscus cement at grain contacts (arrows); well: PW 13-06, sample 6, 5539.5 ft.; PPL. (F) TLP of molds of bioclasts filled with blocky calcite cement (arrow); well: UT 15-13, sample 5, 6982.2 ft.; PPL

#### **5.1.1.5 Variably lithified sediment – Phase 2c**

Variable lithification of sediment by early meniscus and blocky calcite cement.

#### **5.1.1.6 Replacive dolomite - Phase 3a**

This section provides petrographic observations on the thin section scale, however, characterization of individual dolomite crystals is not possible using the petrographic microscope because the crystals are too small. This characterization was therefore conducted by virtue of SEM images (see Sections 5.2.1.1 and 5.2.2.1 for further analysis). Replacive dolomite is brown to green in colour, with crystal size ranges from aphanocrystalline to very finely crystalline. Replacive dolomite is found in the matrix (Figure 5.4A), as well in peloids, intraclasts (Figure 5.4B), ooids, and pellets; however, dolomite generally do not replace bioclasts (Figure 5.4C).

#### **5.1.1.7 Dolomite cement - Phase 3b**

Dolomite cement is clean microcrystalline crystals and partially fills intraparticle pores, usually present as overgrowth of dolomitized internal sediment (Figure 5.4D to F). Most crystals are euhedral to subhedral, crystal size varies from 10 to 20  $\mu\text{m}$ . Dolomite cement is preferentially developed at nearshore areas within the ostracod grainstone and ooid grainstone facies (F8 and F9). In contrast, the basinward facies (F3, F4, and F5) do not display this type of cement.



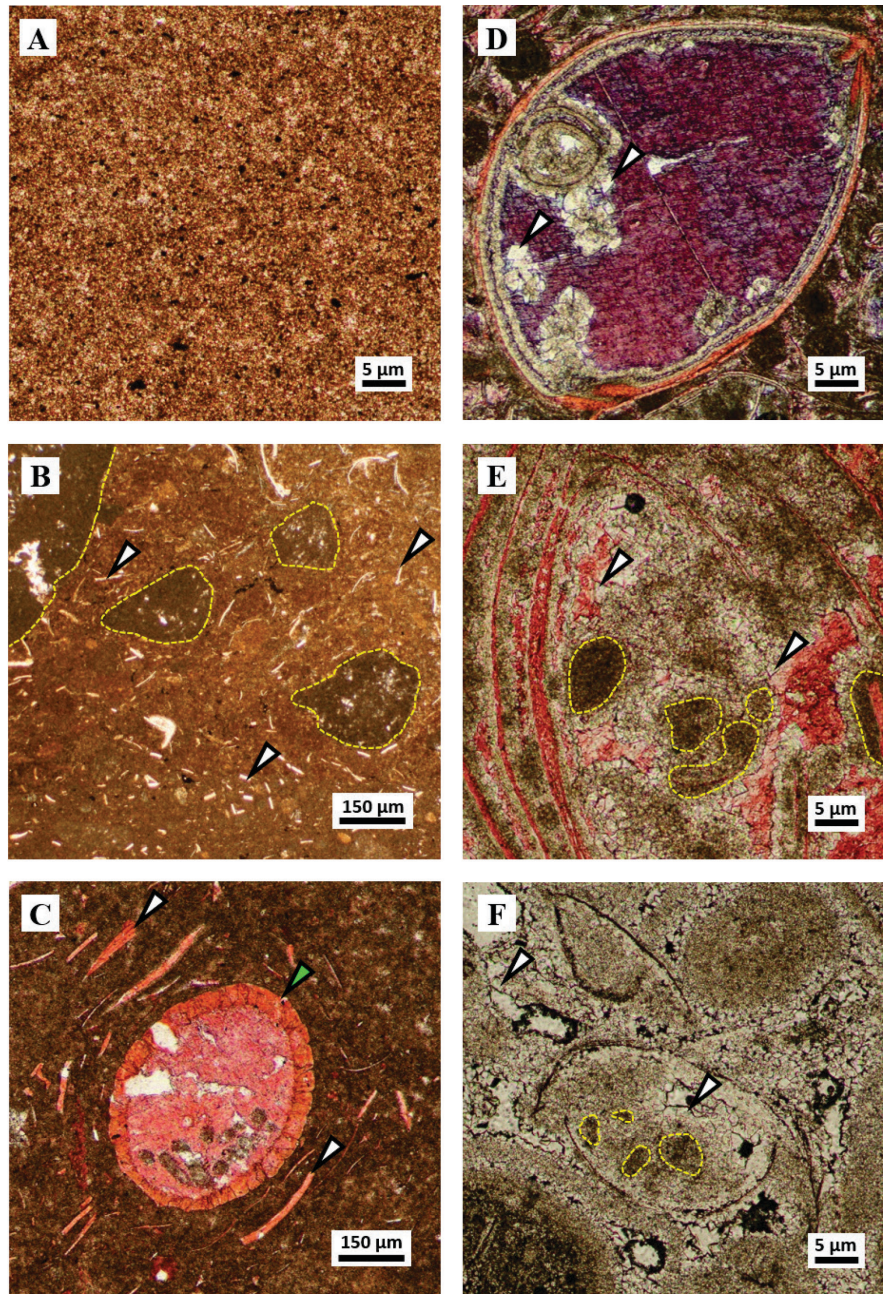


**Figure 5.4:** (A) TLP of very fine dolomite in matrix; pyrite and hydrocarbon droplets (black spots); well: BBC 14-1, sample: 17, 6692.6 ft.; PPL. (B) TLP of very fine dolomite in matrix (light brown area) and dolomitized intraclasts (yellow dashed outlines), bioclasts (arrows) not dolomitized; well: BBC 14-1, sample: 13, 6684.9 ft.; PPL. (C) TLP of matrix-selective dolomitization (dark brown area), shell fragments (white arrows) and gyrogonite bioclast (green arrow) not dolomitized; well: BBC 14-3, sample: 27, 7373.6 ft.; PPL. (D) TLP of planar-c dolomite cement (arrows) partially fills intraparticle pore; well: IU 16, sample: 14, 4729.9 ft.; PPL. (E) TLP of rims of planar-c dolomite cement (arrows) grow around dolomitized peloids and ooids (yellow dashed outlines); well: DS 11-20, sample 12, 4999.35 ft.; PPL. (F) TLP of planar-c dolomite cement (arrows) around dolomitized peloids (?) within ostracod shells; well: PW 13-06, sample: 6, 5539.5 ft.; PPL.

#### **5.1.1.8 Molds II – Phase 4**

Molds developed by partial to complete dissolution of calcite bioclasts (Figures 5.5A to C). Dissolution of bivalves not previously filled with mud were later filled with fibrous chert (Figures 5.5A and B), whereas bivalves filled with mud formed molds only as narrow as the shells (Figure 5.5C).

#### **5.1.1.9 Isopachous quartz cement rims – Phase 5a**

Quartz crystals size ranges from 5 to 20  $\mu\text{m}$ , with bladed to equant shapes. This quartz cement lines interparticle pores (Figures 5.5D and E), and in rare cases intraparticle pores (Figure 5.5F). This cement is preferentially developed in the nearshore area within the intraclast, ostracod, and ooid grainstone facies (F6, F7, and F8).

#### **5.1.1.10 Chert nodules – Phase 5b**

Silica forms elongated and irregular chert nodules (up to several decimetres in dimension) within dolomite layers PZ1, PZ1' and PZ2. The nodules are composed of assorted silica varieties: length-fast and length-slow (quartzine) chalcedony (Flöerke et al., 1991), megaquartz (Folk and Weaver, 1952), and granular microcrystalline quartz (Knauth, 1994). Colourless, fibrous, and aphanocrystalline chalcedony cement also fills intraparticle pores (Figures 5.5A and B) and vugs.



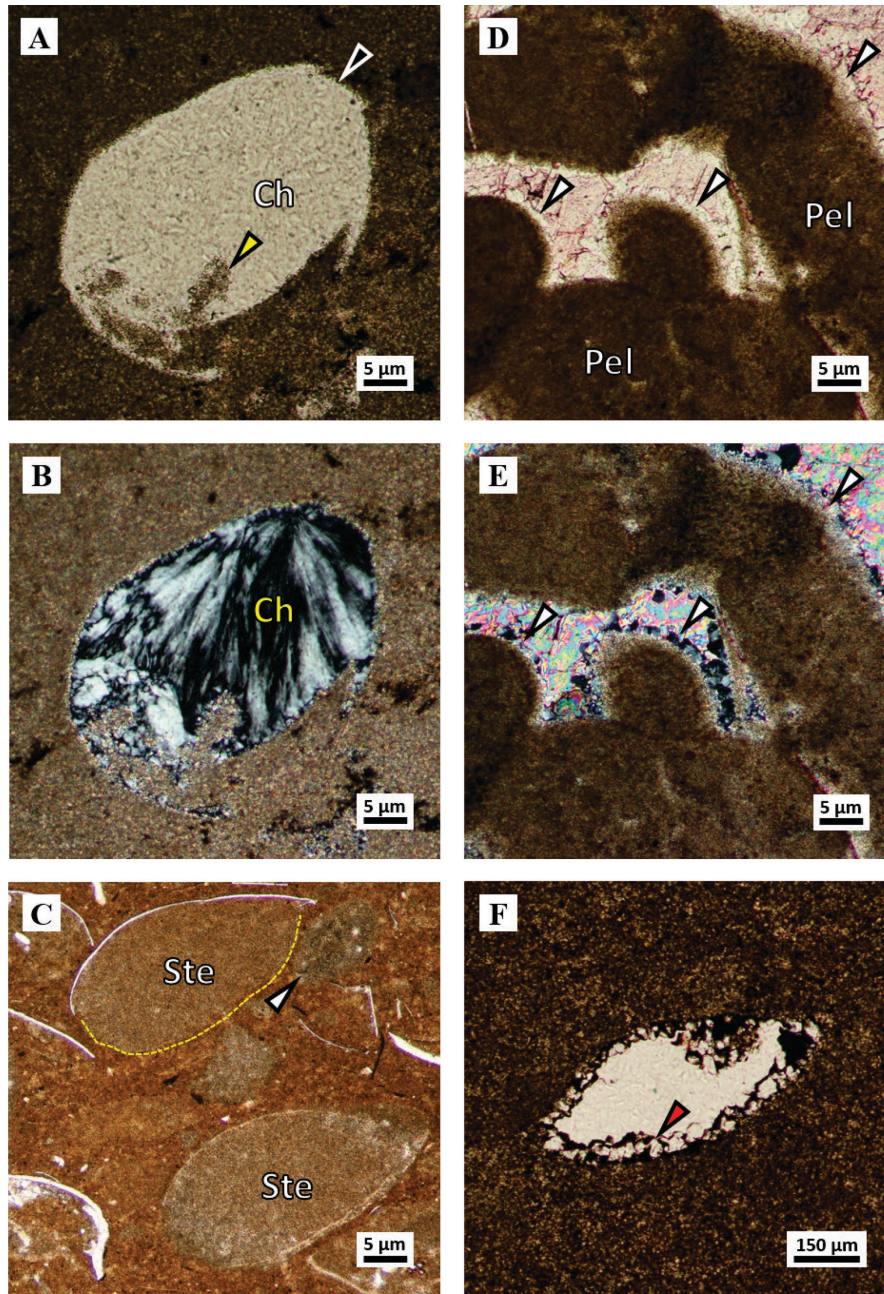


**Figure 5.5:** (A) TLP of ostracod mold (black arrow) filled with dolomite (yellow arrow) and chalcedony (Ch); well: PW 13-06, sample: 8, 5543.5 ft.; PPL. (B) Crossed-polarized light image of (A). Feathered texture of the chalcedony that fills internal ostracod (?) pore; XPL. (C) Partial (yellow dashed line) and complete dissolution (arrow) of ostracod shells; steinkerns (Ste) within an aphanocrystalline dolomitized matrix; well BBC 14-1, sample: 9, 6680.1 ft.; PPL. (D) TLP of rims of very fine crystalline quartz as cement (arrows) around dolomitized peloids (Pel); well: BBC 14-1, sample: 12, 6683.95 ft.; PPL. (E) Crossed-polarized light image of (D). Quartz cement (arrows), and calcite cement (yellow, green, and blue area); XPL. (F) TLP of rims of equant quartz cement (arrow) in intraparticle pore. Dark brown and black spots are hydrocarbons; well: N 6-28, sample: 7, 8230.2 ft.; PPL.

Both length-slow (Figures 5.6A to C) and length-fast (Figures 5.6D and E) chalcedony display a spherulitic fibrous habit and/or a radial fibrous to feathered habit (Figures 5.5B, 5.6B and E), nucleated along pore walls. Megaquartz crystals show a polygonal crystal habit with irregular interlocking crystals, located at the centers of voids, filling remaining space (Figure 5.6F). Granular microcrystalline quartz (anhedral quartz crystals around bioclast in Figure 5.6A to D) composes the majority volume of the chert nodules.

#### **5.1.1.11 Euhedral quartz – Phase 5c**

Quartz of phase 5c is colourless, clean, commonly hexagonal and double-terminated euhedral crystals of quartz that vary in size from 5 to 20  $\mu\text{m}$ . Euhedral quartz crystals contain very fine crystalline dolomite inclusions (Figure 5.7A). They formed around chert nodules and within bioclasts (Figures 5.7B and C), overall in random distribution within the dolomitized matrix of facies F2, F3, and F4.

#### **5.1.1.12 Pyrite – Phase 6**

Very fine crystalline and octahedral pyrite crystals associated with calcite within chert nodules (Figure 5.7D). Crystal size varies from 10 to 100  $\mu\text{m}$ . Some pyrite crystals encase very fine crystalline and planar-e dolomites (Figure 5.7E). There are also disseminated crystals of very fine to fine crystalline pyrite within very fine crystalline dolomite (matrix) (Figure 5.7F). Pyrite crystals range in size from 5 to 10  $\mu\text{m}$ .



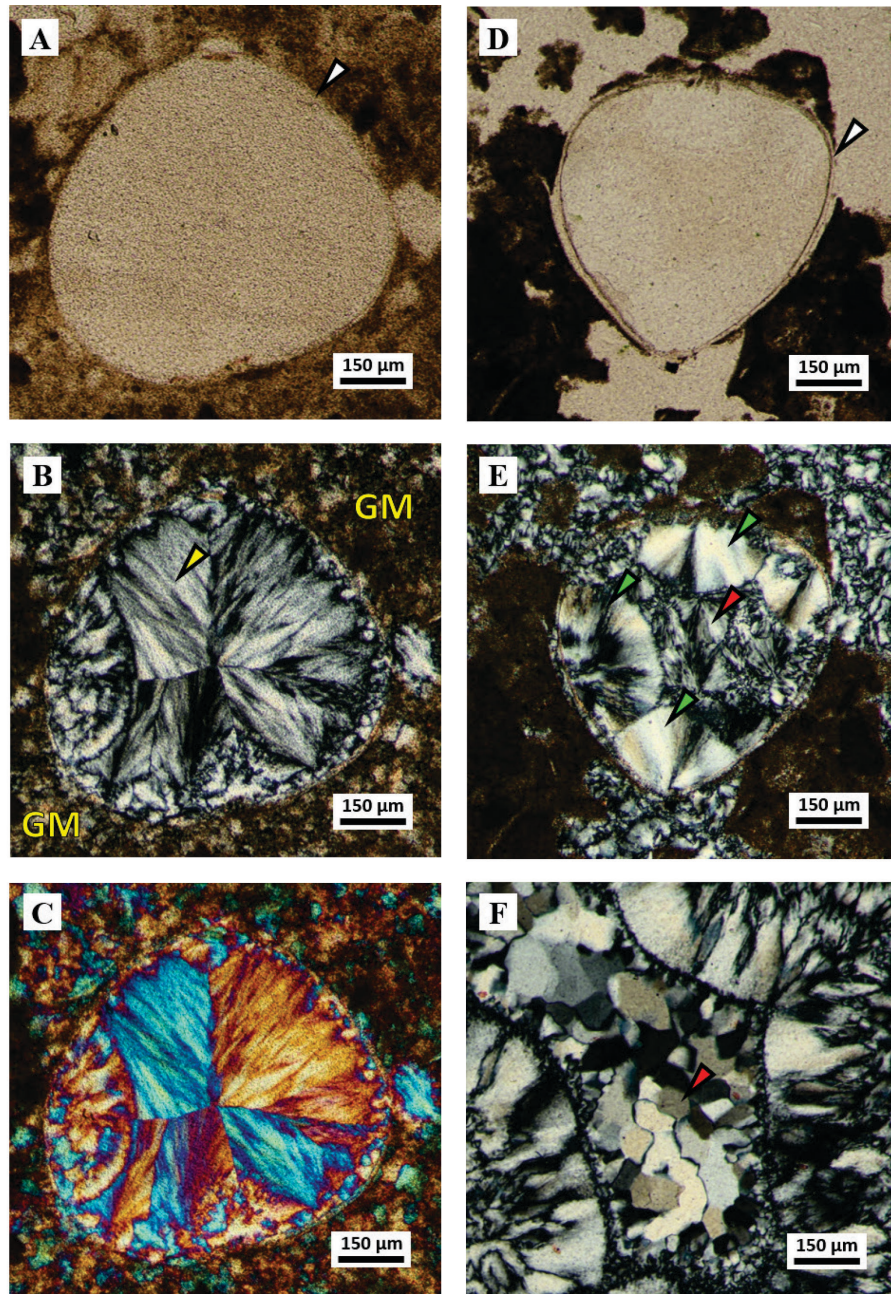


**Figure 5.6:** (A) TLP of a chert nodule. Ostracod shells (arrow) mimetically replaced by microcrystalline quartz. Intraparticle pore filled by chalcedony (light brown area); well: BBC 14-3, sample: 28, 7374 ft.; PPL. (B) Crossed-polarized light image of (A), quartzine (arrow) nucleated at the walls of the ostracod shells. Granular microcrystalline quartz (GM) precipitated around bioclasts; XPL. (C) Same image (A) and (B); XPL + gypsum plate. (D) TLP of a chert nodule with an articulated ostracod (arrow) partially replaced by quartz and dolomite, internal void filled with chalcedony; well: BBC 14-3, sample: 29, 7375 ft.; PPL. (E) Crossed-polarized light image of (D), several chalcedony nucleated along the internal walls of the ostracod shell (green arrows); some chalcedony have radial fibrous to feathered habit (red arrow); XPL. (F) TLP of megaquartz crystals (red arrow) fill a void post-dating chalcedony cement (feathered crystals); well: BBC 14-3, sample: 29, 7375 ft.; XPL.



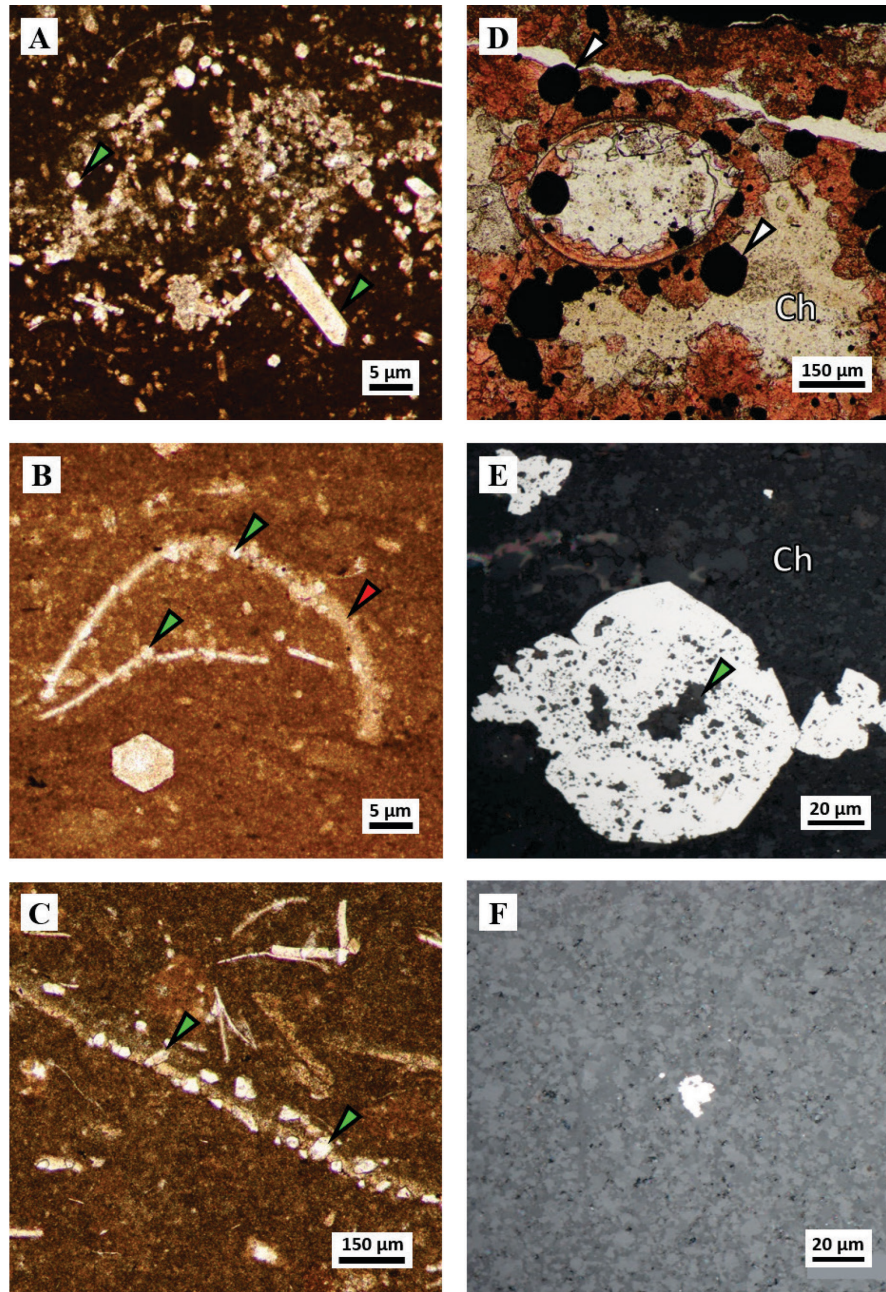


**Figure 5.7:** (A) TLP of euhedral quartz (arrows) within an aphanocrystalline dolomite matrix (dark brown area). Quartz crystals with dolomite inclusions; well: UT 15-13, sample: 11, 7009.9 ft.; PPL. (B) and (C) TLP of euhedral quartz within aphanocrystalline dolomite matrix (light brown area). Some quartz (green arrows) crystallized along shells (red arrow); (B) Well: UT 15-13, sample: 11, 7009.9 ft.; PPL. (C) Well: BBC 14-3, sample: 28, 7374.05 ft.; PPL. (D) TLP of fine crystalline pyrite with cubic and octahedral shape (arrows) associated with calcite (red areas) within a chert nodule (Ch); well: PW 13-06, sample: 11, 5552.3 ft. (E) Reflected light photomicrograph of medium to coarse pyrite with octahedral shapes (bright area) that encloses aphanocrystalline dolomite (arrow) within a chert nodule (Ch); well: N 6-28, sample: 6, 8223.7 ft. (F) Reflected light photomicrograph of very fine crystalline and framboidal pyrite (bright area) within dolomitized matrix; well: PW 13-06, sample: 10, 5545.3 ft.

#### **5.1.1.13 Mechanical compaction features – Phase 7**

Several mechanical compaction features are present: (i) Broken and flattened bioclasts (Figures 5.8A, 5.9A and B); (ii) peloids elongated and/or amalgamated parallel to bedding (Figure 5.8B); (iii) concavo-convex contacts between grains; and (iv) breakage of ooids and peloids.

#### **5.1.1.14 Equant calcite – Phase 8**

Equant calcite forms mosaics of mostly anhedral crystals with size varying from 10 to 50  $\mu\text{m}$ . This calcite also fills interparticle pores as cement. It is more abundant toward nearshore areas (facies F6, F7, and F8), especially within the ostracod grainstone facies (F8) (Figure 5.8C). Equant calcite cement is not present toward the basin center (F2, F3, and F4 facies).

#### **5.1.1.15 Molds and vugs – Phase 9**

Partial dissolution of equant calcite cement created vugs, which were completely filled with ferroan calcite cement in Phase 10 (Figures 5.8D and E). Partial dissolution of bioclasts (preferentially pelecypods and gastropods) created moldic pores, which was also filled by ferroan calcite cement (Figure 5.8F).



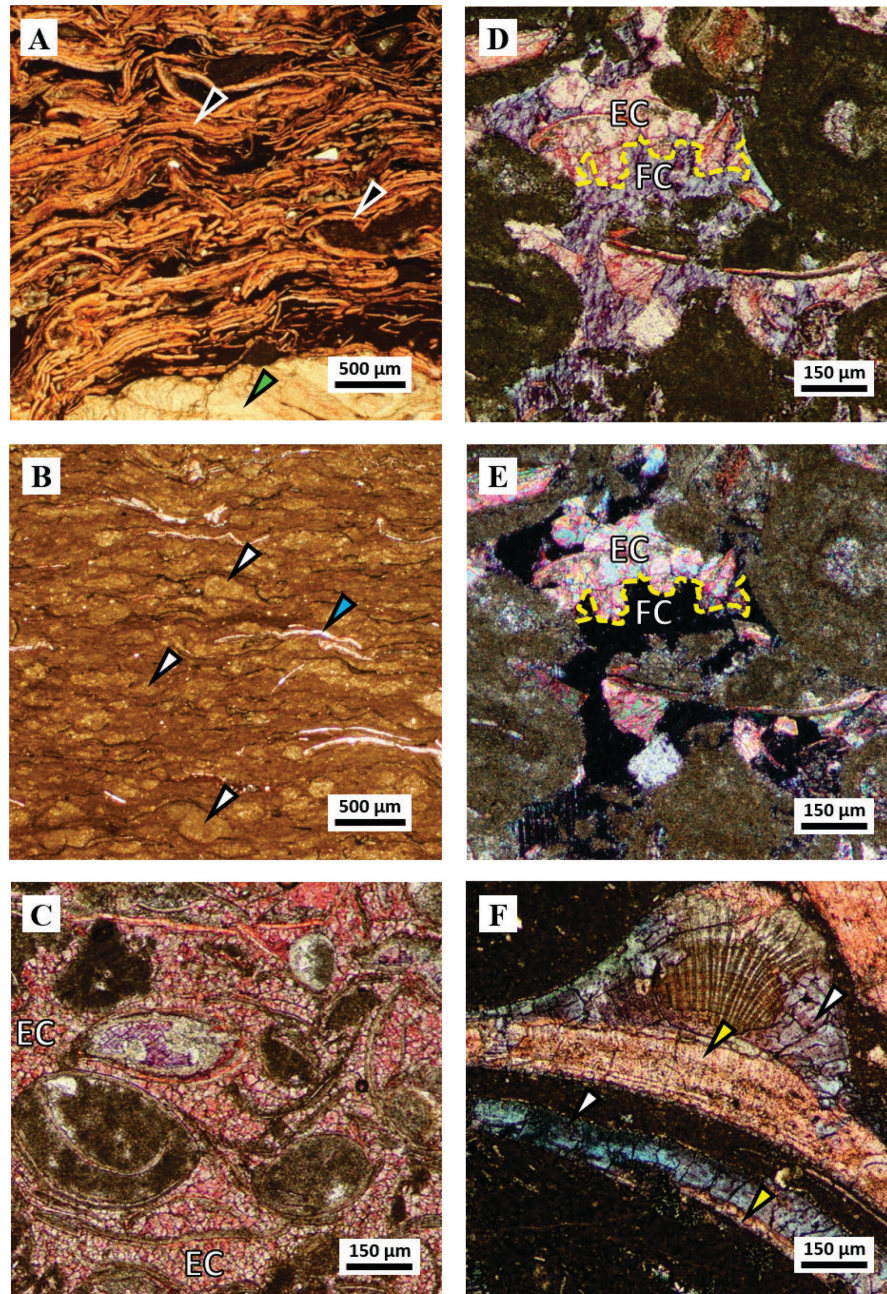


**Figure 5.8:** (A) TLP of densely packed ostracod (black arrows) and gastropod shell (yellow arrow); well: DS 11-20, sample 14, 5017 ft.; PPL. (B) TLP of elongated and dolomitized peloids (steinkerns?) (white arrows), and flattened ostracod shells (yellow arrow) aligned parallel to bedding; well: UT 15-13, sample: 7, 6989 ft.; PPL. (C) TLP of equant calcite (EC) in interparticle pores. Crystal size ranges from 10 to 20  $\mu\text{m}$ ; well: IU 16, sample: 14, 4729.9 ft.; PPL. (D) TLP of equant calcite cement (EC) and ferroan calcite cement (FC) in contact along a possible dissolution front (yellow dashed line); well: DS 11-20, sample: 13, 5000.3 ft.; PPL. (E) Crossed-polarized image of (D). (F) TLP of partial dissolution of bioclast. Original metastable calcium carbonate of gastropod shell fragments (yellow arrows), which was partially dissolved and then filled by blocky ferroan calcite cement (white arrows); well: PW 13-06, sample: 14, 5565.9 ft.



#### **5.1.1.16 Blocky ferroan calcite cement– Phase 10**

Blocky ferroan calcite is a cement with crystals that vary in size from 50 to 200  $\mu\text{m}$ . Ferroan calcite cement mainly fills intraparticle and interparticle pores and it is normally associated with equant calcite cement of Phase 8 (Figures 5.9A and B). In some cases this type of cement fills pores that resulted from the dissolution of shells of pelecypods and gastropods (Figure 5.9C).

#### **5.1.1.17 Subhorizontal stylolites and sutured seams– Phase 11**

Subhorizontal stylolites and sutured seams are nearly parallel to bedding. Subhorizontal stylolites have an irregular to hummocky shape (Logan and Semeniuk, 1976) with amplitudes up to 20  $\mu\text{m}$ . In some cases, a set of stylolites composes an irregular anastomosing set (Figure 5.9D). Swarms of microstylolites or sutured seams are common in dolostones (Figure 5.9E).

#### **5.1.1.18 Oil impregnation– Phase 12**

Black oil (liquid phase) fills intercrystal, interparticle, and moldic pores (Figure 5.9F), fractures, stylolites, and solution seams. Oil is present in all carbonate facies (F2 to F8). Textural relationship between oil impregnation and blocky calcite cement (phase 15) does not clarify the time occurrence between these phases.

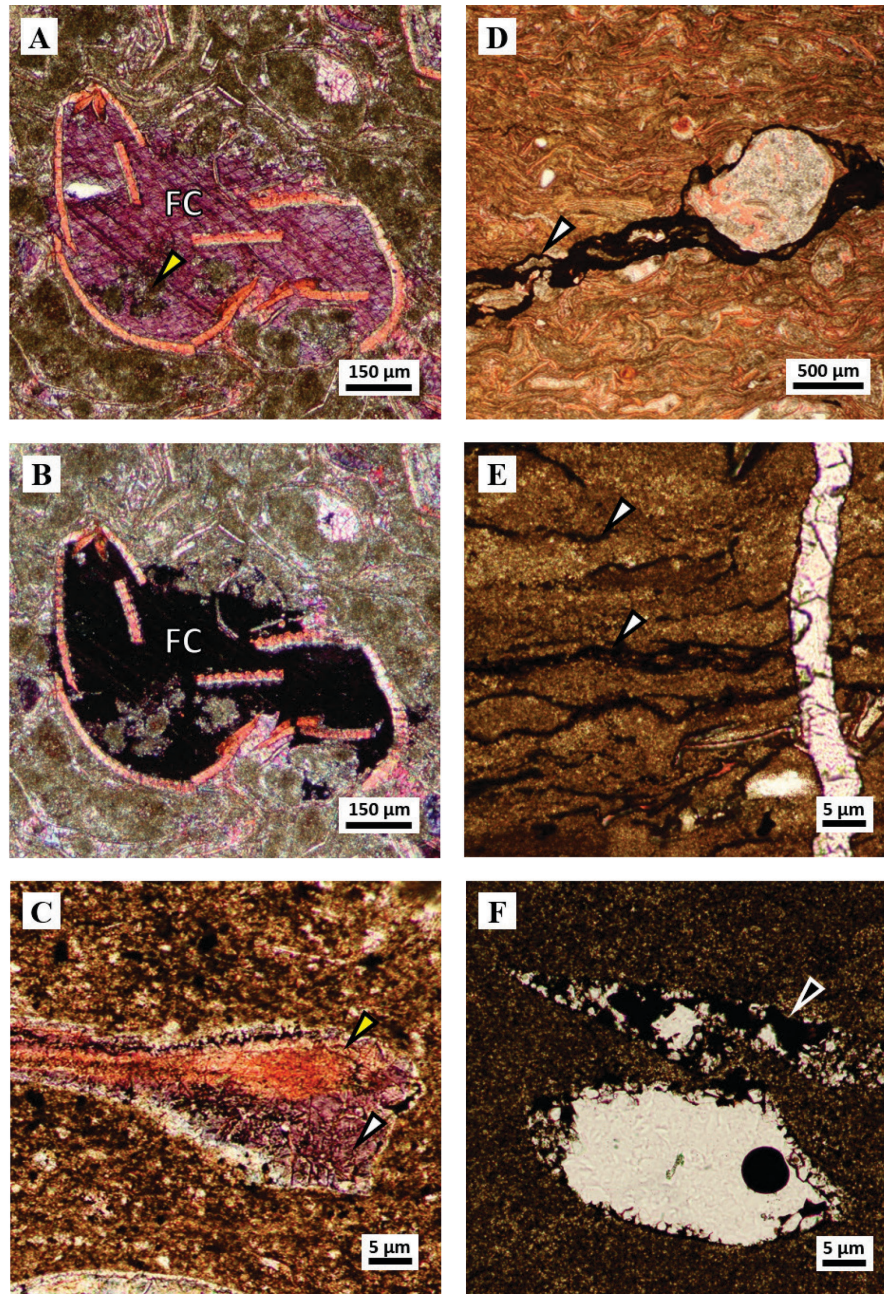


**Figure 5.9:** (A) TLP of blocky ferroan calcite cement (FC) in ostracod intraparticle pore (dark purple), encasing patches/clusters of microcrystalline dolomite (arrow); well: IU 16, sample: 14, 4729.9 ft.; PPL. (B) Crossed-polarized light image of (A). (C) TLP of blocky ferroan calcite cement (white arrow) in space developed by partial dissolution of shell fragment (yellow arrow); well: BBC 14-1, sample: 6, 6666.5 ft.; PPL. (D) TLP of irregular to hummocky subhorizontal stylolites forming an anastomosing set (arrow); well: IU 16, sample: 16, 4733.2 ft.; PPL. (E) TLP of swarms of microstylolites or sutured seams (arrows), subvertical fracture post-dates stylolites and is completely filled by blocky calcite cement; well: UT 15-13, sample: 6, 6983.9 ft.; PPL. (F) TLP of hydrocarbon within intercrystal pores of dolomitized matrix and moldic pores; well: N 6-28, sample: 7, 8230.2 ft.; PPL.

#### **5.1.1.19 Subvertical stylolites and solution seams– Phase 13**

Vertical stylolites are characterized by sharp to wavy boundaries, and commonly columnar to wave-like peak stylolites (Logan and Semeniuk, 1976) with amplitudes up to 2500  $\mu\text{m}$ , which crosscut bedding planes and carbonate grains (Figure 5.10A). Subvertical stylolites are associated with subvertical fractures (Figure 5.10A) and occur in both limestones and dolostones. Insoluble material has thicknesses ranging from 50 to 200  $\mu\text{m}$  (Figure 5.10B). These stylolites are preferentially developed toward the basin center in wells BBC 14-1, BBC 14-3, N 6-28, and UT 15-13.

#### **5.1.1.20 Vertical fractures– Phase 14**

Single or cluster vertical fractures are characterized by straight, branching, and stepped profiles nearly perpendicular to stratification (Figure 5.10C). Fractures display apertures (space between walls) up to 50  $\mu\text{m}$ . Fractures crosscut carbonate grains, chert nodules, and stylolites. Fractures are partially to completely fill with calcite cement of phase 15. There is no evidence of relative movement between fracture walls.

#### **5.1.1.21 Drusy calcite cement– Phase 15**

Fibrous to bladed calcite crystals that vary from medium crystalline to blocky and very coarse crystalline in size (center of the void), with well-defined twining (Figures 5.10D and E). Calcite cement fills vertical fractures (Phase 14) and stylolites (Phase 13). These calcite crystals commonly contain hydrocarbons (oil) in fluid inclusions (Figure 5.10F).



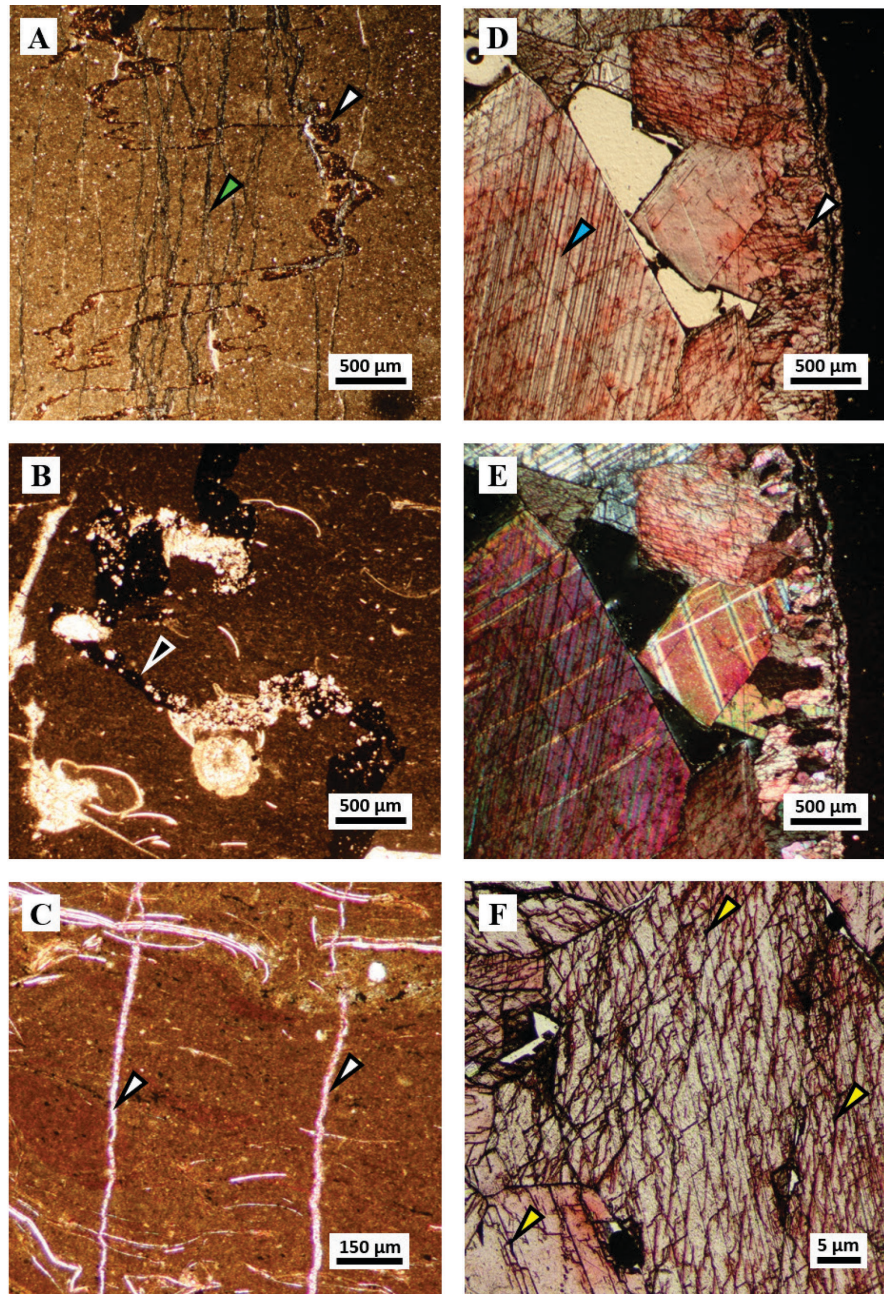


**Figure 5.10:** (A) TLP of subvertical serrated stylolites (white arrow) with amplitude up to 2500  $\mu\text{m}$  associated to subvertical fractures (green arrow); well: N 6-28, sample: 1, 8199.3 ft.; PPL. (B) TLP of anastomosing sutured seam (arrow) that crosscuts stratification (horizontal axis); well: N 6-28, sample: 8, 8234.6 ft.; PPL. (C) TLP of subvertical fractures (arrows) that crosscut stratification (horizontal axis) and ostracod shells. Fractures filled by blocky calcite cement; well: BBC 14-1, sample: 20, 6701.4 ft.; PPL. (D) TLP of drusy calcite cement with crystal size increasing from medium crystalline (white arrow) at the stylolite wall toward a very coarse crystalline (blue arrow) in the center; well: N 6-28, sample: 12, 8267.4 ft.; PPL. (E) Crossed-polarized light image of (A). (F) TLP of hydrocarbon (arrows) as inclusions in calcite crystals (entire photomicrograph); well: N 6-28, sample: 12, 8267.4 ft.

### 5.1.2 Interpretation

The paragenetic sequence defined in Table 5.1 chronologically lists the products that were formed over the entire stratigraphic section of interest. The top of the table shows timing from early (after deposition) to late (present). Additionally, the base of the table shows diagenesis environments that correlate diagenetic setting as proposed by Machel (1999). The near-surface diagenetic setting is located at depths of zero to maximum a few meters and is controlled by surface waters, be they marine, fresh or evaporitic. The shallow burial diagenetic setting is located below the near-surface diagenetic setting down to about 1000 m, still heavily influenced, if not controlled by, surface-derived waters. The intermediate burial diagenetic setting is located between about 1000 and 3000 m in depth, the bottom being defined as coinciding with the top of the liquid oil window, which varies in depth and it is controlled by geothermal gradient and kerogen type. Finally, the deep burial diagenetic setting encompasses the liquid oil window and reaches down to the top of the metamorphic realm (Machel 1999).

This section interprets the diagenetic processes that created the various diagenetic products described in the previous section, and provides an interpretation of the temporal designation for each diagenetic product based on textural relationships such as crosscutting features and cement textures. The term ‘phase’ is defined here as the time interval during which a particular diagenetic process created the product(s) listed in Table 5.1.

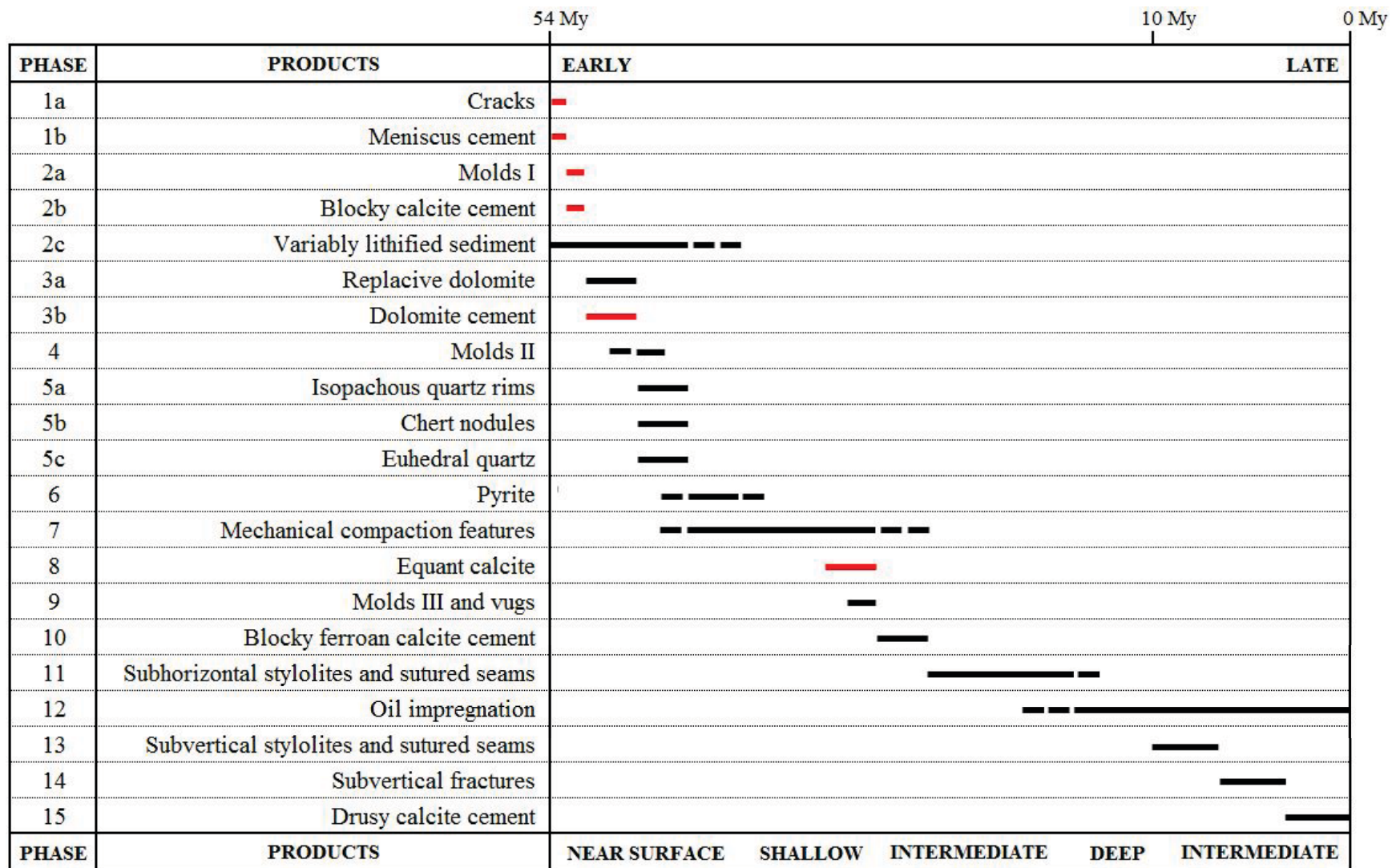


**Table 5.1:** Paragenetic sequence. Phases 1 (cracks and meniscus cement), 2 (molds and equant-blocky calcite cement), 3b (dolomite cement), and 8 (equant calcite cement) took place along the near shoreline area only. These diagenetic products are highlighted red.

#### **5.1.2.1 Phase 1a – 1b**

Diagenesis transformed precursor lime sediments just after deposition in the near-surface diagenetic setting. The first diagenetic processes formed two products: cracks (phase 1a) and meniscus cement (phase 1b). These features were likely developed by subaerial exposure of unlithified sediment, in which, due to pore water evaporation, soft sediment shrinkage produced crack networks and/or circumgranular cracks (Esteban and Klappa, 1983). This process took place along the shoreline area, presumably during periods of subaerial exposure, although the observed cracks may also have formed subaqueously due to syneresis.

The progressive evaporation of pore water in the vadose zone allowed crystallization of calcite as meniscus cement (James and Choquette, 1984) at or near carbonate grain boundaries. Vadose diagenesis took place only along the shore belt area located near the southern limits of the study area.

#### **5.1.2.2 Phase 2a – 2b – 2c**

Vertical fluctuations in the water table formed several diagenetic products. In phase 2a, meteoric water probably promoted dissolution of metastable carbonate minerals (Scholle and Ulmer-Scholle, 2003), forming molds and vugs. Cracks that had formed in phase 1 as well as molds and vugs of Phase 2a were then completely filled with equant calcite cement. The dissolution of bioclasts and subsequent precipitation of equant and blocky calcite cement suggest early diagenesis within the meteoric-phreatic zone (Pingitore, 1976; Scholle and Ulmer-Scholle, 2003), which overlaps the near-surface and shallow burial diagenetic settings defined by Machel (1999).

Also during phase 2, lime mud likely was partially lithified to limestone (here identified as phase 2c), perhaps only partially and variably depending on proximity to the fluctuating lake shore line, thereby forming semi-lithified carbonate material by virtue of an interplay of recrystallization (stabilization of metastable aragonite and/or high-Mg calcite) and minor intergranular cementation (blocky calcite cement). The petrographic evidence currently available does not permit to judge the degree of mineralogical stabilization and induration of the sediments prior to Phase 3.

#### **5.1.2.3 Phase 3a – 3b**

Dolomite was formed by two different processes: the replacement of the precursor micrite matrix (phase 3a), and crystallization as cement (phase 3b). Moreover, dolomite cement crystals overgrew dolomite replacement crystals. This relationship suggests that these products (replacement and cements) precipitated from the same parental dolomitized fluid. Furthermore, the preservation of the parental limestone textures (Figures 5.3, 5.4 and 6.8) and the fact that dolomitization was stratiform and created layers PZ1, PZ1', and PZ2 that alternate with limestone layers suggests that dolomitization was a nearly syndimentary process in the near-surface diagenetic environment. As such, the Uteland Butte dolomite layers conform to the type of dolomite known as penecontemporaneous (Budd, 1997; Warren, 2000; Machel 2004). Dolomite formation likely was driven by slight to moderate degrees of evaporation, as further discussed in Section 5.2 and Chapter 6, Section 6.3.



#### **5.1.2.4 Phase 4**

Molds were created by the dissolution of bioclasts. This process occurred in the near-surface diagenetic environment where fluids dissolved ostracod shells and fragments (Figures 5.5A to C). The dissolution of bioclasts may have been a by-product of dolomitization. Alternatively, and perhaps more likely, incursions of relatively fresh lake water and/or rain water during periods of subaerial exposure facilitated dissolution of non-dolomitized bioclasts.

#### **5.1.2.5 Phase 5a – 5b – 5c**

Bioclast dissolution and quartz crystallization likely took place at the same time (Maliva and Siever, 1989) and nearly contemporaneously with dolomitization and/or very soon thereafter. Furthermore, considering that silicified bioclasts do not show any reworking (disarticulated shells) or mechanical deformation (broken shells), silicification took place prior to mechanical compaction, thus also in the near-surface diagenetic environment. Primary calcium carbonate matrix and carbonate grains (intraclasts and peloids) now contained within chert nodules consist of dolomite, which indicates that dolomitization predated silicification.

Quartzine within chert nodules suggest that the silicification process probably was driven by evaporation (Folk and Pittman, 1971; Siedlecka, 1972; Heaney, 1995; Warren, 2006). The source of silica likely was the river water that fed the lake, and thereby from the eroding hinterland. Furthermore, the only recognizable evaporite mineral in the stratigraphic interval of interest is chert, and it is present as nodules encapsulating dolomite crystals within the PZ layers.

#### **5.1.2.6 Phase 6**

Pyrite can be formed as a by-product of either bacterial sulfate reduction (BSR) or thermochemical sulfate reduction (TSR) (Machel 2001). BSR occurs at low temperatures commonly between 60 to 80 °C, whereas TSR occurs at in deep burial diagenetic settings at temperatures between 100 °C to 140 °C (Machel, 2001). In the UBm, pyrite formation must have taken place within the near-surface to shallow burial diagenetic settings. This interpretation is based on the textures and the occurrence of pyrite in the paragenetic sequence, as well as on the recognition that the maximum burial temperature of the study area. According to Schamel (2015), the maximum temperature likely was near 110 °C based on burial history curves, which in turn is too low for thermochemical sulfate reduction. The fact that pyrite is overall very low in abundance likely reflects that the lake water had a very low sulfate concentration, rather than low concentrations of iron or organic matter, both of which were abundant.

#### **5.1.2.7 Phase 7**

Mechanical compaction deformed the entire stratigraphic section of interest, generating densely packed mollusk layers, broken bioclasts, and elongation parallel to the bedding of semi-lithified components. Mechanical compaction likely took place throughout the near-surface and shallow burial diagenetic settings. The fact that many bioclasts show evidence of breakage further suggests that early diagenetic lithification was rather ‘weak’ overall, thus leaving many semi-plastic sedimentary layers into the shallow burial diagenetic setting (see

phase 2c above). Phase 7 might have overlapped with dolomitization (Phase 3a and 3b), and silicification (phases 5a, 5b, and 5c), pyritization (phase 6).

#### **5.1.2.8 Phase 8**

Equant calcite cement likely took place during and after mechanical compaction. The temporal interpretation of this calcite cement is based on crystal morphology and superposition with other diagenetic products.

#### **5.1.2.9 Phase 9**

A third generation of mold formed along with some vugs during phase 8, considering the types of cements that are fill them (Figures 5.8D to F), notably ferroan calcite. The cause for this dissolution phase cannot be ascertained but may have been another temporal freshening of the pore water after previous phases of evaporation that had formed dolomite and/or chert.

#### **5.1.2.10 Phase 10**

Ferroan calcite cement fills remaining pores left by partial dissolution of calcite cement (Figures 5.8D to F and 5.9C). The precipitation of ferroan calcite cement requires a reducing environment, which preferentially develops within intermediate and deep burial diagenetic settings (Machel 1999; Scholle and Ulmer-Scholle, 2003, Flügel, 2010). The textural relationship of ferroan calcite cement with previous diagenetic products confirms this interpretation.

#### **5.1.2.11 Phase 11**

Continuous burial led to the development of subhorizontal stylolites and sutured seams caused by chemical compaction. Stylolitization took place in the intermediate and deep burial diagenetic settings (Machel, 1999; Flügel, 2010).

#### **5.1.2.12 Phase 12**

Oil was generated likely in the upper levels of the deep burial diagenetic setting, considering the (lacustrine) type of kerogen [types I and II, Schamel, 2015)] contained in the Green River Basin. According to Schamel (2015), the stratigraphic interval of interest underwent differential burial, in which the maximum depth for the northern part of the study area (depocenter) is estimated at 3700 m, and for the southern part of the study area (near-shore line) is around 2550 m. Schamel (2015) estimated that the northern part of the study area is nowadays within the wet gas window.

#### **5.1.2.13 Phase 13**

The subvertical stylolites likely were created by a tectonic compressive event (Ebner et al., 2010), in which the direction of the maximum compressive stress was likely subhorizontal, probably associated to the fast uplifting and/or erosion rates (Schamel, 2015).

#### **5.1.2.14 Phase 14**

Vertical fractures may have formed during tectonic compression in a tri-axial stress field, or during uplift and/or the erosion that took place 0.5 millions of years ago (Mya) (Schamel, 2015). Considering the current post-uplift depth of the strata of interest, phase 14 must be placed into the intermediate burial diagenetic environment.

#### **5.1.2.15 Phase 15**

Drusy calcite cement partially fills some open subvertical fractures and stylolites (Figures 5.10D to F). Calcite crystal sizes and texture variation suggest an intermediate burial diagenetic setting (Machel, 1999). Along the walls of subvertical stylolites and/or fractures, calcite crystals are characterized by medium crystalline in size with bladed texture, whereas at the center of the void, calcite crystals are characterized by very coarse crystalline in size with blocky texture.

### **5.1.3 Burial history**

Schamel (2015) designed a burial history model for the GRF. In this model, the base of the GRF is defined by the UBm, which is located at the base of the GR-7 unit (Figure 5.11). The maximum temperature that unit GR-7 reached was between 95 °C and 120 °C at a geothermal gradient of 25 °C/km. However, the highest temperature of 120 °C does not apply to the current study area because it was calculated for a synthetic well located farther north, representing the region of maximum burial.

Considering that the current study area is located between the depocenter and the nearshore settings of the Uinta Basin, the maximum burial temperature in the current study area is estimated to be  $\sim 110^{\circ}\text{C}$  [based on extrapolation of Schamel (2015) model] (Figure 5.11).

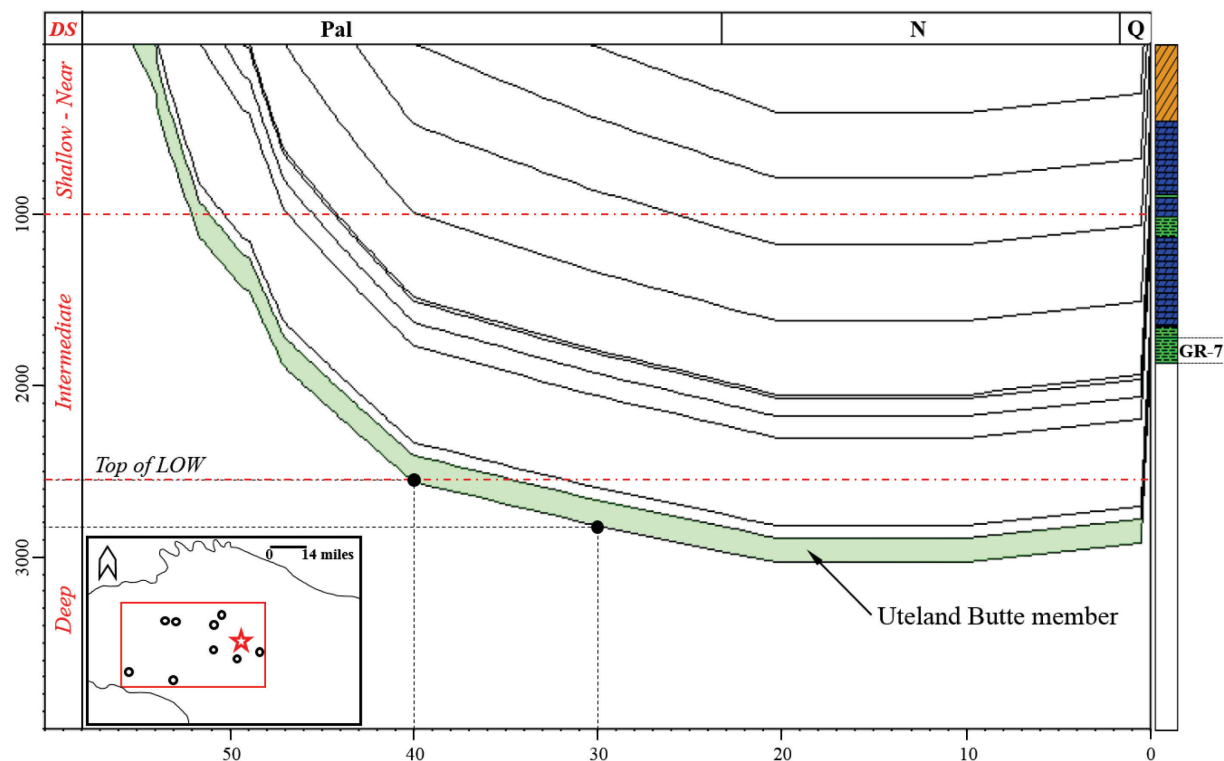


**Figure 5.11:** Burial curve of a synthetic well located within the study area (red star in the inset map) correlated with diagenetic environments as identified in this study (left column), modified from Schamel (2015); DS: Diagenetic settings based on Machel's (1999) diagenetic environments; Pal: Paleogene, N: Neogene, Q: Quaternary, LOW: Liquid oil window.

The burial curve (Figure 5.11) describes a high burial rate in the time interval from 55 to 40 My. Most of the identified diagenetic phases took place in the near-surface and shallow diagenetic settings from phase 1 up to phase 9 between the time of deposition at about 55 Mya and 52 Mya; all of them in the first three millions of years (My) of the deposition. Later on, phases 10 and 11 occurred in the intermediate diagenetic setting between about 52 and 40

Mya. Thereafter, the burial rate decreased, as defined by reduction of the negative slope at 40 Mya, reaching the maximum burial depth around 3050 m at 20 Mya. Schamel (2015) estimated that the liquid oil window (phase 12) has passed between about 40 and 30 Mya (black dots in Figure 5.11). Oil generation window defines the intermediate – deep diagenetic settings boundary (Machel, 1999) located around 2550 and 2850 m; followed by an extended period of no additional burial, as described by the horizontal contours between 20 and 10 Mya. Uplift of the basin started at about 10 Mya with an abrupt slope change at around 0.5 Mya, likely generated by high erosion rates (Schamel, 2015).

## **5.2 Dolomite**

### **5.2.1 Observations**

This section presents petrographic characteristics of dolomite obtained by means of scanning electron microscopy and cathodoluminescence microscopy, as well as compositional data, such as  $\text{Ca}^{2+}$  content and cation ordering, stable isotope and elemental composition.

#### **5.2.1.1 Crystal shapes**

A dip cross-section was selected to identify variations dolomite textures from the nearshore areas toward the basin center, by wells N 6-28, UT 15-06, and PW 13-06. Three thin sections were selected for PZ1, four thin sections were selected for PZ1', and three thin sections were selected for PZ2 (Figure 5.12).

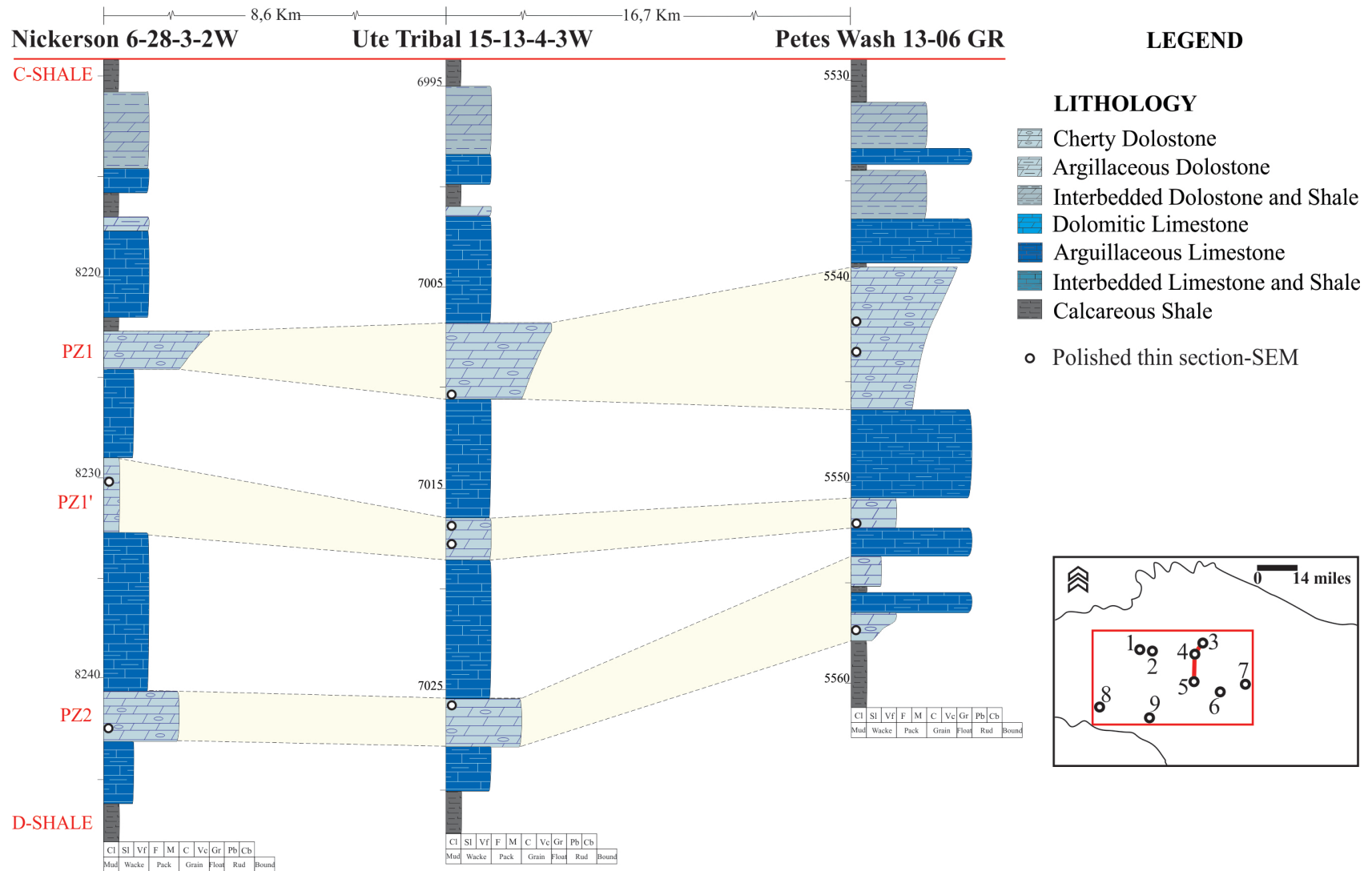


**Figure 5.12:** Stratigraphic correlation of PZ layers with location (depth) of selected polished thin section for layers PZ1, PZ1', and PZ2. Numbers in the inset map stand for wells/outcrops as 1: BBC 14-1, 2: BBC 14-3, 3: N 6-28, 4: UT 15-13, 5: PW 13-06, 6: DS 11-20, 7: UI 16, 8: WCC, and 9: NMC



PZ1, PZ1', and PZ2 layers display four dolomite textures: planar-e (Figure 5.13A), planar-s (Figure 5.13B), nonplanar-a (Figure 5.13C), and planar-c (Figure 5.13D). Intercrystal voids are present in planar-s and nonplanar-a dolomites, probably from dissolution of calcium carbonate cores in phase 4 and/or phase 9 (Table 5.1).

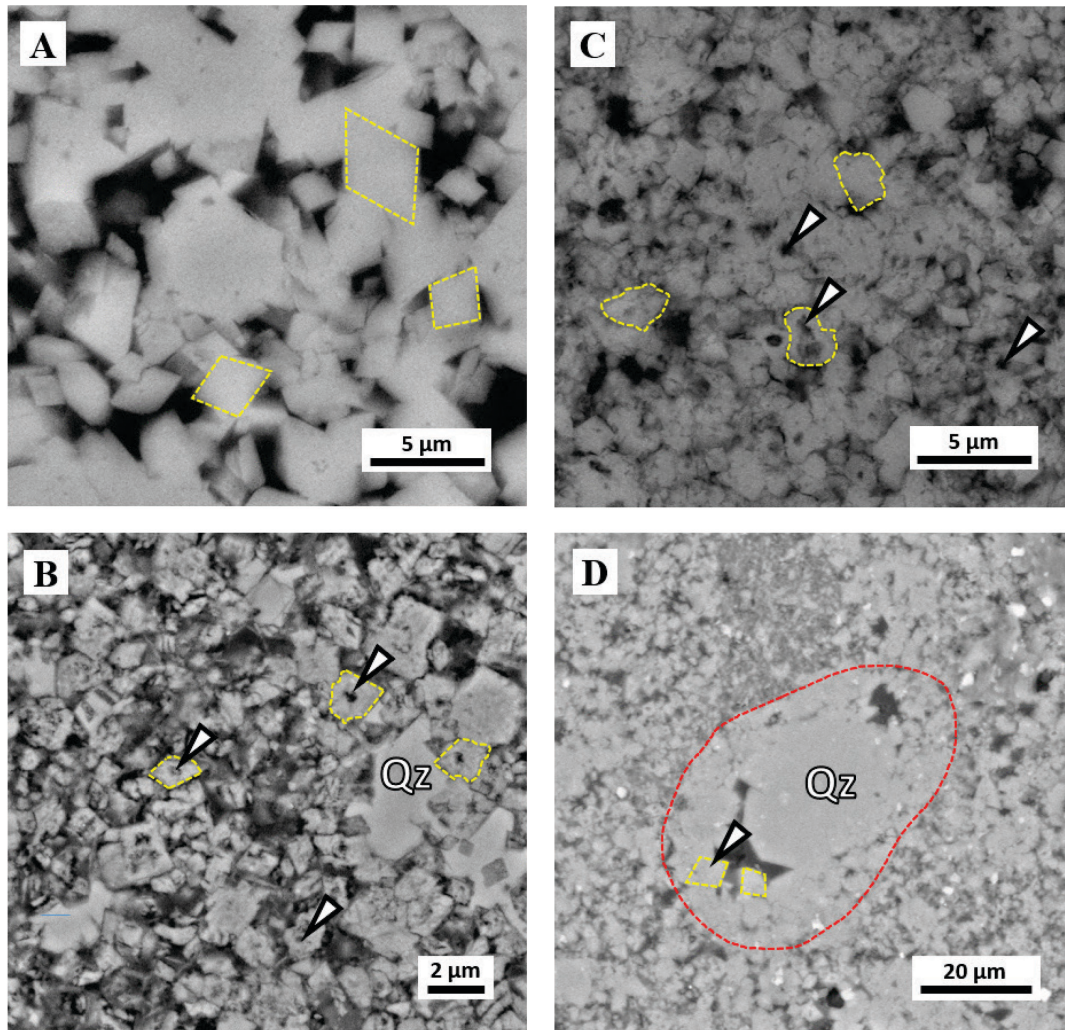


**Figure 5.13:** (A) SEM image of planar-e dolomite texture. Note the straight dolomite faces and well defined rhombohedral habit (yellow dashed lines); well: N 6-28, sample: 7, 8230.2 ft. (B) SEM image of planar-s dolomite, some dolomite crystals have irregular faces (yellow dashed lines) and internal holes (white arrows); post-dolomitization authigenic quartz (Qz) encases some dolomite crystals; well: PW 13-06, sample: 12, 5557.4 ft. (C) SEM image of nonplanar-a dolomite, dolomite crystals have irregular and lobate crystal faces (yellow dashed outlines) and internal holes (white arrows); well: UT 15-13, sample: 11, 7009.9 ft. (D) SEM image of planar-c dolomite; interparticle pore (red dashed line) partially filled by dolomite cement (yellow dashed outlines) and authigenic quartz (Qz); well: N 6-28, sample: 9, 8242.5 ft.

These textures display a distinctive distribution across the study area. For layer PZ1, planar-e dolomite is predominant in well PW 13-06 located nearshore, while nonplanar-a dolomite is more common in well UT 15-13 located in an intermediate zone. PZ1' consists entirely of planar-e dolomite in the near-shore area (Well PW 13-06) and near the basin center (Well N 6-28), while nonplanar-a and planar-s dominate at an intermediate zone. PZ2 layer presents a different pattern in which the most abundant texture is planar-s dolomite in all three locations (Figure 5.14).

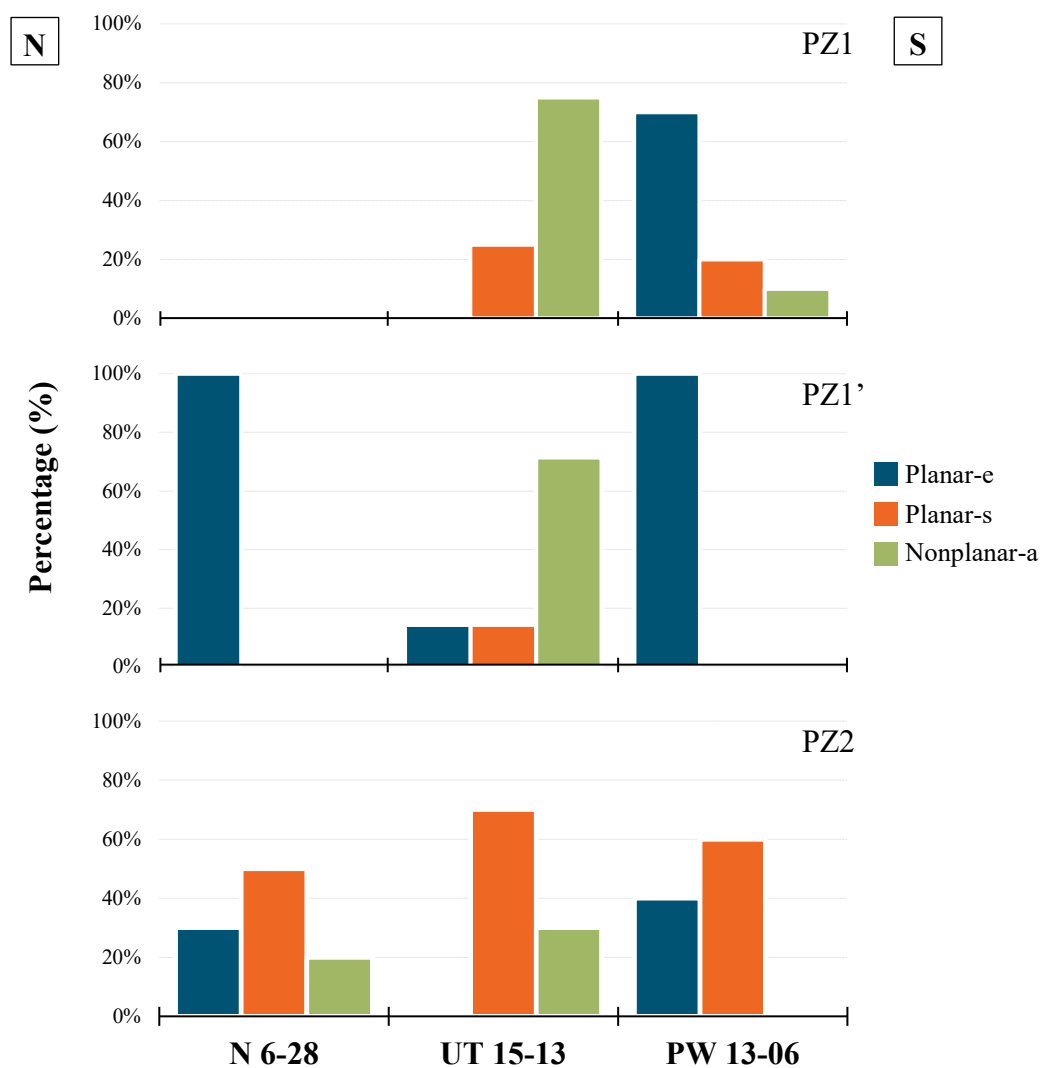


**Figure 5.14:** Distribution of dolomite textures for each PZ layer. N: North, S: South. The cross section is shown in Figure 5.12.

### 5.2.1.2 Crystal sizes

Identification of dolomite crystal sizes was based on the following steps: First, individual dolomite crystal size was measured according to crystal shape. For euhedral and subhedral crystals, two of the straight edges of the rhomb were measured. For anhedral crystals, the largest and shortest crystal diameter were measured. Secondly, the crystal sizes were grouped according to crystal size frequency distribution. Clustering dolomite crystal sizes using frequency distribution shape was inconclusive because the histograms do not show natural breaks (valleys). The Jenks natural breaks classification method was used because it minimizes the standard deviation of the selected group and maximizes the standard deviation between groups (Jenks, 1967).

As a result, three dolomite crystal populations emerged: population one (POP 1), ranging from 0.25 to 1.5  $\mu\text{m}$ ; population two (POP 2), ranging from 1.5 to 3.0  $\mu\text{m}$ ; and population three (POP 3), ranging from 3.0 to 6.0  $\mu\text{m}$ . POP 1 is the most abundant with 53.7%, followed by POP 2 with 37.7%, and POP 3 with 8.6 % (Figure 5.15). These three dolomite populations are present in all measured samples in about the same relative proportion. The means and standard deviations of the measured crystals are summarized in Table 5.2, grouped by dolomite layer. The dolomite crystal size populations do not present any preferential distribution along the N-S cross-section of Figure 5.12.

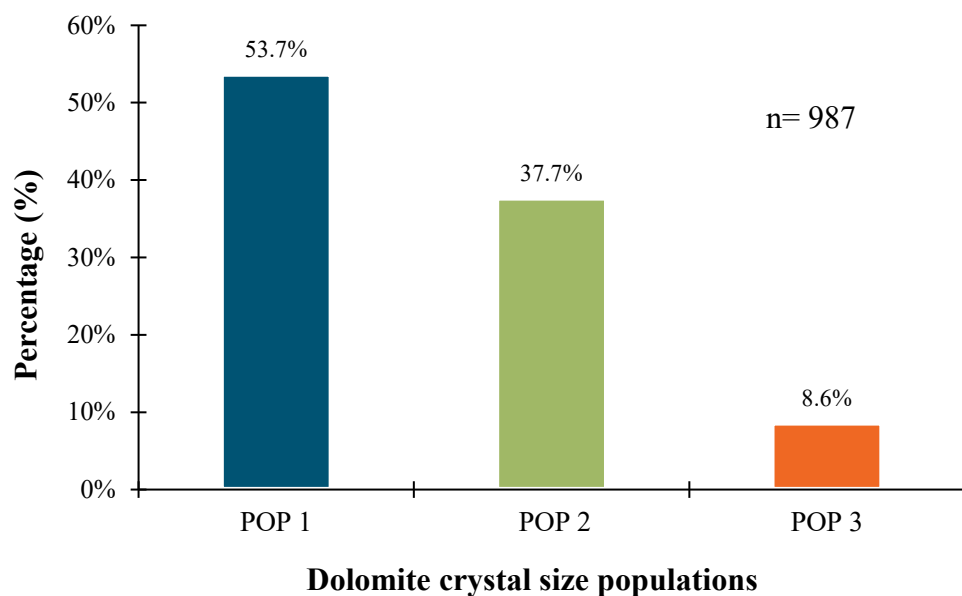


**Figure 5.15:** Percentage distribution of dolomite crystal size populations. POP 1: 0.25  $\mu\text{m}$  to 1.5  $\mu\text{m}$ , POP 2: 1.5  $\mu\text{m}$  to 3.0, POP 3: 3.0  $\mu\text{m}$  to 6.0  $\mu\text{m}$ .

Well	Sample	Depth (ft)	Layer	Mean size ( $\mu\text{m}$ )	St.Dev ( $\mu\text{m}$ )	n
UT 15-13	11	7009.9	PZ1	1.3	0.67	193
PW 13-06	7	5541.9	PZ1	2.4	0.94	80
PW 13-06	8	5543.5	PZ1	2.2	0.98	86
N 6-28	7	8230.2	PZ1'	2.0	0.90	78
UT 15-13	12	7016.4	PZ1'	1.6	0.80	125
UT 15-13	13	7017.4	PZ1'	1.5	0.50	54
PW 13-06	11	5552.3	PZ1'	2.7	1.11	19
N 6-28	9	8242.5	PZ2	1.7	0.78	100
UT 15-13	14	7025.2	PZ2	1.4	0.65	128
PW 13-06	12	5557.4	PZ2	1.3	0.54	124

**Table 5.2:** Mean size and standard deviation (St.Dev) of dolomite crystals.

The dolomite crystal size distribution (CSD) shows a right-skewed distribution with major crystal size concentration around the lowest values (0.25  $\mu\text{m}$  to 2.5  $\mu\text{m}$ ) and a tail located at the highest values (6  $\mu\text{m}$ ) (Figure 5.16). The peak around 0.25  $\mu\text{m}$  to 2.5  $\mu\text{m}$  is composed of POP 1 and POP 2, whereas the tail (3  $\mu\text{m}$  to 6  $\mu\text{m}$ ) is composed mainly of POP3. All dolomite PZ layers display the same distribution.

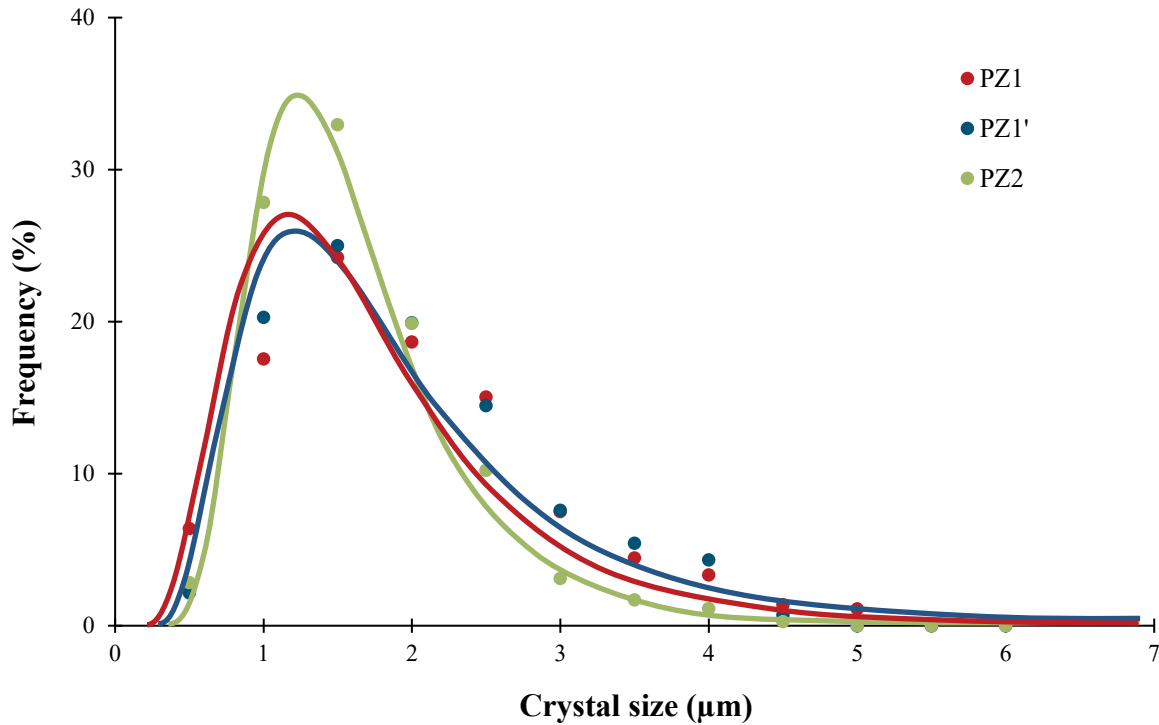


**Figure 5.16:** Dolomite crystal size distribution for each PZ layer. All PZ layers present a right-skewed and left tail distribution.

Validation of the right-skewed and left tail distribution was validated through the Anderson-Darling statistical test (Anderson and Darling, 1954), considering the normal distribution as the null hypothesis. In Figure 5.17A, the data (red dots) deviate from the normal probability (blue line), obtaining an AD (Anderson-Darling) value of 16.301. In contrast, in

Figure 5.17B most of data (red dots) fit with the lognormal probability (blue line), with an AD value of 1.617. Comparing AD values of both cases (A and B), the normal distribution has the highest AD value. In this case, the null hypothesis (CDS as normal distribution) is rejected. Dolomite CSD for PZ layers presents a better approach to a lognormal distribution.

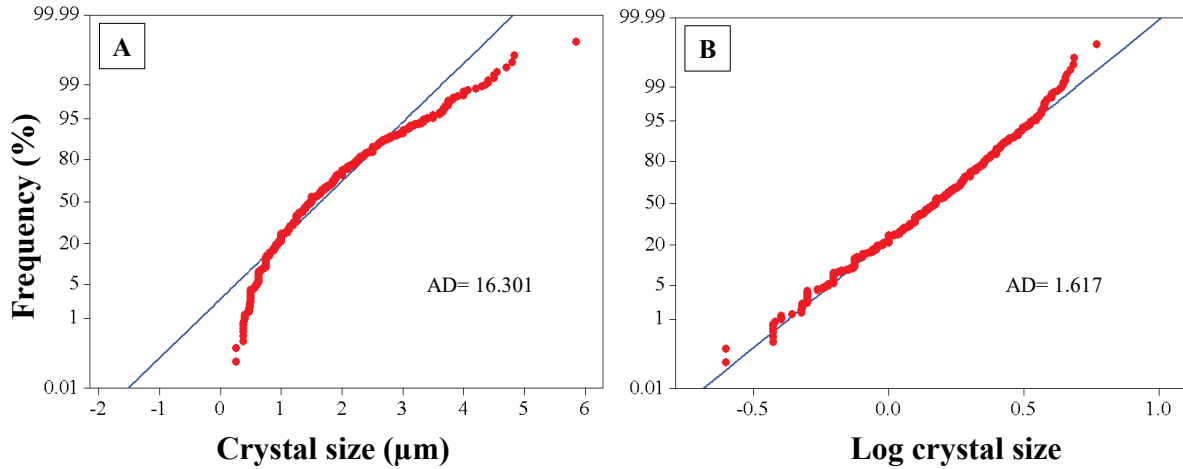


**Figure 5.17:** Validation of dolomite CSD: (A) Normal and (B) lognormal distributions. AD: Anderson-Darling value.

### 5.2.1.3 Cathodoluminescence

The electron beam excitation on the surface of dolomite crystals do not display any visible luminescence characteristics either through a microscope (Figure 5.18) or through the cathodoluminescence (CL) detector attached to the SEM.



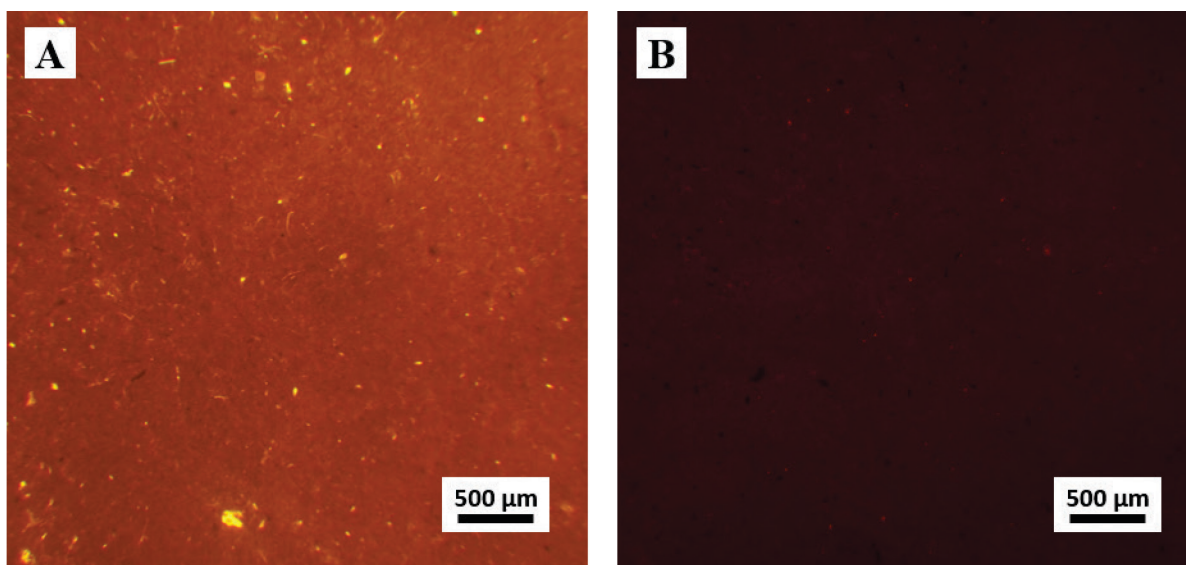


**Figure 5.18:** (A) TLP of dolomudstone at the base of PZ1 with dolomite crystals in matrix (dark red area); well: PW 13-06, sample: 10, 5545.3 ft. (B) Cathodoluminescence photomicrograph of the same area in (A) with no visible luminescence contrast.

#### 5.2.1.4 Stoichiometry

Dolomite stoichiometry was identified by means of XRD and EMPA data. This section compares the dolomite calcium mole percentage from XRD and EMPA. The XRD data considered here is from Indiana University because the diffractograms from this lab show the greatest detail (split peaks, asymmetries). Comparison and discussion of XRD data from different laboratories is detailed in Appendix 5.

The high resolution diffractograms from Indiana University display three remarkable characteristics: (i) a  $d_{104}$  dolomite peak is displaced toward lower  $2\theta$  values relative to the ideal dolomite peak; (ii) the  $d_{104}$  dolomite peak is usually split into “subpeaks” with side humps (asymmetrical peak); and (iii) the  $d_{104}$  dolomite peak shows is rather broad (Figure 5.19). All dolomite samples run at Indiana University (14 samples) show the same or similar pattern.

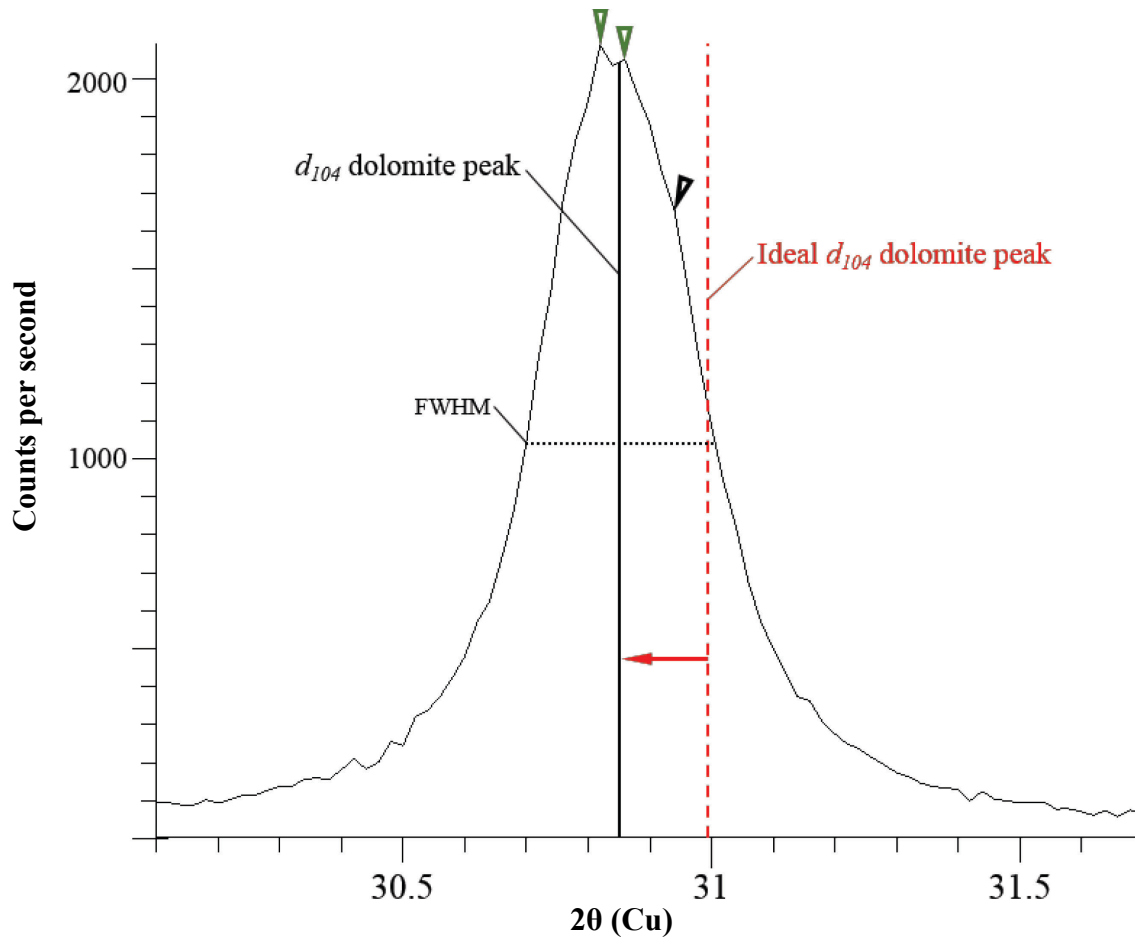


**Figure 5.19:** High-resolution diffractogram of the  $d_{104}$  dolomite peak that displays three remarkable characteristics: (i)  $d_{104}$  peak ( $30.86^\circ 2\theta$  represented by vertical black line) shifted toward lower  $2\theta$  values (ideal dolomite  $d_{104}$  peak, red dashed line), in this particular sample =  $0.13^\circ 2\theta$  (left red arrow); (ii) split  $d_{104}$  peak (green arrows) and side humps (black arrow) that define an asymmetrical  $d_{104}$  reflection; and (iii) wide peak with a full width of half maximum intensity (FWHM) of  $0.31^\circ 2\theta$ , higher than the ideal dolomite [FWHM =  $0.155^\circ 2\theta$  for Eugui dolomite (Jones et al., 2001)]. Well PW 13-06, sample: 8, 5543.5 ft. XRD diffractogram from Indiana University (Cu $\alpha$  radiation).

The observed XRD diffraction pattern could be related to: (i) iron substituting for magnesium, (ii) calcium substituting for magnesium, and/or (iii) different dolomite chemical populations (Kaczmarek and Sibley, 2011). Both  $\text{Fe}^{2+}$  and excess  $\text{Ca}^{2+}$  cations within the crystals lattice causes a shift of the  $d_{104}$  dolomite peak toward lower  $2\theta$  values.

The possibility of  $\text{Fe}^{2+}$  causing the observed broadening and/or the shifting of the  $d_{104}$  peak can be discounted in the basis of energy-dispersive X-ray spectroscopy (EDS), EMPA, and ICP-MS data (Appendix 4, 6, and 7 respectively), none of the which showed  $\text{Fe}^{2+}$  values higher than 1 %Fe (EDS = 0.2%, EMPA = 0.2%, ICP-MS = 0.9%; all values are arithmetic means). Hence, the observed patterns are interpreted as resulting from  $\text{Ca}^{2+}$  excesses. Furthermore, the split in the  $d_{104}$  dolomite peak is likely generated by at least two calcian dolomite populations (e.g., Jones et al., 2001).

The dolomite calcium mole percentage ( $\%\text{Ca}_{\text{Dol}}$ ) was calculated using the equation proposed by Lumsden (1979), in which there is a direct correlation between the  $\text{Ca}^{2+}$  mole percentage and the position of the  $d_{104}$  peak of dolomite crystals (Equation 1):

$$\text{NCaCO}_3 = 333.33 * d - 911.99 \quad (\text{Equation 1})$$

where  $\text{NCaCO}_3$  is the dolomite calcium content in mole percentage, and  $d$  is the d-spacing of the  $d_{104}$  peak, calculated using the Bragg law (Equation 2):

$$\sin \theta = \lambda / 2d \quad (\text{Equation 2})$$

where  $\theta$  is the reflected angle,  $\lambda$  is the wavelength of Cu  $K\alpha$  radiation, and  $d$  is the spacing value between crystal lattices. Equation 2 in 1:

$$\text{NCaCO}_3 = [333.33 * (\lambda / 2 * \sin \theta)] - 911.99 \quad (\text{Equation 3})$$

The resulting  $\%\text{Ca}_{\text{Dol}}$  values for all samples analyzed are listed in Appendix 5. The calculated  $\%\text{Ca}_{\text{Dol}}$  values, obtained using Lumsden's equation, are subject to errors as neither Equations 1 nor 3 consider other features that affect the d-spacing. These features include

heterogeneous cation replacement that causes an estimated error between 1 to 2.5 %Ca<sub>Dol</sub> (Reeder and Sheppard, 1984). However, the error could be even larger given the presence of several dolomite populations, each of them with a different %Ca<sub>Dol</sub> composition (Reeder and Sheppard, 1984).

For the dolomites of the UBm, an estimation of the %Ca<sub>Dol</sub> error using the Lumsden equation was performed by comparing the %Ca<sub>Dol</sub> values calculated from XRD data to the %Ca<sub>Dol</sub> values measured from EMPA data (Table 5.3 and Figure 5.20). The EMPA %Ca<sub>Dol</sub> values were taken as base of reference because (i) the precision and accuracy (0.4 to 0.5 %Ca<sub>Dol</sub>) is considerably smaller than the XRD data and (ii) EMP is capable to measure individual dolomite crystals. Previous to the measurement, the EMPA was calibrated against dolomite (internal) standard for Ca, Mg, Sr, Fe, and Mn. The calculated %Ca<sub>Dol</sub> values from EMPA data were determined by the relationship between the Ca and Mg molar fraction as defined in Equation 4:

$$\%Ca_{Dol} = ({}^mCa / ({}^mCa + {}^mMg)) \times 100 \quad (\text{Equation 4})$$

where <sup>m</sup> is the molar fraction.

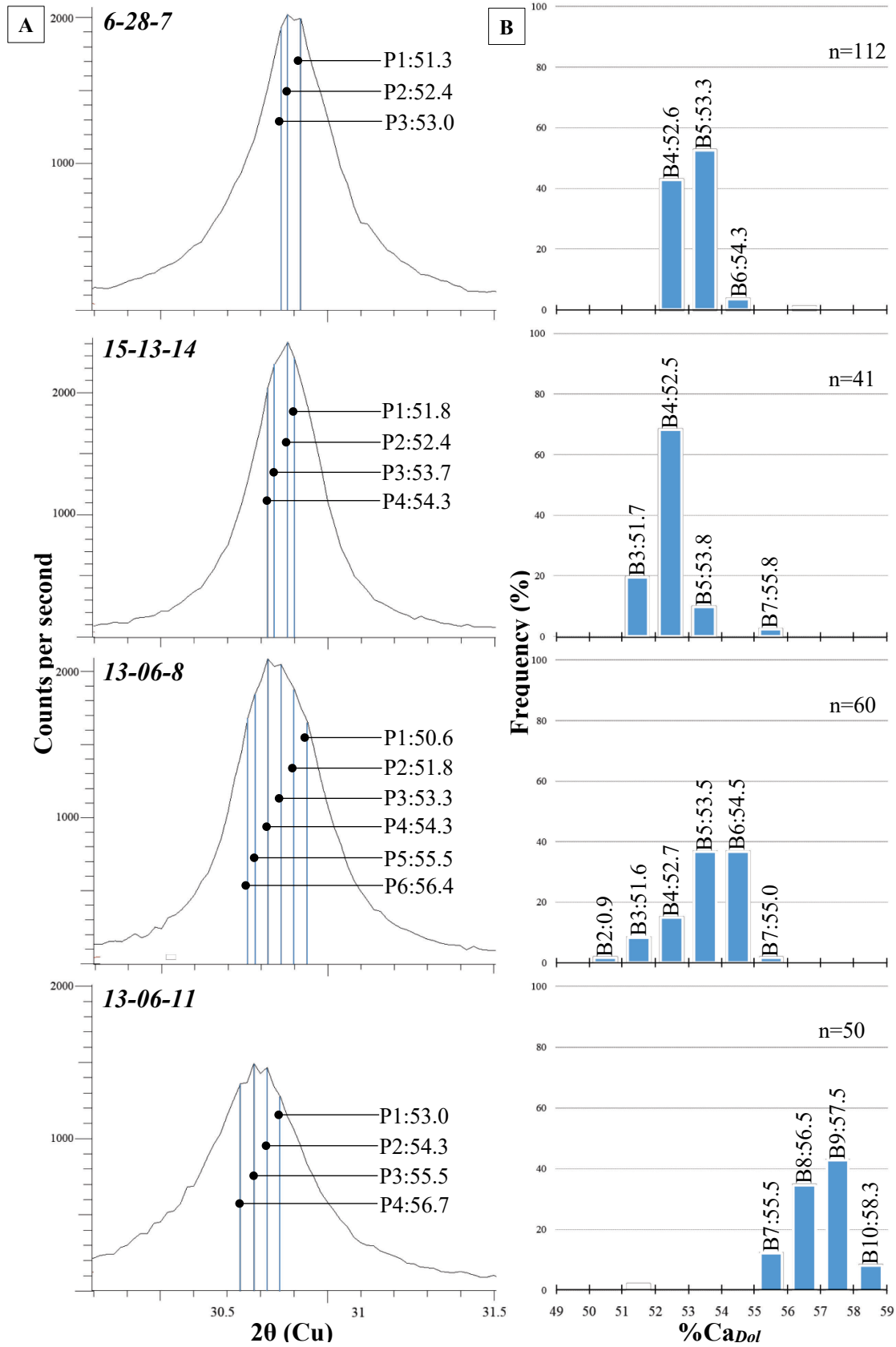
The frequency distribution of the EMPA data was plotted for each sample (Figure 5.20B). Each bin represents a different %Ca<sub>Dol</sub> population (Bin in Table 5.3, “B” in Figure 5.20B). The arithmetic mean of each bin was compared to the probable correlative %Ca<sub>Dol</sub> population (from XRD data) represented by sub-peaks and humps recorded in each diffractogram (blue vertical lines in Figure 5.20A). The calculated difference of %Ca<sub>Dol</sub> (arithmetic mean) between EMPA and XRD is 0.5 %Ca. As result, the difference between EMPA and XRD data from Indiana University laboratory is considered negligible.

This affirmation is additionally confirmed by the strong positive correlation ( $R^2=0.7$ ) between the %Ca<sub>Dol</sub> (EMPA data) versus the  $d_{104}$  spacing (calculated from XRD data using equation 2) (Figure 5.21). As result, the XRD data from Indiana University laboratory is considered the base of reference between the University of Alberta and Western Michigan University laboratories.

	XRD			EMPA			$\Delta$
	Subpeak	$d_{104}$ (2 $\theta$ )	%Ca <sub>Dol</sub>	Bin	n	%Ca <sub>Dol</sub>	EMPA-XRD
6-28-7	P1	30.92	51.22	B4	48	52.6	1.4
	P2	30.88	52.43	B5	60	53.3	0.9
	P3	30.86	53.04	B6	4	54.3	1.3
15-13-14	P1	30.90	51.83	B3	8	51.7	-0.1
	P2	30.88	52.43	B4	28	52.5	0.1
	P3	30.84	53.65	B5	4	53.8	0.1
	P4	30.82	54.27	B7	1	55.8	1.5
13-06-8	P1	30.94	50.61	B2	1	50.9	0.3
	P2	30.90	51.83	B3	5	51.6	-0.2
	P3	30.85	53.35	B4	9	52.7	-0.6
	P4	30.82	54.27	B5	22	53.5	-0.7
	P5	30.78	55.49	B6	22	54.4	-1.1
	P6	30.75	56.41	B7	1	55.0	-1.4
13-06-11	P1	30.86	53.04	B7	6	55.5	2.5
	P2	30.82	54.27	B8	18	56.5	2.2
	P3	30.78	55.49	B9	22	57.5	2.0
	P4	30.74	56.72	B10	4	58.3	1.6

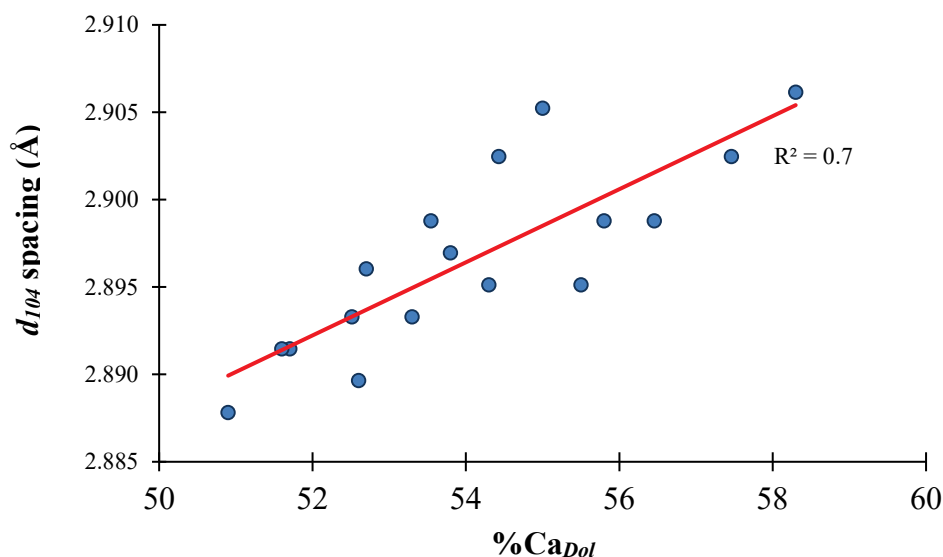
**Table 5.3:** Comparison of %Ca<sub>Dol</sub> values obtained from XRD (Indiana University) and EMPA. The difference of the %Ca between XRD and EMPA ( $\Delta$ ) was calculated taking as base of reference the values from EMPA data. EMPA-XRD arithmetic mean = 0.5.

Figure 5.20





**Figure 5.20:** Graphic comparison between the %Ca<sub>Dol</sub> values calculated from (A) XRD data and (B) EMPA data. (A) All samples show a split  $d_{104}$  peak with one or several humps, each of them possibly represent a different %Ca<sub>Dol</sub> population with a unique  $d_{104}$  at different  $2\theta$  value. Each  $d_{104}$  “subpeak” is represented by a blue line. The calculated value of %Ca<sub>Dol</sub> for each inferred population is indicated at the right side of each  $d_{104}$  “subpeak”. (B) %Ca<sub>Dol</sub> frequency distribution for each sample measured by EMPA. The %Ca<sub>Dol</sub> arithmetic mean for each population is indicated at the top of each bin.



**Figure 5.21:** Correlation between  $d_{104}$  (vertical axis) calculated from XRD data and %Ca<sub>Dol</sub> (horizontal axis) calculated from EMPA data. Red line: linear regression.

The Uteland Butte dolomites display a wide range of %Ca<sub>Dol</sub>, from 49% to 59%. The %Ca<sub>Dol</sub> distribution for each PZ layer is shown in Figure 5.22. Each dolomite layer displays a different frequency distribution. PZ1 has a multimodal %Ca<sub>Dol</sub> distribution with the near stoichiometric mode between 49 and 52 %Ca<sub>Dol</sub> (14%), followed by a strong mode between 53 and 55 %Ca<sub>Dol</sub> (83%), and a third mode between 58 and 59 %Ca<sub>Dol</sub> (3%). PZ1' displays a multimodal % Ca<sub>Dol</sub> distribution with three different modes: a near stoichiometric mode between 51 and 54 %Ca<sub>Dol</sub> (65%), a second mode between 55 and 56 %Ca<sub>Dol</sub> (23%), and a third one between 57 and 58 %Ca<sub>Dol</sub> (12%). In contrast, PZ2 describes a bimodal distribution with a

broad mode between 51 and 55 %Ca<sub>Dol</sub> (85%) and a second mode between 56 and 58 %Ca<sub>Dol</sub> (15%) (Figure 5.22).

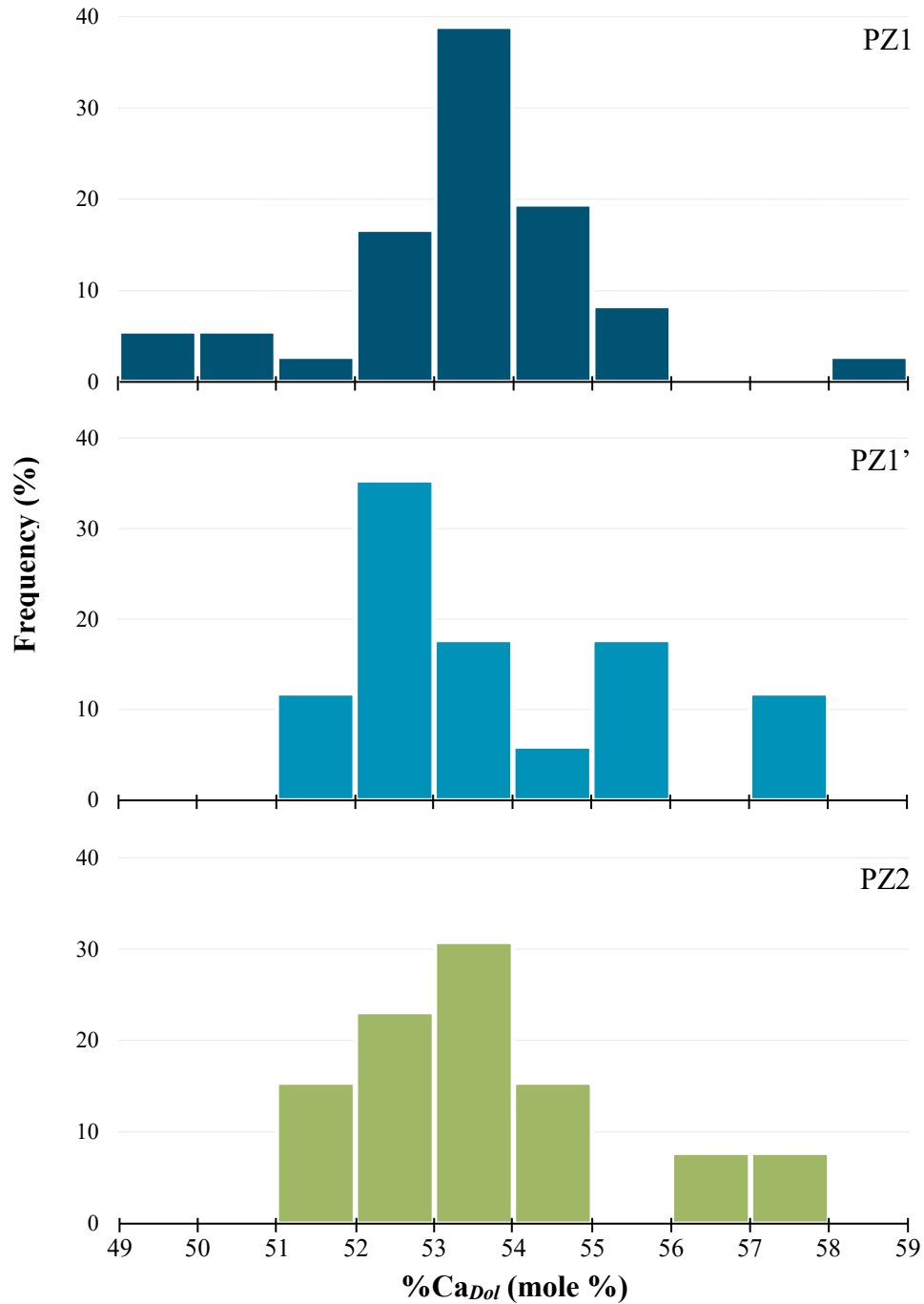


**Figure 5.22:** Frequency distribution of calcium mole percentage in dolomite crystals (%Ca<sub>Dol</sub>) for each PZ layer. %Ca<sub>Dol</sub> calculated by mean of the equation by Lumsden (1979).

Combining all data, the dolomites form two major populations: (i) Population 1 (POP1%Ca) varies in a wide range from 49 to 56 %Ca<sub>Dol</sub>, and (ii) Population 2 (POP2%Ca) ranges from 56 to 59 %Ca<sub>Dol</sub> (Figure 5.23). POP1%Ca contains 92% of all data. These dolomites are calcium-rich (or calcian) dolomites according to the Gregg et al. (2015) definition.

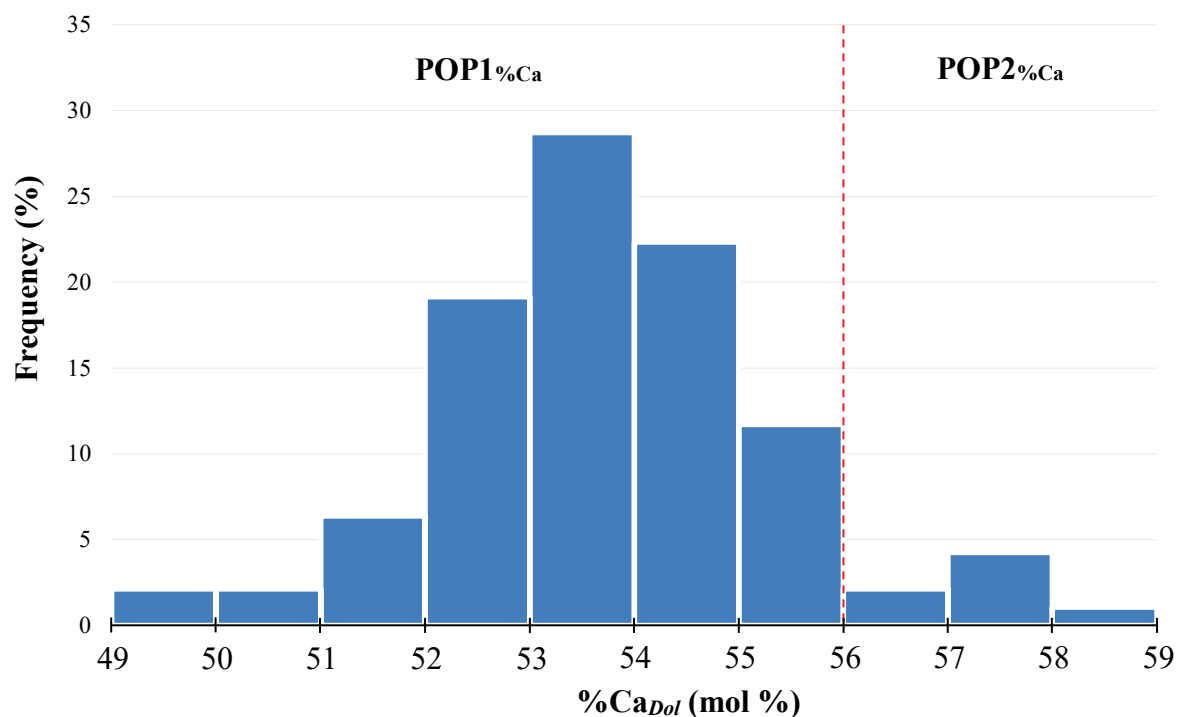


**Figure 5.23:** %Ca<sub>Dol</sub> populations. POP1%Ca fluctuates between 49 to 56.5 %Ca and POP2%Ca fluctuates between 56.5 to 59 %Ca. POP1%Ca is the most abundant (92%).

Calcium excess in dolomite crystals also displays a vertical trend in which the more stoichiometric dolomite are located preferentially at the tops of the PZ layers, whereas the non-stoichiometric dolomite crystals are preferentially located at the bases of the PZ layers (Figure 5.24). This trend is clearly defined in the PZ1 layer, well PW 13-06, in which there is a strong correlation between %Ca<sub>Dol</sub> and depth ( $R^2=0.8$ ) (Figure 5.25).

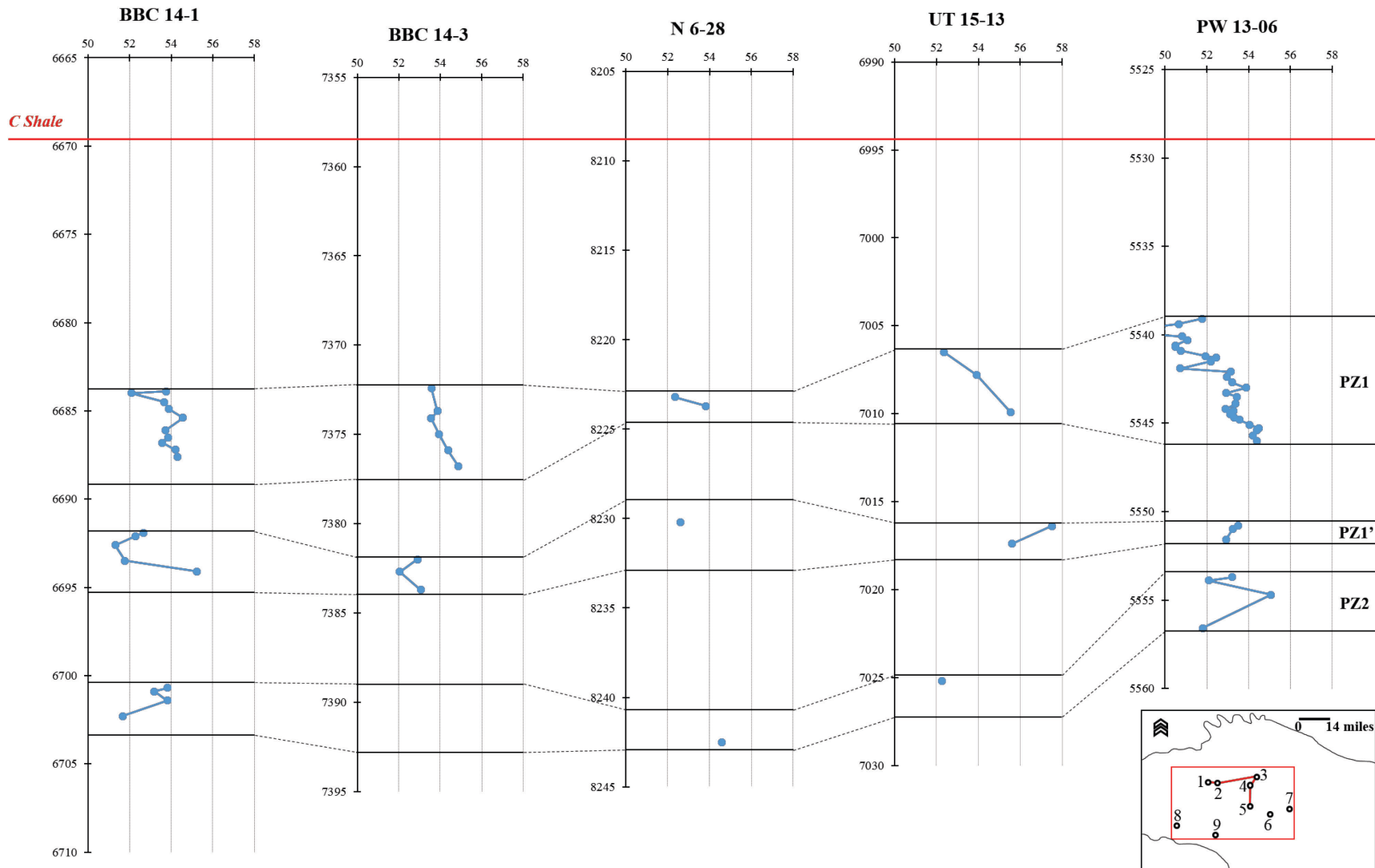


**Figure 5.24:** Dolomite stoichiometry variation in depth; horizontal axis:  $\%Ca_{Dol}$  (%), vertical axis: depth (ft). See map inset for well locations; numbers in the inset map stand for wells/outcrops as 1: BBC 14-1, 2: BBC 14-3, 3: N 6-28, 4: UT 15-13, 5: PW 13-06, 6: DS 11-20, 7: UI 16, 8: WCC, and 9: NMC.

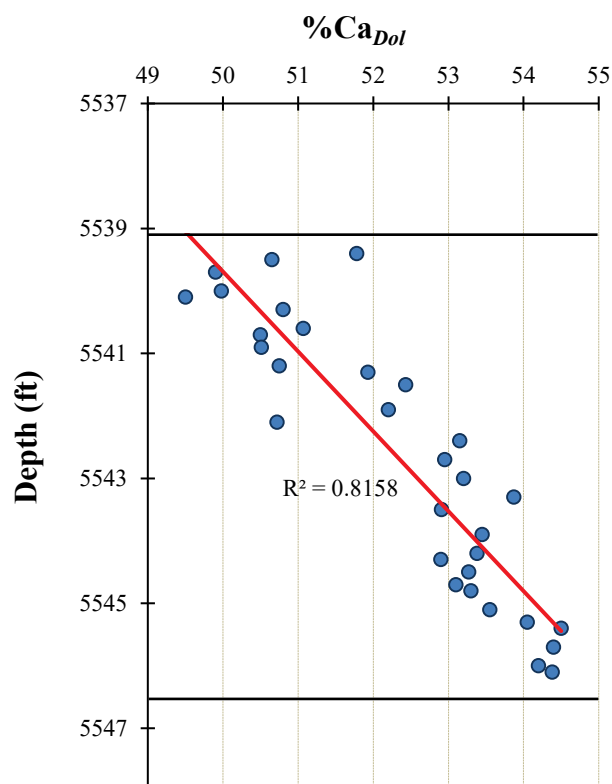


**Figure 5.25:** %Ca<sub>Dol</sub> variation with depth. Data for PZ1 layer, well PW 13-06. Black horizontal lines: top and base of the PZ layer, red line: linear regression.

### 5.2.1.5 Ordering

The XRD diffractogram also offers information on dolomite cation ordering characteristics. Goldsmith and Graf (1958) defined a calcium-magnesium bearing carbonate mineral as dolomite if the crystal displays  $d_{110}$ ,  $d_{015}$ , and  $d_{021}$  ordering peaks relative to the 100% of  $d_{104}$  dolomite peak. The degree of cation ordering was calculated according to the Goldsmith and Graf's (1958) definition ( $d_{015} / d_{101}$ ).

Intensities of  $d_{015}$  and  $d_{101}$  peaks were obtained from XRD data. Dolomites are thus characterized by low cation ordering values varying from 0.1 to 0.5, with a mean of 0.27 and standard deviation of 0.03 (Table 5.4). The dolomite cation ordering and %Ca<sub>Dol</sub> relationship

shows a trend, in which the highest cation ordering values ( $>0.3$ ) are from nearly stoichiometric dolomites (49 to around 54 %Ca), whereas the lowest cation ordering values (0.1 to 0.3) are from calcium-rich dolomite (around 54 to 58 %Ca) (Figure 5.26).

Well	PZ	Ordering		
		Mean	St.Dev	n
BBC 14-1	PZ1	0.21	0.05	10
	PZ1'	0.34	0.06	5
	PZ2	0.28	0.06	4
BBC 14-3	PZ1	0.21	0.01	6
	PZ1'	0.25	0.03	3
N 6-28	PZ1	0.27	0.03	2
	PZ1'	0.30		1
	PZ2	0.24		1
UT 15-13	PZ1	0.29	0.08	3
	PZ1'	0.24		1
	PZ2	0.33		1
PW 13-06	PZ1	0.32	0.09	12
	PZ1'	0.25	0.03	3
	PZ2	0.33	0.03	3
DS 11-20	PZ1	0.27		1
	PZ1'	0.22		1
	PZ2	0.20		1
I16	PZ1	0.23	0.03	2
	PZ1'	0.27	0.00	2
	PZ2	0.24	0.04	2

**Table 5.4:** Cation ordering and %Ca<sub>Dol</sub> by well and PZ layer (n = 64). Data from XRD.

Ordering also varies with depth in which the more ordered dolomites are located at the tops of the PZ layers, whereas the disordered dolomites are preferentially located at the bases of the PZ layers. This trend is also well defined in the PZ1 layer, well PW 13-06, in which there is a strong correlation between ordering and depth ( $R^2=0.7$ ) (Figure 5.27).



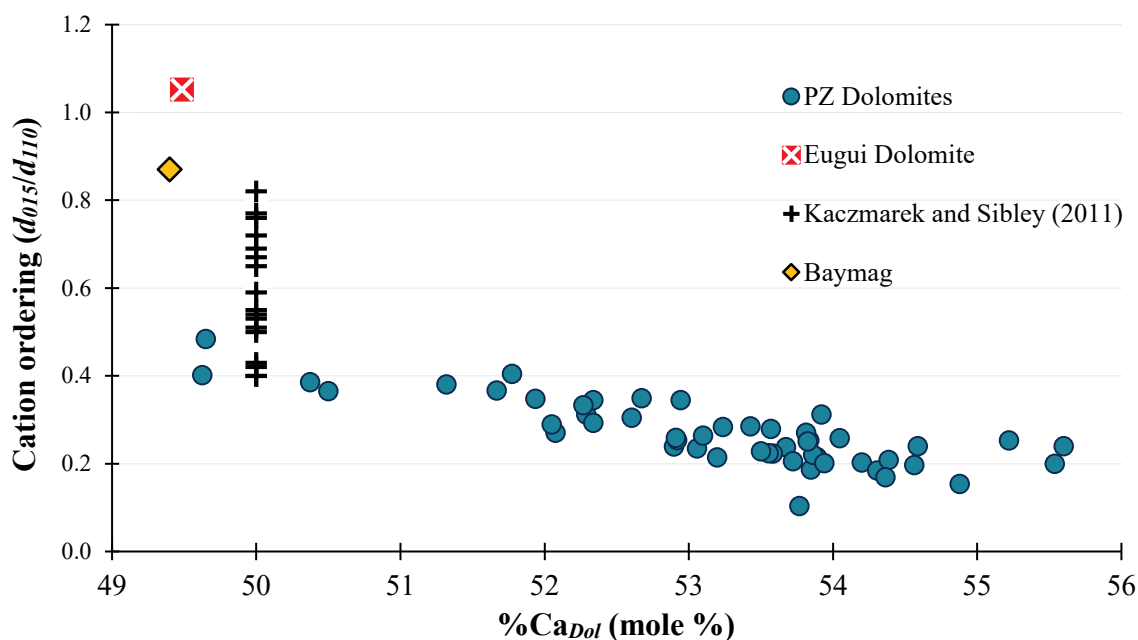


**Figure 5.26:** Correlation between cation ordering and %Ca<sub>Dol</sub> populations for all PZ layers combined. Baymag dolomite, synthetic dolomites (Kaczmarek and Sibley, 2011), and Eugui dolomite ([www.ruff.info](http://www.ruff.info)) values plotted as reference.

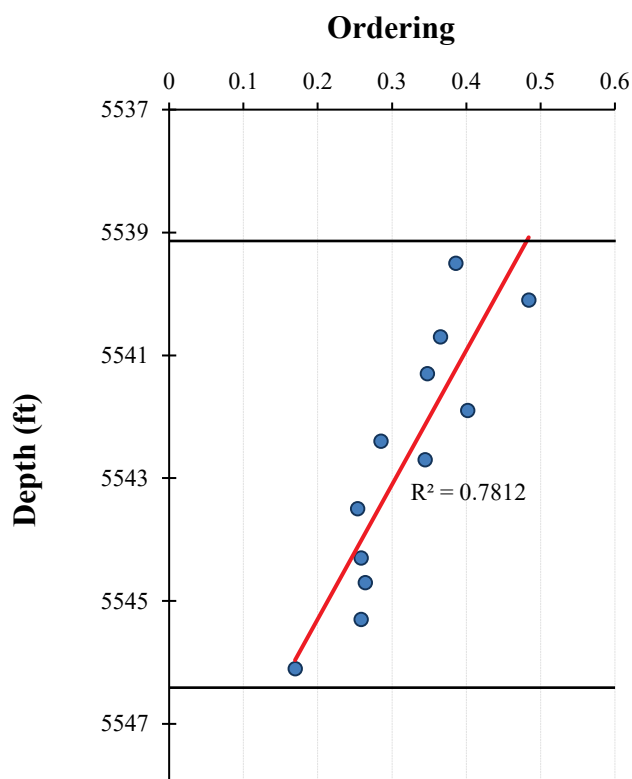


**Figure 5.27:** Ordering variation with depth. Data for PZ1 layer, well PW 13-06. Black horizontal lines: top and base of the PZ layer, red line: linear regression.

### 5.2.1.6 Conventional carbon and oxygen isotope data

The carbon and oxygen isotope values for all dolomite PZ layers display a wide spectrum.  $\delta^{13}\text{C}$  of dolomite ( $\delta^{13}\text{C}_{Dol}$ ) varies from 6.0‰ to -5.2‰ relative to Vienna Pee Dee Belemnite (VPDB), and  $\delta^{18}\text{O}$  of dolomite ( $\delta^{18}\text{O}_{Dol}$ ) varies from 0.9‰ to -10.4‰ (VPDB). In contrast, carbon and oxygen isotopic values for the selected limestone samples show smaller ranges:  $\delta^{13}\text{C}$  of calcite ( $\delta^{13}\text{C}_{Cal}$ ) varies from -1.0‰ to 1.0‰ (VPDB), and  $\delta^{18}\text{O}$  of calcite ( $\delta^{18}\text{O}_{Cal}$ ) varies from -10.1‰ to -5.8‰ (VPDB). Table 5.5 shows the summary of the isotopic composition for each dolomite layer and limestone samples.

Layer	Mineral	$\delta^{13}\text{C}$ (VPDB)			$\delta^{18}\text{O}$ (VPDB)		
		Values (‰)	Range	Mean	Values (‰)	Range	Mean
PZ1	Dolomite	-5.4 to 4.8	10.2	1.8	-7.3 to 0.9	8.2	-2.6
PZ1'	Dolomite	-3.3 to 5.2	8.5	1.5	-6.2 to 0.1	6.3	-3.0
PZ2	Dolomite	-1.1 to 6.0	7.1	1.3	-6.0 to -0.7	5.3	-3.3
Limestone	Calcite	-1.0 to 1.0	2.0	-0.3	-10.1 to -5.8	4.3	-7.7

**Table 5.5:** Isotopic signatures for PZ layers and interbedded limestone layers.

Assuming isotopic equilibrium, the broad  $\delta^{13}\text{C}_{Dol}$  distribution can be separated in two groups: (i) a set of  $\delta^{13}\text{C}_{Dol}$  values depleted by 1‰ to 6‰ relative to  $\delta^{13}\text{C}_{Cal}$  (left arrow Figure 5.28), and (ii) a set of  $\delta^{13}\text{C}_{Dol}$  values enriched by 1‰ to 6‰ relative to  $\delta^{13}\text{C}_{Cal}$  (right arrow Figure 5.28).

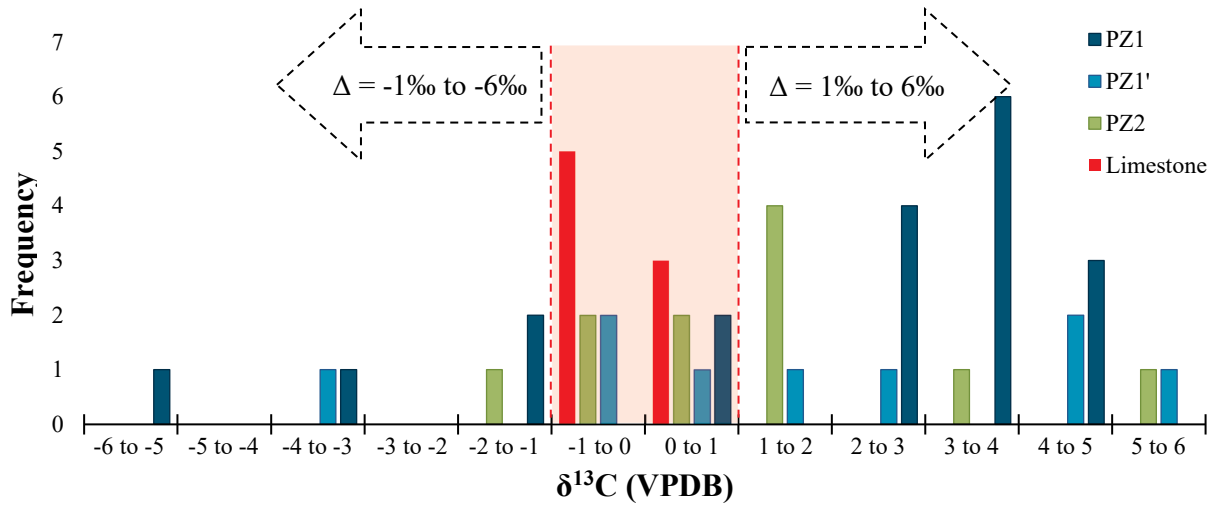


**Figure 5.28:**  $\delta^{13}\text{C}$  frequency distribution for dolomites (all PZ dolomite layers) and calcites (interbedded limestones).

The  $\delta^{18}\text{O}_{Dol}$  values are generally significantly less depleted than those from the limestones (Figure 5.29). Moreover, dolomites of PZ1 display the highest  $\delta^{18}\text{O}_{Dol}$  mean value (-2.6‰ VPDB), whereas dolomites in PZ2 show the lowest  $\delta^{18}\text{O}_{Dol}$  mean value (-3.4‰ VPDB). However, the  $\delta^{18}\text{O}_{Dol}$  values range of the PZ1 is broader (8.2‰) than those from PZ2 (5.3‰).

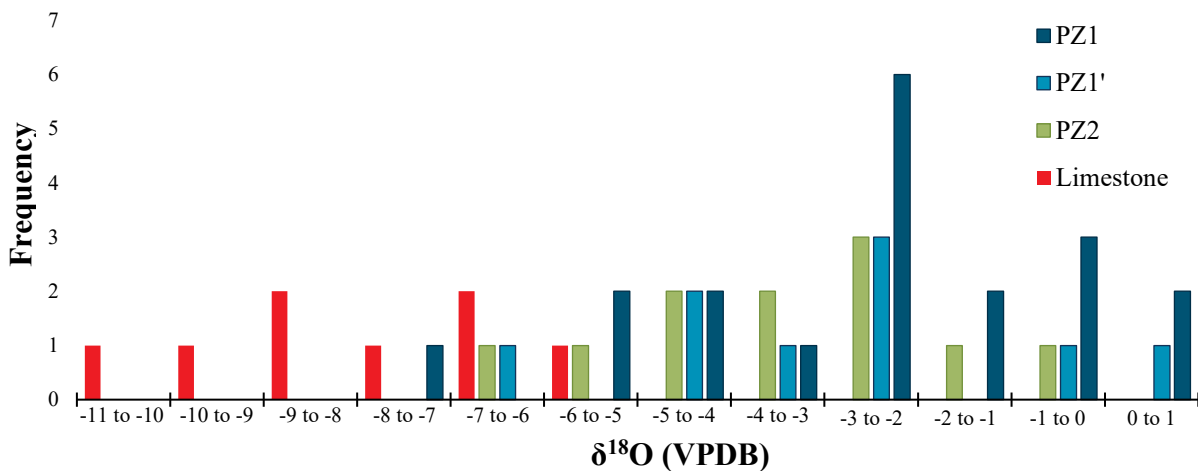


**Figure 5.29:**  $\delta^{18}\text{O}$  frequency distribution of dolomite (all PZ dolomite layers) and calcite (interbedded limestone).  $\delta^{18}\text{O}_{Dol}$  increment from parental  $\delta^{18}\text{O}$  calcite from -5‰ and 1‰ (VPDB).

### 5.2.1.7 Clumped-isotopes thermometry

A different method for determining the temperature of dolomitization is from the clumped-isotopes technique. According to this method, the calculated temperature of dolomite formation varies from 30 to 59 °C. Furthermore, the calculated temperature of calcite formation is higher than dolomite temperature and varies from 79 to 84 °C (Table 5.6).

Sample	Depth	Litho	PZ Layer	%Dol	$\delta^{13}\text{C}$ (VPDB)	$\delta^{18}\text{O}$ (VPDB)	$\Delta_{47}$	T (°C)
13-06-5	5537.3	L		1.8%	-0.46 -0.51	-9.74 -9.77	0.555	79
13-06-7	5541.9	D	PZ1	100%	3.30 3.31 3.30	-4.54 -4.43 -4.37	0.679	30
13-06-12	5557.4	D	PZ2	100%	1.34	-4.60	0.599	59
6-28-1	8199.3	D		100%	0.55 0.58	-2.39 -2.36	0.609	55
6-28-7	8230.2	D	PZ1'	100%	4.57 4.56	-2.30 -2.22	0.627	48
6-28-8	8234.6	L		5.3%	0.72 0.72	-10.40 -10.36	0.545	84

**Table 5.6:** Calculated dolomitizing fluid temperature (T) for PZ layers in wells PW 13-06 and N 6-28. Litho: Lithology, L: Limestone, D: Dolostone, %Dol: Dolomite percentage in the carbonate fraction.

### 5.2.1.8 Elemental compositions

The major elements Ca and Mg and the trace elements Na, Al, Fe, Mn, Si, Zn, Sr, and Pb were measured in 43 dolomite samples (from dolostones) and seven calcite samples (from limestones). The Na, Al, Fe, Mn, Si, Zn, Sr, and Pb concentration values are presented graphically in Figure 5.30 and tabulated in Appendix 7.

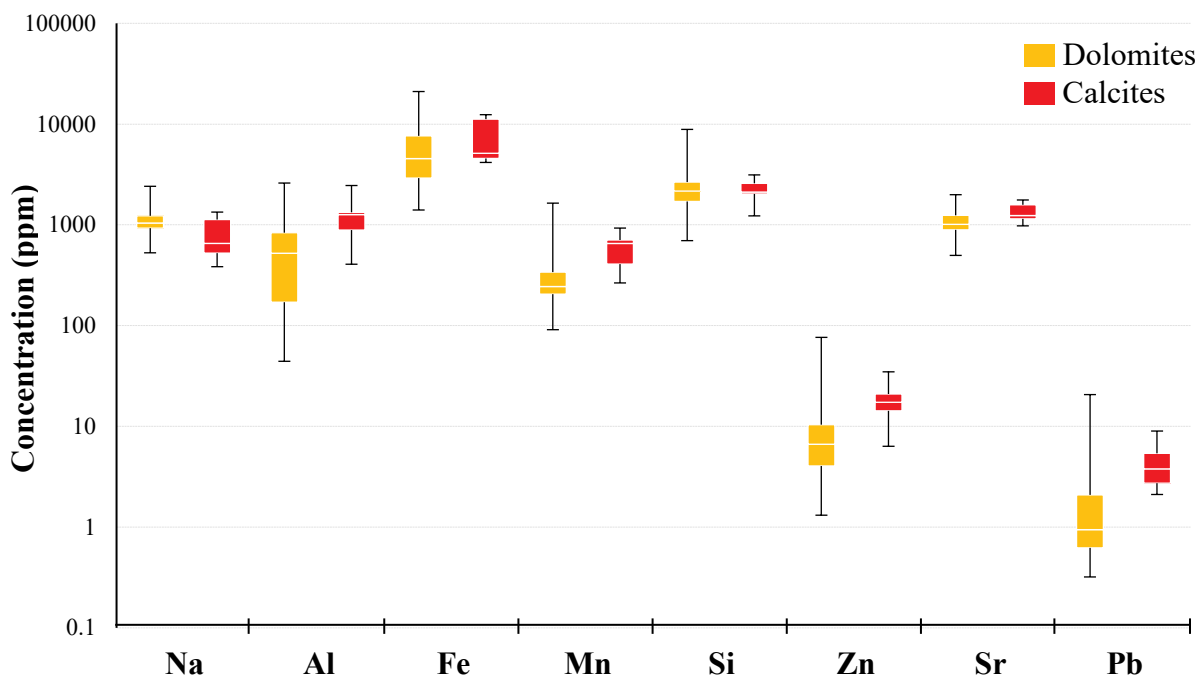


**Figure 5.30:** Elemental compositions of dolomites and calcites.

*Sodium:* Dolomites have higher Na values than calcites. Dolostones values range from 528 to 2412 ppm (average 1113 ppm), and calcite values range from 348 to 1338 ppm (average 812 ppm) (Figure 5.30). Furthermore, the higher Na values are located toward the near shore area (Figure 5.31A).

*Strontium:* Dolomites show lower Sr values than calcites. Dolomites values range from 497 to 1991 ppm (average 1092 ppm), and calcites values range from 977 to 1765 ppm (average 1348 ppm) (Figure 5.30). There is an Sr trend in which the highest values are located toward the centre of the basin in wells N 6-28, UT 15-13, and PW 13-06 (Figure 5.31B).

*Iron:* Dolomites have lower Fe values than calcites. Dolostones values range from 1404 to 21044 ppm (average 5861 ppm), and calcites values range from 4162 to 12397 ppm

(average 7598 ppm) (Figure 5.30). There is no discernible geographical distribution for Fe (Figure 5.31C).

*Manganese:* Dolomites have lower Mn values than calcites. Dolomites values range from 91 to 1642 ppm (average 322 ppm), and calcite values range from 265 to 929 ppm (average 583 ppm) (Figure 5.30). There is no discernible geographical distribution for Fe (Figure 5.31D).

*Aluminium:* Dolomites have relatively lower Al values than calcites. Dolomites values range from 44 to 2599 ppm (average 664 ppm), and calcite values range from 407 to 2456 ppm (average 1224 ppm) (Figure 5.30). Furthermore, there is an Al trend in which the higher values are located toward the near shore area (Figure 5.32A).

*Silicon:* Dolomites have around the same Si values as calcites. Dolomites values range from 697 to 8856 ppm (average 2475 ppm), and calcites values range from 1227 to 3131 ppm (average 2241 ppm) (Figure 5.30). There is no discernible geographical distribution for Si (Figure 5.32B).

*Zinc:* Dolomites show lower Zn values than calcites. Dolomites values range from 1.3 to 76.4 ppm (average 12.09 ppm), and calcites values range from 6.3 to 34.8 ppm (average 18.4 ppm) (Figure 5.30). There is no discernible geographical distribution for Zn (Figure 5.32C).

*Lead:* Dolomites show lower Pb values than calcites. Dolomites values range from 0.32 to 20.67 ppm (average 2.12 ppm), and calcites values range from 2.11 to 8.98 ppm (average 4.45 ppm) for calcite (Figure 5.30). There is no discernible geographical distribution for Zn (Figure 5.32D).



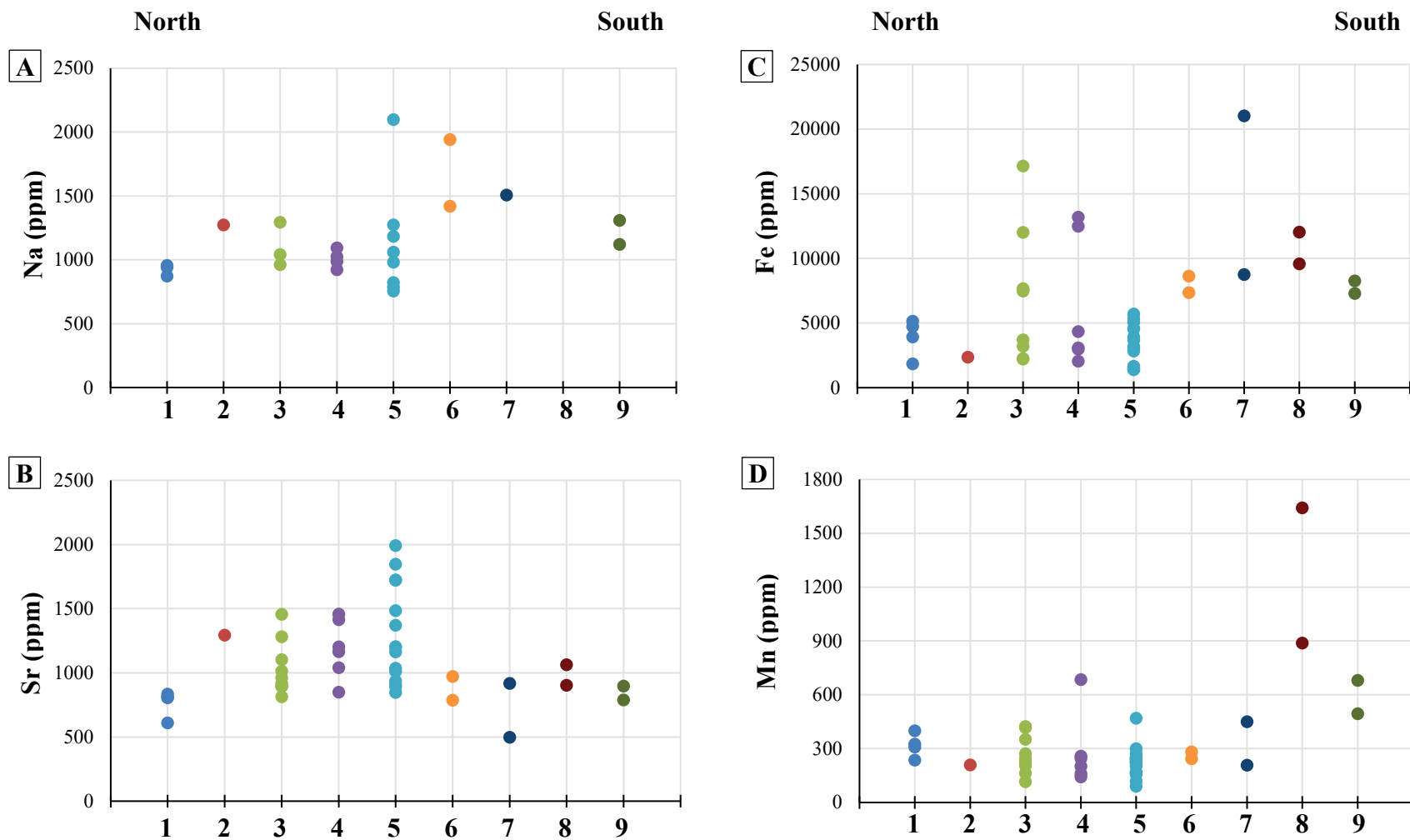


**Figure 5.31:** Na, Sr, Fe, and Mn concentration in dolomites and geographical distribution. Numbers in the horizontal axis stand for wells/outcrops as; 1: BBC 14-1, 2: BBC 14-3, 3: N 6-28; 4: UT 15-13; 5: PW 13-06; 6: DS 11-20; 7: I 16; 8: WCC; 9: NMC.

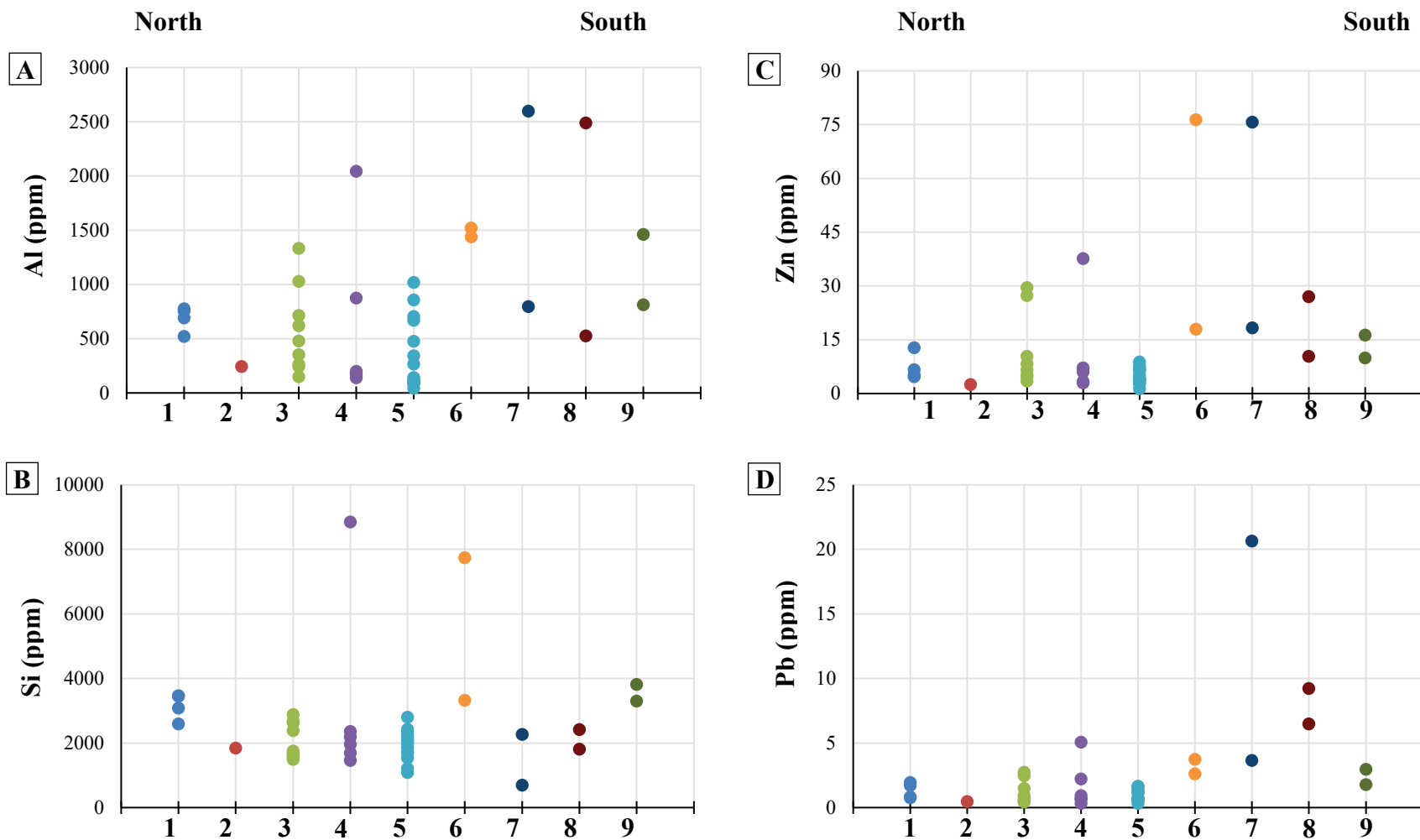


**Figure 5.32:** Al, Si, Zn, and Pb concentration in dolomites and geographical distribution. Numbers in the horizontal axis stand for wells/outcrops as; 1: BBC 14-1, 2: BBC 14-3, 3: N 6-28; 4: UT 15-13; 5: PW 13-06; 6: DS 11-20; 7: I 16; 8: WCC; 9: NMC.

## **5.2.2 Interpretations**

### **5.2.2.1 Crystal shapes**

Proper identification of dolomite texture and crystal size is very important for making interpretations about dolomitizing fluid characteristics (Machel, 2004; Warren, 2000; Sibley and Gregg, 1987; Gregg and Sibley, 1984). The coexistence of planar-e, planar-s, and nonplanar-a textures suggests either a variation over time in the composition of the dolomitizing fluid (Sibley and Gregg, 1987), or a different dolomitization phases, each from different fluid (Sibley and Gregg, 1987; Machel 2004), or inheritance of crystal size variations from the lime(stone) precursors.

Sibley and Gregg (1987) recognized that the crystal shapes of dolomite correlate with supersaturation of the dolomitizing fluids and with the temperature of dolomitization. Straight crystal faces in planar-e dolomite commonly tend to develop at “low supersaturation and/or low temperatures” (Sibley and Gregg, 1987, p. 968). In contrast, nonplanar-a textures tend develop from highly supersaturated fluids and/or at “high” temperatures (Sibley and Gregg, 1987), for example, at temperatures higher than the so-called “critical roughening temperature”, which is around 50 to 100 °C for dolomite (Sibley and Gregg, 1987).

Regional distribution of dolomite textures (Figure 5.14) can be interpreted to be the result of geographic variations of the chemical composition of the dolomitizing fluid. In nearshore areas, the fluid composition may have been only slightly supersaturated with respect to dolomite, leading to the development of mainly planar-e textures, whereas in the intermediate zone between the nearshore and basin center areas the dolomitizing fluid was probably more

highly supersaturated, thus creating planar-s textures. However, more data must be acquired to confirm this interpretation.

#### **5.2.2.2 Crystal size**

Dolomite crystal sizes and populations offer important information about the history of diagenesis related to dolomitization events or recrystallization. Dolomite crystal size populations may be inherited or controlled by the crystal sizes of the precursor limestone, by recrystallization of metastable dolomite precursor mineral phases, or by different dolomitization events (Sibley and Gregg, 1987; Sibley et al., 1993; Machel, 2004).

The right-skewed dolomite crystal size distribution (Figure 5.16) probably was created by recrystallization, which involves an increase of crystal size (Gregg, and Shelton, 1989; Gregg et al., 1992; Sibley et al., 1983). This is likely the case of the dolomite in all PZ layers, in which the original crystal size was modified from small crystals size (POP1 and POP2) to larger crystals size (POP3).

#### **5.2.2.3 Cathodoluminescence**

According to Machel et al. (1991), luminescence in the carbonate minerals is the emission of light (photons) from certain elements (mainly  $\text{Mn}^{2+}$ , Rare Earth Elements, and  $\text{Pb}^{2+}$ ). Photon emission is produced when an external source of energy (such as an electron beam) excites an electron, moving it toward a higher energetic band. When the excited electrons

lose energy, they return to lower energy levels and release energy difference as photons (Boggs and Krinsley, 2006).

The lack of luminescence in the dolomite crystals of this study can be attributed to either or both of the following:

- (i) Low concentrations of activator  $\text{Mn}^{2+}$  and sensitizer  $\text{Pb}^{2+}$  elements (Machel, 1985; Machel and Burton, 1991; Machel, 2000) coupled with a high concentration of quencher  $\text{Fe}^{2+}$ . Machel (1995) indicates that luminescence is related to the activator-sensitizer and quenchers concentration ratio up to the point that high concentrations of  $\text{Fe}^{2+}$  (principal quencher) may constrain luminescence behaviour. To identify luminescence using a standard luminescence microscope, Machel (2000) suggests a minimum concentration of 10 to 20 ppm for  $\text{Mn}^{2+}$  coupled with a concentration of 150 ppm for  $\text{Fe}^{2+}$  ( $\text{Mn}/\text{Fe} = 0.1$ ). A higher  $\text{Fe}^{2+}$  concentration creates a lower Mn/Fe ratio, which quenches luminescence. The Mn/Fe ratio was calculated from EMPA data with a value of 0.05, and from ICP-MS data with a value of 0.06. The low Mn/Fe ratio likely is the reason for the absence of cathodoluminescence.
- (ii) A later recrystallization event that destroyed the initial activator-sensitizer and quenchers zonation (Machel, 2000).

#### 5.2.2.4 Stoichiometry

Dolomite calcium percentages can be related to environments of dolomitization (Lumsden and Chimahusky, 1980; Searl, 1994; Gregg et al, 1992). In general, evaporitic settings correlate with nearly stoichiometric dolomites (50 - 52 % $\text{Ca}_{\text{Dol}}$ ) and non-evaporitic settings correlate with non-stoichiometric dolomites (55 - 56 % $\text{Ca}_{\text{Dol}}$ ). However, a potential

recrystallization event, which is probably reflected by the left-skewed CSD (Figure 5.16), might have altered the original %Ca<sub>Dol</sub> chemical signature (Mazzullo, 1992; Machel, 1997; Gregg, et al., 2015) from non-stoichiometric dolomite (POP2%Ca) to nearly stoichiometric dolomite (POP1%Ca).

#### 5.2.2.5 Ordering

Based on experimental data (synthetic dolomite), Kaczmarek and Sibley (2011) concluded that dolomite cation ordering and stoichiometry characteristics are related to parental fluid composition. They argue that the more supersaturated dolomitizing fluid is, the higher the Mg content in dolomite, despite variable dolomite cation ordering. Some of the synthetic dolomite crystals resulting from the Kaczmarek and Sibley experiments are plotted in Figure 5.26. These dolomite crystal series precipitated from supersaturated fluids (Mg/Ca molar ratio  $\geq 1$ ) with a wide range of cation ordering from about 0.4 to 0.8 (Figure 5.26).

Cation ordering values are relatively low ( $0.27 \pm 0.07$ ) compared to those of ideal dolomite ( $\sim 0.87$  in Figure 5.26 for Baymag dolomite). According to Kaczmarek and Sibley (2011), the first replacement phase during dolomitization (very high magnesium calcite or protodolomite) invariably displays very low degree of cation ordering. If these metastable phases are allowed to recrystallize over time, they assume increasingly higher degrees of ordering (and lower Ca<sup>2+</sup> excess). Hence, it is reasonably inferred that the observed ranges in cation ordering represents various “stages” of progressive recrystallization, which did not go to completion, except for the nearly stoichiometric dolomites in POP1%Ca.

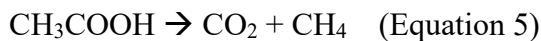
#### 5.2.2.6 Conventional carbon and oxygen isotope data

Environmental interpretations are based on calcite and dolomite isotopic composition relationships. The reference for interpretation of dolomite formation is the  $\delta^{13}\text{C}$  and  $\delta^{18}\text{O}$  values of the calcite (matrix) of the limestones. This assumption is valid only if the calcite (matrix) in limestone did not undergo recrystallization.

$\delta^{13}\text{C}$  values of calcite ( $\delta^{13}\text{C}_{\text{Cal}}$ ) are close to the Vienna Pee Dee Belemnite standard with a narrow variation ( $\pm 1\text{‰}$  PDB) (Figure 5.28). Assuming isotopic equilibrium, this value can be taken to represent the dissolved organic carbon of the lake water ( $\text{DIC}_w$ ).

On the other hand, the  $\delta^{13}\text{C}_{\text{Dol}}$  enrichment (from 1‰ to 6‰ PDB, Figure 5.28) is interpreted to have resulted from one or both of the following two processes:

- (i) A  $\delta^{13}\text{C}_{\text{Dol}}$  enrichment can be caused by high organic activity. In this process organisms preferentially take up  $^{12}\text{C}$ , which increases the  $\delta^{13}\text{C}$  values of the  $\text{DIC}_w$ . Consequently, dolomite formed in isotopic equilibrium with the lake water has elevated  $\delta^{13}\text{C}_{\text{Dol}}$  values. This interpretation is supported by the total organic carbon (TOC) and S2 values in the dolomite PZ layers (Figure 5.33). In Well N 6-28, taken as representative of the other wells, there is a remarkable contrast between the limestone and dolomite PZ layers, in which the dolomite layers consistently have higher TOC and S2 values than the interbedded limestones. The dolomite layers reach the highest TOC values, expressed as wt% HC (see Figure 5.33).
- (ii) Organic matter decay may also play an important role in the  $\delta^{13}\text{C}_{\text{Dol}}$  enrichment. This process could be represented by Equation 5 (Irwin et al., 1977), in which the organic matter (acetate) is fermented to carbon dioxide and methane with a significant isotopic fractionation between the two products (e.g., Tucker and Wright, 1990).





According to Irwing and Curtis (1977), acetate fermentation releases  $\text{CO}_2$  with  $\delta^{13}\text{C}$  values around +15‰ PDB, while the concomitantly formed  $\text{CH}_4$  may have  $\delta^{13}\text{C}$  values around -50‰ PDB. Consequently, dolomite formed in isotopic equilibrium with  $\text{CO}_2$  from acetate fermentation may be significantly enriched in  $^{13}\text{C}$ , whereby the amount of enrichment depends on the relative proportions of  $\text{DIC}_w$  and  $\text{CO}_2$  from fermentation.

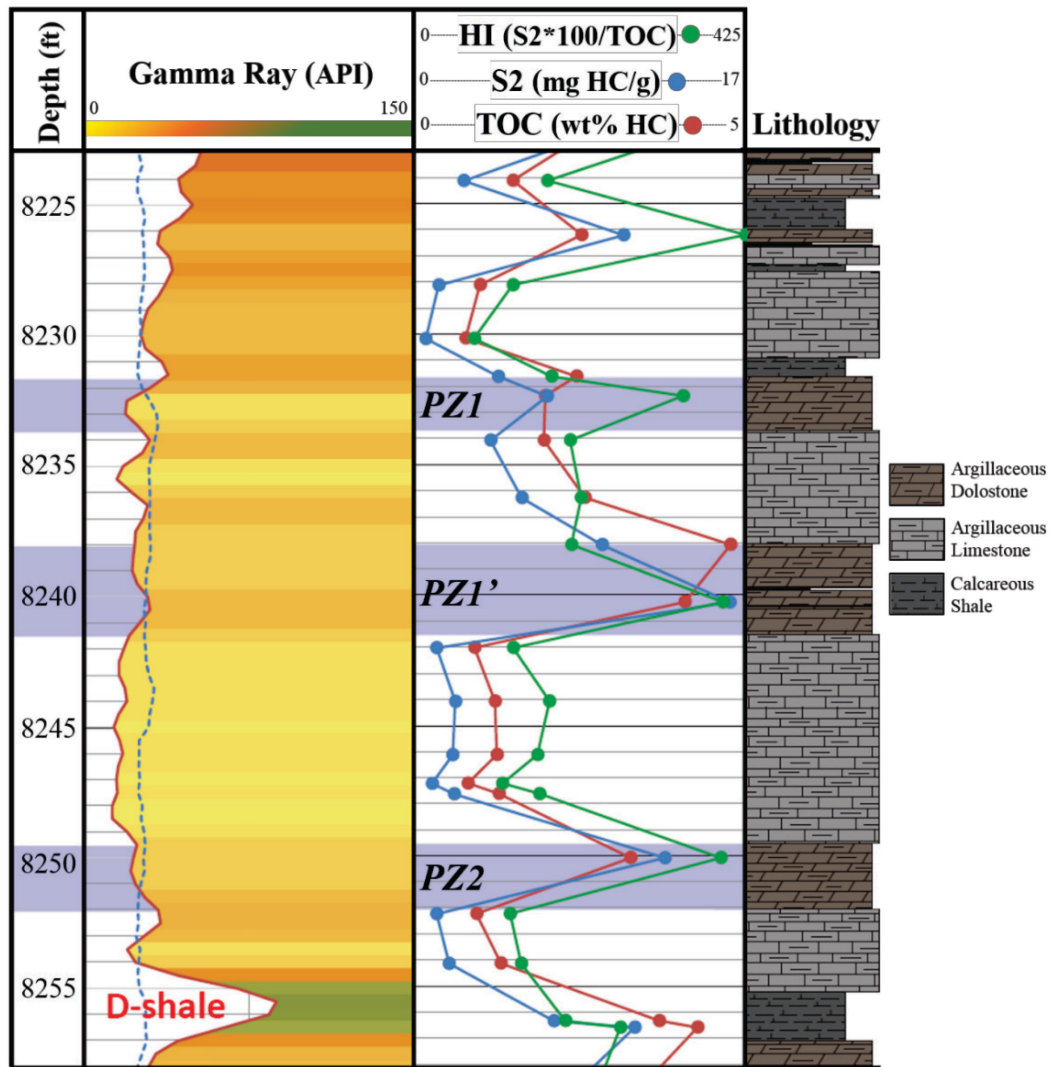
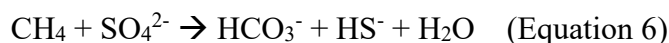


**Figure 5.33:** Total organic carbon (TOC) and S2 logs of well N 6-28. Dolomite PZ layers are highlighted in blue. Logs courtesy of Michael Vanden Berg, 2015.

In contrast, six samples have  $\delta^{13}\text{C}_{\text{Dol}}$  values significantly depleted relative to the calcite (Figure 5.28). This depletion is here interpreted as the result of organic matter oxidation as represented by Equations 6 and 7:



Biochemical methane ( $\text{CH}_4$ ) oxidation, as represented by Equation 6 (Tucker and Wright, 1990) and carbohydrates ( $2\text{CH}_2\text{O}$ ) oxidation by sulphate-reducing bacteria (Berner et al., 1985; Machel 2001) described by Equation 7 (Berner et al., 1985) leads to the simultaneous formation of  $^{13}\text{C}$ -depleted carbonates (from the  $\text{HCO}_3^-$ ) and pyrite (from the  $\text{HS}^-$ ) (Figure 5.34), if  $\text{Ca}^{2+}$ ,  $\text{Mg}^{2+}$  and  $\text{Fe}^{2+}$  are available. The carbohydrates oxidation process, products (Equation 7), and by-products are represented in Figure 5.34.

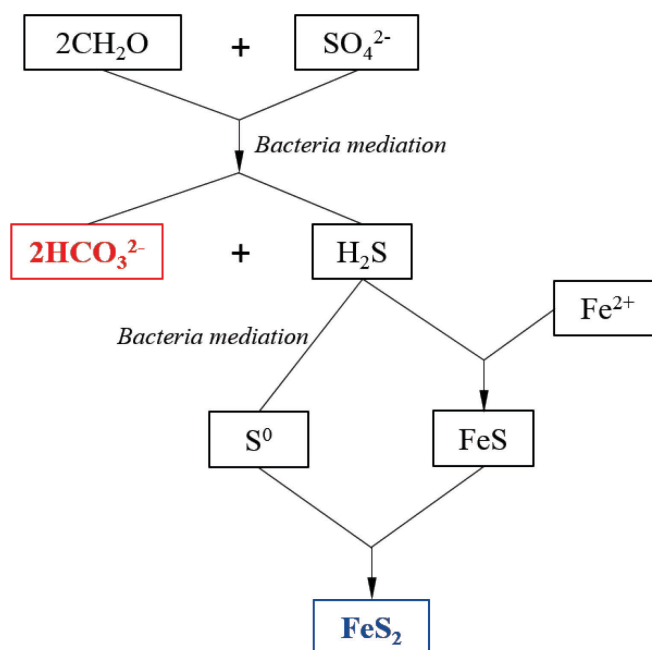


**Figure 5.34:** Idealized processes that may have created low  $\delta^{13}\text{C}$  values in dolomites: Oxidation of low  $\delta^{13}\text{C}$  organic matter [-25 to -30‰ PDB (e.g., Tucker and Wright, 1990; Machel 2001)] created  $^{13}\text{C}$ -depleted bicarbonate anions (red rectangle). Pyrite (blue rectangle) formed as by-product from the hydrogen sulfide and detrital iron ( $\text{Fe}^{2+}$  in lake water) reaction. Modified from Berner et al., 1985.

In either case (Equation 6 or 7), the source of oxygen is the dissolved sulfate ( $\text{SO}_4^{2-}$ ) present in the lake water. Tuttle and Goldhaber (1993), working in the depocenter area of the Uinta Basin, suggested that sulfate anions were supplied by river input and derived from weathering of Jurassic marine evaporite minerals. This interpretation is supported by the occurrence of framboidal pyrite crystals associated to the dolomite crystals (Figure 5.7F).

$\delta^{18}\text{O}$  values of dolomite ( $\delta^{18}\text{O}_{\text{Dol}}$ ) can provide information concerning the temperature of dolomite formation. The low  $\delta^{18}\text{O}_{\text{Cal}}$  values suggests that calcite crystallized in isotopic equilibrium from fresh lake water. This interpretation is supported by fossil associations presented in the limestone facies (F5). According to LaRocque (1956), the pelecypod and gastropod fossils recorded at the base of the GRF (correlated to the UBM) are fresh water mollusc species. Moreover, the wide range of the  $\delta^{18}\text{O}_{\text{Cal}}$  values (from -10.1 to -5.8‰ VPDB, mean: -7.7‰, range: 4.3‰) suggests fluctuations on fluvial inflow rates, variable degrees of rock-water interaction, or variable temperature during subsequent burial recrystallization, or a combination of all three processes/factors.

MacGinitie (1969) described the fossil floral record in the GRF and calculated the average temperature for the coldest months as 12 °C, with a minimum temperatures of about 3 °C. Assuming lake water temperatures from 3 °C to 12°C and precipitation in isotopic equilibrium, the oxygen isotopic composition of the lake water ( $\delta^{18}\text{O}_w$ ) might have fluctuated between -13.13‰ and -6.38‰ SMOW (Standard Mean Oceanic Water) (Table 5.7), with an arithmetic mean of  $-9.55 \pm 1.9\text{‰}$ .

Well	Sample	$\delta^{18}\text{O}_{\text{Cal}}$ (PDB)	$\delta^{18}\text{O}_w @ 3^\circ\text{C}$ (SMOW)	$\delta^{18}\text{O}_w @ 12^\circ\text{C}$ (SMOW)
BBC 14-1	14-1-19	-9.28	-12.27	-10.00
N 6-28	6-28-8	-8.02	-10.97	-8.71
PW 13-06	13-06-4	-8.39	-11.35	-9.09
PW 13-06	13-06-5	-7.48	-10.42	-8.16
PW 13-06	13-06-14	-10.11	-13.13	-10.86
PW 13-06	13-06-18	-6.42	-9.32	-7.06
DS 11-20	11-20-2	-6.47	-9.37	-7.11
I 16	16-5	-5.76	-8.64	-6.38

**Table 5.7:** Calculated  $\delta^{18}\text{O}$  of lake water ( $\delta^{18}\text{O}_w$ ) for calcite precipitation, assuming lake water temperatures between 3 °C and 12°C (MacGinitie, 1969).

The isotopic water composition was calculated using the temperature equation for the calcite–water system proposed by Friedman and O’Neil (1977) (Equation 8).

$$10^3 \text{Ln}\alpha = 2.78 * (10^6/T^2) - 2.89 \quad (\text{Equation 8})$$

A variation from the  $\delta^{18}\text{O}$  values of calcites to the higher  $\delta^{18}\text{O}$  values in dolomites (Figure 5.29) was probably caused by a combination of temperature increase and/or evaporation. During evaporation, the water composition is controlled by equilibrium and kinetic effects (Tucker and Wright, 1990; Gat, 1995; Davis et al., 2009). For the kinetic effect, the lighter water molecules ( $^1\text{H}^{16}\text{O}$ ) diffuse more easily to the atmosphere. For the equilibrium effect, the lighter water molecules have higher vapor-pressure values, which makes it easier for them to pass into the atmosphere. As a result, the lake water becomes enriched in D and  $^{18}\text{O}$ . Consequently, dolomite crystals that form in isotopic equilibrium with lake water are also enriched in  $^{18}\text{O}$ .

The water/fluid temperatures calculated for dolomitization are listed in Table 5.8, based on the measured  $\delta^{18}\text{O}$  of dolomites and the estimated  $\delta^{18}\text{O}$  isotopic composition, using

the dolomite-water system isotopic fractionation proposed by Sheppard and Schwarcz (1970) (Equation 9).

$$10^3 \text{Ln}\alpha = 3.23 * (10^6/T^2) - 3.29 \quad (\text{Equation 9})$$

Pitman (1996), working in the depocenter of the Uinta Basin, estimated the  $\delta^{18}\text{O}$  values of fresh lake water setting (for calcite precipitation) between -12‰ and -6‰ SMOW, which are close to the range calculated for the calcites in this study (see Table 5.7). Furthermore, Pitman (1996) estimates that the  $\delta^{18}\text{O}_w$  was around -5‰ SMOW for a slightly evaporated environment. By comparison, Long (2006), working in the southwest margin of the Uinta Basin, estimated the  $\delta^{18}\text{O}_w$  of fresh lake water setting (calcite precipitation) around -9‰ and -2‰ SMOW, and the  $\delta^{18}\text{O}_w$  for evaporated setting (dolomite precipitation) around -11‰ and -4.5‰ (SMOW). Long (2006) calculated these values assuming a constant temperature of 25 °C for calcite and dolomite precipitation.

Estimation of the  $\delta^{18}\text{O}_w$  during dolomitization considers the  $\delta^{18}\text{O}_w$  values proposed by Pitman (1996), but extending the  $\delta^{18}\text{O}_w$  range in  $\pm 5$ ‰ SMOW, from -10‰ to 0‰ SMOW. The calculated  $\delta^{18}\text{O}_w$  values proposed by Long (2006) are not included in this analysis because he estimated the calcite and dolomite precipitation at the same temperature of 25 °C. This cannot be accurate because a number of reasons, one of them flagged by his assertion that the  $\delta^{18}\text{O}_w$  for dolomitization was lower than  $\delta^{18}\text{O}_w$  for calcite precipitation.

On the contrary, the higher  $\delta^{18}\text{O}$  values of dolomite versus calcite suggest that dolomitization was probably caused by somewhat evaporated lake water with higher  $\delta^{18}\text{O}_w$  from evaporation. Therefore, the temperature of dolomitization must also has been higher than that of the fresh water setting (12 °C).

Based on these considerations, the lake water  $\delta^{18}\text{O}$  isotopic composition during dolomitization is evaluated here in three different  $\delta^{18}\text{O}_W$  settings: (i)  $\delta^{18}\text{O}_W = -10\text{‰}$  (SMOW), (ii)  $\delta^{18}\text{O}_W = -5\text{‰}$  (SMOW), and (iii)  $\delta^{18}\text{O}_W = 0\text{‰}$  (SMOW) (Table 5.8).

$\delta^{18}\text{O}_W = -10\text{‰}$  (SMOW) was not a probable alternative during dolomitization because the majority of the calculated temperatures are lower than 13 °C (values in red, Table 5.8), with some values below 0 °C. Similarly,  $\delta^{18}\text{O}_W = 0\text{‰}$  (SMOW) was not a probable water isotopic composition during dolomitization because the majority of the calculated temperatures are higher than 40 °C (values in red, Table 5.8). On the other hand, an intermediate  $\delta^{18}\text{O}_W = -5\text{‰}$  (SMOW) yields reasonable temperatures between 13 °C to 36°C with four exceptions (in red, Table 5.8).

Current lakes around the Uinta Basin have similar temperatures (variably throughout seasons) (Belovsky et al., 2011; Eardley, 1938), and the calculated temperatures are similar to the estimated paleo-temperatures of the Uinta Lake based on paleo-biological and paleo-climate studies (Rasmussen et al. 1999; MacGinitie, 1969).

Well	Sample	$\delta^{18}\text{O}_{Dol}$ (PDB)	T (°C) @ $\delta^{18}\text{O}_W = -10\text{‰}$ SMOW	T (°C) @ $\delta^{18}\text{O}_W = -5\text{‰}$ SMOW	T (°C) @ $\delta^{18}\text{O}_W = 0\text{‰}$ SMOW
<b>PZ1</b>					
BC 14-1	14-1-14	-2.71	6.3	24.9	47.8
BBC 14-1	14-1-15	-5.05	14.8	35.3	60.9
N 6-28	6-28-5	-2.06	4.0	22.2	44.4
N 6-28	6-28-6	0.87	-5.3	10.8	30.4
UT 15-13	15-13-9	0.04	-2.8	13.9	34.1
UT 15-13	15-13-10	-1.63	2.6	20.4	42.2
UT 15-13	15-13-11A	-7.30	23.8	46.4	75.1
UT 15-13	15-13-11B	-2.59	5.8	24.3	47.1
PW 13-06	13-06-6	-1.55	2.3	20.1	41.8
PW 13-06	13-06-6B	-0.39	-1.4	15.5	36.2

PW 13-06	13-06-7	-2.62	6.0	24.5	47.3
PW 13-06	13-06-7B	-0.69	-0.4	16.7	37.6
PW 13-06	13-06-8	-2.85	6.8	25.5	48.5
PW 13-06	13-06-9	-2.18	4.4	22.6	45.0
PW 13-06	13-06-10	-4.33	12.1	32.0	56.7
PW 13-06	13-06-10A	-3.26	8.2	27.2	50.7
DS 11-20	11-20-4	-0.84	0.0	17.3	38.3
I 16	16-3	-5.61	17.0	37.9	64.3
I 16	16-4	-4.42	12.4	32.4	57.2
<b>PZ1'</b>					
BBC 14-1	14-1-17	-2.37	5.1	23.5	46.0
N 6-28	6-28-7	-0.26	-1.8	15.0	35.6
UT 15-13	15-13-12	-4.63	13.2	33.3	58.4
UT 15-13	15-13-13	-4.83	13.9	34.2	59.5
PW 13-06	13-06-10B	-6.16	19.1	40.6	67.6
PW 13-06	13-06-11	-10.39	37.6	63.8	98.1
DS 11-20	11-20-5	-2.44	5.3	23.7	46.3
I 16	16-7	0.06	-2.8	13.8	34.1
I 16	16-8	-3.00	7.3	26.1	49.3
<b>PZ2</b>					
BBC 14-1	14-1-20	-2.69	6.2	24.8	47.7
BBC 14-1	14-1-21	-0.71	-0.3	16.8	37.7
N 6-28	6-28-9	-2.11	4.2	22.4	44.6
UT 15-13	15-13-14	-1.31	1.5	19.1	40.6
PW 13-06	13-06-11A	-5.37	16.0	36.8	62.8
PW 13-06	13-06-11B	-4.84	14.0	34.3	59.6
PW 13-06	13-06-11C	-2.90	6.9	25.7	48.7
PW 13-06	13-06-12	-6.03	18.6	40.0	66.8
DS 11-20	11-20-8	-4.80	13.8	34.1	59.4
DS 11-20	11-20-9	-3.47	9.0	28.1	51.8
I 16	16-10	-3.62	9.5	28.8	52.7
I 16	16-11	-2.02	3.9	22.0	44.2

**Table 5.8:** Calculated temperatures (T °C) of dolomitizing fluids based on estimated lake water  $\delta^{18}\text{O}$  composition varying from -10‰ to 0‰ SMOW and measured  $\delta^{18}\text{O}_{\text{Dol}}$  values from conventional isotopes analysis. Temperatures values that deemed unreasonable for dolomitization are highlighted in red color; temperatures calculated using the dolomite-water system isotopic fractionation equation proposed by Sheppard and Schwarcz (1970). See text for discussion.



A different estimation of the temperature along dolomitization is based on a comparison between the current lake water temperatures of the Great Salt Lake (Utah, USA) and the estimated temperatures of the Eocene epoch in the study area. The Great Salt Lake was chosen because it is located around the same latitude as the ancient Uinta Lake. The reported maximum water temperature in the summer of Great Salt Lake varies between 26 °C and 32 °C (Belovsky et al., 2011; Eardley, 1938; [www.usclimatedata.com](http://www.usclimatedata.com)). Furthermore, the relationship between lake water and air temperatures is positive and strong (high  $R^2$ ) for the highest lake water-air temperatures (McCombie, 1959). On the other hand, Rasmussen et al. (1999), using fossil of mammals estimated that the coolest temperature in the middle Eocene was at least 4 °C higher than current temperatures. Therefore, it is reasonable to assume that the water temperature of the ancient Uinta Lake could have reached at least 30 °C. This temperature supports the notion that the lake water  $\delta^{18}\text{O}$  isotopic composition fluctuated during dolomitization between -10‰ and 0‰ (SMOW), and most likely was close to -5‰ SMOW.

#### **5.2.2.7 Clumped-isotopes thermometry**

The clumped-isotopes results (Table 5.6), supplement the conventional oxygen isotope results as follows:

- (i) The dolomite PZ1 layer presents a dolomitization temperature of 30 °C (sample 13-06-7), which is close to its temperature of around 24 °C estimated from conventional oxygen isotope geothermometry (see previous section). However, the dolomite PZ1' and PZ2 layers show much higher dolomitization temperatures of 48 °C (sample 6-28-7) and 59 °C (sample 13-06-12), respectively. The discrepancy between the estimated temperature from conventional

oxygen isotopes and clumped-isotopes may due to the following reasons: (1) analytical error (Bernasconi, personal communication, 2016); or (2) the higher “clumped” temperatures do not reflect the dolomitization process, but are due to recrystallization.

(ii) Dolomitization temperature in the two limestone samples analyzed are significantly higher than those calculated temperatures for dolomite samples (79 °C for sample 13-06-5 and 84 °C for sample 6-28-8). These temperatures cannot possibly reflect the lake water at the time of calcite formation and/or deposition, but must be due to recrystallization during burial.

Considering that the calculated clumped-isotopes temperatures are in the range of the estimated maximum burial temperatures (from north to south) in the study area (see Section 5.1.3), it appears that the calcites for the limestones layers were prone to isotopic re-equilibrium during recrystallization near maximum burial whereas the dolomites of the dolostones were not.

#### **5.2.2.8 Elemental compositions**

Trace element concentration in dolomite crystals can be used for interpretations about the dolomitizing fluid, dolomitization environment, and/or recrystallization. The concentration of trace elements concentration in minerals is defined by (i) trace element fluid concentration, (ii) water/rock ratio of the system, and (iii) the distribution coefficient ( $D$ ) (Tucker and Wright, 1990). If an element has a  $D$  value  $>1$ , the resulting crystal is enriched (higher  $^{m}\text{Te}/^{m}\text{Ca}$ ) than the parental fluid. In contrast, if an element has a  $D$  value  $<1$ , the resulting crystal is impoverished (low  $^{m}\text{Te}/^{m}\text{Ca}$ ) than the parental fluid (McIntire, 1963). However, distribution coefficients are not constant. Rather they might vary with the composition of the solid phase, temperature, pressure, and kinetic factors (Veizer, 1983; McIntire, 1963).

The trace element concentration in dolomite is defined by Equation 10 (Gregg and Shelton, 1989), which correlates the molar ratio of the trace element to that of  $\text{Ca}^{2+}$  and  $\text{Mg}^{2+}$  as follows:

$$[\text{mTe}/(\text{mCa} + \text{mMg})]_s = D * [\text{mTe}/(\text{mCa} + \text{mMg})]_l \quad (\text{Equation 10})$$

where “m” is the molar concentration, “Te” stands for trace element, “s” represents the solid phase (calcite), “D” stands for the distribution coefficient, and “l” represents the liquid phase (or dolomitizing lake/pore water in this case). This equation is valid for systems in equilibrium and homogeneous distribution of trace elements during precipitation (Veizer, 1983).

Sr and Na concentrations of the dolomitizing fluids are compared to two specific reference waters: (i) a saline setting represented by the current Great Salt Lake concentration, and (ii) a fresh water setting represented by the average concentration of several lakes. Calculation was based on the distribution coefficients for dolomite proposed by Veizer (1983) ( $D_{\text{Sr}} = 0.025$  to  $0.07$ ,  $D_{\text{Na}} = 2 \times 10^{-5}$  to  $2 \times 10^{-4}$ ), the current Ca, Mg, Sr, and Na concentration of Great Salt Lake water (Whitehead and Feth, 1961); and the Ca, Mg, Sr, and Na average concentration of fresh lake water [Majid, 1983 in Veizer (1983)] (Table 5.9 and Figure 5.35).

	<b>Dolomitizing fluids</b>	<b>Freshwater - Lakes</b>	<b>Saline water - Great Salt Lake</b>
Sr (ppm)	1300	0.07	15
Na (ppm)	1420	50	83600
Ca (ppm)	245701	8	241
Mg (ppm)	133081	6	7200
$\text{mSr}/(\text{mCa} + \text{mMg})$	$2.66 \times 10^{-2}$	$1.79 \times 10^{-3}$	$5.66 \times 10^{-4}$
$\text{mNa}/(\text{mCa} + \text{mMg})$	$9.69 \times 10^1$	$1.28 \times 10^0$	$3.16 \times 10^0$

**Table 5.9:** Sr and Na concentrations and ratios to  $\text{Ca}^{2+}$  of calculated dolomitizing fluid compared to current fresh water from lakes in the region and saline water from Great Salt Lake.

Sr and Na are associated with the degree of salinity of the dolomitization fluids (Land and Hoops, 1973; Tucker and Wright, 1990). Assuming partition equilibrium during dolomitization and no recrystallization, the probable calculated Sr and Na concentrations of the dolomitizing fluid (ancient Uinta Lake water or pore waters derived from it) were greater than the waters references (Figure 5.35), suggesting an evaporitic dolomitizing fluid. This interpretation is valid only if Na is incorporated within the dolomite lattice. Furthermore, the geographical variation of this data, with somewhat elevated values located toward the near-shore area (Figure 5.31A), suggests that the lake/pore water had elevated salinities at least temporarily toward the near shore areas.

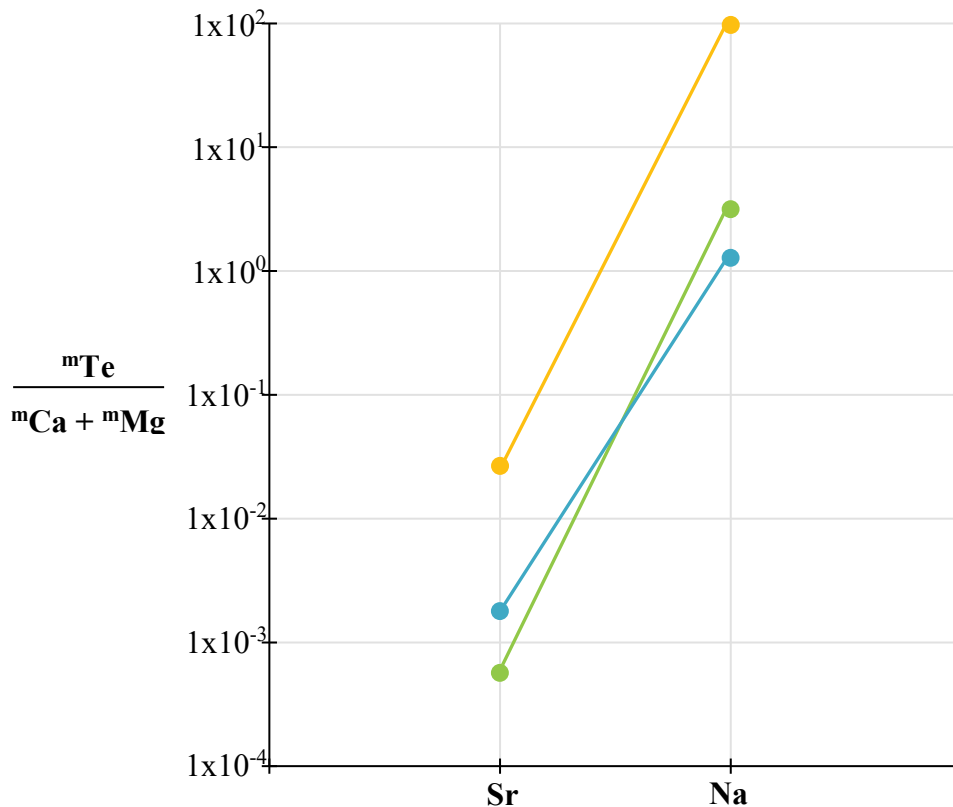


**Figure 5.35:** Calculated Sr/Ca and Na/Ca molar concentration of the ancient Uinta Lake (yellow line), the Great Salt Lake (green line), and fresh lakes waters (blue line).

On the other hand, the Sr concentration in dolomites may be an indicator of dolomitizing fluid flow and Sr/Ca ratio of the dolomitizing fluid. In figure 5.36, the Sr concentration decrease with depth, which probably represent an upward dolomitizing fluid directions (see Chapter six, section 6.1.3 for further discussion).

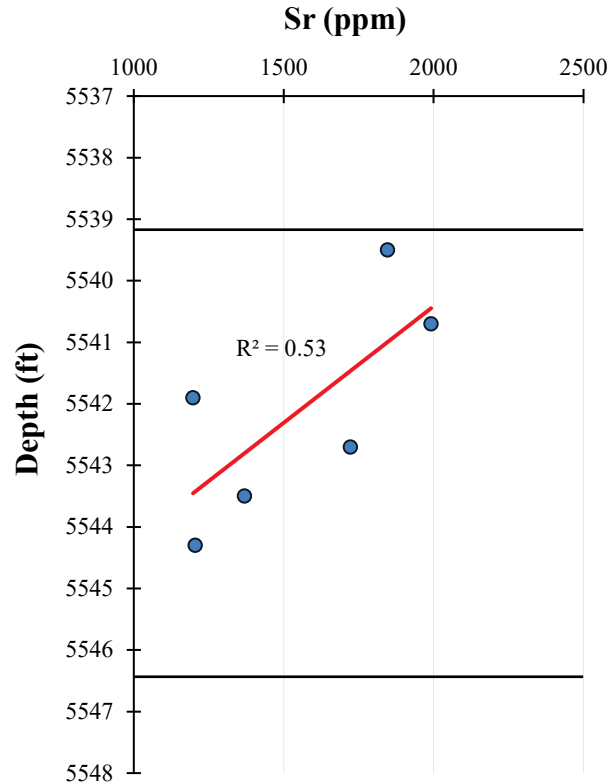


**Figure 5.36:** Sr concentration variation of dolomite crystals with depth. PZ1 layer, well PW 13-06. Horizontal black lines: top and base of the PZ layer, red line: regression line.

Fe and Mn concentrations are indicators of the reduction-oxidation potential of the dolomitization fluid (Davison, 1993; Tucker and Wright, 1990; Machel and Burton, 1991) and the availability of these elements (Budd, 1997). For these elements to be incorporated into the dolomite lattice must be in their divalent forms, which requires a reducing redox potential (Machel and Burton, 1991). Fe and Mn concentrations higher than 1000 ppm and 50 ppm,

respectively, suggests reducing pore waters and Fe-Mn external source (Budd, 1997). The average Fe and Mn concentration (5216 pp and 322 ppm, respectively) in the dolomite samples of this study (Figures 5.31C and D), suggest a reducing lake/pore water setting. This interpretation is valid only if the current Fe and Mg concentrations in dolomite crystals are the original signature.

The Al and Si concentrations are taken as a proxy for the amount of “insoluble residue”, i.e., essentially the clay mineral content in the samples because these elements cannot be incorporated into dolomite at low diagenetic temperatures (Weber, 1964). In the samples of this study, the Al concentrations have a spatial distribution in which the higher values are preferentially located in the near-shore area (Figure 5.32A). This distribution was probably caused by deposition of most of the suspended sediment in the near-shore areas, which led to a consequent decrease of clay sediments toward the basin center. In contrast, the Si concentration shows roughly the same concentration along the basin (Figure 5.32B).

The Zn and Pb concentrations are commonly elevated in basinal brines (e.g., Morrow, 1982), and dolomites formed from them often are associated with galena and/or sphalerite. The PZ layers of the UBm do not have any of these characteristics. In contrast the average Zn and Pb concentrations are low (12 ppm, and 2 ppm, respectively) (Figures 5.32C and D) in comparison with known basinal dolomites, which reach values up to 14 ppm and 50 ppm respectively (Luczaj et al., 2016).

### 5.3 Porosity

This section presents porosity characteristics from different perspectives. First, it describes porosity features by layer, then it describes porosity according to its geographical and vertical distribution using well core plug data, and finally porosity values from SEM images analysis are correlated to dolomite textures.

Core, thin sections, and SEM image petrographic descriptions show fabric and non-fabric selective porosity types (e.g. Figures 5.5C, 5.4A). For fabric selective porosity, four different types are present: intercrystal (IC), moldic (MO), interparticle (IEP), and intraparticle (IAP); and for non-fabric selective, two different types are present: vug (VG) and fractures (FR). IAP is present only in grain-supported facies (ooid grainstone, F7) and some of these pores were occluded by calcite cement (phases 1b, 2b, and 8 in Table 5.1) before oil migration (phase 12). Additionally, MO, IEP, and VG were partially occluded by carbonate and silica cementation phases (phases 2a, 4, 5a, 5b and 9 in Table 5.1).

Among the secondary pore types, IEP has the highest porosity values up to 20% (thin section estimation percentage); however, this porosity is exclusively present within the ooid grainstone facies (F7). FR porosity represents a very low porosity percentage (<1%) and most of the fractures are partially to completely filled by calcite cement (phase 15). In contrast, IC is the most abundant pore type in all PZ layers with a pore size that ranges from microporosity and mesoporosity types.

The geographic distribution of porosity was established based on extant core plug data (Table 5.10; Vanden Berg, personal communication, 2015). According to the most abundant pore type identified in core, thin sections, and SEM images, it is here assumed that porosity values measured from core plugs largely represent the intercrystal porosity type.



Well	Depth (ft)	PZ	Porosity (%)
BBC 14-1	6684.0	PZ1	18.0
BBC 14-1	6685.5	PZ1	31.3
BBC 14-1	6686.2	PZ1	17.9
BBC 14-1	6687.0	PZ1	14.4
BBC 14-1	6688.2	PZ1	15.8
BBC 14-3	7373.7	PZ1	26.5
UT 15-13	7007.4	PZ1	17.8
UT 15-13	7008.2	PZ1	19.7
UT 15-13	7009.6	PZ1	24.8
PW 13-06	5540.1	PZ1	20.6
PW 13-06	5542.3	PZ1	21.9
BBC 14-1	6692.3	PZ1'	10.2
BBC 14-1	6694.0	PZ1'	11.7
BBC 14-3	7381.9	PZ1'	8.7
BBC 14-3	7382.6	PZ1'	2.6
N 6-28	8231.3	PZ1'	16.0
BBC 14-1	6701.6	PZ2	8.6
BBC 14-1	6703.0	PZ2	14.9
N 6-28	8241.1	PZ2	19.2
PW 13-06	5557.7	PZ2	12.6
DS 11-20	4990.5	PZ2	14.8
UI-16	4723.0	PZ2	4.0

**Table 5.10:** Porosity values from plugs. Data furnished by Core Lab and courtesy of Michael D. Vanden Berg.

PZ1 displays a wide porosity variation and it has the highest porosity values of all PZ layers with an average of 17.7% ( $\sigma$ : 7.1%). Wells BBC 14-1, BBC 14-3, and N 6-28 have higher porosity variability in comparison with wells UT 15-13 and PW 13-06. In contrast, PZ1' and PZ2 have the lowest porosity values with an average of 9.4% ( $\sigma$ : 5.9%) and 12.3% ( $\sigma$ : 7.1%) respectively.

The distribution of porosity in the PZ layers do not show distinctive trends laterally, i.e., along bedding. For PZ1, the correlation line (red dashed line in Figure 5.37) between the average porosity values (white line within boxes) is roughly horizontal, but the maximum porosity values (high whiskers in Figure 5.37) are located near the basin center (east-west section). PZ1 has lower porosity values of all PZ layers near the basin center (east-west section) with highest porosity values in well N 6-28. PZ2 has the highest porosity variability, which varies from 20% near the basin center (well N 6-28) to 5% in the center area (well UT 15-13), and increases again in the nearshore line area up to 12% (well PW 13-06) (Figure 5.37).

The distribution of porosity does not show any distinctive vertical trends either. However, the highest porosity values are preferentially located near the tops of the PZ layers, whereas the lowest porosity values are preferentially located near the bases of the PZ layers (Figure 5.38).

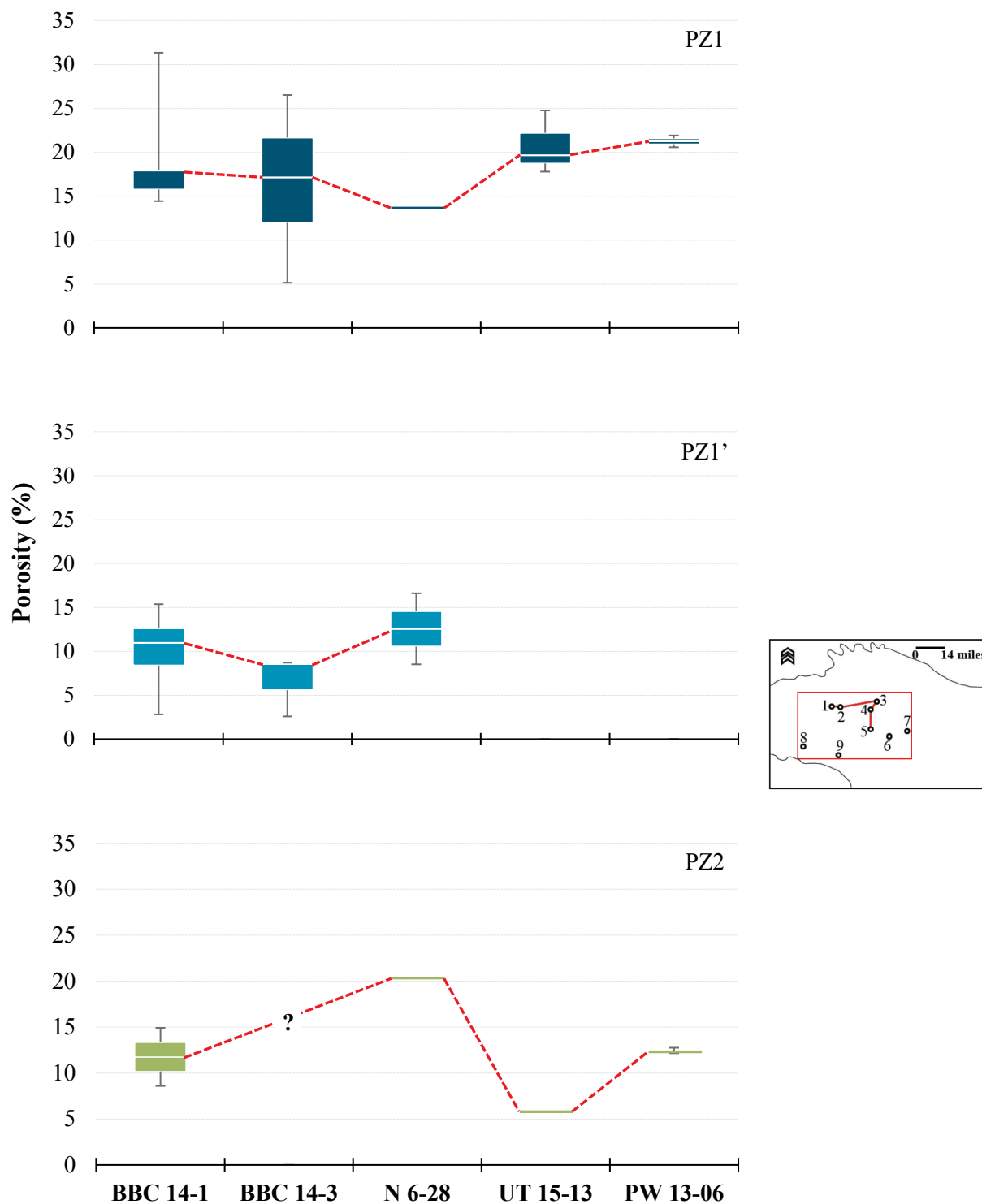


**Figure 5.37:** Horizontal porosity variation for each PZ layer. Porosity values measured from core plug samples. Red dashed line represents porosity average correlation between wells. Numbers along the horizontal axes and in the inset map stand for wells/outcrops as follows: 1: BBC 14-1, 2: BBC 14-3, 3: N 6-28, 4: UT 15-13, 5: PW 13-06, 6: DS 11-20, 7: UI 16, 8: WCC, 9: NMC.

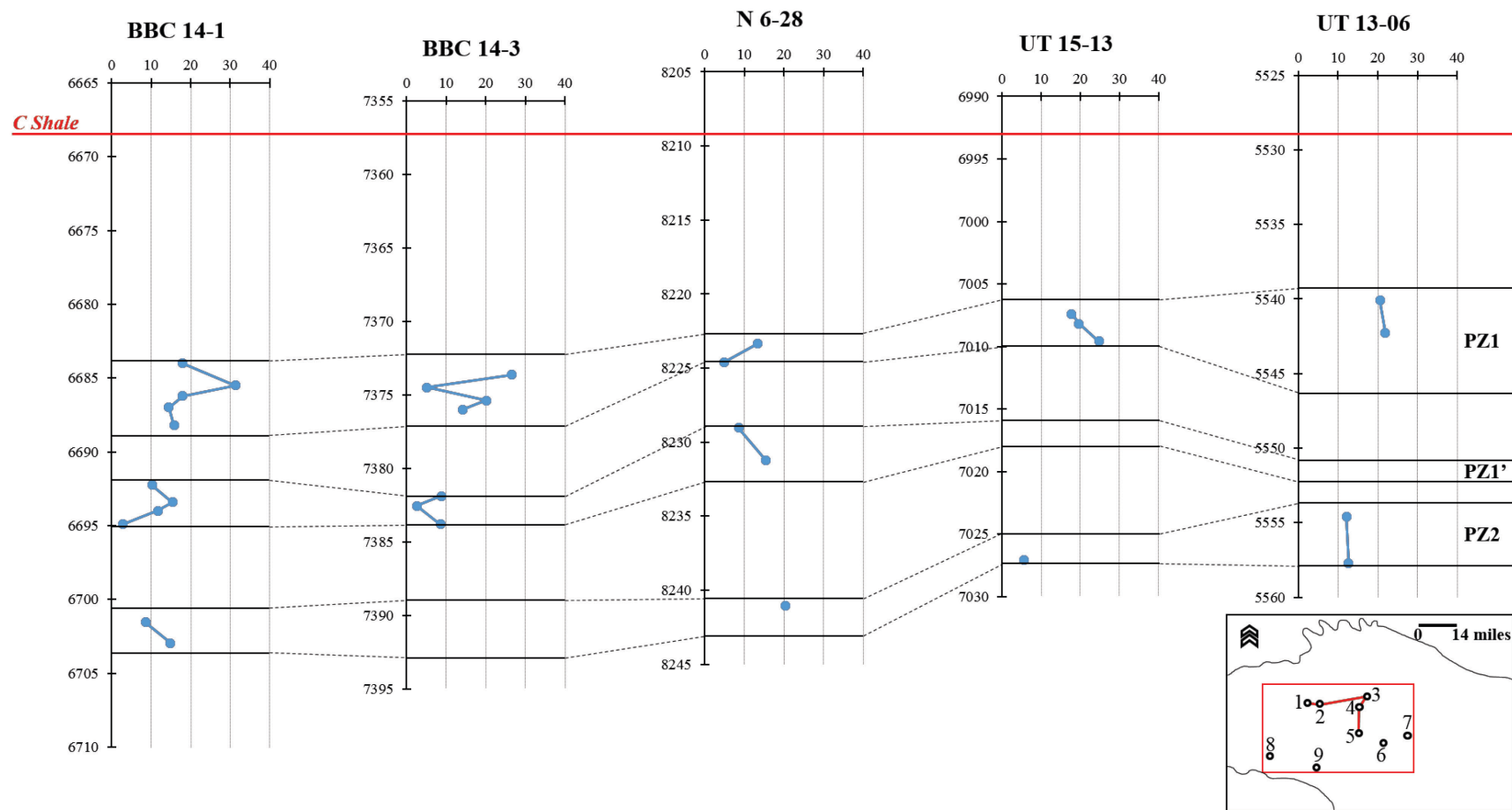


**Figure 5.38:** Porosity variation with depth. Porosity values measured from core plugs; horizontal axis: porosity (%), vertical axis: depth (ft). Number in the inset map 1: BBC 14-1, 2: BBC 14-3, 3: N 6-28, 4: UT 15-13, 5: UT: 13-06, 6: DS 11-20, 7: UI 16, 8: WCC, 9: NMC.

A different porosity measurement arises from SEM images by mean of APS Assess 2.0 image analysis software. In this analysis, the darkest areas represent pores and the brightest areas represent dolomite crystals (Figure 5.39). Three thin sections were selected for PZ1, four thin sections for PZ1', and three thin sections for PZ2 (Figure 5.12). A total of 32 SEM images were used to determine porosity in this manner. Porosity results are summarized in Table 5.11.

**Figure 5.39**

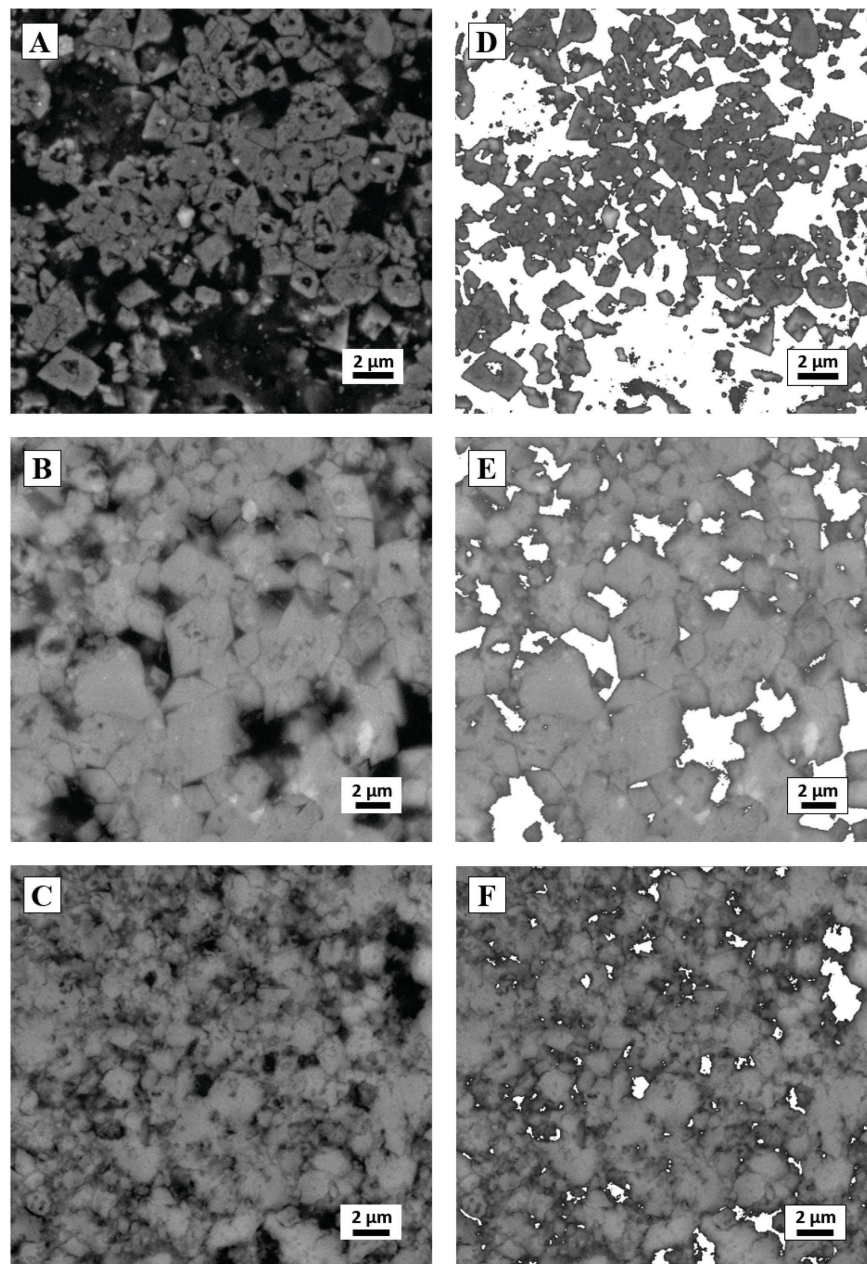


**Figure 5.39:** (A) SEM image of planar-e texture characterized by straight dolomite crystal faces; well: UT 15-13, sample: 13, 7017.4 ft, PZ1' layer. (B) SEM image of planar-s texture characterized by straight and irregular dolomite crystal faces; well: N 6-28, sample: 9, 8242.5 ft, PZ2 layer. (C) SEM image of nonplanar-a texture characterized by irregular dolomite crystal faces and more densely packed crystals; well: UT 15-13, sample: 11, 7009.9 ft, PZ1 layer. (D) Same image as (A) highlighting porosity area (white area), estimated porosity: 43.38%. (E) Same image as (B) highlighting porosity area, estimated porosity: 12.4%. (F) Same image as (C) highlighting porosity area, estimated porosity: 7.82%.

Well	Sample	Depth (ft)	Image	Porosity (%)
PZ1				
UT 15-13	15-13-11	7009.9	3	16.3
			4	13.7
			6	23.6
PW 13-06	13-06-07	5541.9	2	33.2
			3	44.2
	13-06-08	5543.5	2	32.2
			C1	39.6
			C2	38.6
			C3	29.5
			C5	37.3
PZ1'				
N 6-28	6-28-7	8230.2	3	11.4
			4	21.4
			2	13.7
UT 15-13	15-13-12	7016.4	2	23.0
			6	18.1
			7	17.0
			8	17.0
			9	19.5
			4	21.8
PW 13-06	13-06-11	5552.3	1	27.9
PZ2				
N 6-28	6-28-9	8242.5	3	12.5
			4	15.7
			5	12.4
			7	12.4
			9	22.7
			12	18.5
			13	18.9
UT 15-13	15-13-14	7025.2	1	17.4
			2	20.3
PW 13-06	13-06-12	5557.4	3	28.9
			1	30.3
			2	29.6

**Table 5.11:** Porosity estimated from SEM images.

The estimated porosity from SEM images shows a pattern similar to that from plugs. However, the porosity values estimated from image analysis are significantly higher than those measured from plugs. PZ1 has the highest porosity values with an average of 30.8% ( $\sigma$ : 10.1%) versus 17.7% (from plugs). PZ1' has a porosity average of 19.1% ( $\sigma$ : 4.8%) versus 9.4% (from plugs), and PZ2 has a porosity average of 20.0% ( $\sigma$ : 6.6%) versus 12.3% (from plugs). For this study, porosity measured from plugs is considered as base of reference. It is not possible to apply an appropriate correction to the porosity values estimated from SEM image analysis because both types of measurement were made on samples from different depths.

Porosity from well logs show remarkable differences between the PZ layers and the interbedded limestones, in that the dolomite PZ layers consistently have higher porosity values than the interbedded molluscan limestones by about 11%. The porosity of the PZ layers range from 8 to 26% with an average of 16%. In contrast, porosity of the interbedded limestones ranges from 2 to 11% with an average of 5% (Figure 5.40).

The porosity values were calculated from the density logs via equation 11 (Asquith and Gibson, 1982):

$$P_D = (\rho_m - \text{RHOB}) / (\rho_m - \rho_f) \quad (\text{Equation 11})$$

where  $P_D$  is porosity (calculated from density log);  $\rho_m$  is the density of the matrix, which for dolomite is 2.87 g/cm<sup>3</sup> and for calcite is 2.71 g/cm<sup>3</sup>; RHOB is the density data registered by the tool; and  $\rho_f$  is the density of the fluid. The oil in PZ layers is characterized as a highly paraffinic crude oil with API values between 30° and 40° (Birdwell et al., 2016). Therefore, the density value used for porosity calculation was 0.8 g/cm<sup>3</sup>.



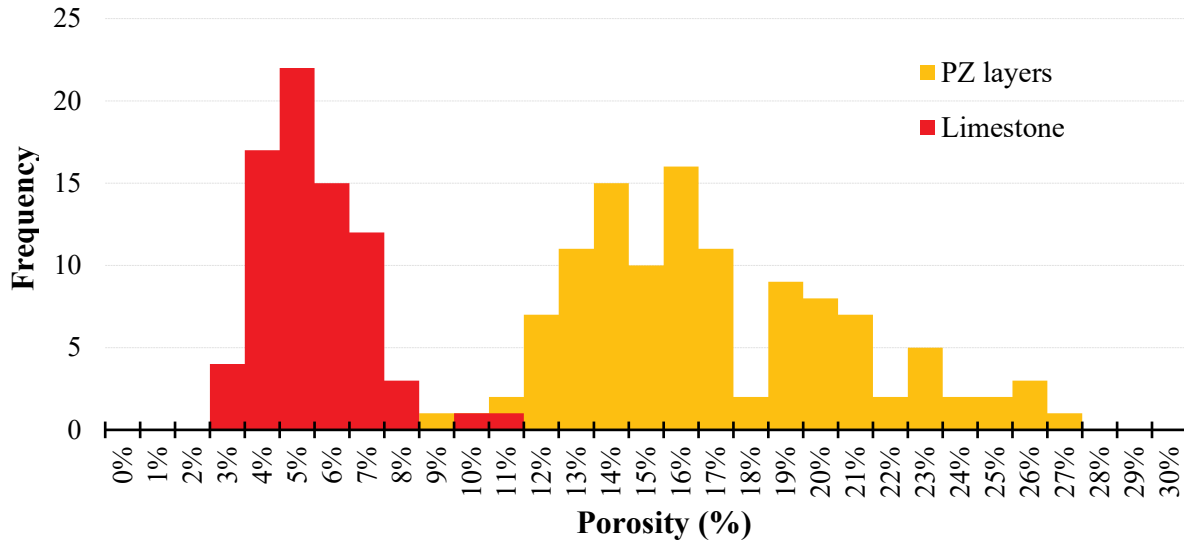


**Figure 5.40:** Frequency distribution of porosity calculated from density logs for PZ layers and interbedded limestones.

Porosity calculated from density logs shows the same pattern as porosity from plugs. PZ1 has the highest porosity values of all PZ layers with an average of 18.8% ( $\sigma$ : 4.0%), PZ1' layer has the lowest porosity values with an average of 13.9% ( $\sigma$ : 1.5%), and PZ2 has an average of 15% ( $\sigma$ : 3.1%). Furthermore, the averaged porosity values calculated from logs are higher than the averaged porosity from plugs. For PZ1, porosity from logs are 1.0% higher than porosity from plugs. For PZ1', porosity from logs are 4.5% higher than porosity from plugs. For PZ2, porosity from logs are 2.7% higher than porosity from plugs. However, there is not possible to make an appropriated correction to the porosity from logs because depth from both measurements are different.

## 5.4 Permeability

Permeability data analysis is based on the extant data (Table 5.12; Michael D. Vanden Berg, personal communication, 2015). The dolomitized PZ layers are characterized by very low permeability values that range from  $1.2 \times 10^{-4}$  to  $2.9 \times 10^{-1}$  mD. PZ1 layer has the highest permeability with an average of  $8.1 \times 10^{-2}$  mD; PZ1' has the lowest permeability values with an average of  $2.0 \times 10^{-2}$  mD; and PZ2 has intermediate permeabilities that average  $5.4 \times 10^{-2}$  mD.

Well	Depth (ft)	Permeability (mD)	PZ
BBC 14-1	6684.0	0.03164	PZ1
BBC 14-1	6685.5	0.19893	PZ1
BBC 14-1	6686.2	0.02634	PZ1
BBC 14-1	6687.0	0.01842	PZ1
BBC 14-1	6688.2	0.00832	PZ1
BBC 14-3	7373.7	0.07700	PZ1
UT 15-13	7007.4	0.01559	PZ1
UT 15-13	7008.2	0.07056	PZ1
UT 15-13	7009.6	0.17472	PZ1
PW 13-06	5540.1	0.12667	PZ1
PW 13-06	5542.3	0.14943	PZ1
BBC 14-1	6692.3	0.00175	PZ1'
BBC 14-1	6694.0	0.07485	PZ1'
BBC 14-3	7381.9	0.00021	PZ1'
BBC 14-3	7382.6	0.00033	PZ1'
N 6-28	8231.3	0.02288	PZ1'
BBC 14-1	6701.6	0.00042	PZ2
BBC 14-1	6703.0	0.00398	PZ2
N 6-28	8241.1	0.29911	PZ2
PW 13-06	5557.7	0.00248	PZ2
DS 11-20	4990.5	0.02225	PZ2
UI-16	4723.0	0.00012	PZ2

**Table 5.12:** Permeability values from plugs. Data furnished by Core Lab and courtesy of Michael D. Vanden Berg

Geographically, the permeability values of PZ1 are approximately the same along the chosen east-west and north-south cross sections (Figure 5.41, top). In contrast, PZ1' and PZ2 have an erratic distribution along the basin and do not show any discernible trends (Figure 5.41, center and bottom).

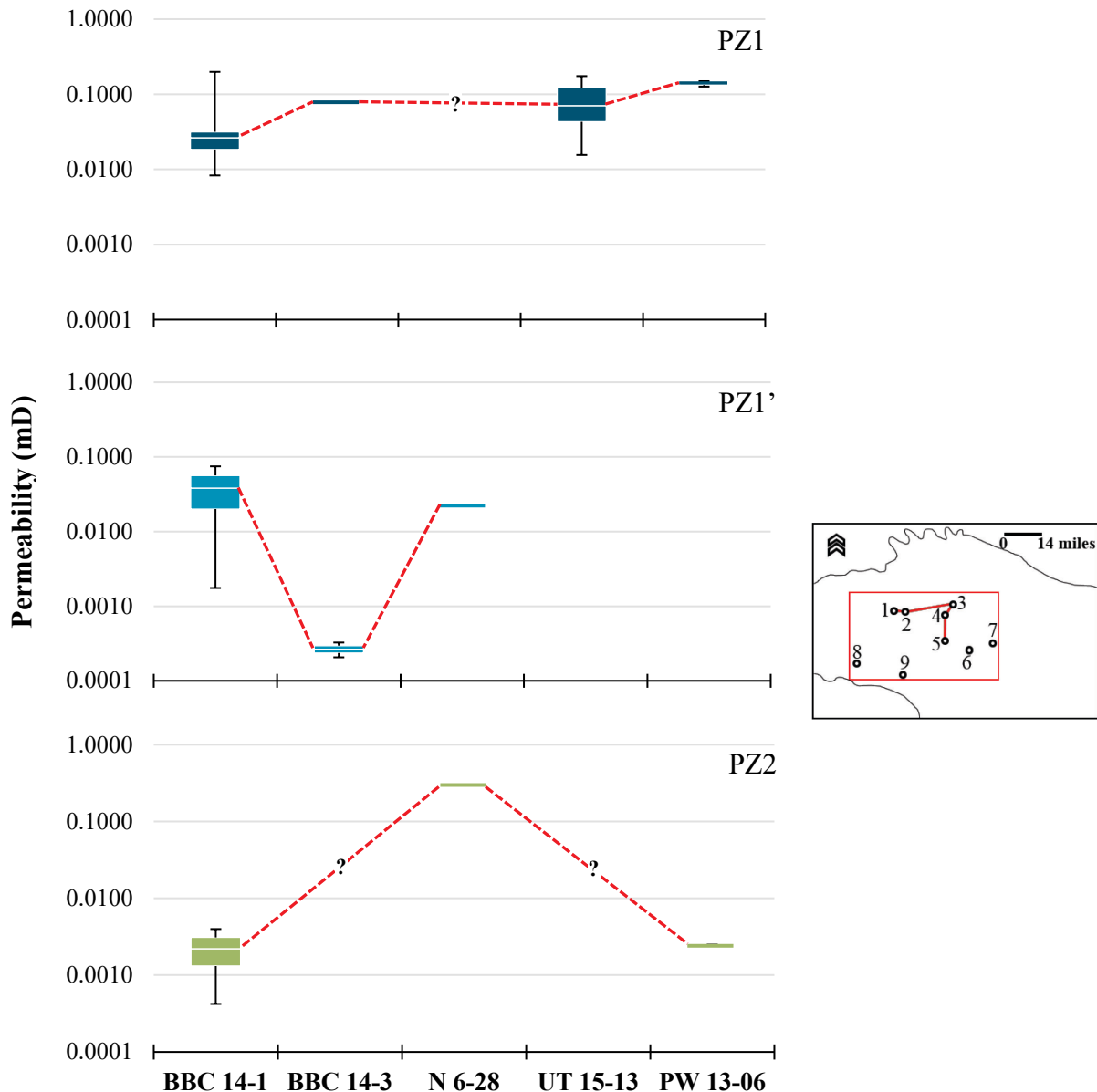


**Figure 5.41:** Geographical distribution of permeability for each PZ layer. Data from core plug samples. Red dashed line represents permeability average correlation between wells. Numbers in the horizontal axis and in the inset map stand for wells/outcrops as 1: BBC 14-1, 2: BBC 14-3, 3: N 6-28, 4: UT 15-13, 5: PW 13-06, 6: DS 11-20, 7: UI 16, 8: WCC, 9: NMC.

On the other hand, the pore throat geometry vary systematically between dolomite textures. The planar-e and planar-s textures have a prismatic throat shape (space between the dolomite crystals) defined by straight and well defined dolomite crystal faces (sheet-like). In contrast, the nonplanar texture has an irregular pore throat shape defined by irregular dolomite crystal faces (Figure 5.42).

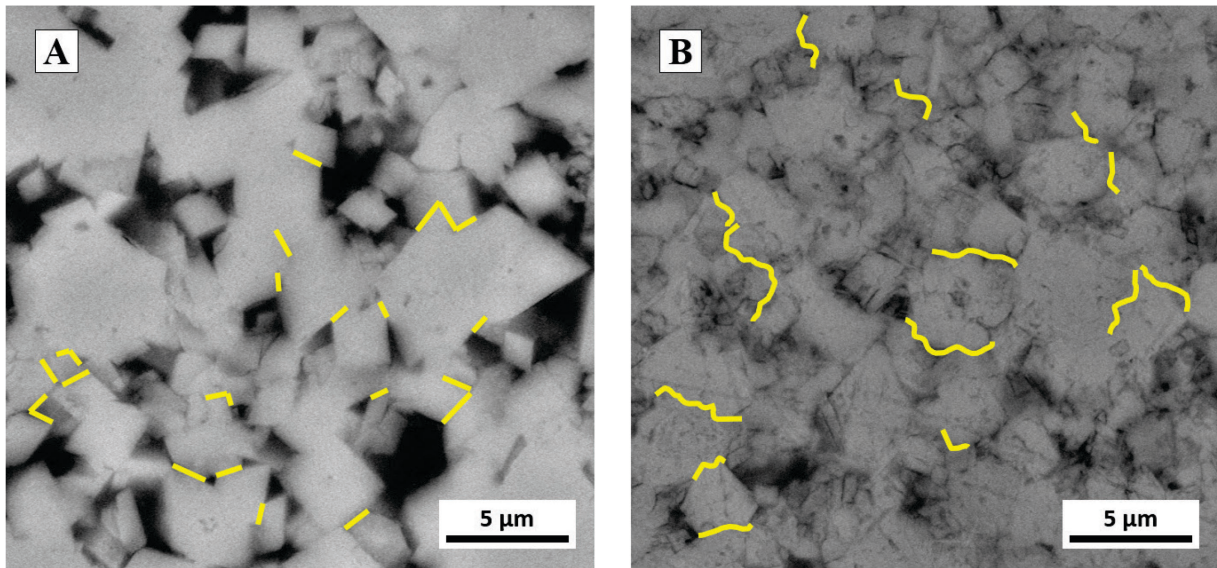


**Figure 5.42:** Pore throat shapes. (A) Sheet-like pore throat shape (yellow lines) between dolomite crystals in planar-e and planar-s textures; well: N 6-28, sample: 7, 8230.20 ft. (B) Irregular pore throat shape (yellow lines) between dolomite crystals in nonplanar-a texture; well UT 15-13, sample: 11, 7009.90 ft.

## **CHAPTER SIX**

### **DISCUSSION**

This chapter provides an interpretation of dolomitization to account for the occurrence of petroliferous dolomite layers on various scales: (i) Individual dolomite layers; (ii) stratigraphic interval between D and C Shales; and (iii) the context of regional paleogeography. It also attempts to correlate dolomitization with reservoir characteristics.

#### **6.1 Individual dolomite layers**

##### **6.1.1 Dolomite: Replacement**

The dolomite crystals of all PZ layers were created as replacement of the lime mud and/or at least partially lithified lime mud. This is shown by distinctive petrographic textural features such as partial or complete matrix-selective replacement, and occurrence of microvugs (Figure 5.4A) and moulds (Tucker and Wright, 1990; Machel 2004) (Figures 5.4C to F and Figure 6.8). These pores were probably generated by dissolution of metastable carbonate grains and/or crystals. Furthermore, there are no petrographic features to suggest direct precipitation of dolomite from the lake water(s). However, it cannot be ruled out that at least some of the dolomite in the PZ layers is a 'cement' or direct formation from aqueous solution.

### 6.1.2 $\text{Mg}^{2+}$ source

Dolomitization is favoured by several factors such as high  $\text{Mg}^{2+}/\text{Ca}^{2+}$  ratio, high alkalinity, and high temperatures (Machel and Mountjoy, 1986; Machel and Mountjoy, 1987; Machel, 2004). According to the geological setting of the Uinta Lake during dolomitization (see Chapter 4, Section 4.2) and the burial history (see Chapter 5, Section 5.1.2), there were two potential  $\text{Mg}^{2+}$  sources: (i) transformation of clay minerals from the shales and (ii) lake water.

The interbedded shales beds are a potential source of  $\text{Mg}^{2+}$  due to the smectite - illite transformation that releases  $\text{Mg}^{2+}$  to the fluids, hence potentially favouring dolomitization (Kahle, 1965). However, this potential source of  $\text{Mg}^{2+}$  is discarded here because (i) petrographic evidence suggests dolomitization at very shallow depth and (ii) the calculated temperature between  $\sim 23$  to  $30^\circ\text{C}$ , with a maximum temperature of about  $40^\circ\text{C}$  (based on the conventional oxygen isotope thermometer; see Chapter 5, Section 5.2.2.6). This temperature range is much lower than the temperature of smectite-illite transformation of about  $70^\circ\text{C}$  (Pytte and Reynolds, 1989), which usually corresponds to a burial depth of about 1-2 km. Therefore, dolomitization occurred well before the release of  $\text{Mg}^{2+}$  from smectite-illite transformation.

Lacustrine environments generally have a low magnesium contents between 2.4 ppm (Turkana Lake) to 756 ppm (Caspian Lake) (Nikanorov and Brazhnikova, 2004). Freshwater lakes can have  $\text{Mg}^{2+}$  concentrations below 1 ppm (Nikanorov and Brazhnikova, 2004), when the water inflow rate is higher than the water outflow in the absence of evaporation (Renaut and Gierloski-Kordes, 2010).

The most probable source of magnesium for dolomite formation in the UBm is from weathering of surrounding igneous rocks with abundant magnesium-rich minerals (pyroxenes and amphiboles) that released magnesium ions, which were then transported by rivers and

groundwater. Igneous rocks that supply relatively high amounts of  $Mg^{2+}$  are gabbros, norites, pyroxenites, harzburgites and dunites and their analogues. Such mafic rocks have high magnesium oxide contents that vary between 6.73% for gabbro and 37.94% for dunite (Best, 1982). Thus, the  $Mg^{2+}$  for dolomitization likely was derived from the magnesium-rich igneous rocks that were located in and around the southwestern region of the Uinta Basin (Hunt, 1956) during deposition of the UBm, notably a Proterozoic metapyroxenite body located within the probable catchment area at the northwestern part of the Uncompahgre Plateau, with magnesium oxide (weight percent) as high as 19.4 % (Case, 1991) (Figure 6.1).

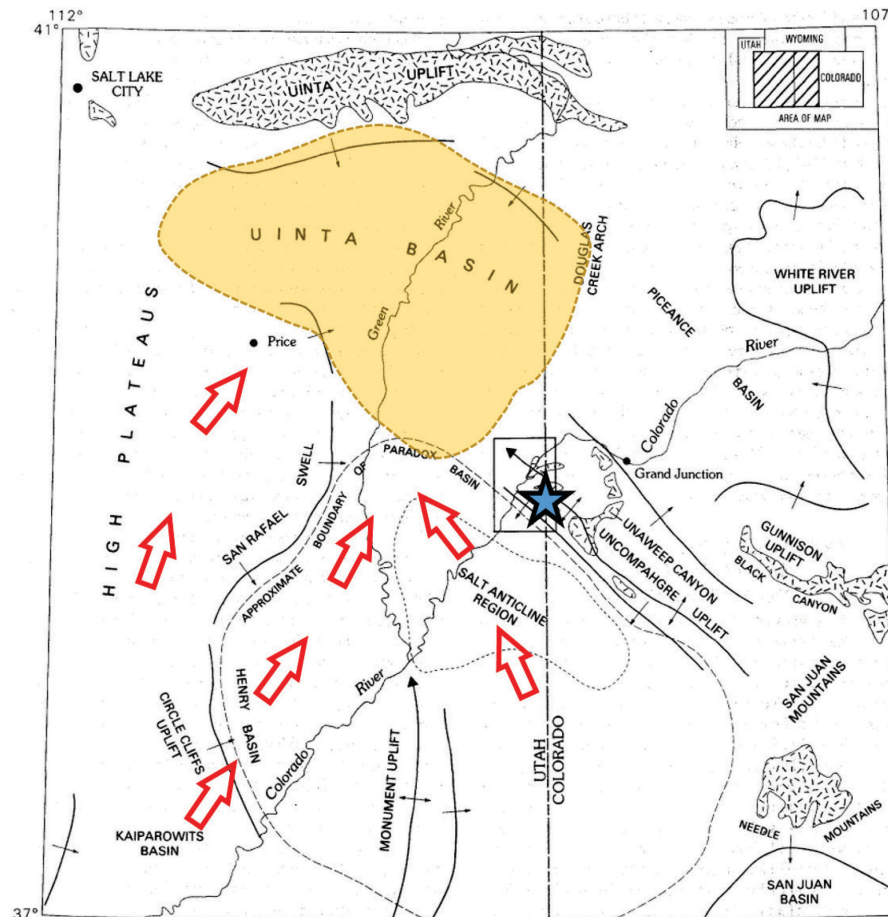
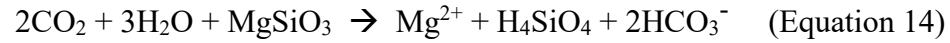


**Figure 6.1:** Location of metapyroxenite (blue star) and the Uinta basin (yellow area). Additional potential sources of  $Mg^{2+}$  were located toward south/southwest of the Uinta Basin (Chapter 2, Section 2.2). Red arrow represents the probable paleo-river drainage. Figure modified from Case (1991).



Chemical weathering is the main process that provides magnesium to surface waters (Nikanorov and Brazhnikova, 2004). An example of this process is defined in Equation 14 (Broecker, 1971), in which enstatite ( $\text{MgSiO}_3$ ), a common component of mafic and ultramafic intrusive rocks (Nesse, 1991), weathers in a subaerial environment as follows:



Chemical weathering of mafic and ultramafic igneous bodies during deposition of the UBm may have been favoured by climate changes, specifically by relatively short term ( $10^3$  to  $10^5$  years) periods of global warming with elevated atmospheric  $\text{CO}_2$  values [higher than 2000 ppm (Pearson and Palmer, 2000)] that took place in the Early Eocene epoch (Zachos et al., 2001) and likely enhanced the rate of the chemical weathering of igneous rocks in the region. In this global climate short-term scenario, the amount of rain increased during cooler periods (Robert and Kennett, 1992), whereas the atmospheric carbon dioxide values increased during warmer periods such as during the Early Eocene Climatic Optimum (EECO), with  $\text{CO}_2$  concentrations almost nine times the current values (Pearson and Palmer, 2000; Zachos et al., 2001). This suggests that the alternating limestone-dolostone layers in the UBm reflect cycles of cooler and warmer climate, with concomitant cyclical changes in temperature, amount of river recharge, evaporation, and  $\text{Mg}^{2+}$  input.

### 6.1.3 Interpretation and model of dolomitization

Most dolomite crystals (about 91%; Chapter 5, section 5.2.1.2) are classified as aphanocrystalline, ranging between 0.25 to 3  $\mu\text{m}$  in size. Dolomite crystal size is controlled by nucleation and growth rates, which are directly regulated by temperature (Gregg and Sibley, 1984; Sibley and Gregg, 1987). The overall very small dolomite crystal size was likely caused by high nucleation rates paired with low growth rates, which commonly are associated with evaporitic (syndepositional) environments. Folk and Siedlecka (1974) stated that very fine dolomite crystals are an indicator of an evaporite cycle in schizohaline environments. Warren (2000) characterized syndepositional dolomite crystals in evaporite settings as very fine in size ( $< 10 \mu\text{m}$ ). Budd (1997) characterized Holocene dolomites that were precipitated directly from seawater also by very fine crystals ( $< 10 \mu\text{m}$ ), and classified them as 'penecontemporaneous' dolomite.

In all these situations, dolomitization was driven by evaporation that also favoured crystallization of evaporite minerals (such as quartzine and gypsum). While there is no evidence that sulfates were formed in the UBm, quartzine and other silica varieties are common (Figures 5.6A to F), suggesting dolomitization occurred in an evaporitic environment. Furthermore, the mineralogical association of dolomite-silica and lack of gypsum suggest that the dolomitizing water in the UBm was Uinta Lake water with very low sulfate concentration paired with relatively high  $\text{Mg}^{2+}$  concentration.

In addition, the north to south preferential distribution of dolomite textures (Figure 5.14) suggest that the chemical composition of the dolomitizing water and its temperature changed over time. Relatively low dolomite-supersaturated water paired with relatively low temperature may have led to the development of rhombohedral dolomite crystals with planar-e

texture, whereas higher dolomite supersaturation paired with higher temperature may have led to the development of planar-s and nonplanar textures (Sibley and Gregg, 1987). Hence, the observed textural distribution may have been generated by variations in dolomite saturation and temperature.

The lake water level was probably controlled by climate changes as well, whereby increased lake water temperature and evaporation paired with decreased river recharge promoted the lake water level to drop.

As a corollary, the lake water density also changed. Because of evaporation the lake water became denser, which forced it to move downward partially dolomitizing the already deposited calcium carbonate sediments. This mode of dolomitization conforms to the reflux model, first proposed by Adams and Rhodes (1960), in which metastable calcium carbonate is replaced by dolomite as the denser evaporated water passes through unconsolidated lime mud.

This interpretation is supported by variations of calcium excess in the dolomites with depth. In the case of reflux dolomitization, nearly stoichiometric dolomite should be located near the top of each PZ layer, whereas calcium-rich dolomite should be preferentially located near the base of each PZ layer, as is observed in the data (Figures 5.24 and 5.25). The level of supersaturation with respect to dolomite would have been highest at the beginning of dolomitization, forming nearly stoichiometric crystals very near to the source of the dolomitizing water, the sediment-water interface. Increasingly Ca-rich crystals would have formed from water with decreasing levels of supersaturation farther down into the sediment. However, later recrystallization would overprint this pattern, likely one of the reasons why the observed pattern in dolomite Ca-excess is not a regular top-down pattern (Figure 5.24).

Furthermore, as Ca-excess and ordering are usually negatively correlated, the ordering of the PZ dolomites should decrease in each layer from the top downwards. The data appear to conform to this pattern, allowing for partial recrystallization. Differential reaction time and/or recrystallization probably created the observed variations in dolomite cation ordering with depth.

Moreover, layer-by-layer dolomite formation via reflux of the UBm implies a progressive increase in thickness of each PZ layer basinward. However, this pattern does not appear to be realized (further discussed in section 6.4.1). This finding suggests that reflux was not the only process responsible for dolomitization in the UBm.

A second process that was likely involved in dolomitization of the UBm was taking place diachronously from south to north in those parts of the lake that became subaerially exposed during progressively falling water level, i.e., in the supralittoral as identified in Chapter 4. This setting likely experienced evaporative pumping of groundwater, with a vertical hydraulic gradient that allowed pore fluids to move upward (Eugster and Surdam, 1973; Hsü and Siegenthaler, 1969). This type of dolomitization conforms to the playa model that was first proposed for the GRF by Eugster and Surdam (1973). Evaporative pumping allowed at least partial recrystallization of the previously dolomitized sediments as well as the formation of additional dolomite.

The Sr concentrations of the Uteland Butte dolomites can be interpreted as a record of such ascending pore water flow. According to Machel (1999), if the dolomitizing fluid has a Sr/Ca ratio equal or lower than that of the limestone, the Sr concentration in dolomite should increase downflow. In contrast, if the dolomitizing fluid has a Sr/Ca ratio higher than that of the limestone, the Sr concentration in dolomite should decrease downflow. Applying this concept,

the evaporated and upward moving pore fluid probably had a Sr/Ca ratio equal or smaller than that of the parental lime mud sediments (Figure 5.36).

A third process that may have contributed to the current distribution of dolomite is mechanical reworking and redeposition of dolomite during episodic, perhaps even seasonal flooding of the area. In this case, dolomite formed in the shallowest parts of the system got episodically washed into the deeper parts of the lake, as proposed by Eugster and Surdam (1973). This process is nearly impossible to verify and likely was of minor importance volumetrically. In any case, this process is not one of dolomitization (or dolomite formation, referring to dolomite that may have formed as 'cement' rather than replacement), and thus is excluded from the following discussion.

Be it reflux or evaporative pumping, dolomitization (or dolomite formation) was controlled by climate. In the warmer periods, freshwater input was diminished and lake water evaporation was promoted, allowing dolomite to form. In the cooler periods, freshwater input increased, diluting the lake water, thereby inhibiting dolomitization. The inferred freshwater – brackish water changes are also recorded by the fossils associations: freshwater molluscs (pelecypods and gastropods) are present and/or dominate in the floatstone layers, whereas more saline-tolerant organisms (ostracods and gyronites) paired with a lack of fresh water molluscs characterize the dolomitized layers. Dolomitization in the UBm is thus interpreted as the result of cyclical fluctuations in lake water levels, salinity, and temperature, all driven by cyclical changes in climate, whereby each layer was dolomitized individually by two processes: reflux in the subaqueous part followed and/or overprinted by evaporative pumping in the subaerial (supralittoral) part. Furthermore, it is likely that most dolomitization took place during the lake level falls, i.e., while the climate was warming, although it cannot be ruled out that the

basinward parts of each layer formed some dolomite and/or recrystallized dolomite also during the rise of the lake level following the lake level low stand.

An idealized representation of this scenario is illustrated in Figure 6.2. This interpretation contemplates the hypothetical variation of the lake/pore water supersaturation with respect to dolomite and temperature at different time intervals ( $t_0$  to  $t_5$  in Figure 6.2), coupled with physiographic changes such that the lake water level went down, and the lake decreased in size, thereby causing the shoreline to move toward the center of the lake.

In the freshwater setting ( $t_0$ ), the lake water was undersaturated for dolomite and the temperature likely was below 12 °C, based on the oxygen isotope data (Chapter 5, Section 5.2.2.6). In this setting lime mud was deposited and remained as calcium carbonate.

In the next phase ( $t_1$ ), the reflux dolomitization started when the lake water had reached and/or exceeded supersaturation for dolomite, driven by increased evaporation and rising water temperature, paired with decreased fresh water inflow. Dolomitization during  $t_1$  likely took place across all submerged lime mud sediments simultaneously, but only replaced them partially.

With continuous increase in temperature the lake water became warmer and possibly even more supersaturated with respect to dolomite (the level of supersaturation was governed by counteracting processes at this time: the increase in temperature and evaporation versus removal of Mg via ongoing dolomite formation). During phase ( $t_2$ ) the lake water level dropped far enough such that the sediments located in the near-shore area were partially exposed. At this time reflux dolomitization continued in the submerged sediments whereas evaporative pumping took place in the subaerial exposed lake sediments ( $t_2$  in Figure 6.2.). Therefore, reflux and evaporative pumping occurred at the same time.

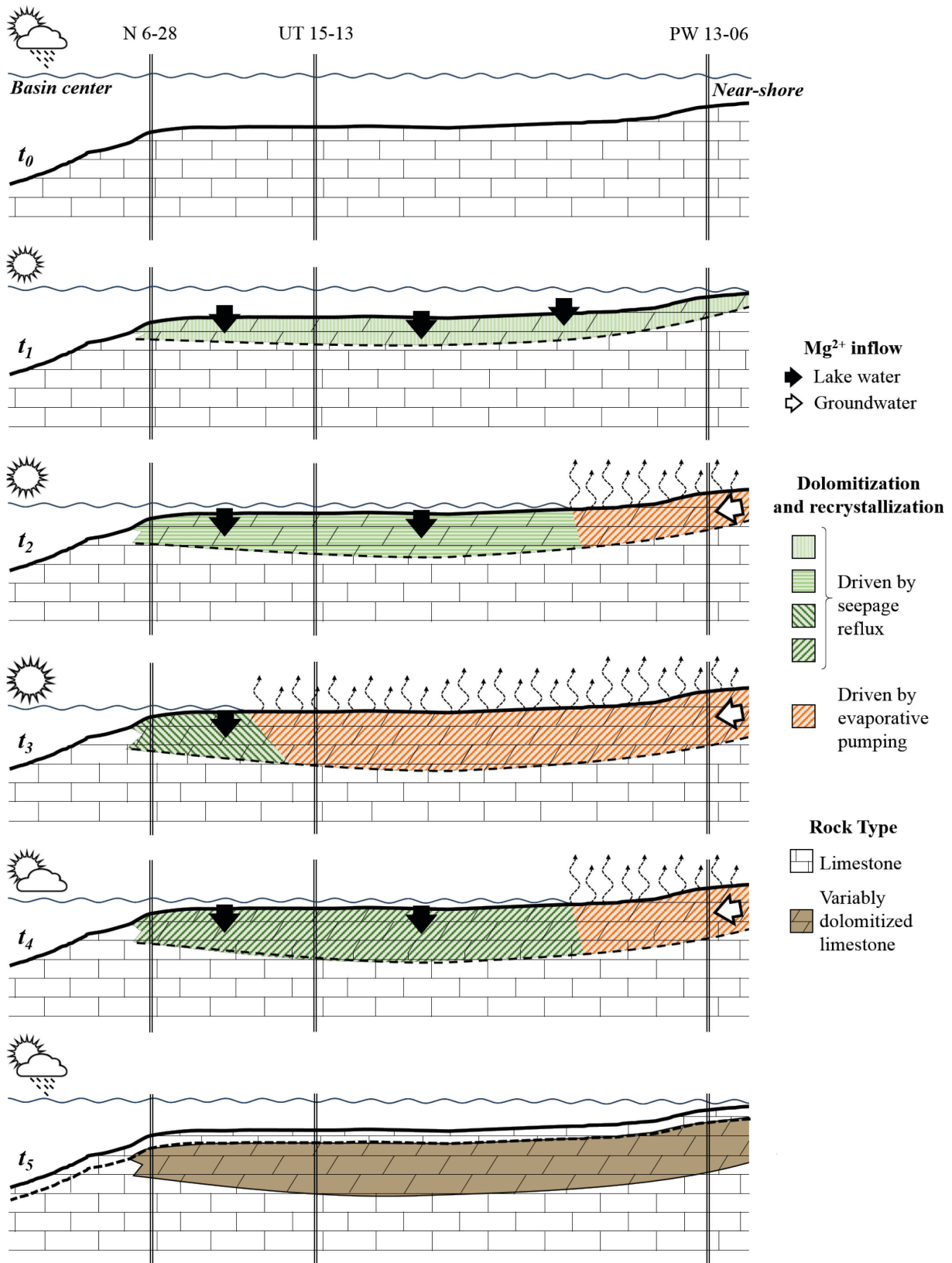


**Figure 6.2:** Interpretation of dolomitization of an individual PZ-layer in the UBm. See text for discussion.



At the maximum regression of the lake water table ( $t_3$ ), the temperature reached the highest values at  $\sim 35^\circ\text{C}$ , based on the oxygen isotope data (Chapter 5, Section 5.2.2.6). The lake/pore water may have reached maximum supersaturation with respect to dolomite (supersaturation on  $t_3 > t_2 > t_1$ ). Sediments deposited near the basin center that remained submerged were still subject to reflux dolomitization process, thus also for a longer period of time compared to the areas farther south that were exposed at this time and now subjected to evaporative pumping.

Following the warmest part of the climate cycle, the lake level would increase due to increased river recharge and reduced evaporation, and the water temperature and level of dolomite supersaturation would decrease ( $t_4$  in Figure 6.2). Renewed flooding of the previously exposed sediments likely overprinted the already formed dolomites to a minor degree of recrystallization as long as the lake water temperature was warm enough to overcome kinetic barriers.

Finally ( $t_5$ ), the system would return to the same or similar conditions that were present at the beginning of the cycle. Lime mud would now form on top of the dolomitized layer as long as the climate was cool and wet enough to allow for calcite precipitation.

Formation of the PZ layers by the combined seepage reflux and evaporative pumping processes necessitates that the inferred climate cycle took place at least as many times as there are dolostone-limestone couplets, i.e., this cycle was repeated at least five times (Figure 4.14). Furthermore, it cannot be ruled out that there were higher order (shorter) climate cycles that are masked within the observed dolostone-limestone couplets, as inferred by Eugster and Surdam (1973) and Eugster and Hardie (1978), who found that certain lacustrine and/or playa

phenomena (such as shrinkage cracks, crusts or nodules of a variety of evaporite minerals) are rather short lived and may not survive into the geologic record.

#### **6.1.4 Calcite – Dolomite – Chert: Chemical Lake water evolution**

The variation in the chemical composition of the lake water can be further characterized by the mineral association and timing between calcite, dolomite, and chert occurrence. The diagenesis of these minerals can be briefly described as: (i) calcite precipitation (deposition of lime mud), (ii) dolomitization of calcite (lime mud sediment and/or limestone), (iii) chert formation within PZ layers, and (iv) continued dolomitization. Precipitation of calcium carbonate was promoted during the fresh water and relatively low temperature phases. Dolomite formation was caused by evaporation of lake/pore water driven by increased temperature (see Chapter 5, sections 5.2.1.6 and 5.2.2.6). According to the estimation of lake water temperatures using  $\delta^{18}\text{O}$  geothermometry (Chapter 5, Section 5.2.2.6), the calcite-dolomite mineral association suggests a gradual increase of the lake water temperature from about 12°C (calcite precipitation) up to about 36° to 40°C (dolomitization).

In the fresh water scenario, calcite precipitated likely by a decrease in  $\text{CO}_2$  concentration either due to photosynthesis (high organic activity) or by lake water degassing (Eugster and Hardie, 1978; Tucker and Wright, 1990). Calcite precipitation led to an increase in the Mg/Ca ratio that, paired with an increase of lake/pore water temperature, favoured dolomitization. Chert, which is the only recognizable evaporite mineral in the stratigraphic interval of interest, and precipitated likely (i) at relatively advanced levels of evaporation of the lake/pore water (Eugster and Hardie, 1978), or (ii) by certain changes in the chemical

composition of the lake water due to increased Si-input from run-off and associated pH changes (Eugster, 1967). Chert formation in Lake Magadi (Kenya) is a good analog for chert formation in the UBm, where syndepositional formation of chert is due to pH reduction of alkaline brines associated to periods of dilution-concentration stages of the lake water driven by periods of rainfall alternating with evaporation (Eugster 1967). Additionally, the position of chert formation within the paragenetic sequence of the UBm (see Chapter 5, Sections 5.1 and 5.2 and Table 5.1) is crucial for the interpretation of dolomitization by virtue of enclosing earlier formed dolomite. Crystals of dolomite thus enclosed were isolated from the bulk formation water(s) during burial and thus hold promise to retain pristine isotopic signatures representing the conditions during dolomitization. Unfortunately, isotopic analysis of dolomite enclosed in chert could not be completed before completing this thesis.

The chemical variations of the lake/pore water proposed herein is in accordance with Eugster and Hardie's (1978) fluid evolution in a hydrologically 'closed' system. They proposed three main possible evolution pathways based on the  $\text{HCO}_3^- / (\text{Mg}^{2+} + \text{Ca}^{2+})$  ratio. In the case of the UBm, the lack of sodium carbonates and calcium sulfates within the stratigraphic interval of interest suggests lake water with an equal bicarbonate ( $\text{HCO}_3^-$ ) and  $\text{Mg}^{2+} + \text{Ca}^{2+}$  ratio. After precipitation of low-Mg calcite and dolomite, the lake water would have been impoverished in alkaline metals, which favored silica precipitation likely as opal (Eugster and Hardie, 1978). The isopachous euhedral quartz cement rims (Figures 5.5D and E) around the dolomitized peloids may represent silica precipitation by nearly complete pore water evaporation.

Last not least, a common way to characterize the chemistry and environment of dolomitization is by stoichiometry (or lack thereof) and ordering (Machel 2004). In the case of the UBm this approach yields a curious result. The dolomite crystals are characterized by a wide

range in Ca-excess (Chapter 5, Section 5.2.1.4) paired with a low cation ordering (Chapter 5, Section 5.2.1.5), suggesting a very low degree – if not nearly the absence of – ‘significant recrystallization’ *sensu* Machel (1999). This is highly unusual for rocks of this age (Chapter 1, Section 2.4) and burial history (Chapter 5, Section 5.1.3).

The low and/or almost lacking recrystallization of the Uteland Butte dolomites is probably due to (i) low permeability of the PZ layers, (ii) low water:rock ratio, (iii) a nearly closed system during burial, or (iv) a combination of these alternatives. This interpretation is supported by the low permeability values of all PZ layers with average values that range from  $8.1 \times 10^{-2}$  for PZ1,  $2.0 \times 10^{-2}$  for PZ1', and  $5.4 \times 10^{-2}$  for PZ2 (see Chapter 5, Section 5.4). On the other hand, Birdwell et al. (2016) measured the pressure gradient in 42 intervals in or near the UBm and found six intervals with pressure gradients equal to greater than 0.5 psi/ft. Anderson and Roesink (2013) calculated the UBm pressure gradient with maximum values of 0.65 psi/ft.

According to the calculated and measured pressures of the UBm, the stratigraphic interval of interest thus is characterized as an overpressured reservoir [based on Dickinson (1953) overpressure definition] with values equal to or higher than 0.5 psi/ft. The resulting low permeability and overpressure conditions of the unconventional reservoirs likely inhibited the dolomites from recrystallization, thereby preventing the calcium excess of the dolomites to get flushed out of the system.

## **6.2 Stratigraphic interval D and C Shales**

Periodic variations in climate are recorded by repetition of the idealized cycle (Figures 4.14 and 6.2), which is present five times within the stratigraphic interval of interest. Dolomite

formation was not possible without the changes in the climate that drove this cyclicity. Dolomitization thus was the result of cyclical variations in climate.

### **6.3 Regional paleogeography**

In addition to climate as the chief driving force of cyclicity and dolomitization in the UBm, tectonism has been recognized as a major factor controlling deposition and diagenesis in the region around the Uinta Basin (Davis et al., 2009; Gierlowski-Kordesch, 2010; Tänavsuu-Milkeviciene et al., 2017). Changes in depositional settings caused by climate variations occurred during relatively short periods of time, whereas changes driven by tectonism took longer periods of time (Tänavsuu-Milkeviciene et al., 2017).

Davis et al. (2009) interpreted the evolution of the catchment area of the lacustrine intermountain and coexisting basins of Claron Lake, Lake Flagstaff, and Uinta Lake (Figure 6.3). These authors identified shifts of the  $\delta^{18}\text{O}$  values in carbonate samples of around +6‰ from the base (UBm) to the middle section (Douglas Creek Member) of the GRF (Figure 6.3). Davis et al. (2009) interpreted these shifts as resulting from changes in the hydrologic closure that led to the evaporation of Uinta Lake at the top of the GRF (saline facies). According to Davis et al. (2009), the change in the catchment area was likely caused by post-depositional diachronous tectonic uplift that elevated the catchment area of Uinta Lake, which was probably higher than 2500 m at the time of deposition of the top of the GRF (saline facies). The  $\delta^{18}\text{O}$  values of the dolomite layers in the UBm are consistent with the values reported by Davis et al. (2009) and correspond to the values located at the base of the Uinta Basin (Figure 6.3C), in which the catchment area was probably lower in altitude.

The dolomite layers of the UBm do not record the regional tectonism because the latter occurred after UBm deposition and on a much larger time scale. The difference in the  $\delta^{18}\text{O}$  values of the dolomites between the PZ2 and PZ1' layers is only 0.3‰ PDB, and between the PZ1' and PZ1 layers it is only 0.4‰ PDB (Chapter 5, Section 5.2.1.6).

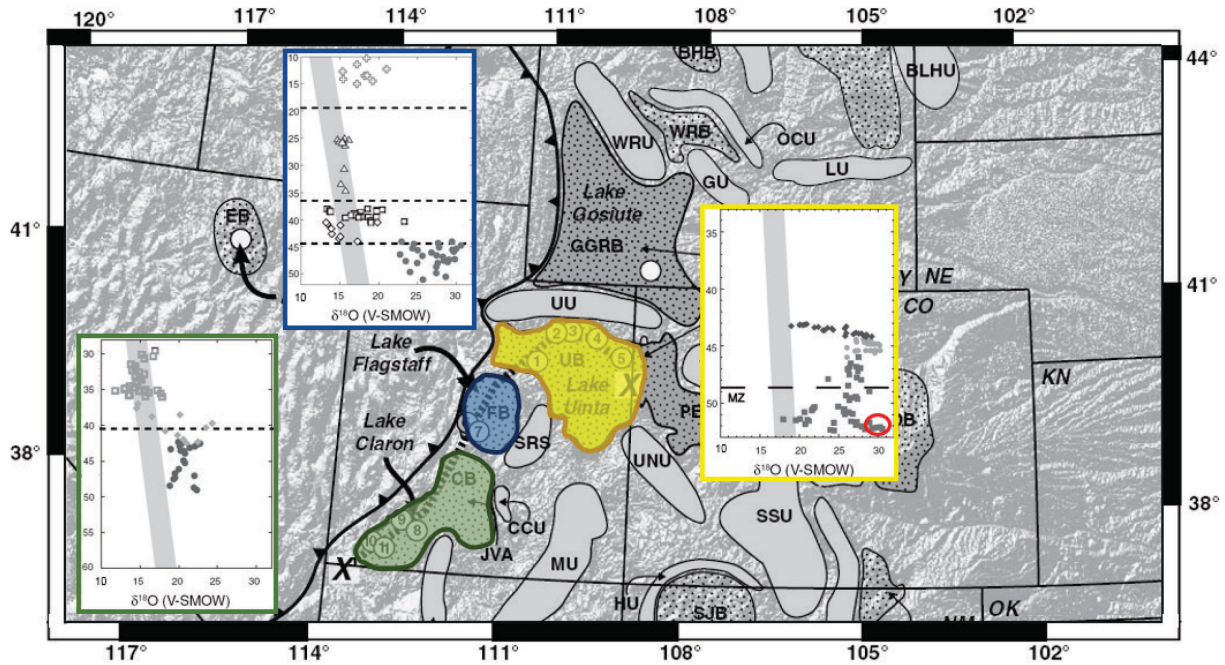


**Figure 6.3:** Decrease of the  $\delta^{18}\text{O}$  values for the Claron Basin (blue area) of about 5‰ (A), Flagstaff Basin (green area) of about 7‰ (B), and Uinta basin (yellow area) of about 6‰ (C), probably caused by tectonism (Davis et al., 2009). (C) Tectonic uplifting took place after UBm deposition around 45 My. The  $\delta^{18}\text{O}$  values of the dolomites in the PZ layers is highlighted by the red oval in the lower right corner of (C). Vertical axis in the inserted  $\delta^{18}\text{O}$  plots is time (My.), figure modified from Davis et al. (2009).

## **6.4 Dolomitization and reservoir properties**

### **6.4.1 Geometry of the dolomite PZ layers**

The dolomite PZ layers display a lenticular geometry variable in thickness, with the thickest sections located in an intermediate position between the near-shore and basin center areas, pinching out basinward (north) and landward (south) (Figures 6.4 to 6.6). PZ1 thickness varies from 1.9 ft (0.6 m) to 7.1 ft (2.2 m); PZ1' from 1.5 ft (0.5 m) to 7.1 ft (1.2 m); and PZ2 from 1.5 ft (0.5 m) to 4 ft (1.2 m). The thickness variations in the PZ layers were probably controlled by several factors, which include availability of dolomitizing fluids, Mg/Ca ratio,  $\text{Mg}^{2+}$  inflow (flux), paleobathymetry of Uinta Lake, porosity and permeability variations of the unconsolidated or partially consolidated lime mud, lake water level fluctuations, or a combination of these alternatives.

The paleobathymetry of the lake during dolomite formation likely was a shallow and flat littoral to sublittoral between the shore line and the lake center (Figures 4.13 and 6.2), possibly isolated at times from the lake center by carbonate shoals that were occasionally subaerially exposed. In this scenario, a "lagoon" would have been located between the shoal and the shore line, wherein the thicker section of the dolomite PZ layers could develop. In addition, and as noted before, it is possible that dolomite that had formed in the shallowest parts of the system got episodically washed into the deeper parts of the lake, either into the "lagoonal" area or farther down toward the lake center, as proposed by Eugster and Surdam (1973), thus increasing the thickness of the PZ layers.

Another factor that defined the thickness of the dolomite PZ layers, at least in part, was porosity variations in the partially consolidated lime mud material. The more porous and more



permeable material allowed the dolomitizing water to percolate and/or get pumped upward more easily than through the less porous and/or less permeable material. Reduction of porosity and permeability of the partially consolidated sediments that took place prior to dolomitization was generated by the calcite cementation phases (meniscus and blocky calcite cement) in the near shore areas (Chapter 5, Sections 5.1.1.2 and 5.1.1.4).

In addition, variations of the lake water level, composition, and temperature, as described in Section 6.1.3 and 6.1.4, may also have controlled the thickness of the PZ layers, at least partially. It is conceivable that the greatest thickness of the PZ layers correspond to those areas where reflux and evaporative pumping superimposed each other for the longest time and larger extent.

PZ1 isopachous map shows the highest thickness values with a southeast to northwest trend (Figure 6.4). This trend is unique for PZ1. In contrast, the PZ1' and PZ2 layers show the same thickness trend with the thicker section with an east – west trend (Figures 6.5 and 6.6). The SE-NW trend of the thicker section for PZ1 could be related to a major  $Mg^{2+}$  flux of groundwater coming from the paleorivers derived from the Uncompahgre uplift, at the southeast area of the Uinta Basin (see Figures 2.2 and 6.1) that favoured dolomitization around the area of the probable  $Mg^{2+}$  flux.

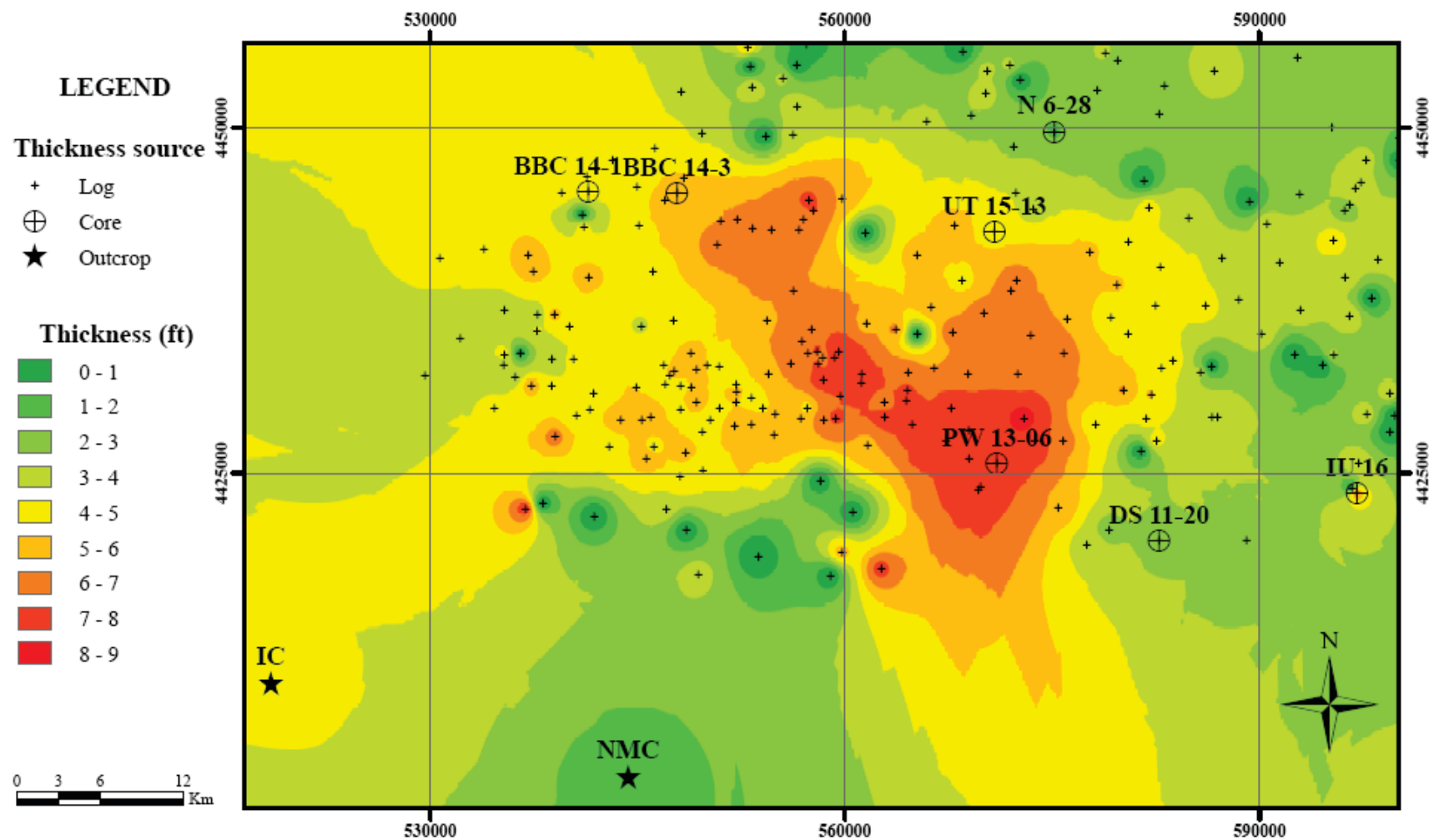


**Figure 6.4:** Isopachous map for PZ1 layer. Thickness measured from logs (data courtesy of Michael D. Vanden Berg, 2015), cores, and outcrops.

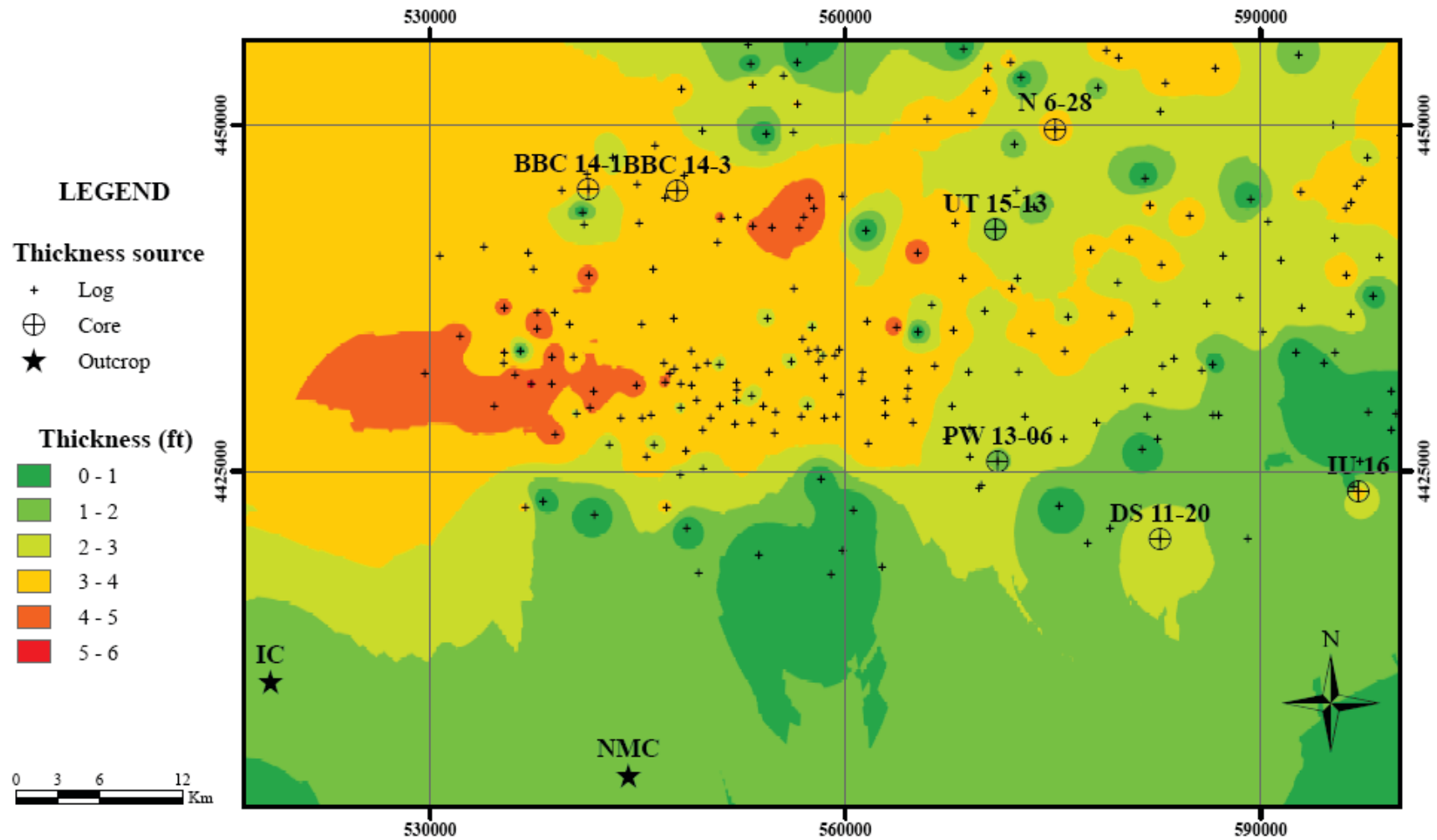


**Figure 6.5:** Isopachous map for PZ1' layer. Thickness measured from logs (data courtesy of Michael D. Vanden Berg, 2015), cores, and outcrops.

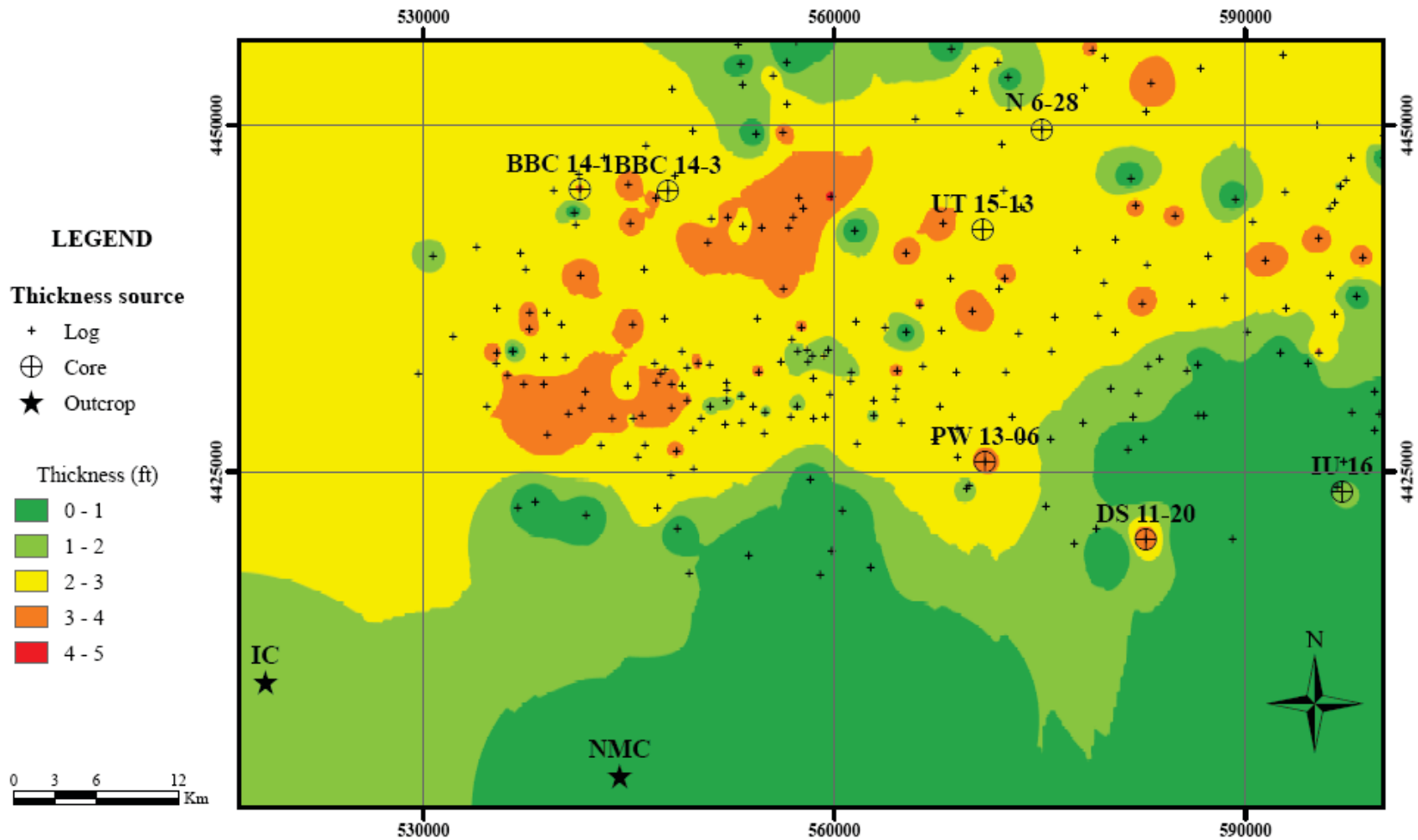


**Figure 6.6:** Isopachous map for PZ2 layer. Thickness measured from logs (data courtesy of Michael D. Vanden Berg, 2015), cores, and outcrops.

#### 6.4.2 Porosity and permeability

Dolomitization and porosity are closely related but there is no general rule that describes this relationship. Machel (2004) defined six potential sources of porosity enhancement related to dolomitization: so called mole-per-mole replacement, calcite dissolution, dolomite dissolution, pH reduction in pore water, fluid mixing, and thermochemical sulfate reduction.

In the stratigraphic section of interest, dolomitization might have increased porosity by itself as result of (i) the so-called mole-per-mole replacement that likely enhanced porosity due to volume loss, as represented by dolomitization (Equation 12), in which two moles of calcite are replaced by one mole of dolomite (Machel 2004), (ii) calcite dissolution (micrite), and (iii) dissolution of metastable dolomite located in the core of the dolomite crystals (Figures 5.13B and C, and 5.39A). Dissolution of these minerals was probably caused in the advanced stage of dolomitization after all available  $\text{Mg}^{2+}$  was exhausted and the fluid remained undersaturated in calcite; or when the fluid was close to the equilibrium and dolomite formation was kinetically inhibited while calcite dissolution was promoted (Machel, 2004).



On the other hand, there is a consistent difference in porosity between PZ layers and interbedded limestones (Figure 6.7). Dolomitized sediments may have had higher porosity compared to those layers that are now present as limestones, or the limestone layers were more prone to lose primary porosity through diagenesis than the dolomite layers. If so, the porosity differences is likely due to differences in the mechanical and chemical behavior of these rocks during mechanical and chemical compaction, respectively (Schmoker and Halley, 1982).

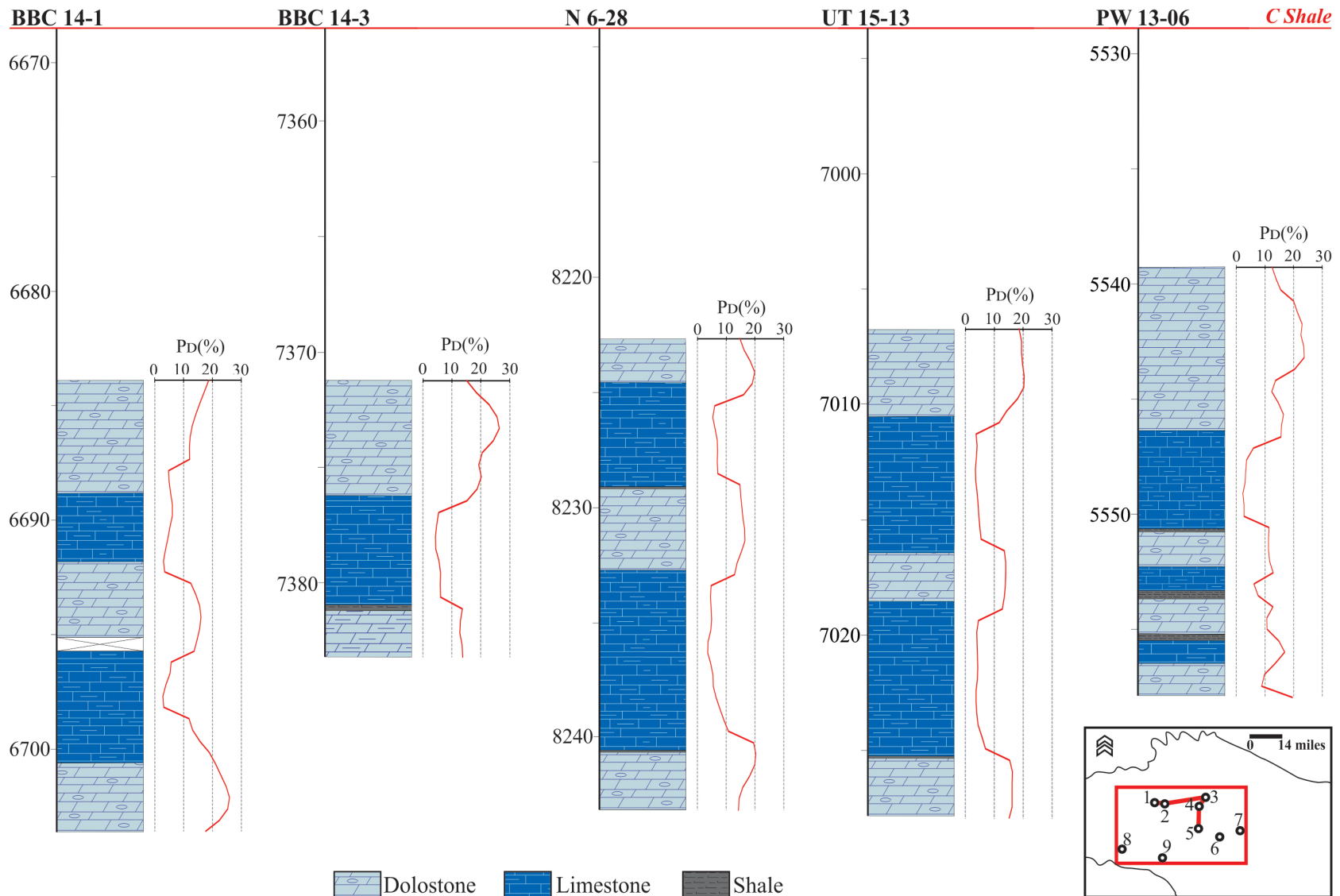


**Figure 6.7:** Porosity ( $P_D$ ) calculated from density logs for PZ layers and interbedded limestones. Numbers in the inset map stand for wells/outcrops as 1: BBC 14-1, 2: BBC 14-3, 3: N 6-28, 4: UT 15-13, 5: PW 13-06, 6: DS 11-20, 7: UI 16, 8: WCC, 9: NMC.

According to Hugman and Friedman (1979), grain size is the most important textural feature in carbonates rocks that controls the response during mechanical compression. Thus, the limestone and dolostone bed layers likely behaved similarly during mechanical compaction, given the same crystal size range for both minerals (calcite and dolomite). In contrast, the susceptibility to dissolve under a stress field is different for calcite and for dolomites. Calcite is more susceptible to dissolve than dolomite (Trurnit, 1968; Tada and Siever, 1989). Therefore, the limestone layers were more susceptible to chemical compaction (Phase 7), with or without the formation of stylolites. The latter form only when siliciclastic impurities are present in sufficient quantities.

Additionally, the dolomitization timing also contributed to preserve the inherited porosity. According to the paragenetic sequence defined for the interval of interest (Chapter 5, Section 5.1.2), dolomitization (Phase 3) took place before mechanical compaction (Phase 7). This circumstance literally solidified the dolomite layers, converting them into a stronger framework, allowing for greater preservation of the porosity during subsequent compaction.

The preservation of the primary porosity is evident in texture of the precursor limestones (Figure 6.8). Conservation of the original textures was achieved by replacement of micrite (in matrix, peloids, ooids, and intraclasts) by dolomite crystals of about the same crystal size of the parental micrite, otherwise the original texture (mudstone, wackestone, etc.) would have been obliterated.



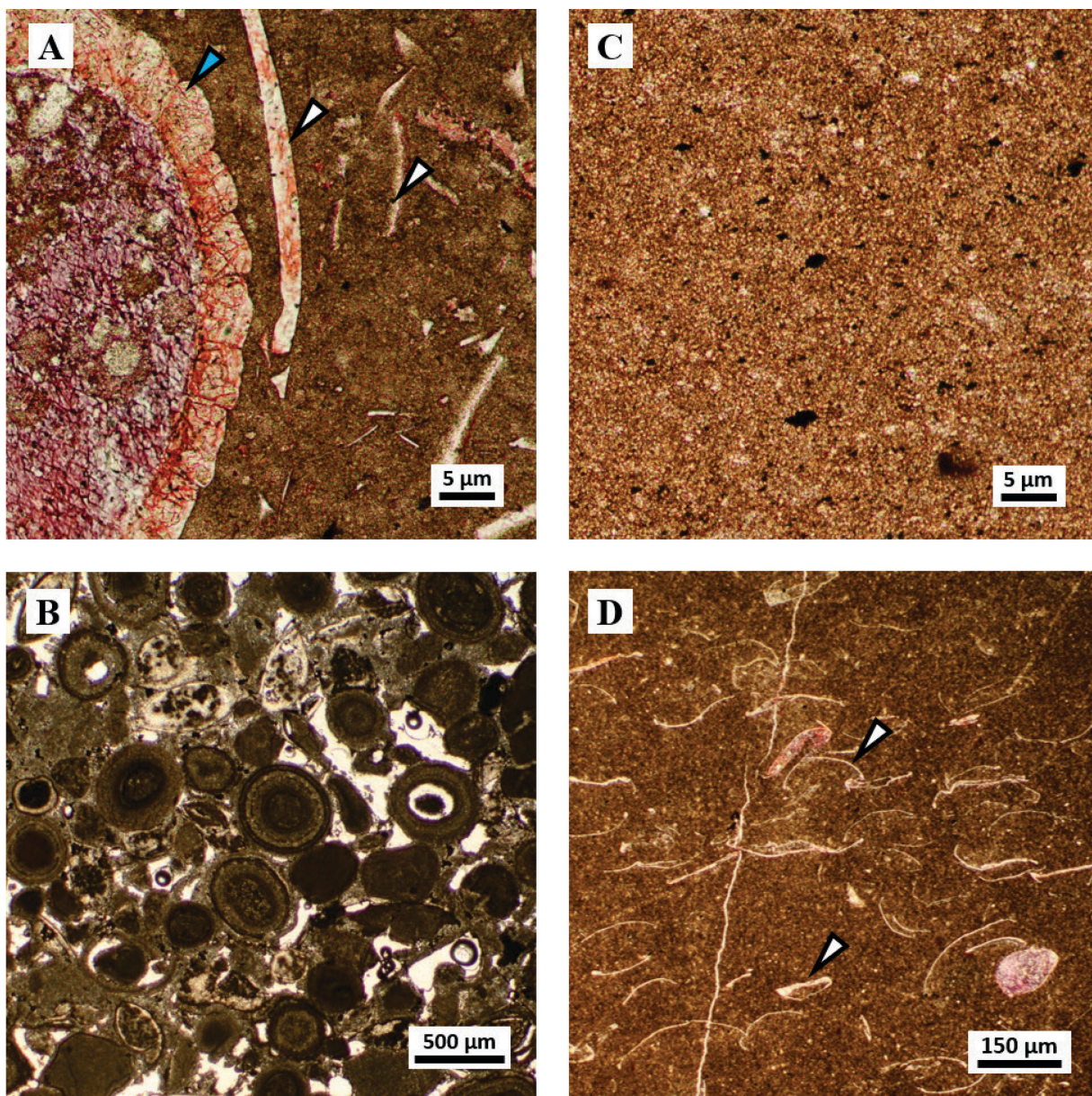


**Figure 6.8:** Preservation of textures from the precursor limestone. (A) TLP of dolopackstone, matrix-selective dolomitization, in which bioclasts (gyronite: blue arrow, ostracods shells: white arrows) were not replaced, well: BBC 14-3, sample: 28, 7374.05 ft. (B) TLP of dolograinstone, mimetic dolomite replacement of ooids, well: PW 13-06, sample: 6, 5539.5 ft. (C) TLP of dolomudstone, aphanocrystalline dolomite matrix and microvugs filled with hydrocarbons (arrows), well: UT 15-13, sample: 5, 6682.2 ft. (D) TLP of intraclastic dolowackestone, matrix completely dolomitized; ostracod shell fragments (arrows) were not dolomitized; well: BBC 14-1, sample: 13, 6684.9 ft.

Dolomite textures and porosity values show a positive correlation in some cases (Woody et al., 1996; Lucia, 2007; Moore, 2001). Woody et al. (1996) correlated planar-e textures with high porosity and high permeability values. In contrast, there is a weak positive correlation between dolomite texture and porosity for the PZ layers of the UBm. However, planar textures (planar-e and planar-s) preferentially show the highest porosity values, whereas nonplanar-a texture shows the lowest porosity values (Figure 6.9).

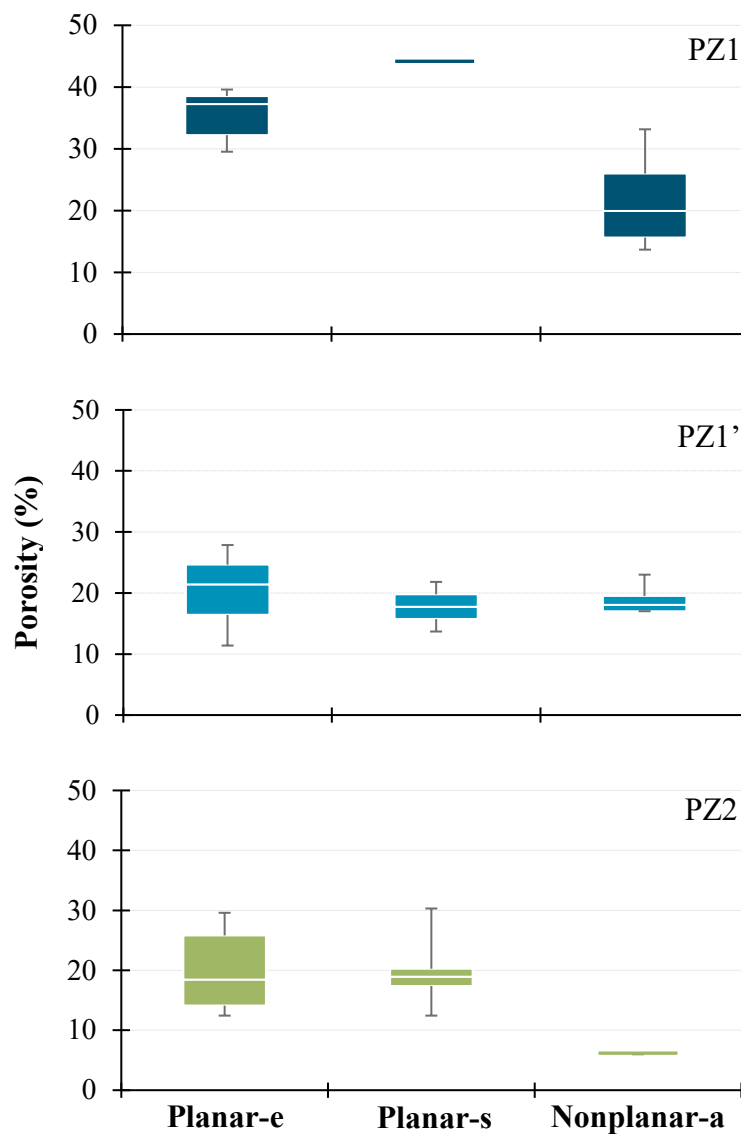


**Figure 6.9:** Dolomite texture versus porosity for each PZ layer. Dolomite texture determined from SEM images and porosity estimated by image analysis software (Chapter 5, Section 5.3.1).

Dolomite texture and crystal shape are also correlated with permeability. The pore throat shape is inversely proportional to permeability and can be expressed by Equation 13 (England et al., 1987) as the tortuosity factor  $\tau$ :

$$k = D * r^2 / \tau^2 \quad (\text{Equation 13})$$

where,  $k$  is permeability,  $D$  is a constant:  $1/8$ ,  $r$  is the mean pore radius, and  $\tau$  is tortuosity.

Furthermore, tortuosity  $\tau$  is also defined by the ratio of the length of the flow pathway relative to the length of the sample (Azar et al., 2008) (Figure 6.10)

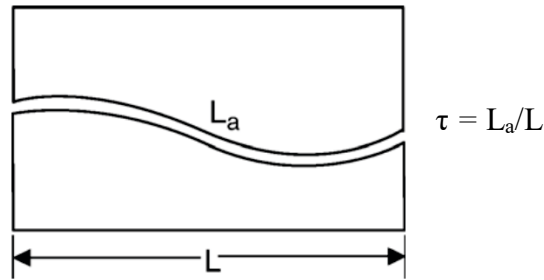


**Figure 6.10:** Scheme representing the tortuosity factor ( $\tau$ ) as the ratio of the length of the fluid flow pathway ( $L_a$ ) to the length of the sample ( $L$ ). Image from Azar et al. (2008).

Planar-e and planar-s textures commonly have short flow pathways ( $L_a$ ) with pore throat shapes defined by prismatic volumes (Figure 5.42A). These characteristics enhance permeability. In contrast, the nonplanar-a texture usually has longer flow pathways ( $L_a$ ) associated with irregular pore throat shapes (Figure 5.42B) that, coupled together, reduce permeability. However, the texture distribution, crystal size, and crystal shape in the PZ layers is highly variable, which is probably result of superimposed dolomitization events (reflux and evaporative pumping) that overprinted the original texture and modified the dolomite crystal size and shape.

The high heterogeneity of porosity and permeability features of these unconventional oil reservoir makes difficult to predict “sweet spots” within the basin. Nevertheless, the PZ1 layer has the highest thickness, porosity and permeability values between all PZ layers (Figure 6.11); a condition that paired with the overpressure setting in the basin center, becomes PZ1 layer as the highest potential reservoir for oil production.

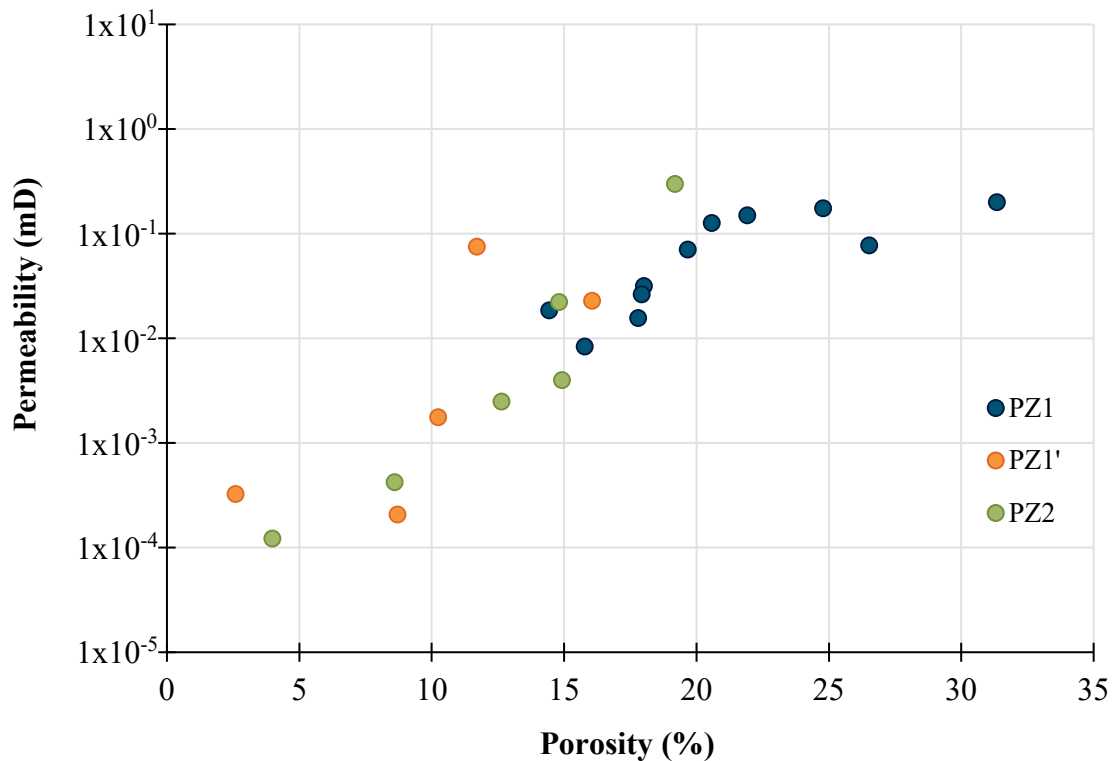


**Figure 6.11:** Porosity vs. permeability plot of the PZ layers. Data from core plugs (Tables 5.10 and 5.12), courtesy of Michael D. Vanden Berg.

The highest values of porosity and permeability of the PZ1 likely are related to the shapes of the dolomite crystals, which may have been controlled by temperature variations. The interpretation for dolomitization of the UBm as previously discussed is a generalized interpretation of dolomite formation for all PZ layers, however, the dolomitizing temperatures

are different for each layer. The average calculated temperature for the PZ1 is around 24 °C, for PZ1' it is around 26 °C, and for PZ2 it is around 28 °C (see Chapter 5, Section 5.2.2.6). The lower temperature of dolomitization for PZ1 favoured the preferential formation of euhedral and subhedral dolomite crystals (planar-e and planar-s textures), which enhanced the porosity – permeability properties of this layer (Figure 6.12).

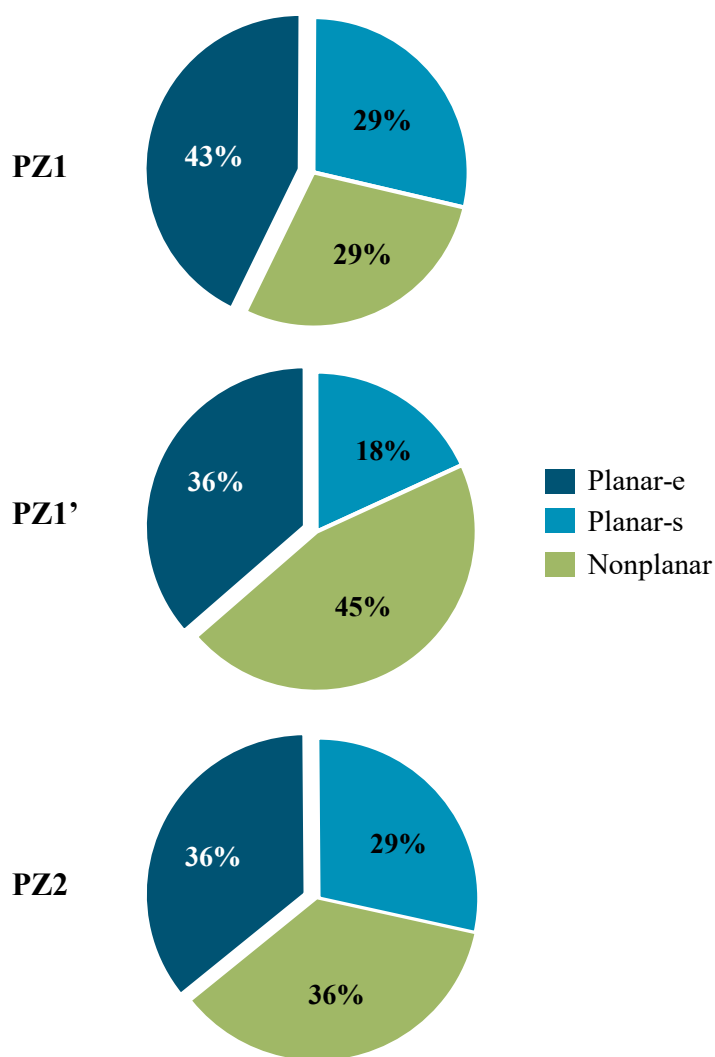


**Figure 6.12:** Dolomite textures percentage for each PZ layer. PZ1 layer has the most abundant planar-e texture of all PZ layers. Data from SEM images petrography.

## CHAPTER SEVEN

### CONCLUSIONS AND FUTURE WORK

#### 7.1 Conclusions

The work conducted in the process of this thesis project successfully addressed the five research objectives outlined in Chapter 1.1 as follows.

**Objective 1:** *Characterization and analysis of facies types for the Uteland Butte member as they relate to dolomitization.*

The Uteland Butte member was deposited in a range of littoral to sublittoral environments, in which ten lithofacies were recognized. The eight carbonate facies are dolomitized to variable degrees and are characterized by (i) selective dolomitization of micrite of matrix, peloids, ooids, and intraclast, and by (ii) variable preservation of the precursor limestone textures. However, bioclasts (mainly ostracods) are not dolomitized. The dolomitization process crosscut all facies boundaries from the distal sublittoral setting (mudstone facies) toward the littoral near-shore area (intraclastic packstone – ooid grainstone facies). Therefore, facies did not control dolomitization. Rather, dolomitization was favoured by variations in the composition and temperature of the lake and pore waters, ultimately driven by climate changes.



**Objective 2:** *Determination of the process(es) of dolomitization.*

Most, perhaps all dolomites in the PZ layers formed by replacement of unconsolidated and/or at least partially lithified lime mud sediments, i.e., by matrix-selective replacement. Dolomites are aphanocrystalline with sizes that range from 0.15 to 6  $\mu\text{m}$ . Ca-contents range widely from 49% to 59%, and cation ordering ( $d_{015} / d_{101}$ ) is generally low range from 0.1 to 0.5. The PZ layers display a tabular geometry pinching out toward the basin center and the near-shore areas. All these features conform to the type of dolomite known as penecontemporaneous, thus they probably formed very early in the diagenetic history.

Dolomitization was driven by climate changes that created distinctive variations in the amount of precipitation, in the amount of river inflow, water temperature, evaporation, and in lake and pore water chemistry. During the warmer climate periods, evaporation and reduced river inflow increased salinity sufficiently to create density-driven reflux of lake water in the subaqueous parts of the lake area, which - together with the attendant increases in temperature and  $\text{Mg}^{2+}/\text{Ca}^{2+}$  ratio in the lake water - resulted in dolomitization. At the same time the landward parts of the lake fell dry to form a playa, which increased in size over time while the actual lake surface and volume shrank. In the playa area dolomite formed from evaporating groundwater by evaporative pumping. Over time this process overprinted the areas formerly affected by reflux. Dolomitization in the UBm is thus interpreted as the result of two different yet superimposed processes: density-driven reflux and evaporative pumping. Dolomitization stopped when the climate turned sufficiently cool again to refill the lake, thereby freshening and cooling the lake water to enable calcite precipitation again.

**Objective 3:** *Investigation of how porosity and permeability are related to dolomitization.*

Dolomitization contributed to the lithification of the lime mud sediments, which also contributed to preserve the primary porosity inherited from the parental lime mud sediments/limestone. Furthermore, it is possible that the so-called mole-per-mole dolomite-calcite replacement enhanced the porosity of the PZ layers. Perhaps most importantly, the stratigraphic interval of interest is significantly overpressured, which inhibits both mechanical as well as chemical compaction, likely the main reason why the UBm has dolomite layers with porosities as high as about 45%, although permeabilities are generally low because of the small crystal sizes and shapes.

Dolomite crystals planar-e, planar-s and nonplanar textures are correlated with porosity and permeability. Planar textures (planar-e and planar-s) are associated with the highest values of porosity and permeability. However, dolomite textures, crystal size, and shapes are highly variable throughout the PZ layers.

**Objective 4:** *Characterization of the geometry (lateral and vertical extent) of the dolomite layers in the study area.*

The thickest sections within the dolomitized PZ layers are developed between the near-shore and the basin enter areas. These thicknesses variations were probably controlled by an interplay of paleobathymetry of Uinta Lake, regional variability of porosity-permeability of the parent lime mud sediments/limestones, fluctuations in the lake water temperature and chemical composition, and possibly by the presence of a sedimentary sill.



**Objective 5:** *Possible implications for petroleum reservoir development.*

Mapping of the most important reservoir characteristics, porosity and permeability, as well as identification of the dolomitization processes, has not led to the recognition of 'sweet spots' for hydrocarbon exploration or extraction. Overall, the variations in porosity and permeability within each PZ layer and across the entire study area are too small to significantly influence exploration or development strategies. The best areas for exploration and development are the ones that are most highly overpressured, generally toward the basin center, which was already known at the beginning of this thesis project.

## **7.2 Future work**

1. One of the most intriguing finding of this study is the relative compositional (high Ca-excess) and structural (low cation ordering) immaturity of the Uteland Butte dolomites. This finding is almost unheard of in dolomites of Tertiary age buried to ~3,000m and to temperatures around 100 °C. The interpretation of this finding given here, i.e., inhibition of recrystallization due to high overpressure, needs verification by further investigation. Does overpressuring inhibit dolomite recrystallization elsewhere? Are all types of dolomite affected or only penecontemporaneous dolomites like the ones in the UBm? What roles do geothermal gradient and the rate of burial play?

2. Another intriguing finding is the discrepancy between the temperatures calculated by the conventional oxygen isotope method and the clumped isotope method. Related to this point is the finding that some temperatures from clumped isotope thermometry are significantly higher than the maximum burial temperature in the area. At this time one is forced to conclude

that the clumped isotope method needs refinement, or that at least some dolomite samples have experienced oxygen isotope exchange despite their compositional and structural immaturity (see Point 1 above). Samples were taken of dolomite pairs within and outside of chert nodules. It is hoped that dolomite encased in chert and thus sheltered from fluid exchange during burial yield more accurate and thus more reliable results of the temperatures of dolomite formation. Unfortunately, the samples taken for this part of the project could not be analysed before completion of this thesis.

## REFERENCES

- Adams, J. E., and Rhodes, M. L., 1960, Dolomitization by seepage refluxion: AAPG Bulletin, v. 44, no. 12, p. 1912-1920, <http://archives.datapages.com/data/bulletns/1957-60/images/pg/00440012/1900/19120.pdf>.
- Al-Aasm, I. S., Taylor, B. E., and South, B., 1990, Stable isotope analysis of multiple carbonate samples using selective acid extraction: Chemical Geology: Isotope Geoscience Section, v. 80, no. 2, p. 119-125, [https://doi.org/10.1016/0168-9622\(90\)90020-D](https://doi.org/10.1016/0168-9622(90)90020-D).
- Analysis of  $^{13}\text{C}$  and  $^{18}\text{O}$  of carbonate minerals by CF-IRMS, <http://www.ucalgary.ca/uofcisl/techniques>.
- Anderson, J. G., and Roesink, J. G., 2013, Reservoir characterization of the Uteland Butte Formation in the Uinta Basin, American Association of Petroleum Geologists Search and Discovery Article #50888, [http://www.searchanddiscovery.com/pdfz/documents/2013/50888anderson/ndx\\_anderson.pdf.html](http://www.searchanddiscovery.com/pdfz/documents/2013/50888anderson/ndx_anderson.pdf.html).
- Anderson, T. W., and Darling, D. A., 1954, A test of goodness of fit: Journal of the American statistical association, v. 49, no. 268, p. 765-769, DOI:10.1080/01621459.1954.10501232.
- Asquith, G. B., and Gibson, C. R., 1982, Basic well log analysis for geologists: American Association of Petroleum Geologists: Tulsa, The American Association of Petroleum Geologist, 216 p.
- Azar, J. H., Javaherian, A., Pishvaie, M. R., and Nabi-Bidhendi, M., 2008, An approach to defining tortuosity and cementation factor in carbonate reservoir rocks: Journal of Petroleum Science and Engineering, v. 60, no. 2, p. 125-131, DOI:10.1016/j.petrol.2007.05.010.
- Baars, D. L., and Stevenson G. M., 1981, Tectonic evolution of western Colorado and eastern Utah, *in* R. C. Epis and J. F. Callender, eds., Western Slope (Western Colorado) - New Mexico Geological Society 32nd Annual Fall Field Conference Guidebook: New Mexico Geological Society, p. 105-112.
- Baccelle, L. and Bosellini, A., 1965, Diagrammi per la stima visiva della composizione percentuale nelle rocche sedimentary: Annali dell'Univrsità di Ferrara (Nuova Serie), Sezione 9, Scienze Geologiche e Paleontologiche, v. 1, no. 3, p. 59-62.
- Banner, J. L., 1995, Application of the trace element and isotope geochemistry of strontium to studies of carbonate diagenesis: Sedimentology, v. 42, no. 5, p. 805-824, DOI:10.1111/j.1365-3091.1995.tb00410.x.

- Barron, E. J, 1990, Climate and Lacustrine Petroleum Source Prediction, *in* Katz, B. J., ed., Lacustrine Basin Exploration, AAPG Memoir 50: The American Association of Petroleum Geologists, p. 1-18.
- Belovsky, G. E., et al., 2011, The Great Salt Lake Ecosystem (Utah, USA): long term data and a structural equation approach: *Ecosphere*, v.2, no. 3, 1-40, DOI:10.1890/ES10-00091.1.
- Bereskin, S. R., Morgan, C. D., and McClure, K. P, 2004, Descriptions, petrology, photographs, and photomicrographs of core from the Green River Formation, south-central Uinta Basin, Utah: Utah Geological Survey Miscellaneous Publication, v. 4, p. 1 – 38, <http://archives.datapages.com/data/utah-geological-survey/data/mp-04-2.pdf>
- Berner, R. A., De Leeuw, J. W., Spiro, B., Murchison, D. G., and Eglinton, G., 1985, Sulphate reduction, organic matter decomposition and pyrite formation [and discussion]: *Philosophical Transactions of the Royal Society of London A: Mathematical, Physical and Engineering Sciences*, v. 315, no. 1531, p. 25-38, <http://www.jstor.org/stable/37702>.
- Best, M.G, 1982, *Igneous and Metamorphic Petrology*: San Francisco, W. H. Freeman and Company, 630 p.
- Bhat, H. L, 2015, *Introduction to crystal growth: principles and practice*: Boca Raton, CRC Press, 238 p.
- Birdwell, J. E., Vanden Berg, M. D. V., Johnson, R. C., and Brownfield, M. E., 2016, Geological, geochemical and reservoir characterization of the Uteland Butte member of the Green River Formation, Uinta Basin, Utah, *in* Michael P. D., Debra K. H., and Paul G. L., *Hydrocarbon Source Rocks in Unconventional Plays, Rocky Mountain Region: The Rocky Mountain Association of Geologist*, p. 352-378.
- Bohrer, B., and Schultze, M, 2008, Stratification of lakes: *Reviews of Geophysics*, v. 46, no. 2, 1-27, <http://onlinelibrary.wiley.com/doi/10.1029/2006RG000210/epdf>.
- Boggs, S. J., and Krinsley, D, 2006, *Application of cathodoluminescence imaging to the study of sedimentary rocks*: New York, Cambridge University Press, 165 p.
- Bradley, W. H, 1931, Origin and Microfossils of the Oil Shale of the Green River Formation of Colorado and Utah: U.S. Geological Survey Professional Paper 168, p. 1-58, <https://pubs.usgs.gov/pp/0168/report.pdf>.
- Broecker, W. S, 1971, A kinetic model for the chemical composition of sea water: *Quaternary Research*, v. 1, no.2, p. 188-207, [https://doi.org/10.1016/0033-5894\(71\)90041-X](https://doi.org/10.1016/0033-5894(71)90041-X).
- Budd, D. A, 1997, Cenozoic dolomites of carbonate islands: their attributes and origin: *Earth-Science Reviews*, v. 42, no 1-2, p. 1-47, [https://doi.org/10.1016/S0012-8252\(96\)00051-7](https://doi.org/10.1016/S0012-8252(96)00051-7).

- Carroll, A. R., and Bohacs, K. M., 1999, Stratigraphic classification of ancient lakes: Balancing tectonic and climatic controls: *Geology*, v. 27, no. 2, p. 99-102, DOI:10.1130/0091-7613(1999)027<0099:SCOALB>2.3.CO;2.
- Case, J. E., 1991, *Geologic Map of the Northwestern Part of the Uncompahgre Uplift, Grand County, Utah, and Mesa County, Colorado, with Emphasis on Proterozoic Rocks*. U.S. Geological Survey.
- Cashion, W. B., 1967, Geology and fuel resources of the Green River Formation, southeastern Uinta basin, Utah and Colorado: U.S. Geological Survey Professional Paper 548, p. 1-48, <https://pubs.usgs.gov/pp/0548/report.pdf>.
- Cashion, W. B., 1995, Stratigraphy of the Green River Formation, Eastern Uinta Basin, Utah and Colorado - A Summary: Grand Junction Geological Society, p. 15 – 21, <http://archives.datapages.com/data/grand-junction-geooc/data/013/013001/pdfs/15>.
- Choquette, W., and Pray, L. C., 1970, Geologic nomenclature and classification of porosity in sedimentary carbonates: American Association of Petroleum Geologist Bulletin, v. 54, no. 2, p. 207-250, <http://archives.datapages.com/data/bulletns/1968-70/images/pg/00540002/0200/02070.pdf>.
- Cohen, A. S., 2003, *Paleolimnology: the history and evolution of lake systems*: New York, Oxford University Press, 500 p.
- Cole, R. D., and Picard, M. D., 1978, Comparative mineralogy of nearshore and offshore lacustrine lithofacies, Parachute Creek Member of the Green River Formation, Piceance Creek Basin, Colorado, and eastern Uinta Basin, Utah: Geological Society of America Bulletin, v. 89, no. 10, p. 1441-1454, DOI:10.1130/0016-7606(1978)89<1441:CMONAO>2.0.CO;2.
- Davis, S. J., 2008, Synorogenic evolution of large-scale drainage patterns: Isotope paleohydrology of sequential laramide basins [Ph.D. thesis]: Stanford, Stanford University, 204 p., <http://search.proquest.com/docview/304471073?accountid=14474>.
- Davis, S. J., Mulch, A., Carroll, A. R., Horton, T. W., and Chamberlain, C. P., 2009, Paleogene landscape evolution of the central North American Cordillera: Developing topography and hydrology in the Laramide foreland: Geological Society of America Bulletin, v. 121, no. 1-2, p. 100-116, DOI:10.1130/B26308.1.
- Davison, W., 1993, Iron and manganese in lakes: *Earth-Science Reviews*, v. 34, no. 2, p. 119-163, DOI: 10.1016/0012-8252(93)90029-7.
- Degens, E. T., and Epstein, S., 1964, Oxygen and carbon isotope ratios in coexisting calcites and dolomites from recent and ancient sediments: *Geochimica et Cosmochimica Acta*, v. 28, no. 1, p. 23-44, [https://doi.org/10.1016/0016-7037\(64\)90053-5](https://doi.org/10.1016/0016-7037(64)90053-5).

- Desborough, G. A., 1978, A biogenic-chemical stratified lake model for the origin of oil shale of the Green River Formation: An alternative to the playa-lake model: Geological Society of America Bulletin, v. 89, no. 7, p. 961-971, DOI:10.1130/0016-7606(1978)89<961:ABSLMF>2.0.CO;2.
- Dickinson, G., 1953, Geological aspects of abnormal reservoir pressures in Gulf Coast Louisiana: AAPG Bulletin, v. 37, no. 2, p. 410-432, <http://archives.datapages.com/data/bulletns/1953-56/images/pg/00370002/0400/04100.pdf>.
- Dickinson, W. R., Klute, M. A., Hayes, M. J., Janecke, S. U., Lundin, E. R., McKittrick, M. A., and Olivares, M. D., 1988, Paleogeographic and paleotectonic setting of Laramide sedimentary basins in the central Rocky Mountain region: Geological Society of America Bulletin, v. 100, no. 7, p. 1023-1039, DOI:10.1130/0016-7606(1988)100<1023:PAPSOL>2.3.CO;2.
- Dickinson, W. R., Lawton, T. F., and Inman, K. F., 1986, Sandstone detrital modes, central Utah foreland region: stratigraphic record of Cretaceous-Paleogene tectonic evolution: Journal of Sedimentary Research, v. 56, no. 2, p. 276-293, <http://archives.datapages.com/data/sepm/journals/v55-58/data/056/056002/pdfs/0276.pdf>.
- Dickinson, W. R., Lawton, T. F., Pecha, M., Davis, S. J., Gehrels, G. E., and Young, R. A., 2012, Provenance of the Paleogene Colton Formation (Uinta Basin) and Cretaceous–Paleogene provenance evolution in the Utah foreland: Evidence from U-Pb ages of detrital zircons, paleocurrent trends, and sandstone petrofacies: Geosphere, v. 8, no. 4, p. 854, DOI:10.1130/GES00763.1.
- Dickson, J. A. D., 1965, A modified staining technique for carbonates in thin section. Nature, v. 205, no. 4971, p. 587, <http://dx.doi.org/10.1038/205587a0>.
- Doelling, H. H., 2002, Interim Geologic Map of the San Rafael Desert 30' x 60' Quadrangle, Emery and Grand Counties, Utah, scale 1:100,000.
- Dunham, R. J., 1962, Classification of carbonate rocks according to depositional textures: The American Association of Petroleum Geologists Memoir 1, p. 108-121, <http://archives.datapages.com/data/specpubs/carbona2/images/a038/a0380001/0100/01080.pdf>.
- Dyni, J.R., Milton, C., and Cashion, W.B., 1985, The saline facies of the upper part of the Green River Formation near Duchesne, Utah, *in* Picard, M.D, ed., Geology and Energy Resources, Uinta Basin of Utah. Salt Lake City: Utah Geological Association Publication, p. 51-60, <http://archives.datapages.com/data/uga/data/055/055001/pdfs/51>.
- Eardley, A. J., 1938, Sediments of Great Salt Lake, Utah: AAPG Bulletin, v. 22, no. 10, p. 1305-1411, <http://archives.datapages.com/data/bulletns/1938-43/images/pg/00220010/1300/13050.pdf>.

- Ebner, M., Toussaint, R., Schmittbuhl, J., Koehn, D., and Bons, P., 2010, Anisotropic scaling of tectonic stylolites: A fossilized signature of the stress field?: *Journal of Geophysical Research: Solid Earth*, v. 115, no. B6, DOI:10.1029/2009JB006649.
- Embry III, A. F., and Klovan, J. E., 1971, A late Devonian reef tract on northeastern Banks Island, NWT: *Bulletin of Canadian Petroleum Geology*, v. 19, no. 4, p. 730-781, <http://archives.datapages.com/data/cspg/data/019/019004/pdfs/0730.pdf>.
- England, W. A., Mackenzie, A. S., Mann, D. M., and Quigley, T. M., 1987, The movement and entrapment of petroleum fluids in the subsurface: *Journal of the Geological Society*, v. 144, no. 2, p. 327-347, DOI: 10.1144/gsjgs.144.2.0327.
- Esteban, M., Klappa, C. F., 1983, Subaerial exposure environment, *in* Scholle, P.A., Bebout, D. G., and Moore, C. H., eds., *Carbonate depositional environments*: American Association of Petroleum Geologists, Memoir, 33, p. 1-54.
- Eugster, H. P., 1967, Hydrous sodium silicates from Lake Magadi, Kenya: Precursors of bedded chert: *Science*, v. 157, no. 3793, p. 1177-1180, DOI: 10.1126/science.157.3793.1177.
- Eugster, H. P., and Hardie, L. A., 1978, Saline lakes, *in* Lerman A. and Baccini P., *Lakes: Chemistry, Geology, Physics*, p. 237-293, New York: Springer-Verlag.
- Eugster, H. P., and Surdam, R. C., 1973, Depositional environment of the Green River Formation of Wyoming: A preliminary report: *Geological Society of America Bulletin*, v. 84, no. 4, p. 1115-1120, DOI:10.1130/0016-7606(1973)84<1115:DEOTGR>2.0.CO;2.
- Flöerke, O. W., Graetsch, H., Martin, B., Röeller, K., and Wirth, R., 1991, Nomenclature of micro- and non-crystalline silica minerals, based on structure and microstructure: *Neues Jahrbuch Fuer Mineralogie. Abhandlungen*, v. 163, no. 1, p. 19-42.
- Flügel, E., 2010, *Microfacies of carbonate rocks: Analysis, interpretation and application*. 2nd edition: Berlin, Springer, 984 p.
- Folk, R. L., and Land, L. S., 1975, Mg/Ca ratio and salinity: two controls over crystallization of dolomite: *American Association of Petroleum Geologists Bulletin*, v. 59, no. 1, p. 60-68, <http://archives.datapages.com/data/bulletns/1974-76/images/pg/00590001/0050/00600.pdf>.
- Folk, R. L., and Pittman, J. S., 1971, Length-slow chalcedony; a new testament for vanished evaporites: *Journal of Sedimentary Petrology*, v. 41, no. 4, p. 1045-1058. DOI:10.1306/74D723F1-2B21-11D7-8648000102C1865D.
- Folk, R. L., and Siedlecka, A., 1974, The “schizohaline” environment: Its sedimentary and diagenetic fabrics as exemplified by Late Paleozoic rocks of Bear Island, Svalbard: *Sedimentary Geology*, v. 11, no. 1, p. 1-15, DOI:10.1016/0037-0738(74)90002-5.

- Folk, R. L., and Weaver, C. E., 1952, A study of the texture and composition of chert: *American Journal of Science*, v. 250, p. 498-510, DOI:10.2475/ajs.250.7.498.
- Foreman, B. Z., Heller, p. L., and Clementz, M. T., 2012, Fluvial response to abrupt global warming at the Palaeocene/Eocene boundary: *Nature*, v. 49, no. 7422, p. 92-95, doi:10.1038/nature11513.
- Fouch, T. D., 1976, Revision of the lower part of the Tertiary System in the central and western Uinta basin, Utah: *Geological Society Bulletin* 1405-C, p. C1-C7, <https://pubs.usgs.gov/bul/1405c/report.pdf>.
- Freytet, P., and Verrecchia, E. P., 2002, Lacustrine and palustrine carbonate petrography; an overview. *Journal of Paleolimnology*, 27(2), p. 221-237.
- Friedman, I., and O'Neil, J. R., 1977, Data of geochemistry: Compilation of stable isotope fractionation factors of geochemical interest: US Geological Survey Bulletin Vol 440-KK, <https://pubs.usgs.gov/pp/0440kk/report.pdf>.
- Gat, J. R., 1995, Stable isotopes of fresh and saline lakes, *in* Lerman, A., Imboden, D. M., and Gat, J. R., eds., *Physics and chemistry of lakes*: Springer-Verlag Heidelberg, p. 139-165.
- Ghosh, P., Adkins, J., Affek, H., Balta, B., Guo, W., Schauble, E. A., Scharg, D., and Eiler, J. M., 2006, 13 C–18 O bonds in carbonate minerals: A new kind of paleothermometer: *Geochimica et Cosmochimica Acta*, v. 70, no. 6, p. 1439-1456, <https://doi.org/10.1016/j.gca.2005.11.014>.
- Gierlowski-Kordesch, E. H., 2010, Lacustrine carbonates, *in* Alonso-Zarzs A. M. and Tanner L. H, eds., *Carbonates in continental settings: Facies, environments, and processes*, *Developments in Sedimentology* 61: Oxford, Elsevier, p. 1-101.
- Gierlowski-Kordesch, E. H., Jacobson, A. D., Blum, J. D., and Garces, B. V., 2008, Watershed reconstruction of a Paleocene–Eocene lake basin using Sr isotopes in carbonate rocks: *Geological Society of America Bulletin*, v. 120, no. 1-2, p. 85-95, DOI:10.1130/B26070.1.
- Goldsmith, J. R., and Graf, D. L., 1958, Structural and compositional variations in some natural dolomites: *The Journal of Geology*, v. 66, no. 6, p 678-693, <http://www.jstor.org/stable/30056855>.
- Gregg, J. M., 1985, Regional epigenetic dolomitization in the Bonnetterre Dolomite (Cambrian), southeastern Missouri: *Geology*, v. 13, no. 7, p. 503-506, DOI:10.1130/0091-7613(1985)13<503:REDITB>2.0.CO;2.



- Gregg, J. M., and Shelton, K. L. (1989). Minor-and trace-element distributions in the Bonneterre Dolomite (Cambrian), southeast Missouri: Evidence for possible multiple-basin fluid sources and pathways during lead-zinc mineralization: *Geological Society of America Bulletin*, v. 101, no. 2, p. 221-230, DOI:10.1130/0016-7606(1989)101<0221:MATEDI>2.3.CO;2.
- Gregg, J. M., and Sibley, D. F, 1984, Epigenetic dolomitization and the origin of xenotopic dolomite texture: *Journal of Sedimentary Research*, v. 54, no. 3, p. 908-931, <http://archives.datapages.com/data/sepm/journals/v51-54/data/054/054003/pdfs/0908.pdf>.
- Gregg, J. M., Bish, D. L., Kaczmarek, S. E., and Machel, H. G., 2015, Mineralogy, nucleation and growth of dolomite in the laboratory and sedimentary environment: A review: *Sedimentology*, v. 62, no. 6, p. 1749-1769, DOI:10.1111/sed.12202.
- Gregg, J. M., Howard, S. A., and Mazzullo, S. J., 1992, Early diagenetic recrystallization of Holocene (< 3000 years old) peritidal dolomites, Ambergris Cay, Belize: *Sedimentology*, v. 39, no. 1, p. 143-160, DOI:10.1111/j.1365-3091.1992.tb01027.x.
- Håkanson, L., and Jansson, M, 1983, *Principles of Lake Sedimentology*: Berlin: Springer-Verlag, 387 p.
- Hansen, W. R., 1965, *Geology of the Flaming Gorge area Utah – Colorado – Wyoming U. S. Geological Survey Professional Paper 490*: Washington, United States Government Printing Office, p. 1-196, <https://pubs.usgs.gov/pp/0490/report.pdf>.
- Hao, F., Zhou, X., Zhu, Y., Bao, X., and Yang, Y., 2009, Charging of the Neogene Penglai 19-3 Field, Bohai Bay Basin, China; oil accumulation in a young trap in an active fault zone: *AAPG Bulletin*, v. 93, no. 2, p. 155-179, doi:10.1306/09080808092
- Hardy, R, and Tucker, M. E., 1988, X-Ray powder diffraction of sediments, *in* Tucker M., ed., *Techniques in sedimentology*: Oxford: Blackwell Scientific Publications. p. 191-228.
- Heaney, P. J., 1995, Moganite as an indicator for vanished evaporites; a testament reborn?: *Journal of Sedimentary Research, Section A: Sedimentary Petrology and Processes*, v. 65, no. 4, pp. 633-638, DOI: 10.1306/D4268180-2B26-11D7-8648000102C1865D.E
- Hintze, L. F., Willis, G. C., Laes, D. Y., Sprinkel, D. A., and Brown, K. D., 2000, *Digital geologic map of Utah*. Utah Geological Survey, Utah Department of Natural Resources, scale 1:500,000.
- Hsü, K. J., and Siegenthaler, C., 1969, Preliminary experiments on hydrodynamic movement induced by evaporation and their bearing on the dolomite problem: *Sedimentology*, v. 12, no. 1-2, p. 11-25, DOI: 10.1111/j.1365-3091.1969.tb00161.x.
- Hudson, J. D., 1977, Stable isotopes and limestone lithification: *Journal of the Geological Society*, v. 133, no. 6, p. 637-660, <http://DOI:10.1144/gsjgs.133.6.0637>.

- Hugman III, R. H. H., and Friedman, M., 1979, Effects of texture and composition on mechanical behavior of experimentally deformed carbonate rocks: American Association of Petroleum Geologists Bulletin, v. 63, no. 9, p. 1478-1489.
- Hunt, C. B., 1956, Cenozoic Geology of the Colorado Plateau: US Geological Survey Professional Paper 279, p. 1-99, <https://pubs.usgs.gov/pp/0279/report.pdf>.
- Irwin, H., Curtis, C., and Coleman, M., 1977, Isotopic evidence for source of diagenetic carbonates formed during burial of organic-rich sediments: Nature, v. 269, p. 209-213, DOI:10.1038/269209a0.
- James, N. P., and Choquette, P. W., 1984, Diagenesis 9. Limestones - The Meteoric Diagenetic Environment: Geoscience Canada, v. 11, no. 4, p. 161-194, <https://journals.lib.unb.ca/index.php/GC/article/view/3395/3909>.
- Johnson, R. C., 1985, Early Cenozoic history of the Uinta and Piceance Creek basins, Utah and Colorado, with special reference to the development of Eocene Lake Uinta, in Flores R. M. and Kaplan, S. S., eds., Cenozoic Paleogeography of the West-Central United States. Rocky Mountain Section (SEPM): Silers Printing, p. 247-276, [http://archives.datapages.com/data/rocky\\_sepm/data/023/023001/pdfs/247.pdf](http://archives.datapages.com/data/rocky_sepm/data/023/023001/pdfs/247.pdf).
- Johnson, R. C., Birdwell, J. E., Mercier, T. J., and Brownfield, M. E., 2016, Geology of tight oil and potential tight oil reservoirs in the lower part of the Green River Formation, Uinta, Piceance, and Greater Green River Basins, Utah, Colorado, and Wyoming: U.S. Geological Survey Scientific Investigations Report 2016–5008, 63 p., <https://pubs.usgs.gov/sir/2016/5008/sir20165008.pdf>.
- Johnson, R. C., Birdwell, J. E., Mercier, T. J., Brownfield, M. E., Charpentier, R. R., Klett, T. R., Leathers, H. M., Schenk, C. J., and Tennyson, M. E., 2015, Assessment of undiscovered oil and gas resources in the Uteland Butte Member of the Eocene Green River Formation, Uinta Basin, Utah: U.S. Geological Survey Fact Sheet 2015–3052, p. 1-2. <http://dx.doi.org/10.3133/fs20153052>.
- Johnson, R., Mercier, T., Brownfield, M., and Self, J., 2010, Assessment of in-place oil shale resources in the Eocene Green River Formation, Uinta Basin, Utah and Colorado: U.S. Geological Survey Digital Data Series DDS–69–BB, [https://pubs.usgs.gov/dds/dds-069/dds-069-y/REPORTS/69\\_Y\\_CH\\_1.pdf](https://pubs.usgs.gov/dds/dds-069/dds-069-y/REPORTS/69_Y_CH_1.pdf).
- Jones, B., Luth, R. W., and MacNeil, A. J., 2001, Powder X-ray diffraction analysis of homogeneous and heterogeneous sedimentary dolostones: Journal of Sedimentary Research, v. 71, no. 5, p. 790-799, <http://archives.datapages.com/data/sepm/journals/v71/071005/pdfs/0790.pdf>.

- Kaczmarek, S. E., 2005, Crystal growth mechanisms in natural and synthetic dolomite: Insight into dolomitization kinetics [Ph.D. thesis]: East Lansing, Michigan State University, 230 p., <http://search.proquest.com/pqdtglobal/docview/305457408/F463BEBFAEEEE4574PQ/1?accountid=14474>.
- Kaczmarek, S. E., and Sibley, D. F., 2011, On the evolution of dolomite stoichiometry and cation order during high-temperature synthesis experiments: an alternative model for the geochemical evolution of natural dolomites: *Sedimentary Geology*, v. 240, no. 1, p. 30-40, <https://doi.org/10.1016/j.sedgeo.2011.07.003>.
- Kahle, C. F., 1965, Possible roles of clay minerals in the formation of dolomite: *Journal of Sedimentary Research*, v. 35, no. 2, p. 448-453.
- Keighley, D., Flint, S., Howell, J., and Moscariello, A., 2003, Sequence stratigraphy in lacustrine basins: a model for part of the Green River Formation (Eocene), southwest Uinta Basin, Utah, USA: *Journal of Sedimentary Research*, v. 73, no. 6, p. 987-1006, <http://archives.datapages.com/data/sepm/journals/v73/data/073/073006/pdfs/0987.pdf>.
- Kile, D. E., Eberl, D. D., Hoch, A. R., and Reddy, M. M., 2000, An assessment of calcite crystal growth mechanisms based on crystal size distributions: *Geochimica et Cosmochimica Acta*, v. 64, no. 17, p. 2937-2950, [https://doi.org/10.1016/S0016-7037\(00\)00394-X](https://doi.org/10.1016/S0016-7037(00)00394-X).
- Kluth, C. F., 1986, Plate tectonics of the ancestral Rocky Mountains, *in* Peterson, J.A., ed., *Paleotectonics and Sedimentation in the Rocky Mountain Region, United States: American Association of Petroleum Geologists Memoir 41*, p. 353-369, Tulsa: The American Association of Petroleum Geologist, <http://archives.datapages.com/data/specpubs/structu1/images/a155/a1550001/0350/03530.pdf>.
- Knauth, L. P., 1994, Petrogenesis of chert, *in* Heaney, P. J., Prewitt, C. T., and Gibbs, G. V., eds., *Silica: physical behavior, geochemistry and materials applications: Mineralogical Society of America*, p. 233-258.
- Land, L. S., and Hoops, G. K., 1973, Sodium in carbonate sediments and rocks: a possible index to the salinity of diagenetic solutions: *Journal of Sedimentary Research*, v. 43, no. 3, p. 614-617, DOI:10.1306/74D7281A-2B21-11D7-8648000102C1865D.
- Land, L.S., 1980, The isotopic and trace element geochemistry of dolomite: the state of the art, *in* Zenger, D. H., Dunham, J. B., and Ethington, R. L., eds., *Concepts and Models of Dolomitization*, SEPM Society for Sedimentary Geology, no. 28, p. 87-110, DOI:10.2110/pec.80.28.0087.
- LaRocque, A., 1956, Tertiary mollusks of central Utah, *in* Peterson, J. A., ed., *Geology and Economic Deposits of East Central Utah: Intermountain Association of Petroleum Geologist*, p. 140-145, <http://archives.datapages.com/data/uga/data/006/006001/pdfs/140.pdf>.

- Logan, B. W., and Semeniuk, V., 1976, Dynamic metamorphism; processes and products in Devonian carbonate rocks, Canning Basin, Western Australia: Special Publication - Geological Society of Australia, v. 6, p. 1-138.
- Logan, S. K., 2015, Lacustrine lithofacies, depositional processes, and diagenesis of the Uteland Butte Member, Green River Formation, eastern Uinta Basin, Utah and Colorado [M.Sc. thesis]: Denver, Colorado School of Mines, 143 p., <http://search.proquest.com/pqdtglobal/docview/1696048147/C9108BE9E31481DPQ/1?accountid=14474>.
- Logan, S. K., Sarg, J. F., and Vanden Berg, M. D., 2016, Lithofacies, deposition, early diagenesis, and porosity of the Uteland Butte member, Green River Formation, eastern Uinta Basin, Utah and Colorado: Utah Geological Survey Open File Report 652, 32 p., [http://ugspub.nr.utah.gov/publications/open\\_file\\_reports/ofr-652.pdf](http://ugspub.nr.utah.gov/publications/open_file_reports/ofr-652.pdf)
- Long, M., 2006, Origin of the Dolomite on the Green River Formation [Ph.D. thesis]: Houston, University of Houston, 336 p., <http://search.proquest.com/pqdtglobal/docview/305320777/fulltextPDF/23BA6849E07A4872PQ/1?accountid=14474>.
- Lucia, F. J., 1995, Rock-fabric/petrophysical classification of carbonate pore space for reservoir characterization: American Association of Petroleum Geologist Bulletin, v. 79, no. 9, p. 1275-1300.
- Lucia, F. Jerry, 2007, Carbonate reservoir characterization: An integrated approach, Second edition: Berlin, Springer, 227 p.
- Luczaj, J. A., McIntire, M. J., and Olson Hunt, M. J., 2016, Geochemical Characterization of Trace MVT Mineralization in Paleozoic Sedimentary Rocks of Northeastern Wisconsin, USA: Geosciences, v. 6, no. 2, p. 1-29, DOI:10.3390/geosciences6020029.
- Lumsden, D. N., 1979, Discrepancy between thin-section and X-ray estimates of dolomite in limestone: Journal of Sedimentary Research, v. 49, no. 2. p. 429-436, <http://archives.datapages.com/data/sepm/journals/v47-50/data/049/049002/pdfs/0429.pdf>.
- Lumsden, D. N., and Chimahusky, J. S., 1980, Relationship between dolomite nonstoichiometry and carbonate facies parameters: Special Publication - Society of Economic Paleontologists and Mineralogists, v.28, p. 123-137, [http://archives.datapages.com/data/sepm\\_sp/SP28/Relationship\\_Between\\_Dolomite.pdf](http://archives.datapages.com/data/sepm_sp/SP28/Relationship_Between_Dolomite.pdf).
- Luo, P., and Machel, H. G., 1995, Pore size and pore throat types in a heterogeneous dolostone reservoir, Devonian Grosmont Formation, Western Canada sedimentary basin: American Association of Petroleum Geologist Bulletin, v. 79, no. 11, p. 1698-1719, <http://archives.datapages.com/data/bulletns/1994-96/images/pg/00790011/1650/1698.pdf>.
- MacGinitie, H. D., 1969, The Eocene Green River flora of northwestern Colorado and northeastern Utah: University of California Publications in Geological Sciences, v. 83, p. 1-203.

- Machel, H. G, 1995, Magnetic mineral assemblages and magnetic contrasts in diagenetic environments - with implications for studies of palaeomagnetism, hydrocarbon migration and exploration: Geological Society, London, Special Publications, v. 98, vo. 1, p. 9-29, doi:10.1144/GSL.SP.1995.098.01.02.
- Machel, H. G, 1997, Recrystallization versus neomorphism, and the concept of 'significant recrystallization in dolomite research: Sedimentary Geology, v. 113, no. 3-4, p. 161-168, [https://doi.org/10.1016/S0037-0738\(97\)00078-X](https://doi.org/10.1016/S0037-0738(97)00078-X).
- Machel, H. G, 1999, Effects of groundwater flow on mineral diagenesis, with emphasis on carbonate aquifers: Hydrogeology Journal, v. 7, no. 1, p. 94-107, DOI: 10.1007/s100400050182.
- Machel, H. G, 2001, Bacterial and thermochemical sulfate reduction in diagenetic settings - old and new insights: Sedimentary Geology, v. 140, no. 1, p. 143-175, DOI: 10.1016/S0037-0738(00)00176-7.
- Machel, H. G., 1985, Cathodoluminescence in Calcite and Dolomite and Its Chemical Interpretation: Geoscience Canada, v. 12, no. 4, p. 139-147, <https://journals.lib.unb.ca/index.php/GC/article/view/3427/3941>
- Machel, H. G., 1988, Fluid flow direction during dolomite formation as deduced from trace-element trends: Special Publication - Society of Economic Paleontologists and Mineralogists, v. 43, p. 115-125, [http://archives.datapages.com/data/sepm\\_sp/SP43/Fluid\\_Flow\\_Direction\\_During\\_Dolomite\\_Formation.htm](http://archives.datapages.com/data/sepm_sp/SP43/Fluid_Flow_Direction_During_Dolomite_Formation.htm).
- Machel, H. G., 2000, Application of cathodoluminescence to carbonate diagenesis, *in* Pagel, M., Barbin, V., Blanc, P., and Ohnenstetter, D., eds., Cathodoluminescence in Geosciences: Springer-Verlag, p. 271-301.
- Machel, H. G., and Mountjoy, E. W, 1987, General constraints on extensive pervasive dolomitization - and their application to the Devonian carbonates of western Canada: Bulletin of Canadian Petroleum Geology, v. 35, no. 2, p. 143-158, <http://archives.datapages.com/data/cspg/data/035/035002/pdfs/0143.pdf>.
- Machel, H. G., and Mountjoy, E. W., 1986, Chemistry and environments of dolomitization - A reappraisal: Earth-Science Reviews, v. 23, no. 3, p. 175-222, DOI: 10.1016/0012-8252(86)90017-6.
- Machel, H. G., Mason, R. A., Mariano, A. N., and Mucci, A., 1991, Causes and emission of luminescence in calcite and dolomite, *in* Barker, C. E. and Kopp, O.C., eds., Luminescence Microscopy and Spectroscopy: Qualitative and Quantitative Applications. SEPM Short Course Notes, 25: Society of Sedimentary Geology, p. 9-25.

- Machel, H.G. and Burton, E.A., 1991, Factors governing cathodoluminescence in calcite and dolomite, and their implications for studies of carbonate diagenesis, *in* Barker, C. E. and Kopp, O. C., eds., *Luminescence Microscopy and Spectroscopy: Qualitative and Quantitative Applications*. SEPM Short Course Notes, 25: Society of Sedimentary Geology, p. 37-57.
- Machel, H.G., 2004, Concepts and models of dolomitization: a critical reappraisal, *in* Braithwaite, C. J. R., Rizzi, G., and Darke, G., eds., *The Geometry and Petrogenesis of dolomite hydrocarbon reservoirs*: London, Geological Society, p. 7-63.
- Maliva, R. G., and Siever, R., 1989, Nodular chert formation in carbonate rocks: *The Journal of Geology*, v. 97, no. 4, p. 421-433, <https://doi.org/10.1086/629320>.
- Mazzullo, S. J., 1992, Geochemical and neomorphic alteration of dolomite; a review: *Carbonates and Evaporites*, v. 7, no. 1, p. 21-37, DOI: 10.1007/BF03175390.
- McCombie, A. M., 1959, Some relations between air temperatures and the surface water temperatures of lakes: *Limnology and Oceanography*, v. 4, no. 3, p. 252-258, <http://dx.doi.org/10.4319/lo.1959.4.3.0252>.
- McCrea, J. M., 1950, On the isotopic chemistry of carbonates and a paleotemperature scale: *The Journal of Chemical Physics*, v. 18, no. 6, p. 849-857, DOI:10.1063/1.1747785.
- McIntire, W. L., 1963, Trace element partition coefficients—a review of theory and applications to geology.: *Geochimica et Cosmochimica Acta*, v. 27, no. 12, p. 1209-1264, [https://doi.org/10.1016/0016-7037\(63\)90049-8](https://doi.org/10.1016/0016-7037(63)90049-8).
- McKenzie, J.A., 1991, The dolomite problem: An outstanding controversy, *in* Mueller, D. W., McKenzie, J. A., and Weissert, H., eds., *Controversies in modern geology; Evolution of geological theories in sedimentology, Earth history and tectonics*: Academic Press, p. 35-54, <http://dx.doi.org/10.1063/1.1747785>.
- Mello, M. R., and Maxwell, J. R., 1990, Organic geochemical and biological marker characterization of source rocks and oils derived from lacustrine environments in the Brazilian continental margin: *AAPG Memoir*, v. 50, p 77-97, <http://archives.datapages.com/data/specpubs/basinar3/images/a133/a1330001/0050/00770.pdf>.
- Millán, M. I., Machel, H., and Bernasconi, S. M., 2016, Constraining Temperatures of Formation and Composition of Dolomitizing Fluids in the Upper Devonian Nisku Formation (Alberta, Canada) with Clumped Isotopes: *Journal of Sedimentary Research*, 86(2), p. 107-112, DOI:10.2110/jsr.2016.6.
- Moore, C. H., 2001, *Carbonate reservoirs: Porosity evolution and diagenesis in a sequence stratigraphic framework*: Amsterdam: Elsevier, 461 p.

- Morgan, C. D., and Bereskin, S. R., 2003, Characterization of Petroleum Reservoirs in the Eocene Green River Formation, Central Uinta Basin, Utah: *The Mountain Geologist*, v. 39, p. 111-127, <http://archives.datapages.com/data/rmag/mg/2003/morgan.pdf>.
- Morrow, D. W., 1982, Diagenesis 2. Dolomite-Part 2 Dolomitization Models and Ancient Dolostones: *Geoscience Canada*, v. 9, no. 2, p. 95-107, <https://journals.lib.unb.ca/index.php/GC/article/view/3299/3816>.
- Nesbitt, B. E., and Muehlenbachs, K., 1994, Paleohydrogeology of the Canadian Rockies and origins of brines, Pb-Zn deposits and dolomitization in the Western Canada Sedimentary Basin: *Geology*, v. 22, no. 3, p. 243-246, DOI: 10.1130/0091-7613(1994)022<0243:POTCRA>2.3.CO;2.
- Nesse, W. D., 1991, *Introduction to Optical Mineralogy*: New York, Oxford University Press.
- Nikanorov, M., and Brazhnikova, L.V., 2004, Water chemical composition of rivers, lakes and wetlands, *in* M. G. Khublaryan, ed., *Types and Properties of Waters*, *Encyclopedia of Life Support Systems (EOLSS)*: Oxford, Eolss Publishers Co., p. 42-79.
- Pearson, P. N., and Palmer, M. R., 2000, Atmospheric carbon dioxide concentrations over the past 60 million years: *Nature*, v. 406, no. 6797, p. 695-9, DOI: 10.1038/35021000.
- Picard, M. D., 1971, Petrographic criteria for recognition of lacustrine and fluvial sandstone, PR Spring oil-impregnated sandstone area, southeast Uinta Basin, Utah: *Utah Geological and Mineralogical Society, Special Studies*, p. 1-24, <http://repository.icse.utah.edu/dspace/bitstream/123456789/5335/1/Utah-Tar-360.pdf>.
- Picard, M. D., 1955, Subsurface stratigraphy and lithology of Green River Formation in Uinta Basin, Utah: *American Association of Petroleum Geologists Bulletin*, v. 39, no. 1, p. 75-102. DOI:10.1306/5CEAE0E5-16BB-11D7-8645000102C1865D.
- Pingitore, N. J., 1976, Vadose and phreatic diagenesis; processes, products and their recognition in corals: *Journal of Sedimentary Petrology*, v. 46, no. 4, p. 985-1006, <http://archives.datapages.com/data/sepm/journals/v42-46/data/046/046004/pdfs/0985.pdf>.
- Pitman, J. K., 1996, Origin of primary and diagenetic carbonates in the lacustrine Green River Formation (Eocene), Colorado and Utah: *US Geological Survey Bulletin* 2157, p. 1-17, <https://pubs.usgs.gov/bul/2157/report.pdf>.
- Pittman, J. S., and Folk, R. L., 1971, Length-slow chalcedony after sulphate evaporite minerals in sedimentary rocks. *Nature Physical Science*, v. 230, no. 11, p. 64-65, <https://www.nature.com/nature-physci/journal/v230/n11/pdf/physci230064a0.pdf>.

- Purser, B. H., Tucker, M. E., and Zenger, D. H., 1994, Problems, progress and future research concerning dolomites and dolomitization, *in* Purser, B. H., Tucker, M. E., and Zenger, D. H., eds., *Dolomites: A volume in honour of Dolomieu*: Blackwell Scientific Publications, p. 3-21.
- Pusca, V. A., 2003, Wet/dry, terminal fan-dominated sequence architecture: A new, outcrop-based model for the Lower Green River Formation, Utah [Ph.D. thesis]: Laramie, University of Wyoming, 175 p., <http://search.proquest.com/docview/305284786/513A6C6E6A9942C6PQ/1?accountid=14474>.
- Pytte, A. M., and Reynolds, R. C., 1989, The thermal transformation of smectite to illite, *in* Naeser N.D., and McCulloh T.H. eds., *Thermal history of sedimentary basins*: Springer, New York, NY., p. 133-140.
- Rasmussen, D. T., Conroy, G. C., Friscia, A. R., Townsend, K. E., and Kinkel, M. D., 1999, Mammals of the middle Eocene Uinta Formation, *in*, Gillette, D. D., ed., *Vertebrate paleontology in Utah*: Salt Lake, Utah State Geological Survey, p. 401-420.
- Ray, J. S., and Ramesh, R., 1998, Stable carbon and oxygen isotope analysis of natural calcite and dolomite mixtures using selective acid extraction: *Journal-Geological Society of India*, 52, p. 323-332, <http://www.geosocindia.org/index.php/jgsi/article/view/68815>.
- Reeder, R. J., and Sheppard, C. E., 1984, Variation of lattice parameters in some sedimentary dolomites: *American Mineralogist*, v. 69, no. 5-6, p. 520-527, DOI:10.1086/626547.
- Reinson, G. E., 1992, Transgressive barrier island and estuarine systems, *in* Walker, R. G, and James, N. P, eds., *Facies models: response to sea level change*: Geological Association of Canada, p. 179-194.
- Remy, R. R., 1992, Stratigraphy of the Eocene Part of the Green River Formation in the South-Central Part of the Uinta Basin, Utah: U.S. Geological Survey Bulletin, 1787 - BB, p. 1-79, <https://pubs.usgs.gov/bul/1787bb/report.pdf>.
- Renaut, R. W., and Gierloswki-Kordes, E. H., 2010, Lakes, *in* James, N. P. and Dalrymple, R. W., eds., *Facies Models*: Geological Association of Canada, p. 541-575.
- Robert, C., and Kennett, J. P., 1992, Paleocene and Eocene kaolinite distribution in the South Atlantic and Southern Ocean: Antarctic climatic and paleoceanographic implications: *Marine Geology*, v. 103, no. 1-3, p. 99-110, [https://doi.org/10.1016/0025-3227\(92\)90010-F](https://doi.org/10.1016/0025-3227(92)90010-F).
- Roehler, H. W., 1991, Revised stratigraphic nomenclature for the Wasatch and Green River formations of Eocene age, Wyoming, Utah, and Colorado. U.S. Geological Survey Professional Paper 1506-B, <https://pubs.usgs.gov/pp/1506b/report.pdf>.



- Ryder, R. T., Fouch, T. D., and Elison, J. H., 1976, Early Tertiary sedimentation in the western Uinta basin, Utah: Geological Society of America Bulletin, v. 87, no. 4, p. 496-512, DOI:10.1130/0016-7606(1976)87<496:ETSITW>2.0.CO;2.
- Schamel, S, 2015, Shale oil resource play potential of the Green River Formation, Uinta Basin, Utah: Utah Geological Survey Open-File Report 639, 65 p., [http://ugspub.nr.utah.gov/publications/open\\_file\\_reports/ofr-639/ofr-639.pdf](http://ugspub.nr.utah.gov/publications/open_file_reports/ofr-639/ofr-639.pdf)
- Schmoker, J. W., and Halley, R. B., 1982, Carbonate porosity versus depth: a predictable relation for south Florida: American Association of Petroleum Geologists Bulletin, v. 66, no. 12, p. 2561-2570.
- Scholle, P. A., and Ulmer-Scholle, D. S., 2003, A Color Guide to the Petrography of Carbonate Rocks: Grains, Textures, Porosity, Diagenesis, AAPG Memoir 77, v. 77: Tulsa, American Association of Petroleum Geologist, 459 p.
- Searl, A., 1994, Discontinuous solid solution in Ca-rich dolomites: the evidence and implications for the interpretation of dolomite petrographic and geochemical data, *in* Purser, B., Tucker, M., and Zenger, D., eds., Dolomites, A Volume in Honour of Dolomieu: International Association of Sedimentologists, Special Publication 21: Blackwell Scientific Publications, p. 361-376.
- Sheppard, S. M., and Schwarcz, H. P, 1970, Fractionation of carbon and oxygen isotopes and magnesium between coexisting metamorphic calcite and dolomite: Contributions to Mineralogy and Petrology, v. 26, no. 3, p. 161-198, DOI: 10.1007/BF00373200.
- Sibley, D. F., and Gregg, J. M, 1987, Classification of dolomite rock textures: Journal of Sedimentary Petrology, v. 57, no. 6, p. 967-975, <http://archives.datapages.com/data/sepm/journals/v55-58/data/057/057006/pdfs/0967.pdf>.
- Sibley, D. F., Gregg, J. M., Brown, R. G., and Laudon, P. R., 1993, Dolomite crystal size distribution, *in* Rezak, R. and Lavoie, D. L., eds., Carbonate microfabrics: Springer-Verlag, p. 195-204.
- Siedlecka, A., 1972, Length-slow chalcedony and relicts of sulphates; evidences of evaporitic environments in the Upper Carboniferous and Permian beds of Bear Island, Svalbard: Journal of Sedimentary Petrology, v. 42, no. 4, pp. 812-816, DOI:10.1306/74D7263A-2B21-11D7-8648000102C1865D.
- Smith, M. E, 2007, The stratigraphy and geochronology of the Green River Formation, Western U.S [Ph.D. thesis]: Madison, University of Wisconsin-Madison, 318 p., <http://search.proquest.com/docview/304776713/A64EEBCAC5A64C64PQ/2?accountid=14474>.

- Smith, M. E., Carroll, A. R., and Singer, B. S., 2008, Synoptic reconstruction of a major ancient lake system: Eocene Green River Formation, western United States: Geological Society of America Bulletin, v. 120, no. 1-2, p. 54-84, DOI:10.1130/B26073.1.
- Smith, M. E., Carroll, A. R., Scott, J. J., and Singer, B. S., 2014, Early Eocene carbon isotope excursions and landscape destabilization at eccentricity minima: Green River Formation of Wyoming: Earth and Planetary Science Letters, v. 403, p. 393-406, DOI:10.1016/j.epsl.2014.06.024.
- Swart, P. K., Burns, S. J., and Leder, J. J., 1991, Fractionation of the stable isotopes of oxygen and carbon in carbon dioxide during the reaction of calcite with phosphoric acid as a function of temperature and technique: Chemical Geology: Isotope Geoscience section, v. 86, no. 2, p. 89-96, [https://doi.org/10.1016/0168-9622\(91\)90055-2](https://doi.org/10.1016/0168-9622(91)90055-2).
- Sweet, D. E., and Soreghan, G. S., 2012, Late Paleozoic tectonics and paleogeography of the ancestral Front Range: Structural, stratigraphic, and sedimentologic evidence from the Fountain Formation (Manitou Springs, Colorado): Geological Society of America Bulletin, v. 122, no. 3/4, p. 575-594, DOI:10.1130/B26554.1.
- Symcox, C., 2015, Facies, stratigraphy, and mineralogy of the Carbonate marker and D marker units, lower Green River Formation, Uinta Basin, Utah [M.Sc. thesis]: Denver, Colorado School of Mines, 162 p., <http://search.proquest.com/docview/1720262797/E8F7EDE79523463CPQ/1?accountid=14474>.
- Tada, R., and Siever, R., 1989, Pressure solution during diagenesis: Annual Review of Earth and Planetary Sciences, v. 17, no. 1, p. 89-118, DOI:10.1146/annurev.earth.17.050189.000513.
- Talbot, M. R., and Kelts, K., 1990, Palaeolimnological signatures from carbon and oxygen isotopic ratios in carbonates from organic-rich lacustrine sediments, *in* Katz B. J., ed., Lacustrine exploration: Case studies and modern analogs, American Association of Petroleum Geologists Memoir 50: Tulsa, American Association of Petroleum Geologists, p. 99-112.
- Tānavsuu-Milkeviciene, K., and Frederick Sarg, J., 2012, Evolution of an organic-rich lake basin; stratigraphy, climate and tectonics; Piceance Creek basin, Eocene Green River Formation: Sedimentology, v. 59, no. 6, p. 1735-1768, DOI:10.1111/j.1365-3091.2012.01324.x.
- Tānavsuu-Milkeviciene, K., Sarg, J. F., and Bartov, Y., 2017, Depositional Cycles and Sequences in an Organic-Rich Lake Basin: Eocene Green River Formation, Lake Uinta, Colorado and Utah, USA: Journal of Sedimentary Research, v. 87, no. 3, p. 210-229, <http://archives.datapages.com/data/sepm/journals/087/087003/pdfs/210.pdf>.










- Trurnit, P., 1968, Pressure solution phenomena in detrital rocks: *Sedimentary Geology*, v. 2, no. 2, p. 89-114, DOI:10.1016/0037-0738(68)90030-4.
- Tucker, M. E., and Wright, V. P., 1990, *Carbonate sedimentology*: Oxford, Blackwell Scientific Publications.
- Tukey, J. W., 1977, *Exploratory data analysis*, Addison-Wesley Publishing Company.
- Tuttle, M. L., and Goldhaber, M. B., 1993, Sedimentary sulfur geochemistry of the Paleogene Green River Formation, western USA: implications for interpreting depositional and diagenetic processes in saline alkaline lakes: *Geochimica et Cosmochimica Acta*, v. 57, no. 13, p. 3023-3039, [https://doi.org/10.1016/0016-7037\(93\)90291-4](https://doi.org/10.1016/0016-7037(93)90291-4).
- Tweto, O., 1975, Laramide (late Cretaceous-early Tertiary) orogeny in the southern Rocky Mountains: *Memoir - Geological Society of America*, v. 144, p. 1-44, <https://dx.doi.org/10.1130/MEM144-p1>.
- Ulmer-Scholle, D. S., Scholle, P. A., and Brady, P. V., 1993, Silicification of evaporites in Permian (Guadalupian) back-reef carbonates of the Delaware Basin, West Texas and New Mexico: *Journal of Sedimentary Research*, v. 63, no. 5, p. 955-965.
- Vanden Berg, M. D., Morgan C. D., Chidsey, T. C., and Nielsen, P., 2013, The Uteland Butte Member of the Eocene Green River Formation: An Emerging Unconventional Carbonate Tight Oil Play in the Uinta Basin, Utah: Poster presented at the AAPG Eastern Section Meeting, Pittsburgh, PA, September 6-10.
- Vanden Berg, M. D., Wood, R. E., Carney, S. M., and Morgan C. D., 2014, Geological Characterization of the Uteland Butte Member of the Eocene Green River Formation: An Emerging Unconventional Carbonate Tight Oil Play in the Uinta Basin, Utah. Paper presented at Rocky Mountain Section AAPG Annual Meeting, Denver, CO.
- Veizer, J., 1983, Chemical diagenesis of carbonates: theory and application of trace element technique, [http://archives.datapages.com/data/sepm\\_sp/SC10/Chemical\\_Diagenesis.pdf](http://archives.datapages.com/data/sepm_sp/SC10/Chemical_Diagenesis.pdf).
- Walters, L. J., Claypool, G. E., and Choquette, P. W., 1972, Reaction rates and  $\delta^{18}\text{O}$  variation for the carbonate-phosphoric acid preparation method: *Geochimica et Cosmochimica Acta*, v. 36, no. 2, p. 129-140, [https://doi.org/10.1016/0016-7037\(72\)90002-6](https://doi.org/10.1016/0016-7037(72)90002-6).
- Warren, J. K., 2006, *Evaporites: Sediments, Resources, and Hydrocarbons*: New York, Springer Berlin Heidelberg, 1035 p.
- Warren, J., 2000, Dolomite: occurrence, evolution and economically important associations: *Earth-Science Reviews*, 52(1), p. 1-81, [https://doi.org/10.1016/S0012-8252\(00\)00022-2](https://doi.org/10.1016/S0012-8252(00)00022-2).
- Weber, J. N., 1964, Trace element composition of dolostones and dolomites and its bearing on the dolomite problem: *Geochimica et Cosmochimica Acta*, v. 28, no. 10-11, p. 1817-1832, DOI:10.1016/0016-7037(64)90023-7.

- Weiss, M., P., Witkind, I. J., and Cashion, W. B., 1981, Geologic map of the Price 30'X60' Quadrangle, Carbon, Duchesne, Uintah, Utah, and Wasatch Counties, Utah. U.S. Geological Survey Miscellaneous Investigations Series Map I-1981, 1 sheet, 1:100,000.
- Whitehead, H. C., and Feth, J. H., 1961, Recent chemical analyses of waters from several closed-basin lakes and their tributaries in the western United States: Geological Society of America Bulletin, v. 72, no. 9, p. 1421-1425, DOI: 10.1130/0016-7606(1961)72[1421:RCAOWF]2.0.CO;2
- Williamson, C. R., and Picard, M. D., 1974, Petrology of carbonate rocks of the Green River Formation (Eocene): Journal of Sedimentary Research, v. 44, no. 3, p. 738-759, <http://archives.datapages.com/data/sepm/journals/v42-46/data/044/044003/pdfs/0738.pdf>.
- Willis, G.C, 1999, The Utah thrust system - An overview: Utah Geological Association Publication 27, p. 1-9, <http://archives.datapages.com/data/uga/data/070/070001/pdfs/1.pdf>.
- Woody, R. E., Gregg, J. M., and Koederitz, L. F., 1996, Effect of texture on petrophysical properties of dolomite: evidence from the Cambrian-Ordovician of southeastern Missouri: Association of Petroleum Geologist Bulletin, v. 80, no. 1, p. 119-131, <http://archives.datapages.com/data/bulletns/1994-96/images/pg/00800001/0100/0119.pdf>
- Zachos, J., Pagani, M., Sloan, L., Thomas, E., and Billups, K., 2001, Trends, rhythms, and aberrations in global climate 65 Ma to present: Science, v. 292, no. 5517, p. 686-693, DOI:10.1126/science.1059412.

## APPENDIX 1

### LEGEND







#### LITHOLOGY

	Cherty Dolostone
	Argillaceous Dolostone
	Interbedded Dolostone and Shale
	Dolomitic Limestone
	Arguillaceous Limestone
	Interbedded Limestone and Shale
	Calcareous Shale
	Clastic Limestone
	Calcareous Siltstone
	Siltstone
	Sandstone
○	Sample

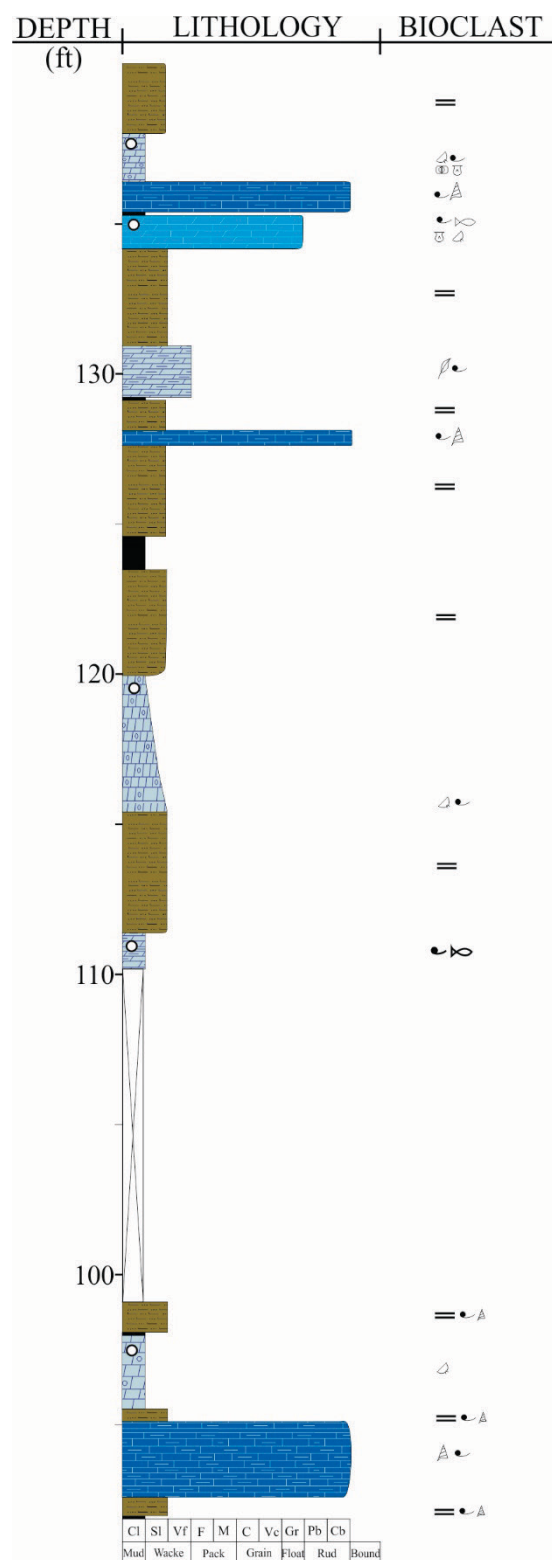
#### BIOCLASTS

	Ostracods
	Pelecypods
	Gastropods
	Shell fragments
	Charophytes
	Fish Bones
	Algae

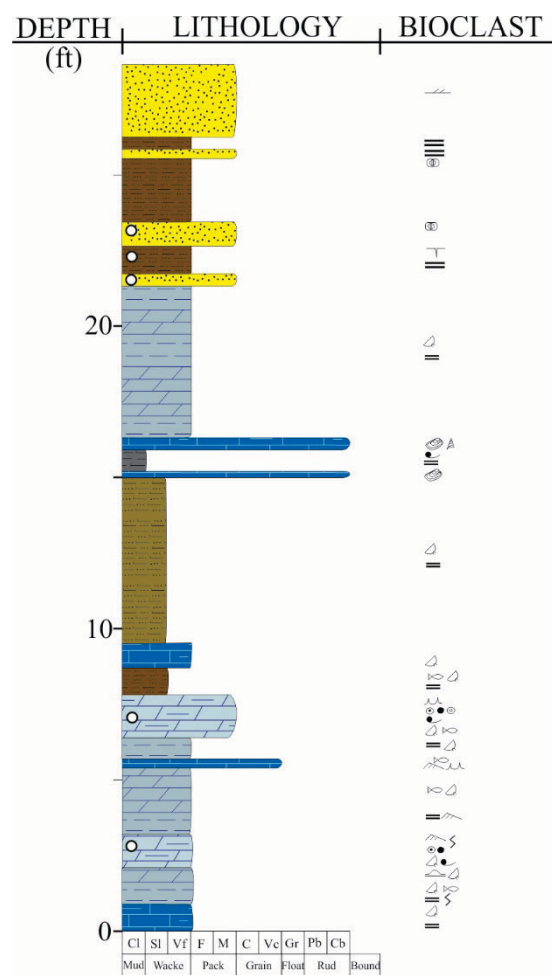
#### STRUCTURES

	Planar Parallel
	Planar no Parallel
	Irregular
	Curved Parallel
	Wavy Parallel
	Wavy Discontinuous
●	Peloids
◎	Ooids
◎	Oncoids
⊗	Nodule

Outcrop: Willow Creek Canyon, code: WCC.

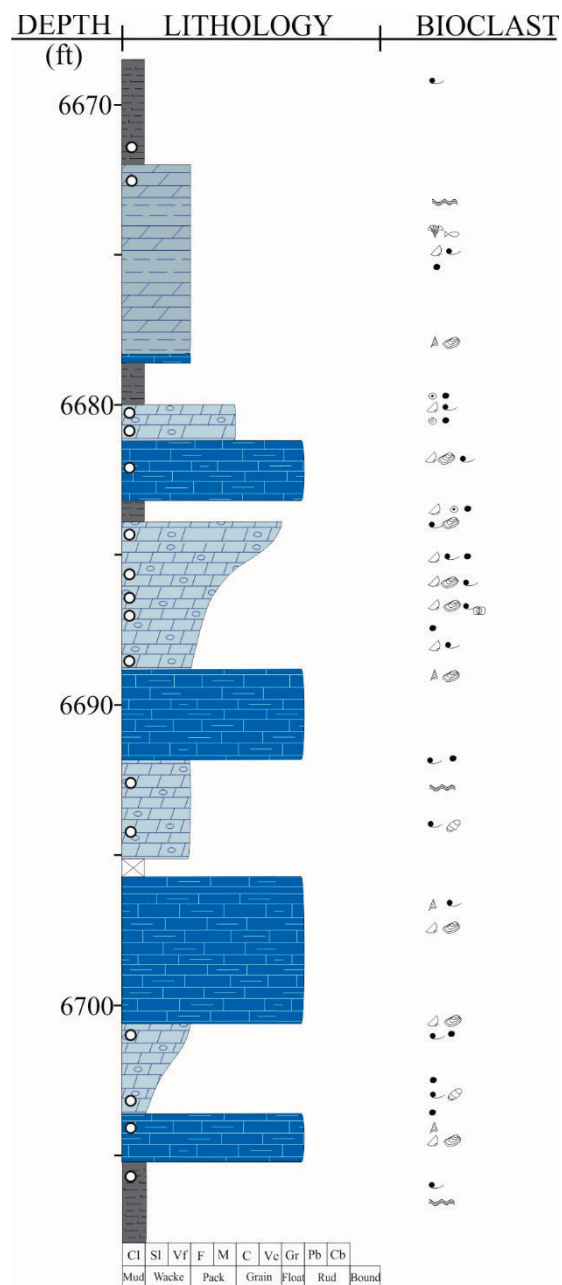


Outcrop: Nine Mile Canyon, code: NMC.



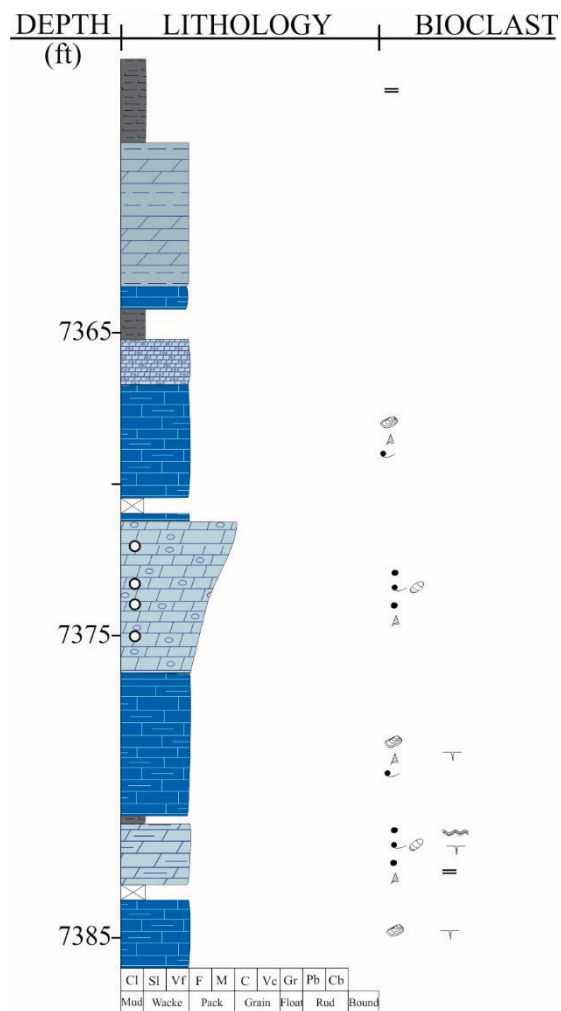
## APPENDIX 2

Well: 14-1-46, code: BBC 14-1.

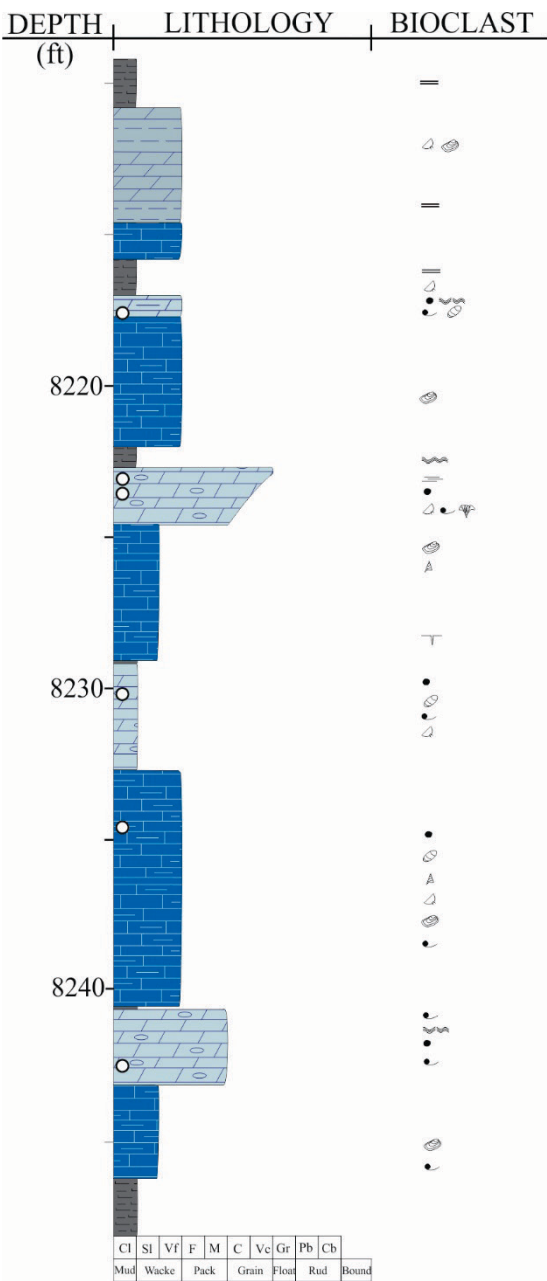




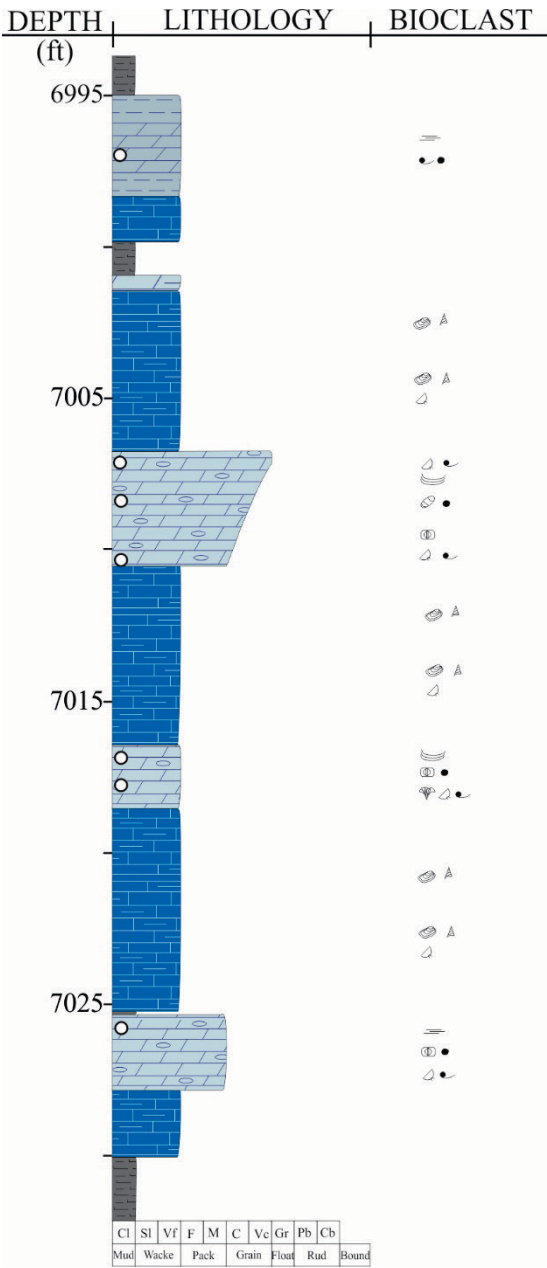
Well: 14-3-45, code: BBC 14-3.



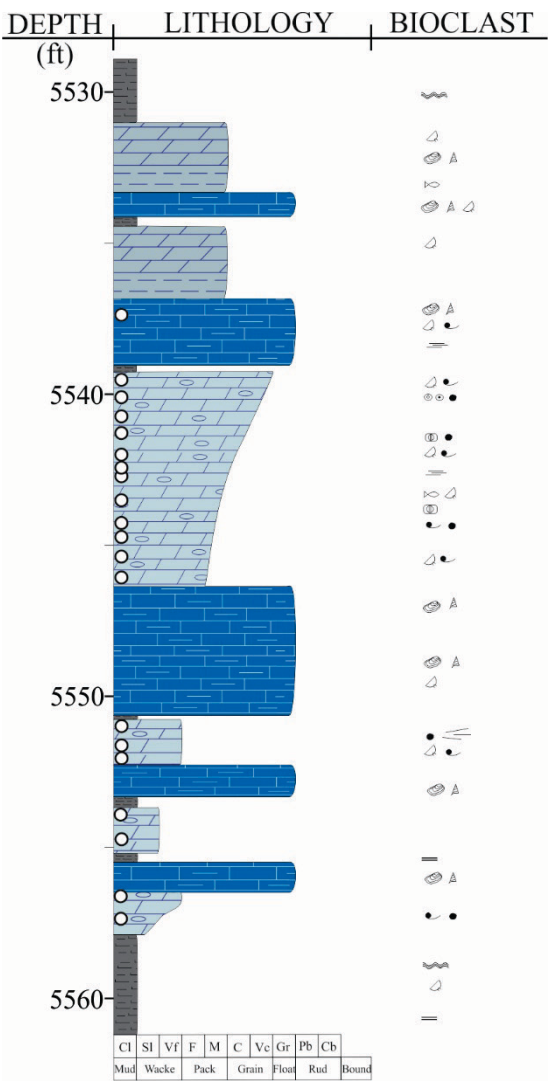
Well: Nickerson 6-28-3-2W, code: N 6-28.



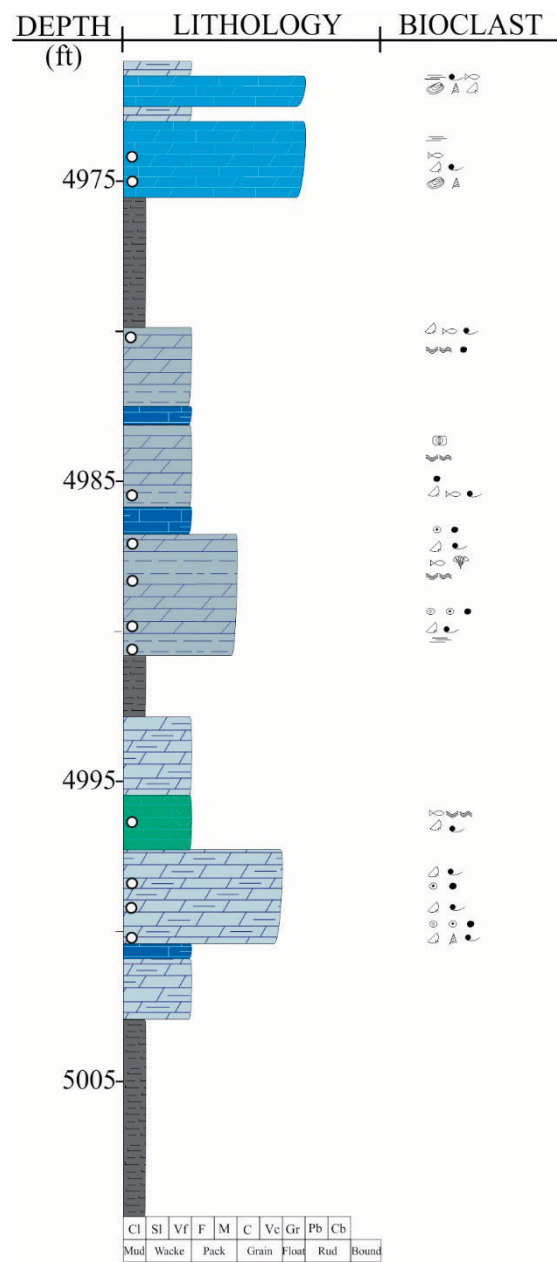
Well: Ute Tribal 15-13-4-3W, code: UT 15-13.



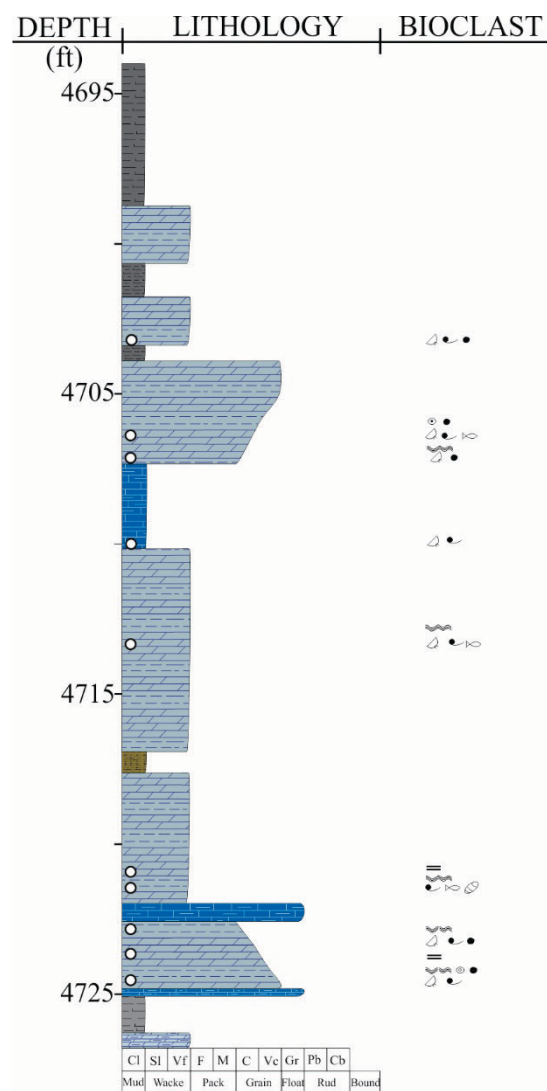
Well: Petes Wash 13-06 GR, code: PW 13-06.



Well: West Desert Spring 11-20-10-17, code: DS 11-20.



Well: Island Unit 16, code: IU 16.



## APPENDIX 3

Codes used for thin sections description:

ROCK TYPE		CARBONATE GRAINS (CG)		STRATIFICATION	
D	Dolomitized (>75% Dol)	RF	Rock fragments	I	Irregular stratification
M	Mudstone	On	Oncoids	M	Massive (lack)
W	Wackestone	Oo	Ooids	PP	Plana Parallel
P	Packstone	Pel	Peloids	PW	Parallel wavy
G	Grainstone	Cor	Corticoids	WD	Wavy discontinuous
F	Floatstone	MAA	Most Abundant CG	CP	Curved Parallel
R	Rudstone			SL	Structureless
d	Dolomitic (<75% Dol)			WN	Wavy non parallel
S	Silty	NON CARBONATE GRAINS (NCG)		PNP	Planar non parallel
SS	Siltstone	Qz	Quartz	PD	Planar discontinuous
Mud	Mudstone	Cla	Clay		
A	Arenaceous	Sil	Silt	LAYER THICKNESS	
SSt	Sandstone	San	Sand	TNL	Thinly laminated
Ar	Argillaceous	VF	Very Fine	TCL	Thickly laminated
C	Calcareous	F	Fine	VTB	Very thinly bedded
Sh	Shale	M	Medium	TB	Thinly bedded
CL	Claystone	C	Coarse		
		VC	Very coarse		
MINERALOGY				GRADATION	
Cal	Calcite		FABRIC	A	Agradational
FCal	Ferroan Calcite	MS	Matrix Supported	CU	Coarsening upward
Dol	Dolomite	GS	Grain Supported	FU	Fining upward
Sil	Silica	Ratio	MS/GS		
Pyr	Pyrite				
Gyp	Gypsum				
		SORTING			
		MS	Moderately sorted		
	BIOCLASTS	WS	Well sorted		
O	Ostracods	PS	Poorly sorted		
P	Pelecypods	VWS	Very well sorted		
G	Gastropods				
SF	Shell fragments				
FS	Fish scales	ROUNDING			
CH	Charophyte	S	Subrounded		
FB	Fish Bones (Undefined)	R	Rounded		
AM	Alga Mats	SA	Subangular		
MAB	Most abundant Bioclast	A	Angular		

				MINERALOGY							BIOCLASTS										CABONATE GRAINS						NCG					FABRIC					STRATIFICATION						
Well/Outcrop	Sample	Depth	Rock Type	Cal	FCal	Dol	Sil	Pyr	Gyp	Ox	P	G	SF	FS	FB	CH	AM	%	MAB	RF	On	Oo	Pel	Cor	%	MACG	Cl	Sil	San	Qz	NCG%	MS	GS	Ratio	Sor	Rou	Bedding	LT	Bio	A	CU	FU	
BBC 14-1	7	6672.80	Sh	10	0	0	10	0	1	0	0	0	0	1	0	0	0	0	1	SF	0	0	0	0	0	0	0	1	C	0	1	4	1	0	80/20	WS	S	PP	VBT	0	1	0	0
BBC 14-1	8	6675.30	D-W	5	1	65	20	4	0	5	1	0	0	1	0	1	0	1	5	SF	0	0	0	1	0	25	Pel	0	M	0	1	5	1	0	80/20	WS	S	PP-W	VBT	0	0	1	0
BBC 14-1	9	6680.10	D-P	5	3	75	10	2	0	5	1	0	0	1	0	0	0	0	5	SF	0	1	0	1	0	25	Pel	0	C	VF	1	5	0	1	30/70	WS	S	PNP	VBT	0	1	0	0
BBC 14-1	10	6680.35	D-P	1	3	80	15	1	0	0	1	0	0	1	0	0	0	0	5	SF	0	0	1	1	0	15	Pel	0	M	0	1	3	1	0	50/50	MS	S	M	VBT	0	1	0	0
BBC 14-1	11	6683.15	F	74	1	5	20	0	0	0	1	1	0	1	0	0	0	0	40	P	0	0	0	0	0	0	0	0	M	0	1	10	1	0	60/40	PS	SA	I	VBT	0	1	0	0
BBC 14-1	12	6683.95	d-G	2	40	50	8	0	0	0	1	0	0	1	0	0	0	0	3	SF	1	1	0	1	1	30	Pel	0	0	0	1	0	0	1	30/70	-	-	M	VBT	0	1	0	0
BBC 14-1	13	6684.90	D-P	2	3	80	10	1	0	4	1	0	0	1	0	0	0	0	15	SF	1	0	0	1	0	25	Pel	0	F	0	1	1	0	1	40/60	-	-	M	VBT	0	1	0	0
BBC 14-1	14	6685.40	D-W	3	5	77	10	5	0	0	1	1	0	1	0	0	0	0	10	SF	0	0	0	1	0	3	Pel	0	M	0	0	3	1	0	80/20	-	-	M	VBT	0	1	0	0
BBC 14-1	15	6686.80	D-W	5	3	80	10	2	0	0	1	1	0	1	0	0	0	0	15	SF	0	0	0	1	0	20	Pel	0	M	0	0	5	1	0	70/30	-	-	I	VBT	1	1	0	0
BBC 14-1	16	6688.35	D-P	3	1	89	5	1	0	1	1	0	0	1	0	0	0	0	5	SF	0	0	0	1	0	3	Pel	0	M	0	1	1	1	0	90/10	-	-	M	VBT	0	1	0	0
BBC 14-1	17	6692.60	C-D-M	30	0	60	4	3	0	3	0	0	0	1	0	0	0	0	1	SF	0	0	0	1	0	30	Pel	0	F	0	1	3	1	0	50/50	PS	SA	PP-W	TCL	0	1	0	0
BBC 14-1	18	6693.50	D-M	1	0	95	3	1	0	0	0	0	0	1	0	0	1	0	1	SF	0	0	0	0	0	0	0	0	M	0	1	2	1	0	95/5	WS	R	M	VTB	0	1	0	0
BBC 14-1	19	6696.10	F-R	90	5	3	2	0	0	0	1	1	1	1	0	0	0	0	45	G	0	0	0	0	0	0	0	0	M	0	1	7	1	0	50/50	MS	S	M	VTB	0	1	0	0
BBC 14-1	20	6701.40	D-W	5	3	85	5	1	0	1	1	1	0	1	0	0	0	0	10	SF	0	0	0	1	0	15	Pel	0	M	0	1	7	1	0	80/20	WS	S	CP	VTB	1	1	0	0
BBC 14-1	21	6703.10	D-M	0	0	79	20	1	0	0	0	0	0	1	0	0	1	0	1	SF	0	0	0	1	0	1	Pel	0	M	0	1	2	1	0	99/1	WS	R	M	VTB	0	1	0	0
BBC 14-1	22	6703.75	F	4	0	0	95	1	0	0	0	0	0	0	0	0	0	0	30	P	0	0	0	1	0	0	0	0	M	0	1	5	1	0	50/50	MS	S	M	VTB	0	1	0	0
BBC 14-1	23	6704.50	F	90	1	0	8	1	0	0	1	1	0	1	0	0	0	0	30	P	0	0	0	0	0	0	0	0	M	0	1	5	1	0	50/50	MS	S	M	VTB	0	1	0	0
BBC 14-1	24	6705.30	Sh	70	0	0	20	1	0	0	0	0	0	1	0	0	0	0	50	SF	0	0	0	0	0	0	0	0	F	0	1	10	0	1	30/70	PS	A	PW	VTB	0	1	0	0
BBC 14-3	26	7372.35	D-W	5	0	70	20	5	0	0	1	0	0	1	0	0	0	0	10	SF	0	0	0	1	0	2	Pel	0	F	0	0	1	1	0	75/25	-	-	M	VTB	0	1	0	0
BBC 14-3	27	7373.65	D-W	6	1	70	20	3	0	0	1	0	0	1	0	0	1	0	10	SF	0	0	0	1	0	1	Pel	0	F	0	0	1	1	0	60/30	-	-	M	VTB	0	1	0	0
BBC 14-3	28	7374.05	d-W	10	5	30	50	3	0	2	1	0	0	1	0	0	1	0	15	O	0	0	0	1	0	2	Pel	1	F	0	0	1	1	0	70/30	-	-	WD	VTB	0	1	0	0
BBC 14-3	29	7375.00	D-P	5	2	70	20	3	0	0	1	0	0	1	0	0	1	0	15	SF	0	0	0	1	0	20	Pel	1	F	0	0	1	1	0	70/30	-	-	M	VTB	0	1	0	0
N 6-28	4	8217.60	D-W	1	0	90	7	2	0	0	0	0	0	1	0	0	1	0	0	0	0	0	0	1	0	30	Pel	1	M	0	1	5	1	0	80/20	-	-	WD	VTB	1	0	0	1
N 6-28	5	8223.20	D-W	40	0	40	15	5	0	0	1	0	0	1	0	0	0	0	1	SF	0	0	0	1	0	20	Pel	0	0	0	0	0	1	0	90/10	-	-	M	VTB	0	1	0	0
N 6-28	6	8223.70	D-W	15	0	70	10	5	0	0	1	0	0	1	0	0	0	1	3	O	0	0	0	1	0	5	Pel	1	M	0	0	3	1	0	80/20	-	-	SL	VTB	1	1	0	0
N 6-28	7	8230.20	D-M	1	0	80	18	1	0	0	1	0	0	1	0	0	1	0	1	O	0	0	0	1	0	20	Pel	1	M	0	0	1	1	0	95/5	-	-	M	VTB	0	1	0	0
N 6-28	8	8234.60	W	90	0	8	1	1	0	0	1	1	1	1	0	0	1	0	15	O	0	0	0	1	0	0	0	0	M	0	0	10	1	0	80/20	-	-	M	VTB	0	1	0	0
N 6-28	9	8242.50	D-P	3	0	75	20	2	0	0	0	0	0	1	0	0	0	0	5	SF	0	0	0	1	0	50	Pel	1	M	0	1	2	1	0	50/50	WS	R	WD	VTB	0	1	0	0
UT 15-13	8	6996.40	D-W	5	0	85	9	1	0	0	0	0	0	1	0	0	0	0	1	SF	0	0	0	1	0	20	Pel	1	M	0	1	10	1	0	70/30	WS	S	PD	TCL	0	1	0	0
UT 15-13	9	7006.50	D-G	0	0	80	18	2	0	0	1	0	0	1	0	0	0	0	5	SF	1	1	0	1	0	40	Pel	0	C	0	1	7	1	0	55/45	-	-	CP	TCL	0	1	0	0
UT 15-13	10	7007.80	D-M	1	0	90	8	1	0	0	0	0	0	0	0	0	1	0	1	CH	0	0	0	1	0	1	Pel	1	F	0	0	1	1	0	95/5	-	-	M	VTB	1	1	0	0
UT 15-13	11	7009.90	D-W	1	0	80	18	1	0	0	1	0	0	1	0	0	0	0	1	SF	0	0	0	1	0	10	Pel	1	F	0	1	5	1	0	80/20	-	-	M	VTB	1	1	0	0
UT 15-13	12	7016.40	D-W	2	0	80	10	8	0	0	1	0	0	1	0	0	0	0	20	O	0	0	0	1	0	10	Pel	1	M	0	0	2	1	0	60/40	-	-	PW	VTB	0	1	0	0
UT 15-13	13	7017.40	D-W	5	0	80	13	2	0	0	1	0	0	1	0	0	0	1	7	O	0	0	0	1	0	5	Pel	1	F	0	0	1	1	0	90/10	-	-	CP	VTB	1	1	0	0
UT 15-13	14	7025.20	D-P	3	0	85	10	2	0	0	1	0	0	1	0	0	0	0	5	SF	0	0	0	1	0	15	Pel	0	0	0	0	0	1	0	70/30	-	-	SL	VTB	1	1	0	0
PW 13-06	6	5537.30	F	70	5	5	15	0	0	0	1	1	1	1	0	0	0	0	40	O	0	0	0	0	0	0	0	0	C	VF													



Well/Outcrop	Sample	Depth	Rock Type	MINERALOGY							BIOCLASTS										CABONATE GRAINS						NCG				FABRIC					STRATIFICATION						
				Cal	Fcal	Dol	Sil	Pyr	Gyp	Ox	O	P	G	SF	FS	FB	CH	AM	%	MAB	RF	On	Oo	Pel	Cor	%	MACG	Cl	Sil	San	Qz	NCG%	MS	GS	Ratio	Sor	Rou	Bedding	LT	Bio	A	CU
UI 16	2	4705.40	D-W	5	0	70	20	4	0	1	1	0	0	1	0	0	0	1	O	0	0	0	1	0	15	Pel	1	0	0	0	0	1	0	90/10	-	-	M	VTB	1	1	0	0
UI 16	3	4706.30	d-G	60	2	30	5	1	1	1	1	0	0	1	0	0	40	SF	1	1	0	1	0	30	Pel	0	F	0	1	5	0	1	30/70	-	-	WP	VTB	0	1	0	0	
UI 16	4	4707.00	D-P	5	2	70	20	3	0	0	1	0	0	0	0	0	7	O	0	0	0	1	0	40	Pel	1	M	0	0	5	1	0	90/10	-	-	WP	VTB	0	1	0	0	
UI 16	5	4710.00	M	75	1	10	10	4	0	0	1	0	0	1	0	0	0	2	SF	0	0	0	0	0	0	0	1	M	0	1	7	1	0	95/5	WS	R	M	VTB	0	1	0	0
UI 16	6	4713.20	S-CL	20	0	0	10	10	0	2	1	0	0	1	0	1	0	10	SF	0	0	0	0	0	0	0	1	F	0	1	5	1	0	70/30	WS	R	WP	VTB	0	1	0	0
UI 16	7	4720.80	D-W	5	0	80	10	5	0	0	0	0	0	1	0	1	0	2	SF	0	0	0	1	0	15	Pel	1	M	0	1	10	1	0	80/20	MS	S	PP	TNL	0	0	1	0
UI 16	8	4721.25	C-D-W	15	0	75	8	2	0	0	0	0	0	1	0	1	0	10	SF	0	0	0	1	0	10	Pel	1	F	0	1	5	1	0	60/40	WS	R	WP	VTB	0	1	0	0
UI 16	9	4722.50	C-D-P	15	0	80	3	2	0	0	1	0	0	1	0	0	0	10	SF	0	0	0	1	0	25	Pel	1	F	0	1	5	1	0	55/45	WS	R	WD	TNL	0	1	0	0
UI 16	10	4723.30	D-W	5	0	83	10	2	0	0	1	0	0	1	0	0	0	5	SF	0	0	0	1	0	5	Pel	1	F	0	1	3	1	0	80/20	WS	S	PP	VTB	0	1	0	0
UI 16	11	4724.20	C-D-G	40	0	53	5	2	0	0	1	0	0	1	0	0	0	1	O	0	0	1	1	0	60	Pel	1	0	0	0	0	0	1	40/60	-	-	WD	TCL	0	0	1	0
WCC	1	-	C-D-M	1	24	65	5	2	0	3	1	0	0	1	0	0	0	5	SF	0	1	0	0	0	1	On	1	M	0	1	1	1	0	70/30	-	-	SL	VTB	1	1	0	0
WCC	2	-	d-G	45	0	50	4	1	0	0	1	0	0	1	0	0	0	20	O	1	1	0	1	0	50	On	0	F	0	0	1	0	1	10/90	-	-	SL	VBT	0	1	0	0
WCC	3	-	D-M	5	0	90	3	2	0	0	1	0	0	1	0	0	0	5	SF	0	0	0	0	0	0	0	1	F	0	1	3	1	0	90/10	-	-	SL	VBT	1	1	0	0
WCC	4	-	D-M	5	0	90	3	1	0	2	0	0	0	1	0	0	1	1	FB	0	0	0	0	0	0	0	1	F	0	1	3	1	0	90/10	WS	R	SL	VBT	1	1	0	0
WCC	5	-	D-M	3	0	90	3	1	0	3	1	0	0	1	0	0	0	2	SF	0	0	0	0	0	0	0	1	F	0	1	3	1	0	90/10	WS	S	SL	VBT	1	1	0	0
WCC	6	-	d-F	82	0	15	0	2	0	1	1	1	0	1	0	0	0	15	SF	0	0	0	0	0	0	0	1	F	0	1	3	1	0	60/40	-	-	SL	VBT	0	1	0	0
WCC	7	-	D-M	5	0	60	30	5	0	0	1	0	0	1	0	0	0	5	SF	0	0	0	0	0	0	0	1	F	0	1	3	1	0	80/20	WS	R	WD	VBT	1	1	0	0
WCC	8	-	F	80	0	0	15	5	0	0	1	1	1	1	0	1	0	0	60	G	0	0	0	0	0	0	1	F	0	1	5	0	1	10/90	-	-	SL	VBT	0	1	0	0
NMC	3	-	d-Sst	10	0	45	40	5	0	0	0	0	0	0	0	0	0	0	0	1	0	0	0	0	0	0	1	C	F	1	60	1	0	60/40	VWS	R	SL	VTB	0	1	0	0
NMC	41	-	C-Sst	2	28	5	60	0	0	5	0	0	0	0	0	0	0	0	0	1	0	0	0	0	0	0	1	C	F	1	80	1	0	50/50	WS	S	SL	VTB	0	1	0	0
NMC	42	-	C-Sst	1	24	5	65	0	0	5	0	0	0	0	0	0	0	0	0	1	0	0	0	0	0	0	1	C	F	1	80	1	0	50/50	WS	S	SL	VTB	0	1	0	0
NMC	43	-	C-Sst	1	19	5	70	0	0	5	0	0	0	0	0	0	0	0	0	1	0	0	0	0	0	0	1	C	F	1	80	1	0	50/50	WS	S	SL	VTB	0	1	0	0
NMC	44	-	C-Sst	1	3	10	80	1	0	5	0	0	0	0	0	0	0	0	0	1	0	0	0	0	0	0	1	C	F	1	60	1	0	50/50	WS	S	SL	VTB	0	1	0	0
NMC	45	-	C-Sst	1	0	40	50	4	0	5	0	0	0	0	0	0	0	0	0	0	0	0	0	0	0	0	1	C	VF	1	50	1	0	70/30	PS	R	SL	VTB	0	1	0	0
NMC	2	-	C-D-P	25	2	60	10	3	0	0	1	0	0	1	0	0	1	20	O	0	1	1	1	0	40	Pel	1	C	0	1	10	1	0	40/60	MS	SA	WN	VTB	0	1	0	0
NMC	1	-	C-D-P	15	0	79	5	1	0	0	1	0	0	1	0	0	0	20	O	0	1	0	1	0	60	On	1	C	0	1	5	0	1	20/80	MS	S	PW	VTB	0	1	0	0

# APPENDIX 4

Well	Sample	Spot	Atomic %							
			O	Mg	Al	Si	S	Cl	K	Ca
N 6-28	7	6-28-7_1	71.8	10.5		1.0				16.7
N 6-28	7	6-28-7_10	65.4	12.9		3.3				18.3
N 6-28	7	6-28-7_11	66.9	12.3		2.6				18.1
N 6-28	7	6-28-7_2	71.7	10.7		1.3				16.2
N 6-28	7	6-28-7_3	71.8	10.8		1.1				16.2
N 6-28	7	6-28-7_4	67.4	12.7		2.3				17.6
N 6-28	7	6-28-7_5	66.8	13.3		2.1				17.7
N 6-28	7	6-28-7_6	66.9	12.6		2.0				18.4
N 6-28	7	6-28-7_7	66.7	13.7		2.0				17.6
N 6-28	7	6-28-7_8	66.7	12.5		2.7				18.1
N 6-28	7	6-28-7_9	68.0	11.4		3.5				17.1
N 6-28	7	6-28-9_1	66.3	9.2	1.5	3.3	0.2	3.4	0.4	15.4
N 6-28	7	6-28-9_2	57.1	15.1	0.4	2.8	0.1	2.7	0.1	21.4
N 6-28	7	6-28-9_3	63.5	14.3		1.5		1.5		18.9
N 6-28	7	6-28-9_4	61.4	13.8		1.5		2.0		21.2
N 6-28	7	6-28-9_5	63.1	13.7		1.5		2.3		19.2
N 6-28	7	6-28-9_6	64.8	5.2		19.3		1.4		9.3
N 6-28	7	6-28-9_7	59.3	11.0		12.1		2.0		15.5
N 6-28	7	6-28-9_8	59.0	14.4		4.2		2.4		19.7
N 6-28	7	6-28-9_9	61.1	7.0		17.3		2.0		12.4
UT 15-13	13	15-13-13_1		39.4						60.2
UT 15-13	13	15-13-13_2		40.6						59.1
UT 15-13	13	15-13-13_3		43.0						57.0
UT 15-13	13	15-13-13_5		38.8						61.2
UT 15-13	13	15-13-13_6		39.8						60.2
UT 15-13	13	15-13-13_7		39.3						60.6
UT 15-13	13	15-13-13_8		39.1						60.8
UT 15-13	13	15-13-13_9		38.9						61.1
UT 15-13	14	15-13-14_1	65.8			34.2				
UT 15-13	14	15-13-14_10		44.0						56.0
UT 15-13	14	15-13-14_11		41.1						57.7
UT 15-13	14	15-13-14_12		42.3						57.0
UT 15-13	14	15-13-14_13		43.1						56.9
UT 15-13	14	15-13-14_14		45.6						54.4
UT 15-13	14	15-13-14_15		43.4						56.1
UT 15-13	14	15-13-14_16		44.1						55.9
UT 15-13	14	15-13-14_17		44.1						55.9
UT 15-13	14	15-13-14_18		42.1						57.8
UT 15-13	14	15-13-14_19		43.4						56.3
UT 15-13	14	15-13-14_2		43.6						56.4
UT 15-13	14	15-13-14_20		43.0						56.5
UT 15-13	14	15-13-14_21		42.5						57.2

Well	Sample	Spot	O	Mg	Al	Si	S	Cl	K	Ca
UT 15-13	14	15-13-14_4		43.6						56.2
UT 15-13	14	15-13-14_5		43.6						56.2
UT 15-13	14	15-13-14_6		43.8						56.2
UT 15-13	14	15-13-14_7		41.4						58.3
UT 15-13	14	15-13-14_8		41.8						57.2
UT 15-13	14	15-13-14_9		42.6						56.5
PW 13-06	7	13-06-07_1		41.1						58.7
PW 13-06	7	13-06-07_2		38.8						61.1
PW 13-06	7	13-06-07_3		44.4						55.5
PW 13-06	7	13-06-07_4		37.9						62.0
PW 13-06	7	13-06-07_5		42.5						57.3
PW 13-06	7	13-06-07_6		43.7						56.1
PW 13-06	7	13-06-07_7		44.4						55.5
PW 13-06	8	13-06-08_C_21		39.6						59.7
PW 13-06	8	13-06-08_C_15		45.7						53.5
PW 13-06	8	13-06-08_C_14		46.5						52.7
PW 13-06	8	13-06-08_C_20		41.6						57.7
PW 13-06	8	13-06-08_C_9		45.5						53.9
PW 13-06	8	13-06-08_C_13		42.8						56.7
PW 13-06	8	13-06-08_C_18		43.8						55.8
PW 13-06	8	13-06-08_C_19		40.5						59.1
PW 13-06	8	13-06-08_C_8		40.3						59.3
PW 13-06	8	13-06-08_C_17		45.7						54.0
PW 13-06	8	13-06-08_C_4		47.7						52.0
PW 13-06	8	13-06-08_C_5		43.7						56.0
PW 13-06	8	13-06-08_C_11		44.8						55.0
PW 13-06	8	13-06-08_C_10		42.0						57.9
PW 13-06	8	13-06-08_6	69.0	6.5		12.3	0.2	1.3		10.7
PW 13-06	8	13-06-08_7	70.7	10.3		1.3	0.1	1.0		16.4
PW 13-06	8	13-06-08_12		44.2						55.7
PW 13-06	8	13-06-08_8	69.0	11.7		0.9	0.1	0.8		17.5
PW 13-06	8	13-06-08_C_7		39.7						60.2
PW 13-06	8	13-06-08_C_6		39.8						60.2
PW 13-06	8	13-06-08_C_26		41.8						58.2
PW 13-06	8	13-06-08_C_25		43.4						56.6
PW 13-06	8	13-06-08_C_24		38.1						61.9
PW 13-06	8	13-06-08_C_22		41.6						58.4
PW 13-06	8	13-06-08_C_16		43.9						56.1
PW 13-06	8	13-06-08_C_1		40.7						59.3
PW 13-06	8	13-06-08_C_3	64.9			35.1				
PW 13-06	8	13-06-08_C_2	63.5		0.1	32.6		2.6		
PW 13-06	8	13-06-08_9	65.8	3.2		23.5	0.2	0.8		6.5
PW 13-06	8	13-06-08_4	68.1	12.6		0.4		0.9		17.9
PW 13-06	8	13-06-08_3	61.9	4.3	6.0	13.0		0.9	5.3	8.2
PW 13-06	8	13-06-08_2	63.0	3.5	6.2	13.6		0.9		6.9
PW 13-06	8	13-06-08_12	67.2	4.2		18.9	0.2	0.9		8.7
PW 13-06	8	13-06-08_11	65.8	3.6		23.3	0.1	0.8		6.4
PW 13-06	8	13-06-08_10	65.6	3.4		23.1	0.2	0.9		6.8
PW 13-06	8	13-06-08_1	61.7	3.0	7.4	15.5		0.8		4.8
PW 13-06	11	13-06-11_1		37.6						61.6

Well	Sample	Spot	O	Mg	Al	Si	S	Cl	K	Ca
PW 13-06	11	13-06-11_10		39.2						60.6
PW 13-06	11	13-06-11_2		38.3						61.4
PW 13-06	11	13-06-11_3		39.8						59.6
PW 13-06	11	13-06-11_4		36.7						61.6
PW 13-06	11	13-06-11_5		40.7						59.1
PW 13-06	11	13-06-11_6		36.5						63.5
PW 13-06	11	13-06-11_7		35.1						64.7
PW 13-06	11	13-06-11_8		42.2						57.4
PW 13-06	11	13-06-11_9		36.7						61.9
PW 13-06	12	13-06-12_1		43.2						56.8
PW 13-06	12	13-06-12_10		41.7						57.8
PW 13-06	12	13-06-12_11		41.7						58.3
PW 13-06	12	13-06-12_2		39.5						60.0
PW 13-06	12	13-06-12_3		41.2						58.8
PW 13-06	12	13-06-12_4		39.3						59.9
PW 13-06	12	13-06-12_5		43.2						56.8
PW 13-06	12	13-06-12_6		45.4						54.2
PW 13-06	12	13-06-12_7		43.4						56.6
PW 13-06	12	13-06-12_8		41.4						58.3
PW 13-06	12	13-06-12_9		42.4						57.3

## APPENDIX 5

Well	Sample	Depth	Lithology	%CaCO <sub>3</sub>		
				IU	U of A	WMU
BBC 14-1	2	6657.8	D		55.2	
BBC 14-1	4	6665.5	D		53.4	
BBC 14-1	8	6675.3	D		55.5	
BBC 14-1	12	6684.0	PZ1			53.8
BBC 14-1	12B	6684.5	PZ1			52.1
BBC 14-1	13	6684.9	PZ1			53.7
BBC 14-1	14	6685.4	PZ1		55.2	53.9
BBC 14-1	14A	6686.1	PZ1			54.6
BBC 14-1	14B	6686.5	PZ1			53.7
BBC 14-1	15	6686.8	PZ1		55.5	53.8
BBC 14-1	14A	6687.2	PZ1			53.6
BBC 14-1	15B	6687.6	PZ1			54.2
BBC 14-1	16	6688.4	PZ1			54.3
BBC 14-1	16A	6692.1	PZ1'			52.7
BBC 14-1	17	6692.6	PZ1'		54.2	52.3
BBC 14-1	18	6693.5	PZ1'			51.3
BBC 14-1	18A	6694.1	PZ1'			51.8
BBC 14-1	18B	6694.9	PZ1'			55.2
BBC 14-1	19	6700.9	PZ2		53.3	53.8
BBC 14-1	20	6701.4	PZ2		54.8	53.2
BBC 14-1	20A	6702.3	PZ2			53.8
BBC 14-1	21	6703.1	PZ2		53.7	51.7
BBC 14-3	26	7372.4	PZ1		55.3	53.6
BBC 14-3	27	7373.7	PZ1			53.9
BBC 14-3	28	7374.1	PZ1			53.6
BBC 14-3	29	7375.0	PZ1			53.9
BBC 14-3	30	7375.9	PZ1			54.4
BBC 14-3	31	7376.8	PZ1			54.9
BBC 14-3	32	7382.0	PZ1'			52.9
BBC 14-3	33	7382.7	PZ1'			52.1
BBC 14-3	34	7383.7	PZ1'			53.1
N 6-28	1	8199.3	D	55.2	52.7	
N 6-28	2	8203.6	D		53.7	
N 6-28	3	8205.6	D		52.1	
N 6-28	4	8217.6	D	55.8	53.3	
N 6-28	5	8223.2	PZ1		52.3	
N 6-28	6	8223.7	PZ1	54.9	53.8	
N 6-28	7	8230.2	PZ1'	51.8	52.6	
N 6-28	9	8242.5	PZ2	54.9	54.6	
N 6-28	10	8248.9	D		55.5	
N 6-28	12	8267.4	D		51.0	
N 6-28	13	8270.3	D		54.7	

Well	Sample	Depth	Lithology	IU	U of A	WMU
UT 15-13	15-13-5	6982.2	D		53.7	
UT 15-13	15-13-6	6983.9	D		54.7	
UT 15-13	15-13-7	6989.0	D		53.7	
UT 15-13	15-13-9	7006.5	PZ1		52.3	
UT 15-13	15-13-10	7007.8	PZ1		53.9	
UT 15-13	15-13-11B	7009.9	PZ1	55.5	55.5	
UT 15-13	15-13-12	7016.4	PZ1'		57.5	
UT 15-13	15-13-13	7017.4	PZ1'	55.2	55.6	
UT 15-13	15-13-14	7025.2	PZ2	52.7	52.3	
PW 13-06	13-06-1	5524.2	D		55.0	
PW 13-06	13-06-2	5524.7	D		55.5	
PW 13-06	13-06-3	5527.3	D		52.6	
PW 13-06	13-06-6	5539.5	PZ1		51.6	50.4
PW 13-06	13-06-6A	5540.1	PZ1			49.7
PW 13-06	13-06-6B	5540.7	PZ1		51.8	50.5
PW 13-06	13-06-6C	5541.3	PZ1			51.9
PW 13-06	13-06-7	5541.9	PZ1	52.7	51.1	49.6
PW 13-06	13-06-7A	5542.4	PZ1		53.1	53.4
PW 13-06	13-06-7B	5542.7	PZ1			52.9
PW 13-06	13-06-8	5543.5	PZ1	53.3	54.2	52.9
PW 13-06	13-06-9	5544.3	PZ1			52.9
PW 13-06	13-06-9A	5544.7	PZ1		54.9	53.1
PW 13-06	13-06-10	5545.3	PZ1	55.5	53.1	54.0
PW 13-06	13-06-10A	5546.1	PZ1		56.0	54.4
PW 13-06	13-06-10B	5551.0	PZ1'		55.7	53.5
PW 13-06	13-06-10C	5551.6	PZ1'		55.5	53.2
PW 13-06	13-06-11	5552.2	PZ1'	55.2	54.6	52.9
PW 13-06	13-06-11A	5553.9	PZ2		53.9	53.2
PW 13-06	13-06-11B	5554.7	PZ2		53.4	52.1
PW 13-06	13-06-11C	5556.6	PZ3			55.1
PW 13-06	13-06-12	5557.4	PZ2	54.3	55.7	51.8
PW 13-06	13-06-13	5563.3	D		55.0	
PW 13-06	13-06-14	5565.9	L		53.9	
PW 13-06	13-06-15	5580.8	D		50.3	
PW 13-06	13-06-16	5595.4	D		54.2	
PW 13-06	13-06-17	5596.0	D		54.2	
PW 13-06	13-06-18	5603.4	L		53.1	
PW 13-06	13-06-19	5607.8	D		54.9	
DS 11-20	11-20-1	4972.5	D		56.2	
DS 11-20	11-20-2	4974.5	L		54.0	
DS 11-20	11-20-4	4980.1	PZ1		56.0	
DS 11-20	11-20-5	4985.5	PZ1'		55.5	
DS 11-20	11-20-8	4989.5	PZ2		52.2	
DS 11-20	11-20-9	4990.5	PZ2		57.7	
I 16	16-2	4705.4	D		55.5	
I 16	16-3	4706.3	PZ1	57.0	58.2	
I 16	16-4	4707.0	PZ1		55.2	
I 16	16-7	4720.8	PZ1'		54.9	
I 16	16-8	4721.3	PZ1'		57.1	

Well	Sample	Depth	Lithology	IU	U of A	WMU
I 16	16-10	4723.3	PZ2		56.5	
I 16	16-11	4724.2	PZ2		55.0	

## APPENDIX 6

SAMPLE	Point	Concentration (WT %)						
		Fe	Mn	Mg	Ca	Sr	C	O
13-06-11 t1A	1	0.06	0.00	11.46	23.41	0.10	12.71	50.78
13-06-11 t1A	2	0.52	0.00	10.89	23.90	0.07	12.66	50.61
13-06-11 t1A	3	0.49	0.00	11.12	23.71	0.09	12.72	50.82
13-06-11 t1A	4	0.51	0.02	11.18	23.72	0.08	12.76	51.00
13-06-11 t1A	5	0.10	0.00	10.86	24.55	0.08	12.76	50.98
13-06-11 t1A	6	0.56	0.04	11.11	23.87	0.08	12.78	51.08
13-06-11 t1A	7	0.37	0.00	11.42	23.71	0.08	12.84	51.31
13-06-11 t1A	8	0.55	0.00	10.93	24.25	0.08	12.80	51.15
13-06-11 t1A	9	0.35	0.00	6.22	31.01	0.10	12.46	49.77
13-06-11 t1A	10	0.52	0.00	11.51	23.71	0.07	12.92	51.63
13-06-11 t1A	11	0.14	0.00	10.91	24.85	0.12	12.89	51.49
13-06-11 t2	1	0.26	0.07	10.76	24.22	0.10	12.66	50.59
13-06-11 t2	2	0.61	0.00	10.62	24.24	0.06	12.65	50.56
13-06-11 t2	3	0.31	0.00	11.45	23.57	0.09	12.80	51.15
13-06-11 t2	4	0.18	0.00	10.97	24.33	0.09	12.77	51.02
13-06-11 t2	5	0.37	0.03	11.28	23.83	0.08	12.81	51.20
13-06-11 t2	6	0.34	0.00	11.00	24.31	0.07	12.80	51.17
13-06-11 t2	7	0.73	0.00	10.54	24.62	0.09	12.76	50.99
13-06-11 t2	8	0.59	0.00	10.77	24.48	0.07	12.79	51.13
13-06-11 t2	9	0.05	0.02	12.75	22.48	0.00	13.05	52.15
13-06-11 t3	1	0.41	0.00	11.11	23.66	0.07	12.68	50.67
13-06-11 t3	2	0.40	0.00	11.08	23.80	0.04	12.70	50.75
13-06-11 t3	3	0.51	0.00	10.99	23.93	0.07	12.72	50.85
13-06-11 t3	4	0.55	0.02	11.02	23.90	0.07	12.74	50.93
13-06-11 t3	5	0.29	0.00	10.80	24.49	0.10	12.75	50.96
13-06-11 t3	6	0.06	0.00	11.08	24.30	0.10	12.79	51.10
13-06-11 t3	7	0.37	0.00	11.35	23.92	0.07	12.87	51.42
13-06-11 t3	8	0.43	0.00	11.10	24.31	0.08	12.88	51.46
13-06-11 t3	9	0.52	0.04	11.11	24.20	0.09	12.88	51.46
13-06-11 t4	1	0.40	0.00	11.06	23.70	0.07	12.66	50.61
13-06-11 t4	2	0.44	0.00	11.14	23.58	0.07	12.68	50.66
13-06-11 t4	3	0.43	0.00	11.16	23.58	0.12	12.69	50.71
13-06-11 t4	4	0.49	0.00	11.00	23.79	0.07	12.68	50.67
13-06-11 t4	5	0.53	0.00	11.48	23.35	0.05	12.79	51.11
13-06-11 t4	6	0.33	0.00	10.78	24.47	0.09	12.74	50.92
13-06-11 t4	7	0.24	0.00	11.18	24.04	0.10	12.80	51.14
13-06-11 t4	8	1.36	0.00	10.26	24.46	0.05	12.70	50.75
13-06-11 t4	9	0.74	0.00	10.51	24.69	0.08	12.76	51.01
13-06-11 t4	10	0.68	0.00	11.03	24.15	0.06	12.84	51.33
13-06-11 t5	2	0.95	0.05	10.78	23.79	0.04	12.68	50.66
13-06-11 t5	3	0.35	0.03	10.66	24.49	0.10	12.70	50.77
13-06-11 t5	4	0.48	0.02	10.72	24.33	0.10	12.71	50.78



SAMPLE	Point	Fe	Mn	Mg	Ca	Sr	C	O
13-06-11 t5	5	0.30	0.02	11.16	23.94	0.09	12.77	51.05
13-06-11 t5	6	0.38	0.02	10.77	24.46	0.10	12.75	50.97
13-06-11 t5	7	0.39	0.03	10.83	24.38	0.10	12.76	51.00
13-06-11 t5	8	0.13	0.00	10.95	24.44	0.14	12.78	51.08
13-06-11 t5	9	0.17	0.00	11.06	24.29	0.13	12.80	51.15
13-06-11 t5	10	0.14	0.03	11.35	24.06	0.07	12.87	51.42
13-06-11 t5	11	0.48	0.00	10.92	24.41	0.08	12.83	51.25
13-06-11 t5	12	0.40	0.00	11.40	23.86	0.08	12.88	51.47
13-06-11 t5	13	0.16	0.00	3.78	34.75	0.13	12.33	49.29
13-06-8 t1	1	0.06	0.04	11.74	23.03	0.10	12.74	50.89
13-06-8 t1	2	0.09	0.04	12.02	22.68	0.09	12.77	51.05
13-06-8 t1	3	0.07	0.06	11.83	22.92	0.11	12.76	50.99
13-06-8 t1	4	0.06	0.04	11.58	23.33	0.10	12.75	50.97
13-06-8 t1	5	0.10	0.00	11.95	22.85	0.08	12.79	51.10
13-06-8 t1	6	0.08	0.04	11.77	23.11	0.09	12.78	51.07
13-06-8 t1	7	0.08	0.03	12.08	22.69	0.08	12.80	51.17
13-06-8 t1	8	0.09	0.06	12.02	22.73	0.11	12.80	51.15
13-06-8 t1	9	0.09	0.04	12.26	22.43	0.10	12.82	51.24
13-06-8 t1	10	0.06	0.05	11.71	23.29	0.12	12.81	51.18
13-06-8 t1	11	0.10	0.05	12.49	22.20	0.11	12.87	51.44
13-06-8 t1	12	0.09	0.03	11.81	23.22	0.09	12.83	51.28
13-06-8 t1	13	0.10	0.04	11.93	23.06	0.10	12.85	51.35
13-06-8 t1	14	0.07	0.04	12.00	23.00	0.09	12.86	51.39
13-06-8 t1	15	0.05	0.03	11.76	23.37	0.09	12.85	51.34
13-06-8 t1	16	0.08	0.06	11.99	23.02	0.11	12.87	51.43
13-06-8 t1	17	0.12	0.03	11.91	23.17	0.09	12.87	51.43
13-06-8 t1	18	0.12	0.03	12.01	23.16	0.10	12.92	51.64
13-06-8 t2	1	0.09	0.05	12.00	22.65	0.11	12.76	50.99
13-06-8 t2	2	0.08	0.03	11.92	22.78	0.12	12.75	50.97
13-06-8 t2	3	0.06	0.04	11.83	22.91	0.14	12.75	50.96
13-06-8 t2	4	0.08	0.04	11.74	23.06	0.10	12.75	50.95
13-06-8 t2	5	0.09	0.03	12.26	22.41	0.11	12.82	51.22
13-06-8 t2	6	0.07	0.05	11.76	23.13	0.10	12.78	51.09
13-06-8 t2	7	0.05	0.05	12.13	22.67	0.10	12.82	51.24
13-06-8 t2	8	0.12	0.03	11.97	22.91	0.08	12.82	51.25
13-06-8 t2	9	0.06	0.03	11.73	23.29	0.10	12.81	51.19
13-06-8 t2	10	0.06	0.06	11.65	23.40	0.10	12.81	51.19
13-06-8 t2	11	0.09	0.04	11.79	23.22	0.08	12.82	51.25
13-06-8 t2	12	0.11	0.03	12.02	22.87	0.11	12.84	51.32
13-06-8 t2	13	0.10	0.06	12.13	22.76	0.12	12.87	51.42
13-06-8 t2	14	0.09	0.04	12.63	22.12	0.13	12.92	51.62
13-06-8 t2	16	0.10	0.06	12.13	22.81	0.11	12.88	51.48
13-06-8 t2	17	0.05	0.05	11.70	23.56	0.13	12.88	51.48
13-06-8 t2	18	0.10	0.03	12.09	23.01	0.11	12.92	51.62
13-06-8 t2	19	0.09	0.04	12.16	22.94	0.09	12.93	51.65
13-06-8 t2	20	0.06	0.04	11.88	23.59	0.10	12.97	51.85
13-06-8 t3	1	0.07	0.03	12.57	21.83	0.13	12.79	51.12
13-06-8 t3	2	0.07	0.04	11.90	22.79	0.12	12.75	50.95
13-06-8 t3	3	0.06	0.06	11.76	23.01	0.09	12.75	50.94
13-06-8 t3	4	0.10	0.04	12.25	22.44	0.10	12.83	51.25

SAMPLE	Point	Fe	Mn	Mg	Ca	Sr	C	O
13-06-8 t3	5	0.12	0.02	12.52	22.13	0.10	12.86	51.41
13-06-8 t3	6	0.08	0.04	12.04	22.93	0.09	12.86	51.39
13-06-8 t3	7	0.11	0.03	12.29	22.59	0.11	12.89	51.49
13-06-8 t3	8	0.10	0.05	11.90	23.33	0.11	12.92	51.62
13-06-8 t3	9	0.07	0.04	12.32	22.81	0.08	12.96	51.79
13-06-8 t4	1	0.07	0.05	12.15	22.42	0.10	12.76	51.00
13-06-8 t4	2	0.08	0.05	12.44	22.10	0.11	12.81	51.19
13-06-8 t4	3	0.09	0.06	11.80	23.14	0.09	12.81	51.20
13-06-8 t4	4	0.34	0.05	11.89	22.84	0.09	12.82	51.22
13-06-8 t4	5	0.07	0.04	11.72	23.30	0.14	12.81	51.21
13-06-8 t4	6	0.07	0.00	12.80	21.90	0.15	12.92	51.64
13-06-8 t4	7	0.10	0.03	11.84	23.26	0.10	12.86	51.39
13-06-8 t4	8	0.07	0.03	12.17	22.90	0.11	12.91	51.60
13-06-8 t4	9	0.09	0.00	12.35	22.73	0.08	12.94	51.72
13-06-8 t5	1	0.14	0.07	12.19	22.34	0.06	12.77	51.04
13-06-8 t5	2	0.05	0.06	11.82	23.07	0.13	12.80	51.13
13-06-8 t5	3	0.25	0.03	12.20	22.59	0.11	12.87	51.44
13-06-8 t5	4	0.09	0.04	12.11	23.20	0.10	12.98	51.87
15-13-14 t1	1	0.04	0.00	12.41	22.11	0.10	12.78	51.07
15-13-14 t1	2	0.10	0.00	12.37	22.18	0.10	12.79	51.13
15-13-14 t1	3	0.11	0.00	12.20	22.41	0.09	12.78	51.08
15-13-14 t1	4	0.23	0.04	12.12	22.41	0.08	12.77	51.04
15-13-14 t1	5	0.08	0.00	12.35	22.42	0.09	12.85	51.35
15-13-14 t1	6	0.08	0.00	12.52	22.38	0.09	12.93	51.65
15-13-14 t1	7	0.08	0.00	12.55	22.62	0.12	13.01	52.01
15-13-14 t2	1	0.05	0.00	12.46	22.16	0.09	12.82	51.24
15-13-14 t2	2	0.11	0.00	12.30	22.34	0.08	12.81	51.19
15-13-14 t2	3	0.02	0.00	12.57	22.03	0.10	12.83	51.29
15-13-14 t2	4	0.05	0.00	12.70	21.86	0.10	12.85	51.35
15-13-14 t2	5	0.04	0.00	12.21	22.57	0.09	12.82	51.23
15-13-14 t2	6	0.05	0.00	12.49	22.16	0.13	12.84	51.31
15-13-14 t2	7	0.00	0.00	11.48	23.89	0.00	12.84	51.30
15-13-14 t2	8	0.09	0.00	12.47	22.49	0.11	12.94	51.70
15-13-14 t3	2	0.11	0.00	12.27	22.31	0.07	12.78	51.07
15-13-14 t3	3	0.05	0.00	12.43	22.11	0.10	12.79	51.13
15-13-14 t3	4	0.04	0.03	12.03	22.67	0.11	12.77	51.03
15-13-14 t3	5	0.07	0.00	12.32	22.37	0.08	12.82	51.23
15-13-14 t3	6	0.08	0.00	12.37	22.32	0.09	12.84	51.29
15-13-14 t3	7	0.10	0.00	12.15	22.67	0.06	12.83	51.25
15-13-14 t3	8	0.04	0.00	12.28	22.58	0.09	12.85	51.37
15-13-14 t3	9	0.11	0.00	12.22	22.64	0.12	12.86	51.39
15-13-14 t3	10	0.17	0.00	12.28	22.54	0.06	12.87	51.44
15-13-14 t3	11	0.03	0.00	12.35	22.82	0.04	12.95	51.76
15-13-14 t3	12	0.16	0.04	12.48	22.47	0.07	12.95	51.77
15-13-14 t4	1	0.05	0.00	12.31	22.47	0.11	12.84	51.31
15-13-14 t4	2	0.19	0.00	12.34	22.32	0.10	12.84	51.31
15-13-14 t4	3	0.46	0.00	12.27	22.19	0.10	12.83	51.27
15-13-14 t4	4	0.00	0.00	12.58	22.39	0.10	12.94	51.71
15-13-14 t4	5	0.10	0.00	12.42	22.59	0.09	12.94	51.72
15-13-14 t4	6	0.09	0.00	12.44	22.72	0.07	12.99	51.90

SAMPLE	Point	Fe	Mn	Mg	Ca	Sr	C	O
15-13-14 t5	1	0.10	0.00	12.15	22.49	0.07	12.77	51.04
15-13-14 t5	2	0.10	0.00	12.33	22.38	0.07	12.83	51.27
15-13-14 t5	3	0.18	0.00	12.13	22.60	0.09	12.81	51.21
15-13-14 t5	4	0.05	0.00	12.45	22.37	0.09	12.88	51.46
15-13-14 t5	5	0.26	0.00	12.01	22.91	0.08	12.87	51.41
15-13-14 t5	6	0.09	0.00	12.33	22.60	0.08	12.90	51.54
15-13-14 t5	7	0.04	0.00	12.33	22.80	0.08	12.95	51.74
15-13-14 t5	8	0.08	0.00	12.53	22.65	0.06	13.01	51.99
6-28-7 t1	1	0.00	0.03	12.26	22.36	0.07	12.77	51.05
6-28-7 t1	2	0.11	0.00	12.26	22.30	0.07	12.77	51.05
6-28-7 t1	3	0.00	0.00	12.18	22.52	0.07	12.78	51.06
6-28-7 t1	4	0.00	0.00	12.05	22.68	0.09	12.77	51.02
6-28-7 t1	5	0.03	0.00	12.36	22.27	0.05	12.79	51.13
6-28-7 t1	6	0.00	0.00	12.10	22.68	0.06	12.78	51.08
6-28-7 t1	7	0.13	0.00	11.94	22.78	0.11	12.77	51.03
6-28-7 t1	8	0.06	0.00	11.96	22.83	0.09	12.78	51.06
6-28-7 t1	9	0.07	0.00	12.13	22.56	0.12	12.79	51.11
6-28-7 t1	10	0.06	0.00	12.02	22.77	0.08	12.79	51.10
6-28-7 t1	11	0.09	0.00	12.10	22.66	0.07	12.80	51.14
6-28-7 t1	12	0.00	0.00	12.23	22.56	0.06	12.81	51.21
6-28-7 t1	13	0.04	0.00	12.01	22.83	0.07	12.79	51.13
6-28-7 t1	14	0.03	0.00	12.31	22.48	0.04	12.83	51.28
6-28-7 t1	15	0.05	0.00	12.37	22.39	0.07	12.84	51.33
6-28-7 t1	16	0.08	0.00	12.05	22.83	0.07	12.82	51.25
6-28-7 t1	17	0.04	0.00	12.09	22.80	0.09	12.83	51.27
6-28-7 t1	18	0.03	0.00	12.19	22.71	0.09	12.85	51.34
6-28-7 t1	20	0.11	0.00	12.19	22.71	0.06	12.86	51.39
6-28-7 t1	21	0.00	0.00	12.23	22.78	0.05	12.88	51.47
6-28-7 t1	22	0.08	0.00	12.21	22.74	0.05	12.88	51.46
6-28-7 t1	23	0.04	0.00	12.44	22.48	0.05	12.90	51.55
6-28-7 t1	24	0.04	0.00	12.24	23.01	0.06	12.96	51.80
6-28-7 t2	1	0.04	0.00	12.24	22.37	0.06	12.77	51.03
6-28-7 t2	2	0.08	0.00	12.11	22.50	0.08	12.76	50.99
6-28-7 t2	3	0.12	0.00	11.26	23.68	0.06	12.69	50.73
6-28-7 t2	4	0.02	0.00	12.00	22.72	0.07	12.76	50.98
6-28-7 t2	5	0.06	0.00	12.15	22.53	0.06	12.77	51.05
6-28-7 t2	6	0.00	0.00	12.24	22.47	0.07	12.79	51.12
6-28-7 t2	7	0.00	0.00	12.29	22.47	0.04	12.81	51.20
6-28-7 t2	8	0.05	0.00	12.05	22.74	0.06	12.79	51.11
6-28-7 t2	9	0.09	0.00	12.16	22.61	0.05	12.81	51.19
6-28-7 t2	10	0.05	0.00	12.18	22.62	0.06	12.82	51.21
6-28-7 t2	11	0.02	0.00	12.45	22.31	0.03	12.85	51.34
6-28-7 t2	12	0.00	0.00	12.12	22.76	0.10	12.82	51.24
6-28-7 t2	13	0.00	0.00	12.21	22.74	0.08	12.86	51.40
6-28-7 t2	14	0.09	0.00	12.16	22.76	0.07	12.86	51.40
6-28-7 t2	15	0.04	0.00	12.40	22.60	0.06	12.92	51.63
6-28-7 t2	16	0.03	0.02	12.25	22.80	0.06	12.91	51.58
6-28-7 t2	17	0.00	0.00	12.13	23.06	0.08	12.92	51.62
6-28-7 t2	18	0.11	0.00	12.27	22.84	0.07	12.94	51.72
6-28-7 t2	19	0.00	0.00	12.08	23.18	0.09	12.93	51.68

SAMPLE	Point	Fe	Mn	Mg	Ca	Sr	C	O
6-28-7 t2	20	0.21	0.00	11.93	23.36	0.06	12.95	51.74
6-28-7 t3	1	0.15	0.00	12.02	22.65	0.05	12.77	51.02
6-28-7 t3	2	0.02	0.00	12.31	22.34	0.08	12.79	51.12
6-28-7 t3	3	0.03	0.00	12.09	22.66	0.06	12.78	51.07
6-28-7 t3	4	0.07	0.00	12.09	22.63	0.06	12.78	51.07
6-28-7 t3	5	0.13	0.00	12.06	22.62	0.09	12.78	51.06
6-28-7 t3	6	0.05	0.00	12.25	22.42	0.07	12.80	51.14
6-28-7 t3	7	0.05	0.00	12.24	22.48	0.07	12.80	51.16
6-28-7 t3	8	0.03	0.00	12.33	22.39	0.03	12.81	51.20
6-28-7 t3	9	0.03	0.00	12.13	22.66	0.04	12.80	51.15
6-28-7 t3	10	0.03	0.00	12.25	22.53	0.05	12.82	51.23
6-28-7 t3	11	0.11	0.00	12.13	22.60	0.11	12.81	51.17
6-28-7 t3	12	0.07	0.00	12.13	22.67	0.06	12.81	51.19
6-28-7 t3	13	0.06	0.00	12.23	22.53	0.09	12.82	51.22
6-28-7 t3	14	0.07	0.00	12.20	22.59	0.07	12.83	51.26
6-28-7 t3	15	0.02	0.02	12.11	22.76	0.06	12.82	51.25
6-28-7 t3	16	0.03	0.00	12.16	22.81	0.07	12.86	51.39
6-28-7 t3	17	0.30	0.03	11.66	23.28	0.07	12.82	51.21
6-28-7 t3	18	0.04	0.00	12.29	22.62	0.10	12.88	51.45
6-28-7 t3	19	0.09	0.00	12.27	22.65	0.06	12.88	51.47
6-28-7 t3	21	0.14	0.00	12.29	22.63	0.07	12.89	51.53
6-28-7 t3	22	0.00	0.00	12.01	23.21	0.10	12.90	51.57
6-28-7 t3	23	0.06	0.00	12.26	22.99	0.05	12.97	51.82
6-28-7 t3	24	0.37	0.00	11.94	23.30	0.04	12.97	51.82
6-28-7 t4	1	0.00	0.00	12.39	22.20	0.09	12.79	51.09
6-28-7 t4	2	0.04	0.00	12.09	22.60	0.06	12.77	51.02
6-28-7 t4	3	0.11	0.00	11.95	22.81	0.05	12.77	51.05
6-28-7 t4	4	0.07	0.00	12.13	22.59	0.08	12.79	51.11
6-28-7 t4	5	0.16	0.00	11.86	22.91	0.08	12.77	51.05
6-28-7 t4	6	0.07	0.00	12.28	22.43	0.06	12.81	51.20
6-28-7 t4	7	0.14	0.00	12.22	22.47	0.10	12.82	51.23
6-28-7 t4	8	0.10	0.00	12.25	22.52	0.05	12.83	51.27
6-28-7 t4	9	0.00	0.00	12.40	22.41	0.07	12.85	51.36
6-28-7 t4	10	0.05	0.03	12.09	22.77	0.09	12.83	51.27
6-28-7 t4	11	0.04	0.00	12.25	22.62	0.07	12.85	51.35
6-28-7 t4	12	0.04	0.02	12.29	22.57	0.04	12.86	51.38
6-28-7 t4	13	0.11	0.00	12.13	22.78	0.07	12.85	51.36
6-28-7 t4	14	0.08	0.02	12.19	22.71	0.08	12.86	51.39
6-28-7 t4	15	0.00	0.00	12.38	22.55	0.06	12.88	51.49
6-28-7 t4	16	0.06	0.00	12.20	22.75	0.07	12.87	51.43
6-28-7 t4	17	0.03	0.00	12.27	22.76	0.12	12.91	51.58
6-28-7 t4	18	0.05	0.00	12.36	22.69	0.08	12.92	51.65
6-28-7 t4	19	0.00	0.00	12.13	23.04	0.10	12.91	51.60
6-28-7 t4	20	0.21	0.00	12.36	22.58	0.09	12.93	51.68
6-28-7 t4	21	0.10	0.00	12.20	23.08	0.07	12.98	51.87
6-28-7 t4	22	0.06	0.02	12.60	22.57	0.05	13.02	52.02
6-28-7 t5	1	0.05	0.00	12.07	22.62	0.04	12.76	50.99
6-28-7 t5	2	0.03	0.00	12.26	22.42	0.06	12.79	51.13
6-28-7 t5	3	0.06	0.00	12.14	22.56	0.08	12.78	51.09
6-28-7 t5	4	0.03	0.00	12.26	22.48	0.06	12.81	51.20

<b>SAMPLE</b>	<b>Point</b>	<b>Fe</b>	<b>Mn</b>	<b>Mg</b>	<b>Ca</b>	<b>Sr</b>	<b>C</b>	<b>O</b>
6-28-7 t5	5	0.05	0.00	12.20	22.57	0.08	12.82	51.21
6-28-7 t5	6	0.12	0.00	11.93	22.92	0.05	12.80	51.14
6-28-7 t5	7	0.05	0.00	12.24	22.57	0.08	12.83	51.27
6-28-7 t5	8	0.16	0.00	12.02	22.82	0.00	12.81	51.21
6-28-7 t5	9	0.00	0.00	12.27	22.61	0.08	12.85	51.35
6-28-7 t5	10	0.09	0.00	12.13	22.80	0.05	12.85	51.36
6-28-7 t5	11	0.03	0.00	12.22	22.75	0.06	12.87	51.44
6-28-7 t5	12	0.03	0.00	12.11	22.93	0.07	12.87	51.44
6-28-7 t5	13	0.00	0.00	12.24	22.78	0.07	12.89	51.50
6-28-7 t5	14	0.03	0.00	12.17	22.89	0.07	12.89	51.50
6-28-7 t5	15	0.03	0.00	11.98	23.16	0.08	12.88	51.46
6-28-7 t5	16	0.13	0.00	12.13	22.87	0.09	12.89	51.51
6-28-7 t5	17	0.04	0.00	12.27	22.79	0.06	12.91	51.59
6-28-7 t5	18	0.04	0.00	12.21	22.89	0.06	12.91	51.59
6-28-7 t5	20	0.05	0.00	12.35	22.73	0.08	12.94	51.71
6-28-7 t5	21	0.07	0.00	12.35	22.80	0.06	12.96	51.79
6-28-7 t5	22	0.04	0.00	12.07	23.35	0.06	12.98	51.87

## APPENDIX 7

W/O	Sample	Litho	Depth	Concentration (ppm)									
				Ca	Mg	Na	Al	Si	Fe	Mn	Zn	Sr	Pb
BBC-14-1	4	D	6665.5	248675	149442	931.8	693.4	3451.7	5149.6	399.6	5.2	833.2	0.8
BBC-14-1	14	PZ1	6685.4	225617	120877	955.7	777.3	3089.6	4748.1	308.6	12.8	608.5	1.9
BBC-14-1	17	PZ1'	6692.6	244420	126593	873.3	755.8	3467.8	3924.9	326.2	6.7	803.9	1.7
BBC-14-1	19	L	6696.1	372918	15518	425	951	2675	4271	705	17.3	1662	2.69
BBC-14-1	21	PZ2	6703.1	267000	140463	942.2	522.4	2597.5	1848.3	236.3	4.7	811.4	0.8
BBC-14-3	26	PZ1	7372.4	263715	141876	1273.1	243.7	1850.0	2359.4	209.5	2.6	1292.4	0.5
N 6-28	1	D	8199.3	208594	107159	1065.5	1334.8	2885.7	17164.6	207.1	29.6	1012.4	2.5
N 6-28	2	D	8203.6	214855	108400	914.0	621.2	2636.0	7671.4	243.5	10.4	916.8	0.6
N 6-28	3	D	8205.6	254435	130130	741.4	714.2	2678.1	12020.6	352.6	8.3	893.6	1.5
N 6-28	4	D	8217.6	244175	122682	954.0	1029.2	2386.0	7492.0	417.4	27.3	813.8	2.7
N 6-28	6	PZ1	8223.7	252341	137474	1293.9	150.5	1582.8	3205.8	224.4	6.6	1454.9	0.5
N 6-28	7	PZ1'	8230.2	269703	141954	962.5	264.6	1751.3	2224.1	116.1	3.5	892.6	0.6
N 6-28	9	PZ2	8242.5	278704	135641	1042.6	353.6	1683.1	3713.8	423.6	4.7	960.3	0.5
N 6-28	10	D	8248.9	282808	120591	820.3	480.4	1604.9	7606.9	272.8	5.3	1101.1	0.9
N 6-28	13	D	8270.3	254046	136813	1409.5	244.6	1500.7	2255.5	163.2	3.2	1280.7	0.3
UT 15-13	1	L	6945.9	353004	11190	623	1264	2115	12397	929	34.8	1135	8.98
UT 15-13	5	D	6982.2	221106	112451	1161.3	2044.1	2362.7	12491.5	258.6	37.7	848.2	5.1
UT 15-13	7	D	6989.0	268080	148742	1065.7	200.3	1964.1	13188.6	684.5	6.9	1039.9	0.7
UT 15-13	9	PZ1	7006.5	232123	149330	1094.3	181.7	2199.3	4354.4	202.8	7.2	1412.3	2.2
UT 15-13	10	PZ1	7007.8	255347	161219	922.5	159.7	1693.4	2990.9	142.8	3.0	1456.6	0.7
UT 15-13	11B	PZ2	7009.9	253364	129550	988.4	139.3	1462.7	2054.7	245.1	3.4	1200.8	0.3
UT 15-13	14	PZ2	7025.2	232868	147531	1025.4	874.4	8855.6	3092.5	160.1	6.0	1164.7	0.9
PW 13-06	1	D	5524.2	269433	101397	935.1	344.3	1540.2	4600.1	225.3	4.0	935.0	1.6
PW 13-06	2	D	5524.7	277323	115555	1028.8	476.6	2012.0	4545.6	221.9	6.8	1483.2	0.6
PW 13-06	3	D	5527.3	276877	130559	808.1	142.2	1694.0	5340.8	234.9	4.2	905.9	0.3
PW 13-06	4	L	5528.3	407091	6315	384	407	1227	11547	709	13.4	1765	2.11
PW 13-06	6	PZ1	5539.5	282515	164765	822.0	44.2	2159.1	1429.8	91.1	1.3	1846.2	1.4
PW 13-06	6B	PZ1	5540.7	245014	161206	2098.7	119.8	1718.3	1669.5	241.8	7.7	1991.5	0.8
PW 13-06	7B	PZ1	5542.7	264659	146416	1274.0	113.0	1985.0	1439.0	299.8	6.3	1722.1	0.6
PW 13-06	8	PZ1	5543.5	261192	132692	787.6	94.2	2236.8	3932.4	469.9	2.9	1368.8	1.7
PW 13-06	9	PZ1	5544.3	248924	131320	755.4	88.6	1863.8	1626.1	271.5	4.1	1204.2	0.7
PW 13-06	10B	PZ1'	5551.0	246686	132581	1184.6	1020.0	2426.3	5077.2	254.0	8.9	1161.6	1.6
PW 13-06	11	PZ1'	5552.2	246342	134757	982.1	857.1	2162.5	5715.4	203.2	6.8	1011.2	1.2
PW 13-06	11B	PZ2	5554.7	236416	124624	1061.2	670.7	2080.4	3197.3	158.0	4.4	846.0	0.7
PW 13-06	14	L	5565.9	370285	6392	654	1291	2050	10833	654	22.4	1500	5.34
PW 13-06	17	D	5596.0	250691	150098	792.8	98.0	1214.8	2831.3	169.3	3.7	1034.6	0.6
PW 13-06	18	L	5604.0	312560	16660	1168	2456	3131	5129	364	19.5	1237	5.46
PW 13-06	19	D	5607.8	233885	129379	1074.3	267.2	2337.2	3696.5	245.1	2.9	892.3	0.6

W/O	Sample	Litho	Depth	Ca	Mg	Na	Al	Si	Fe	Mn	Zn	Sr	Pb
DS 11-20	2	L	4974.5	381082	8069	1338	824	2002	4851	451	6.34	1159	2.77
DS 11-20	4	PZ1	4980.1	215128	106155	1942.4	1520.6	3328.7	8627.6	282.7	18.0	785.6	3.7
DS 11-20	5	PZ1'	4985.5	234295	107464	1421.2	1440.7	7746.7	7353.1	244.2	76.4	969.8	2.6
UI 16	5	L	4710.0	343576	17018	1090	1371	2488	4162	265	15.2	977	3.78
UI 16	7	PZ1'	4720.8	238937	116240	1507.8	796.6	2271.8	8757.7	208.7	18.3	916.4	3.7
NMC	4	D	-	243544	136852	1310.1	814.0	3299.8	7302.2	495.0	10.0	896.9	1.8
NMC	5	D	-	237415	115591	1122.3	1463.0	3815.5	8262.6	680.5	16.3	787.0	3.0

**Detection limit**    10        0.5        0.7        0.1                    7        0.02   0.05   0.01   0.02

## APPENDIX 8

Well	Sample	Depth	$\delta^{13}\text{C}$ (VPDB)	$\delta^{18}\text{O}$ (VPDB)	%Cal	%Dol
BBC 14-1	14-1-2	6657.75	-0.2	-2.8	22.3	77.7
BBC 14-1	14-1-4	6665.5	1.5	-1.5	1.2	98.8
BBC 14-1	14-1-8	6675.3	-1.1	-5.1	15.6	84.4
BBC 14-1	14-1-14	6685.4	-3.3	-2.7	7.0	93.0
BBC 14-1	14-1-17	6692.6	-3.3	-2.4	0.0	100.0
BBC 14-1	14-1-19	6696.1	-1.2	-8.3	99.2	0.8
BBC 14-1	14-1-20	6701.4	1.2	-2.7	16.2	83.8
BBC 14-1	14-1-21	6703.1	1.9	-0.7	1.4	98.6
N 6-28	6-28-1	8199.3	1.4	-0.8	0.0	100.0
N 6-28	6-28-2	8203.6	5.2	-0.1	10.0	90.0
N 6-28	6-28-3	8205.6	6.4	-2.0	0.0	100.0
N 6-28	6-28-4	8217.6	4.1	-1.9	0.0	100.0
N 6-28	6-28-5	8223.2	0.3	-2.1	13.4	86.6
N 6-28	6-28-6	8223.7	2.4	0.9	6.8	93.2
N 6-28	6-28-7	8230.2	5.2	-0.3	0.0	100.0
N 6-28	6-28-8	8234.6	1.3	-7.3	94.7	5.3
N 6-28	6-28-9	8242.5	3.7	-2.1	2.8	97.2
N 6-28	6-28-10	8248.9	2.7	-4.0	7.1	92.9
N 6-28	6-28-11	8256	2.3	-4.9	21.9	78.1
N 6-28	6-28-12	8267.4	3.0	-7.3	21.0	79.0
N 6-28	6-28-13	8270.3	-0.3	-1.3	4.4	95.6
UT 15-13	15-13-1	6945.9	0.1	-7.2	90.4	9.6
UT 15-13	15-13-5	6982.2	2.9	0.1	0.0	100.0
UT 15-13	15-13-6	6983.9	2.0	-2.8	22.4	77.6
UT 15-13	15-13-7	6989	3.5	-2.1	4.0	96.0
UT 15-13	15-13-9	7006.5	4.8	0.0	0.0	100.0
UT 15-13	15-13-10	7007.8	2.1	-1.6	0.0	100.0
UT 15-13	15-13-11A	7009.9	2.9	-7.3	0.0	100.0
UT 15-13	15-13-11B	7009.9	3.9	-2.6	6.1	93.9
UT 15-13	15-13-12	7016.4	4.7	-4.6	14.9	85.1
UT 15-13	15-13-13	7017.4	4.7	-4.8	12.6	87.4
UT 15-13	15-13-14	7025.2	6.0	-1.3	0.0	100.0
PW 13-06	13-06-1	5524.2	2.5	0.5	8.2	91.8
PW 13-06	13-06-2	5524.7	2.3	-4.7	7.3	92.7
PW 13-06	13-06-3	5527.3	3.4	1.1	2.0	98.0
PW 13-06	13-06-5	5537.3	0.4	-6.5	100.0	0.0
PW 13-06	13-06-6	5539.5	4.3	-1.5	1.6	98.4
PW 13-06	13-06-6B	5540.7	3.7	-0.4	0.0	100.0
PW 13-06	13-06-7	5541.9	4.3	-2.6	0.0	100.0
PW 13-06	13-06-7B	5542.7	3.7	-0.7	0.0	100.0
PW 13-06	13-06-8	5543.5	3.5	-2.8	0.0	100.0
PW 13-06	13-06-9	5544.3	2.7	-2.2	0.0	100.0
PW 13-06	13-06-10	5545.3	3.3	-4.3	15.5	84.5



Well	Sample	Depth	$\delta^{13}\text{C}$ (VPDB)	$\delta^{18}\text{O}$ (VPDB)	%Cal	%Dol
PW 13-06	13-06-10A	5546.1	3.5	-3.3	12.9	87.1
PW 13-06	13-06-10B	5551	2.2	-6.2	6.3	93.7
PW 13-06	13-06-11A	5553.9	1.1	-5.4	68.3	31.7
PW 13-06	13-06-11B	5554.7	1.0	-4.8	0.9	99.1
PW 13-06	13-06-11C	5556.6	1.2	-2.9	48.6	51.4
PW 13-06	13-06-12	5557.4	1.9	-6.0	0.0	100.0
PW 13-06	13-06-13	5563.3	1.1	-4.1	20.2	79.8
PW 13-06	13-06-14	5565.9	-0.9	-9.6	98.4	1.6
PW 13-06	13-06-15	5580.8	-0.9	-6.5	40.1	59.9
PW 13-06	13-06-16	5595.4	-0.5	-1.5	0.0	100.0
PW 13-06	13-06-17	5596	2.9	-2.2	0.0	100.0
PW 13-06	13-06-18	5603.4	0.1	-6.1	98.2	1.8
PW 13-06	13-06-19	5607.8	2.5	-1.4	3.4	96.6
DS 11-20	11-20-1	4972.5	-3.0	-3.8	36.7	63.3
DS 11-20	11-20-2	4974.5	-0.7	-5.3	98.5	1.5
DS 11-20	11-20-4	4980.1	-2.0	-0.8	3.5	96.5
DS 11-20	11-20-5	4985.5	-1.0	-2.4	9.5	90.5
DS 11-20	11-20-8	4989.5	-0.1	-4.8	97.5	2.5
DS 11-20	11-20-9	4990.45	-1.1	-3.5	31.9	68.1
I 16	16-1	4701.3	-0.8	0.5	0.0	100.0
I 16	16-2	4705.4	3.1	-4.0	13.3	86.7
I 16	16-3	4706.3	0.9	-5.6	30.5	69.5
I 16	16-4	4707	-1.3	-4.4	13.1	86.9
I 16	16-7	4720.8	-0.9	0.1	4.3	95.7
I 16	16-8	4721.25	0.5	-3.0	28.0	72.0
I 16	16-10	4723.3	0.2	-3.6	14.1	85.9
I 16	16-11	4724.2	-1.0	-2.0	35.7	64.3
I 16	16-19	4735.8	-2.1	-4.6	4.6	95.4

Precision and accuracy as  $1\sigma$  of (n=10) lab standards are (i) 0.2 for  $\delta^{13}\text{C}$  and (ii) 0.2 for  $\delta^{18}\text{O}$ .